

**Investigation into nasal saline irrigation within a  
healthy human nose.**

**Hana Salati**

A thesis submitted to

Auckland University of Technology

in fulfilment of the requirements for the degree of

**Doctor of Philosophy (PhD)**

**2019**

School of Engineering, Computer and Mathematical Sciences

# ABSTRACT

Nasal saline irrigation is a therapy that bathes the nasal mucosa with a liquid saline solution to treat inflammatory nasal and paranasal disease or manage post nasal and sinus surgery recovery. Saline irrigation is thought to improve nasal airway surface liquid (ASL) hydration and mucociliary transport. Also, it has previously shown that mechanical factors, including cyclic pressure and wall shear stresses distribution, may positively influence mucociliary clearance.

A detailed saline flow analysis within the nasal cavities and maxillary sinuses during saline irrigation in various head positions and side directions, in the presence of a nasal cycle geometry, has not previously been investigated. Knowledge of the saline flow fields within the nasal cavities and maxillary sinuses during nasal saline irrigation is essential to an understanding of how different head positions and side directions affect the targeted delivery site, and whether the irrigant has the potential to stimulate the mucociliary functions at different regions of the nasal cavities and maxillary sinuses. In this thesis the distribution and pressure of the irrigant, and the mucosal wall shear stress in the human nasal cavities and maxillary sinuses, have been mapped during nasal saline irrigation using computational fluid dynamics (CFD) simulations in the presence of the nasal cycle at four different head positions: Mygind (lying with head back),  $90^\circ$  (tilting the head sideways at  $90^\circ$ ), head back (head is oriented  $45^\circ$  upward from the ground), and head forward (head is inclined downwards at  $45^\circ$  to the ground).

Particle image velocimetry (PIV) measurements have been applied to confirm the validity of the numerical methodology used in this study. Close agreement was found between numerical and experimental results performed under identical conditions and geometries.

New findings of this study have shown that saline irrigation at different head positions and side directions results in different saline distribution and saline pressure and mucosal wall shear stress distribution.

The findings of this study will allow both clinicians and patients to make better-informed decisions on optimal irrigation techniques to better realise the full benefits of this form of treatment.

# Contents

ABSTRACT.....	i
LIST OF FIGURES .....	vi
LIST OF TABLES .....	xi
ATTESTION OF AUTHORSHIP .....	xii
ACKNOWLEDGMENTS .....	xiii
Chapter 1: Introduction .....	1
1.1    Background .....	1
1.2    Thesis Structure .....	2
Chapter 2: Literature review .....	5
2.1    Nasal anatomy and morphology .....	5
2.1.1    Paranasal sinuses .....	7
2.2    Mucociliary clearance .....	8
2.2.1    Purinergic regulation .....	9
2.2.2    Mechano-stimulation of ATP release .....	11
2.3    Nasal pathophysiology .....	12
2.4    Nasal treatment methods .....	13
2.4.1    Topical treatments .....	13
2.4.2    Nasal saline irrigation .....	13
2.5    Measurement methods .....	20
2.5.1    Particle image velocimetry (PIV) .....	20
2.5.2    Numerical simulation .....	21
2.6    Research questions .....	22
2.7    Research hypotheses.....	22
2.8    Research plan and objective .....	23
2.9    Summary .....	24
Chapter 3: CFD configuration testing in a simplified nasal model.....	26
3.1    Introduction .....	26
3.2    Background .....	26
3.3    Geometry .....	27
3.4    Delivery device, head positions, and flow directions.....	30
3.5    Numerical modelling .....	31
3.6    Experimental setup .....	34
3.7    Validation of results .....	38
3.7.1    Mygind position irrigated from patent side.....	38
3.7.2    Mygind position irrigated from congested side .....	43

3.7.3	90° head position irrigated from patent side .....	47
3.7.4	90° head position irrigated from congested side .....	51
3.7.5	Head back position irrigated from patent side .....	55
3.7.6	Head back position irrigated from congested side .....	58
3.8	Discussion .....	62
3.9	Summary .....	63
Chapter 4:	<i>In-vivo</i> computational and realistic nasal model development .....	65
4.1	Introduction .....	65
4.2	Background .....	65
4.3	Nasal cavities and maxillary sinuses geometry development .....	66
4.3.1	Processing MRI image data .....	66
4.4	Nasal saline irrigation CFD setup .....	70
4.4.1	Model configuration.....	70
4.4.2	Steady state modelling configuration.....	70
4.4.3	Convergence criteria .....	71
4.4.4	Turbulence model .....	72
4.4.5	Boundary conditions .....	72
4.4.6	Head positions.....	73
4.4.7	Meshing and sensitivity analysis.....	75
4.5	Nasal model casting.....	76
4.6	Summary .....	77
Chapter 5:	Validation of CFD realistic nasal Model using Planar PIV .....	78
5.1	Introduction .....	78
5.2	Background .....	78
5.3	Experimental setup .....	81
5.3.1	Fluid circuit.....	81
5.3.2	Validation methodology.....	85
5.4	Results .....	87
5.4.1	Mygind head position irrigated from the right patent side.....	87
5.4.2	Mygind head position irrigated from the left congested side.....	89
5.4.3	90 ° head position irrigated from the right patent side.....	92
5.4.4	90 ° head position irrigated from the left congested side.....	94
5.4.5	Head back position irrigated from the right patent side.....	96
5.4.6	Head back position irrigated from left congested side.....	99
5.4.7	Head forward position irrigated from patent side .....	102
5.4.8	Head forward position irrigated from left congested side.....	104

5.5	Analysis of relative error between PIV and CFD results .....	104
5.6	Summary .....	105
Chapter 6: CFD irrigation flow field results within nasal cavities and maxillary sinuses .....		107
6.1	Introduction .....	107
6.2	Results .....	107
6.2.1	Mygind head position irrigated from right patent side.....	108
6.2.2	Mygind head position irrigated from left congested side.....	113
6.2.3	90° head position irrigated from right patent side.....	117
6.2.4	90° head position irrigated from left congested side.....	122
6.2.5	Head back position irrigated from right patent side.....	126
6.2.6	Head back position irrigated from left congested side.....	131
6.2.7	Head forward position irrigated from right patent side.....	135
6.2.8	Head forward position irrigated from left congested side.....	140
6.3	Discussion .....	144
6.3.1	Mygind head position (patent and congested side irrigation) .....	144
6.3.2	90° head position (patent and congested side irrigation) .....	145
6.3.3	Head back position (patent and congested side irrigation) .....	146
6.3.4	Head forward position (patent and congest side irrigation) .....	147
6.3.5	Nasal cavity distribution (all head positions).....	147
6.3.6	Maxillary sinus penetration.....	149
6.4	Summary .....	154
Chapter 7: Conclusions and future work.....		156
7.1	Conclusions .....	156
7.2	Future work .....	164
REFERENCES.....		165
Appendix A: Sensor data sheet .....		172
Appendix B: Mesh sensitivity analysis .....		173
Appendix C: Model creation.....		175
Appendix D: Clinical guide sheet .....		183

# LIST OF FIGURES

Figure 2.1. Lateral wall of the nasal cavity showing the inferior, middle and superior turbinates (10). .....	5
Figure 2.2. Coronal plane of the nasal cavities including upper (superior), middle, and inferior turbinates and maxillary sinuses (15).....	6
Figure 2.3. Coronal plane through the paranasal sinuses (16). .....	7
Figure 2.4. The mucosal surface lining the nasal airways consists of ciliated pseudostratified columnar epithelium and goblet cells bathed in airway a surface liquid overlaid by a thin mucus layer (26).....	8
Figure 2.5. Effect of hypertonic saline on the airway surface liquid (34). .....	10
Figure 2.6. The effect of a) shear stress (39) b) pressure stress (36) on ATP release.....	12
Figure 2.7. NeilMed Nasaflo Neti Pot (3). .....	15
Figure 3.1. Simplified model a) Isometric view b) Top view. The nasal passages were modelled using two straight pipes and a 180° curved pipe. The pipe cross-section was chosen to be circular with different diameters on the two sides to represent the patent and congested passages in the nasal cycle. The maxillary sinuses were represented using cylinders of equivalent volume.....	29
Figure 3.2. a) Mygind position b) 90° position c) head back position.....	31
Figure 3.3. A representative Neti Pot. H is the height of the 120 ml of saline in the Neti Pot and D is the diameter of the Neti Pot orifice. ....	33
Figure 3.4. Mesh sensitivity analysis at Mygind head position. ....	34
Figure 3.5. 3-D Physical simplified nasal model. ....	35
Figure 3.6. Schematic view of experimental setup. ....	37
Figure 3.7. a) Discharge rate versus time in the Mygind head position with irrigation from the patent side over 25 seconds b) first three seconds of the same result. ....	39
Figure 3.8. a) Physical model and b) Computational model results of liquid irrigation in the Mygind head position from with irrigation from the patent side at different time intervals; t=1.5s, t=15s, and t=23s. (blue= irrigation liquid and red=air). .....	41
Figure 3.9. Amount of irrigation liquid in each of the sinuses at different time intervals in computational and physical models in the Mygind head position when irrigated from patent side. ....	42
Figure 3.10. a) Discharge rate versus time in Mygind head position from the congested side over 25 seconds b) first three seconds of the same result.....	43
Figure 3.11. a) Physical model and b) Computational model results of irrigation at Mygind head position irrigated from the congested side at different time intervals t=0.6s, t=6.1s, and t=25s (Blue= irrigation liquid and red=air). ...	45
Figure 3.12. Amount of irrigation liquid in each of the sinuses at different time intervals in computational and physical models at Mygind head position irrigated from congested side. ....	46
Figure 3.13. a) Discharge rate versus time in 90° head position irrigated from the patent side over 25 seconds. b) First three seconds of the same result. ....	47
Figure 3.14. a) Physical model and b) Computational model results of irrigation at 90° head position irrigated from patent side at different time intervals t=0.55s, t=1.68s, and t=15.96s (Blue= irrigation liquid and Red=air). .....	49

Figure 3.15. Amount of irrigation liquid in the sinus on the congested side at different time intervals in computational and physical models at 90° head position when irrigated from patent side. No liquid enters the maxillary sinus on the patent side.....	50
Figure 3.16. a) Discharge rate versus time in the 90° head position when irrigated from the congested side over 2 seconds. b) First three seconds of the same result. ....	51
Figure 3.17. a) Physical model and b) Computational model results of irrigation in a 90° head position irrigated from the congested side at different time intervals t=1.68s, t=14.94s, and t=26s (blue= irrigation liquid and red=air). ....	53
Figure 3.18. Amount of irrigation liquid in the maxillary sinuses on the patent side at different time intervals in the computational and physical models in a 90° head position when irrigated from the congested side. No liquid enters the maxillary sinus on the congested side. ....	54
Figure 3.19. a) Discharge rate versus time at head back position with irrigation from the patent side over 25 seconds b) First three seconds of the same result. ....	55
Figure 3.20. a) physical model and b) computational model results of irrigation at head back position irrigated from patent side at different time intervals t = 1.2s, t = 7s, and t = 25s (blue= irrigation liquid and red=air). ....	57
Figure 3.21. Amount of liquid in each of the sinuses at different time intervals in computational and physical models at head back position irrigated from patent side.....	58
Figure 3.22. a) Discharge rate versus time at head back position with irrigation from the congested side over 25 seconds. b) First three seconds from the same result. ....	59
Figure 3.23. a) Physical model and b) Computational model results of irrigation at head back position irrigated from congested side at different time intervals t=0.5s, t=1.4s, and t=20s (blue= irrigation liquid and red=air). ....	60
Figure 3.24. Amount of irrigation liquid in each of the sinuses at different time intervals in computational and physical models in the head back position when irrigated from congested side. ....	61
Figure 4.1. Parasagittal slices of the head and neck used to create the nasal physical model a) MRI data set 1230 (T1-weighted) b) MRI data set 1232 (T2-weighted). ....	67
Figure 4.2. Exported geometry from the Scan IP a) prior to and b) after removal of the oropharynx. ....	68
Figure 4.3. Final smoothed nasal and maxillary sinuses solid model. ....	69
Figure 4.4. Cross sectional areas of the current nasal model and the standardized nasal model (113). ....	70
Figure 4.4. Saline flow properties within the nasal cavities and maxillary sinuses during nasal saline irrigation. ....	71
Figure 4.5. Geometry and boundary conditions showing right side irrigation inlet. ....	73
Figure 4.7. Different head positions considered for simulation: a) Mygind, b) 90°, c) head back, and d) head forward. ....	74
Figure 4.8. Meshing of the nasal cavity and maxillary sinus. ....	75
Figure 4.7. Completed transparent silicone nasal cavity and maxillary sinuses physical model. ....	76
Figure 5.1. Basic configuration of a Particle Image Velocimetry system (116). ....	79
Figure 5.2. Schematic view of the experimental fluid circuit. ....	82

Figure 5.3. Refractive index matching of the fluid with silicone model.....	84
Figure 5.4. Images demonstrating the four different head positions a) Mygind b) 90° c) head back d) head forward. ....	86
Figure 5.5. Comparison between CFD predicted results and PIV measurements of the normalized velocity field through a coronal cross-section of the nasal cavity at the Mygind head position irrigated from the right patent side.....	88
Figure 5.6. Comparison between CFD results and PIV measurements of the normalized velocity on a) L1, b) L2, and c) L3 on the coronal cross-section at Mygind head position irrigated from the right patent side (— CFD, ----PIV, and ---- error).....	89
Figure 5.7. Comparison between CFD results and PIV measurements of the normalized velocity field through a coronal cross-section of the nasal cavity at the Mygind head position irrigated from the left congested side.....	90
Figure 5.8. Comparison between CFD results and PIV measurements of the normalized velocity on a) L1, b) L2, and c) L3 on the coronal cross-section at the Mygind head position irrigated from the left congested side (— CFD, ----PIV, and --- error). ....	91
Figure 5.9. Comparison between CFD results and PIV measurements of the normalized velocity field through a coronal cross-section of the nasal cavity at 90° head position irrigated from the right patent side. ....	92
Figure 5.10. Comparison between CFD results and PIV measurements of the normalized velocity on a) L2 and b) L3 on the coronal cross-section at 90° head position irrigated from the right patent side (— CFD, ----PIV, and ---- error).....	93
Figure 5.11. Comparison between CFD results and PIV measurements of the normalized velocity field through a coronal cross-section of the nasal cavity at 90° head position irrigated from the left congested side. ....	94
Figure 5.12. Comparison between CFD results and PIV measurements of the normalized velocity on a) L1 and b) L3 on the coronal cross-section at 90° head position irrigated from the left congested side (— CFD, ----PIV, and ---- error).....	95
Figure 5.13. Comparison between CFD results and PIV measurements of the normalized velocity field through a coronal cross-section of the nasal cavity at head back position irrigated from the right patent side. ....	96
Figure 5.14. Comparison between CFD results and PIV measurements of the normalized velocity on a) L1, b) L2, and c) L3 on the coronal cross-section at head back position irrigated from the right patent side (— CFD, ----PIV, and ---- error). ....	98
Figure 5.15. Comparison between CFD results and PIV measurements of the normalized velocity field through a coronal cross-section of the nasal cavity in head back position irrigated from the left congested side. ....	99
Figure 5.16. Comparison between CFD results and PIV measurements of the normalized velocity on a) L1, b) L2, and c) L3 on the coronal cross-section at head back position irrigated from the left congested side (— CFD, ----PIV, and ---- error).....	101
Figure 5.17. Comparison between CFD results and PIV measurements of the normalized velocity field through a coronal cross-section of the nasal cavity at head forward position irrigated from the patent side.....	102
Figure 5.18. Comparison between CFD results and PIV measurements of the normalized velocity on a) L1, b) L2, and c) L3 on the coronal cross-section at head	

forward position irrigated from the right patent side (— CFD, ----PIV, and -- error). .....	103
Figure 6.1. Nasal geometry and selected planes. ....	108
Figure 6.2. Saline distribution contour at different coronal sections during Mygind head position irrigation from right patent side. ....	109
Figure 6.3. Pressure distribution within the nasal cavity for the Mygind head position irrigated from right patent side.....	110
Figure 6.4. Wall shear stress contour in Mygind head position irrigated from right patent side a) right patent passage b) left congested passage. ....	111
Figure 6.5. Average wall shear stress distribution within the nasal cavity during Mygind head position irrigated from right patent side. ....	112
Figure 6.6. Saline distribution contour at different coronal sections during Mygind head position irrigation from left congested side. ....	114
Figure 6.7. Pressure distribution within nasal cavity for Mygind head position irrigated from left congested side. ....	115
Figure 6.8. Wall shear stress contour in Mygind head position irrigated from left congested side a) right patent passage b) left congested passage. ....	116
Figure 6.9. Average wall shear stress distribution within the nasal cavity during Mygind head position irrigated from left congested side. ....	117
Figure 6.10. Saline distribution contour at different coronal sections during 90° head position irrigation from right patent side. ....	118
Figure 6.11. Pressure distribution within the nasal cavity for 90° head position irrigated from right patent side. ....	119
Figure 6.12. Wall shear stress contour at 90° head position irrigated from the right patent side a) right patent passage b) left congested passage. ....	120
Figure 6.13. Average wall shear stress distribution within the nasal cavity during 90° head position irrigated from right patent side.....	121
Figure 6.14. Saline distribution contour at different coronal sections during 90° head position irrigation from the left congested side.....	122
Figure 6.15. Pressure distribution within the nasal cavity for 90° head position irrigated from left congested side. ....	124
Figure 6.16. Wall shear stress contour at 90° head position irrigated from the left congested side a) right patent passage b) left congested passage. ....	125
Figure 6.17. Average wall shear stress distribution within the nasal cavity during 90° head position irrigated from left congested side.....	126
Figure 6.18. Saline distribution contour at different coronal sections during head back position irrigation from the right patent side.....	127
Figure 6.19. Pressure distribution within the nasal cavity for head back position irrigated from right patent side. ....	128
Figure 6.20. Wall shear stress contour at head back position irrigated from the right patent side a) right patent passage b) left congested passage. ....	129
Figure 6.21. Average wall shear stress distribution within the nasal cavity during head back position irrigated from right patent side. ....	130
Figure 6.22. Saline distribution contour at different coronal sections during head back position irrigation from left congested side. ....	132
Figure 6.23. Pressure distribution within the nasal cavity for head back position irrigated from left congested side. ....	133

Figure 6.24. Wall shear stress contour in head back position irrigated from the left congested passage a) right patent passage b) left congested passage. ....	134
Figure 6.25. Average wall shear stress distribution within the nasal cavity during head back position irrigated from left congested side. ....	135
Figure 6.26. Saline distribution contour at different coronal sections in head forward position irrigated from right patent side. ....	136
Figure 6.27. Pressure distribution within nasal cavity for head forward position irrigated from right patent side. ....	137
Figure 6.28. Wall shear stress contour at head forward position irrigated from the right patent side a) right patent passage b) left congested passage. ....	138
Figure 6.29. Average wall shear stress distribution within the nasal cavity for head forward position irrigated from right patent nasal passage. ....	139
Figure 6.30. Saline distribution contour at different coronal sections in head forward position irrigated from left congested passage. ....	141
Figure 6.31. Pressure distribution within nasal cavity for head forward position irrigated from left congested side. ....	142
Figure 6. 32. Wall shear stress contour at head forward position irrigated from the left congested passage a) right patent passage b) left congested passage. ....	143
Figure 6.33. Average wall shear stress distribution within the nasal cavity for head forward position irrigated from left congested side. ....	143
Figure 6.34. Percentage of saline volume within the nasal cavity at different head positions and inflow directions. ....	150
Figure 6.35. Saline residual in maxillary sinuses at different head positions for a) patent side irrigation b) congested side irrigation. ....	152
Figure B.1. Mesh sensitivity analysis at Mygind head position irrigated from right patent side a) pressure distribution and b) sinus penetration. ....	174
Figure C.1. Designed solid model for model casting. ....	175
Figure C.2. Rapid prototyped model. ....	176
Figure C.3. a) Picture view of casting box and b) constructed casting box. ....	177
Figure C.4. Mixing of the monomer and catalyst. ....	179
Figure C.5. Degassing procedure using vacuum chamber. ....	179
Figure C.6. Silicone pouring using a funnel around the ABS model. ....	180
Figure C.7. Cured silicone and the ABS model a) before and b) after removing the casting box. ....	180
Figure C.8. Schematic view of the model in the ultrasonic resonator. ....	181
Figure C.9. Completed transparent silicone nasal cavity and maxillary sinuses physical model. ....	182
Figure D.1. Clinical treatment guide sheet. ....	184

# LIST OF TABLES

Table 2.1. Classification of nasal irrigation delivery devices (55). .....	14
Table 2.2. Impact of different delivery devices on saline nasal irrigation. ....	17
Table 3.1. Simplified model dimensions. ....	29

## **ATTESTION OF AUTHORSHIP**

I hereby declare that this submission is my own work and that, to the best of my knowledge and belief, it contains no material previously published or written by another person (except where explicitly defined in the acknowledgments), nor material which to a substantial extent has been submitted for the award of any other degree or diploma of a university or other institution of higher learning.

Auckland

Signature\_\_\_\_\_

Hana Salati

# ACKNOWLEDGMENTS

Firstly, I would like to express my sincere gratitude to my supervisors Dr David White, A/Prof. Roy Nates, and A/Prof. Jim Bartley, for their continuous support of my Ph.D study. Their guidance helped me throughout the time of researching and writing this thesis. They were always supportive and calm and they taught me how to be always optimistic.

I would like to express my greatest gratitude to my family, especially my mother, my sister and brother, for supporting me spiritually throughout the writing of this thesis and in my life in general. I'd like to present my sincere thankfulness, and to dedicate this thesis, to my deceased father who always believed in my ability to be successful in life and for his great role in my life. You are gone but your belief in me has made this journey possible.

My sincere thanks also go to Sina Ghafoorpoor Yazdi, Dr Paul Docherty, and Prof. Mark Jermy, without whose precious support it would not have been possible to conduct the experimental part of this study.

I would like to thank my love Mehrdad Khamooshi who has supported me throughout this journey and I would not have been able to finish this work without his support. Also I thank my friends and colleagues at AUT BioDesign Lab: Manpreet Singh, Dr Michael Gschwendtner and Dr Chris Whittington.

## **Ethical Approval**

In this study, the MRI image sets were captured from a 49 year-old European male with approval from the Auckland University of Technology Human Ethics Committee (ref. 10/121 date: 14/07/2010).

# Chapter 1: Introduction

## 1.1 Background

Nasal irrigation describes the process of passing saline solution through the nasal passages which is frequently used in the management of inflammatory nasal and paranasal disease. It is also used to assist in post nasal and sinus surgery recovery. Saline irrigation is thought to improve nasal mucosa function through several physiologic effects including the mechanical removal of inflammatory agents (allergic and infectious), inflammatory byproducts and post-surgical debris and improving the mucociliary function as suggested by increased ciliary beat frequency and airway surface liquid (ASL) hydration. Studies have shown that mechanical factors, including cyclic pressure and wall shear stress distribution, and saline tonicity may influence mucociliary clearance. Previous experimental and numerical studies have recorded saline distribution, however, these studies were limited solely to observation and not include identification of regions where mechano-stimulation occurs. No previous nasal irrigation studies have investigated the saline flow fields including pressure and wall shear stress distributions within the nasal cavities and sinuses during nasal saline irrigation.

Nasal geometry is periodically altered by the nasal cycle, a physiological process that occurs approximately every ninety minutes where airflow in one side of the nose is congested while the other side is more patent. Previous studies have not included the influence of the nasal cycle on nasal resistance and nasal saline irrigation flow, therefore these earlier studies have not considered the effect of different side directions on nasal saline irrigation.

A detailed flow analysis of the nasal cavities and maxillary sinuses during saline irrigation in various head positions and side directions, in the presence of a nasal cycle in

anatomically accurate a nasal cavities and maxillary sinuses' geometry, has not previously been investigated.

Computational fluid dynamics (CFD) is well suited to predicting complex flow patterns including shear and pressure stress distributions, and because of this it was chosen for the current work for measuring the flow field in the nasal cavities and maxillary sinuses. Only a small number of CFD studies of nasal saline irrigation have been undertaken and all have been previously limited to flow visualization (1, 2).

Our current knowledge of nasal saline irrigation is largely based on very limited visualization data over a limited range of head positions and flow directions (3-5). Therefore the aim of this research is to investigate thoroughly the effects of the wide range of head positions and the nasal cycle on saline flow field, including the distribution, pressure, and wall shear stress using CFD simulation. This study contributes to a detailed analysis of saline flow fields at various head positions and inflow side directions during the nasal cycle, leading to a better understanding of how the saline nasal irrigation distribution to different regions of the nasal cavities is influenced by these conditions. This study will also help to establish whether the irrigant has the potential to stimulate the mucociliary functions at specific regions of the nasal cavities and maxillary sinuses based on mucosal pressure and wall shear stress distribution. The findings from this work will allow both clinicians and patients to make better-informed decisions on optimal irrigation techniques to target desired regions for treatment.

## **1.2 Thesis Structure**

The thesis is structured in the following way:

Chapter 2 reviews the current literature on nasal saline irrigation. Nasal and paranasal sinus anatomy, morphology, and common nasal diseases treated by irrigation are described. The common treatment methods are introduced and the benefits of topical

treatments discussed. Different nasal saline irrigation delivery devices and their evaluation methods are described and gaps in the current knowledge identified. This leads to development of the research questions used in this investigation.

Chapter 3 introduces a simplified nasal geometry model in both computational and physical forms. The aim of this chapter is to test and validate the CFD configuration to simulate saline irrigation. In this chapter, a summary of the computational setup to simulate saline irrigation through the nasal cavities and maxillary sinuses geometry is described and validated for later use in more complex *in-vivo* nasal geometry and maxillary sinuses. The results of this initial investigation were used to guide the selection of the most suitable computational method to be later used in the analysis of saline distribution, pressure, and wall shear stress distribution in realistic human nasal cavities and maxillary sinuses during saline irrigation.

Chapter 4 applies the selected computational methodology in an accurate *in-vivo* representation of human nasal geometry and maxillary sinuses, obtained from MRI scans. A summary of the manufacturing procedure for producing an accurate transparent replica physical model of the nasal cavities and maxillary sinuses, suitable for use in validating CFD results using optical flow measurement techniques, is described.

Chapter 5 implements *in-vivo* physical nasal model geometry in a series of planar particle image velocimetry (PIV) measurements which compares the normalized velocity field at a specific region of the nasal cavities with CFD results. These measurements are used to confirm the validity of the applied numerical methodology used in this realistic nasal morphological study.

After validating the numerical methodology, Chapter 6 presents the results of computational testing of saline irrigation through the *in-vivo* nasal cavities and maxillary sinus model. The results include irrigant distribution, pressure, and wall shear stress in different head positions and irrigation mucosal contact through the patent or congested

nasal passages. The results show how different head positions and nasal patency affect the irrigation distribution and target irrigation delivery sites. The influence of different user conditions including different head positions and inflow side directions have on irrigant pressure and wall shear stress distribution in specific regions is also described. Chapter 7 concludes the key original findings of this thesis and presents possible future developments and applications for this research.

The findings of this work show that whenever the irrigation is performed from the congested side, the restricted cross-sectional area of the congested side decreases the irrigant pressure and results in less distribution and penetration on the contralateral side. The ostial orientation, with respect to gravity and irrigant pressure at the sinus ostia entry, also influences irrigation penetration of the sinus. The sinus irrigation penetration at different head positions and side directions is different. For all head positions and side directions, the wall shear stress is higher on the left congested side than that found in the right patent side due to the narrower geometry and higher curvature of the turbinates. The findings of this study provide the answers to the research questions of this study by identifying the irrigation mucosal contact (which regulates the ASL hydration) and by mapping the irrigant pressure and mucosal wall shear stress (which act as mechano-stimulation for nasal mucociliary clearance) at different head positions and inflow side directions.

## Chapter 2: Literature review

### 2.1 Nasal anatomy and morphology

Beginning at the nostrils (external nares), the internal nose consists of two discrete parallel airways with the septum medially and the nasal walls laterally (Figure 2.1) (6, 7). Commencing at the anterior region of the nose, the external nose encloses the nasal vestibule, which is lined with hair (vibrissae) which filter out large particles (8). Moving posteriorly, through the nasal vestibule, the nasal cross-sectional area constricts to a minimum in a region called the nasal valve. The main function of this region is to regulate nasal airflow (9). Posterior to the nasal valve, the lateral nasal wall consists of the inferior, middle and superior turbinates. These turbinates create a large surface area, which aid in the humidification, warming and filtering of inspired air. Olfaction (smell) receptors are located above the superior turbinate in the olfactory epithelium at the top of the nasal cavities. Moving posterior, the separate nasal airways then merge at the posterior choanae joining the nasopharynx. The nasopharynx is the superior part of the pharynx and is positioned above the soft palate (6)

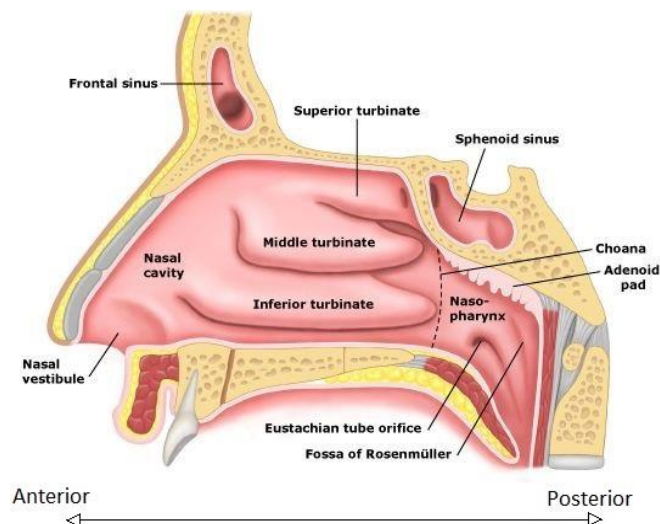


**Figure 2.1. Lateral wall of the nasal cavity showing the inferior, middle and superior turbinates**

(10).

Figure 2.2 shows a coronal plane through both nasal cavities. During inhalation, air enters the nose through both nostrils at different flow rates because each side of the nose has a different air flow resistance. The nasal resistances of the nasal cavities are changing continuously due to alternating congestion and decongestion states of the nasal erectile tissue, including the turbinates within the nose (11). This phenomenon, called the nasal cycle, occurs in 80% of healthy humans, causing one nasal passage to be noticeably more restricted to airflow (congested) than the other (patent), with most of the airflow passing through the more patent nasal passage (12). During periods of nasal infection and inflammation, the amplitude and frequency of the nasal cycle increases (13). This may be due to the higher amplitude of the nasal cycle resulting in a smaller cross-sectional area in the nasal passage, which increases the airflow velocity and therefore the mucosal wall shear stress. Increasing the mucosal wall shear stress improves the mucociliary clearance function, which will be discussed later in this chapter. The nasal cycle is also thought to play a role in regulating simultaneous nasal air conditioning and mucociliary clearance duties within the nose (14). To find which side of the nose is congested, a subject can occlude one nostril with a finger and breathe through the other nostril, and then repeat this for the other nostril. The side in which the subject breathes more easily is the patent side and the other side is the congested side.

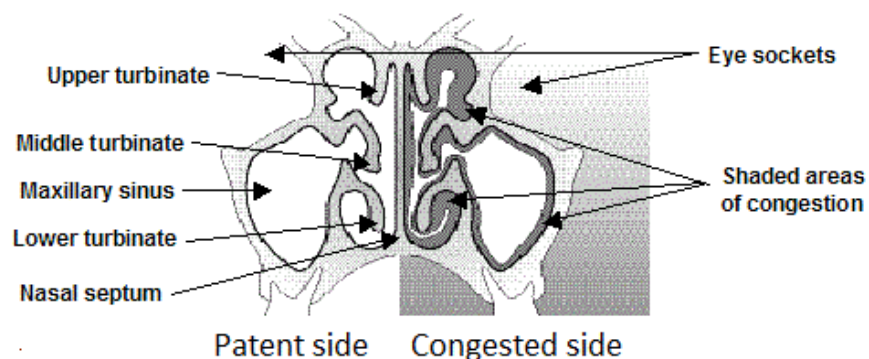


**Figure 2.2. Coronal plane of the nasal cavities including upper (superior), middle, and inferior turbinates and maxillary sinuses (15).**

### 2.1.1 Paranasal sinuses

The paranasal sinuses are an interconnected system of hollow air-filled cavities in the skull which link into the conducting nasal airways. The sinus cavities (Figure 2.3) include (16):

- The maxillary sinuses (the largest), in the cheekbones linked to the middle meatus via the ostium, infundibulum and hiatus semilunaris.
- The frontal sinuses, in the low-centre of the forehead (frontal bones).
- The anterior and posterior ethmoid sinuses, between the eyes, at the nasal bridge.
- The sphenoid sinuses, in the sphenoid bones behind the nasal cavities.

The functions of the paranasal sinuses are currently largely unknown, however they produce nitric oxide (NO) (17) which is known to regulate a number of physiological processes including mucociliary transport and also has antimicrobial actions (18). Other possible functions proposed for the paranasal sinuses are that they reduce the weight of the skull and add resonance to the voice (19). The nasal cycle is thought to also help NO accumulation within the paranasal sinuses (20).

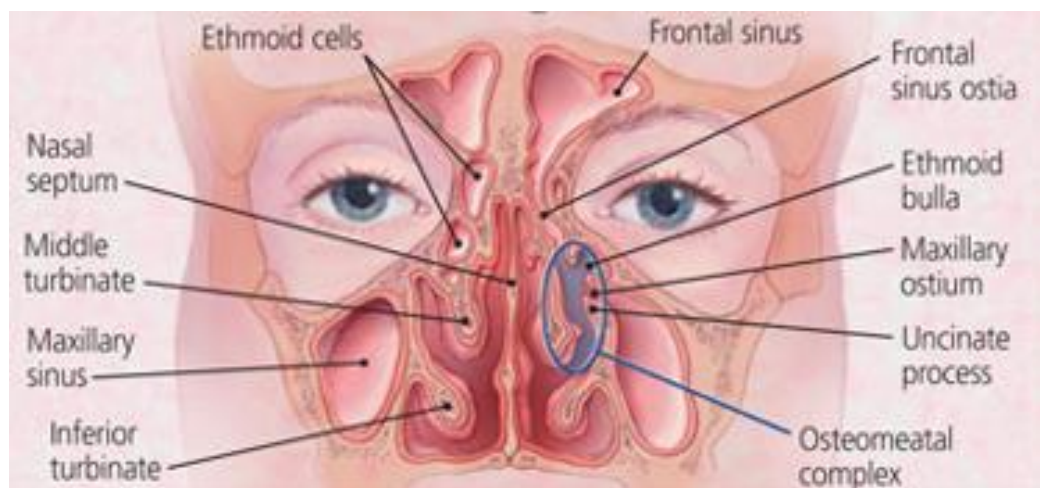
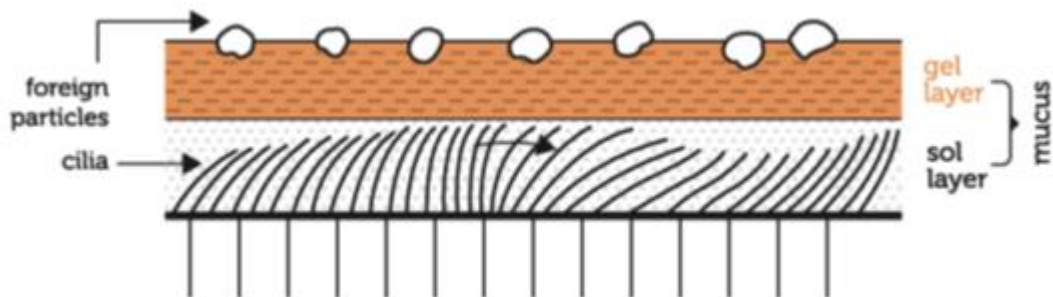


Figure 2.3. Coronal plane through the paranasal sinuses (16).

## 2.2 Mucociliary clearance

Mucociliary clearance provides an important defence mechanism within the human respiratory airways (21). In healthy people, the respiratory tract is protected from airborne infection and debris by a mucociliary layer (22, 23) that lines the sinonasal cavities and the conducting airways. The mucosal surface lining the nasal airways consists of ciliated pseudostratified columnar epithelium and goblet cells bathed in a surface liquid overlaid by a thin mucus layer (Figure 2.4). Inhaled foreign particles, debris, and pathogens are trapped in the sticky mucus layer, which is slowly propelled towards the oropharynx where it is either swallowed or expectorated. The movement of the mucus layer is driven by the coordinated cilia beat. An experimental study showed that bathing the epithelial surface with hypertonic saline solution (1.5-3%) (24) enhances the ciliary beat frequency and is a determining factor in the mucociliary transport rate in the nose (25).



**Figure 2.4.** The mucosal surface lining the nasal airways consists of ciliated pseudostratified columnar epithelium and goblet cells bathed in airway a surface liquid overlaid by a thin mucus layer (26).

A sol layer (periciliary liquid layer [PCL]) keeps mucus at an optimum distance from the underlying beating cilia where the PCL approximate the length of the cilia. The airway surface liquid (ASL) is composed of the mucus and sol layer. For effective mucus clearance, airway surface liquid (ASL) volume regulation is important because the ability of the airway to clear mucus is strongly dependent on the height of the ASL. In the larger airways, mucus comes mostly from sub mucosal glands; the remainder comes from goblet cells in the surface epithelium (27). The removal and disposal of debris, allergens and pathogens occurs normally in healthy nasal passageways, however inefficient mucociliary transport can lead to mucosal infection and inflammation (28).

### **2.2.1 Purinergic regulation**

Absorption and discharge of ASL fluid across epithelia happens by  $\text{Na}^+$  absorption and  $\text{Cl}^-$  secretion through cellular ion channels. Airway epithelial cells respond, to extracellular molecules and ionic concentrations via receptors and channels (29). These responses result in the blocking, or secretion/absorption of specific fluids passing through the cell membrane. The purinergic regulation system is composed of these receptors and channels. Mucin secretion, the release of intracellular ionic fluids, and ciliary driving actions are controlled by epithelial cell purinergic pathways (30). Normally, the NaCl concentration of the periciliary liquid layer (PCL) is essentially the same as in the epithelial cell (31). Secreted salt from the epithelia followed by water in order to maintain tonicity, leads to ASL hydration through a PCL volume increase (32). Conversely, if salt is absorbed by the epithelia, water will follow into the cells, resulting in ASL dehydration and PCL volume reduction. These ion channels can switch between secretion and absorption phenotypes (33).

In a healthy airway epithelia, the hydration of the ASL that consists PCL and the mucus layer is regulated through the ion channels. (Figure 2.5a). Ion channel impairment, such as that which occurs in cystic fibrosis sufferers results in dehydration of the ASL with

thick mucus accumulating causing the PCL to collapse. (Figure 2.5b). Bathing the epithelial surface with hypertonic saline results in an increase in mucus clearance by decreasing the mucus viscosity. The high salt concentration encourages osmosis of water into the ASL rehydrating the mucus and partially restoring the PCL, allowing for easier clearance of mucus (34).

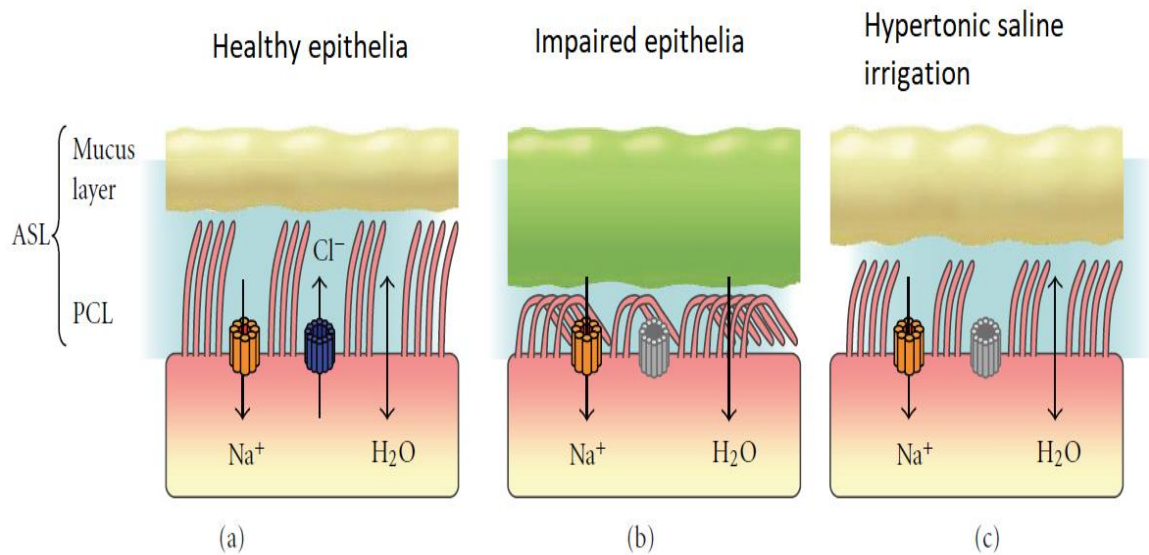


**Figure 2.5. Effect of hypertonic saline on the airway surface liquid (34).**

### **2.2.2 Mechano-stimulation of ATP release**

Epithelial water flux possibly adjusts PCL volume during tidal breathing as a result of tidal breathing induced shear and direct pressures stresses (35). Extracellular nucleotides such as adenosine triphosphate (ATP) are considered essential regulators of mucus clearance in the airways. ATP is capable of stimulating fluid secretion, mucus hydration, and ciliary beat frequency (36). Increasing the ATP-level results in an improvement of mucociliary clearance (35). ATP release is greatly enhanced in human airway epithelia exposed to physical cyclic tidal breathing forces that induce cyclic pressure and shear stress (36). Shear force acts as a physiological stimulus for ATP release within airways and increasing shear force on the epithelial surfaces results in higher ATP release. The ATP levels for wall shear stress of 0.001 Pa (Pascal), and 0.6 Pa, are about 0.1nM (nanoMolar) and 70 nM, respectively (37). During natural breathing, the wall shear stress is estimated to reach 0.3 Pascal (38). The relation between the amounts of secreted ATP on a wide range of shear stress values was discussed by Taran et al. (39). During a cough, the induced flow caused 17 Pascal of shear stress, which was anticipated to release enough ATP to double mucus transport, and maximise pathogen clearance (40).

Cyclic compressive pressure is another mechanical stimulus that increases the release of ATP at the epithelial surface. Button et al. (36) found that at a cyclic pressure stress of between 0 to 490 Pa, the ATP release increased rapidly, and after 490 Pa the rate of increasing ATP release relaxed. The effect of wall shear stress and pressure stress on ATP release is shown in Figure 2.6. It is possible to conclude that by increasing the wall shear and pressure stress, the rate of ATP release is enhanced, which improves the mucociliary clearance functions.

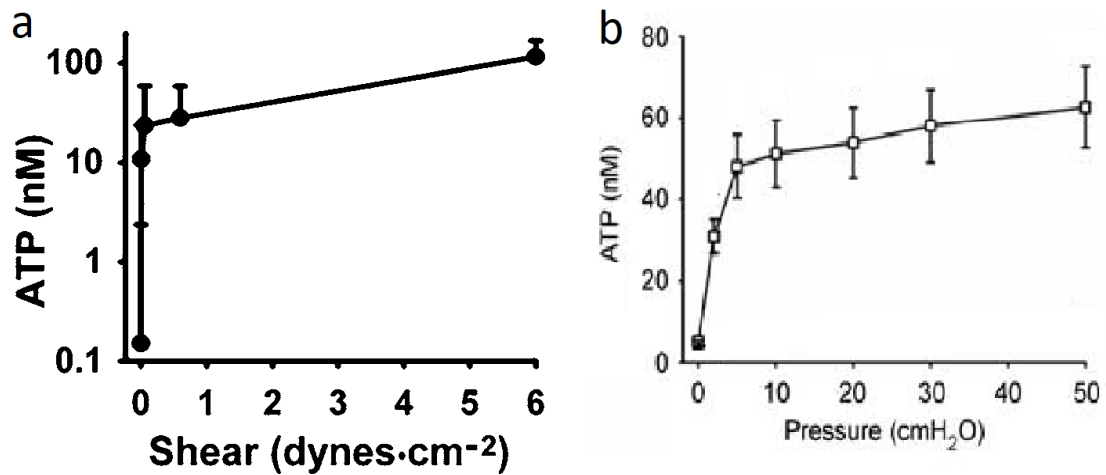


**Figure 2.6.** The effect of a) shear stress (39) b) pressure stress (36) on ATP release.

All previous studies which examined the shear stress distribution within the nasal cavities were devoted to airflow. Saline is a more viscous fluid compared to air, and nasal saline irrigation can provide additional shear stress and pressure (41-43) and stimulate purinergic regulation, all of which can be beneficial to mucociliary clearance.

### 2.3 Nasal pathophysiology

Rhinitis is a term used to describe nasal membrane inflammation characterised by sneezing, nasal congestion, nasal itching, and rhinorrhea. Rhinitis can be caused by allergens (allergic rhinitis (AR)), or viruses and bacteria (infectious rhinitis) (44). Depending on whether sensitisation is due to seasonal pollens or year-round allergens, AR is categorised as seasonal or perennial (45). Nasal saline irrigation is often used to treat rhinitis (46) but there is insufficient knowledge of how different head positions and inflow side directions can target a desired location.

Along with the conducting nasal airways, the paranasal sinuses can also become infected due to their poor mucociliary drainage into the conducting nasal passages. Mucus can accumulate in the sinus cavities due to poor mucociliary transport or the exit points becoming occluded. Inflammation of the paranasal sinus mucosa (rhinosinusitis) is divided into subtypes based on the symptom duration: acute rhinosinusitis (ARS) (less

than 4 weeks), subacute rhinosinusitis (between 4-8 weeks), and chronic rhinosinusitis (CRS) (more than 8 weeks) (47).

## **2.4 Nasal treatment methods**

The treatment of nasal and sinus disease depends on the disease symptom severity and symptom duration (48). A recommended treatment order for CRS patients is firstly nasal saline irrigation, followed by topical intranasal corticosteroids, oral corticosteroids and antibiotics, and lastly sinus surgery (49). Nasal saline irrigation is considered an effective preventative topical treatment, and is also used for post-operative care following functional endoscopic sinus surgery (FESS) (24).

### **2.4.1 Topical treatments**

Topical treatment is an attractive initial choice in the management of nasal and paranasal inflammatory diseases, and for nasal postoperative treatment, because it avoids systemic side-effects and can provide local drug delivery. Topical treatments include saline, anti-inflammatory medications such as steroids and alternative agents such as xylitol, manuka honey, and surfactant-containing solutions (50). Nasal saline irrigation is often used to manage AR and CRS symptoms. It is also considered useful in managing inflammatory nasal diseases in healthy people (51, 52). However, the effect of the nasal cycle on targeted irrigation within the nasal cavities and maxillary sinuses has not been reported. Specifically, saline flow properties, including mucosal pressure and wall shear stress distribution magnitudes in different nasal regions during irrigation, which may influence mucociliary transport have not previously determined.

### **2.4.2 Nasal saline irrigation**

Nasal saline irrigation is a therapy that bathes the nasal mucosa with a hypertonic liquid saline. Nasal saline irrigation improves mucus clearance, enhances ciliary beat activity, removes antigens biofilms and inflammatory mediators, and provides protection for the

sinonasal mucosa (53, 54). As discussed earlier saline irrigation can provide additional shear stress and pressure on the epithelial surface compared to air, and this can increase the ATP level which results in a better mucociliary clearance function. Some studies (55, 56) state that during irrigation, the distribution of saline within the nose is limited so, while it is beneficial, improvement is limited to the regions it can contact. Within the current literature there is no indication as to the influence inflow direction and head positions has on location of treatment.

#### **2.4.2.1 Nasal saline irrigation delivery devices**

In all delivery devices, saline irrigation is introduced into one nostril and drains out through the other nostril. Nasal saline delivery devices are generally categorised according to volume and pressure of delivery (56). Table 2.1 summarises the different delivery devices (55).

**Table 2.1. Classification of nasal irrigation delivery devices (55).**

	Positive/high pressure	Negative/low pressure
High volume	Squeeze bottle Bulb syringe Pressurised sprays Pulsatile jet	Neti Pot, Nasal inhalation
Low volume	Pump sprays Atomisation	Drops, Catheter instillation, Nebuliser

High volume devices, which range from 50 ml to 240 ml, include squeeze bottles, Neti Pots, bulb syringes, and powered irrigation devices. High-volume irrigation devices are more effective than low volume delivery methods in achieving saline delivery to the sinuses (16). This may be due to low volume delivery devices being unable to fill the nasal cavities so that the irrigant may not even reach the sinus ostium connecting the sinus cavity to the nasal cavity.

A Neti Pot (also known as a ‘nasal cup’) is a small container often plastic or ceramic, designed like a flattened tea Pot, that is used in gravity-flow nasal irrigation (57).

Nasal saline irrigation using a Neti Pot is a commonly used and is considered a therapeutically effective method for treating sinus infections (58). Many studies have examined the effect of Neti Pot (high volume delivery device) use on saline irrigation distribution in the nose and paranasal sinuses (43, 58-62). However these studies are limited solely to flow observation and there is no available data on flow field including shear and pressure stress distributions through the nasal cavities during irrigation using a Neti Pot.



Figure 2.7. NeilMed Nasaflo Neti Pot (3).

During Neti Pot nasal irrigation, while the user breathes through their mouth, the saline solution moves through one nasal cavity and its sinuses, distributes through the contralateral passage and its sinuses, before draining out the other nostril. During irrigation it is important that the soft palate needs to be closed so the user does not swallow the saline solution.

Low-volume delivery devices (drops, sprays, and simple nebulisers) range from 100  $\mu$ L to several millilitres are less suitable for nasal cavities treatments as they do not reach the sinus cavities. This may result in unnecessary expense without noticeable clinical benefits (55).

Statistical analysis of nuclear images [35], observation rating on endoscopy videotape [37] and computed tomography (CT) CT images [38], have all been used to evaluate the total distribution of saline irrigation through the nose and paranasal sinuses. Harvey et al. (3) used different nasal irrigation delivery devices including pressurised spray, Neti Pots and squeeze bottles to assess the distribution of solution in the paranasal sinuses after FESS in ten cadaver sinus systems. A high volume Neti Pot was more efficient in distributing saline throughout the nose than the squeeze bottle and pressurised spray respectively (56). This cadaveric study failed to consider the effect of the nasal cycle on nasal geometry. Additionally, the irrigations previously investigated were only performed uni-directionally with saline passing into the oropharynx rather than exiting via the other nasal cavity. During *in-vivo* nasal irrigation, the irrigant moves from one nostril towards the nasopharynx, then turns back to the other passage and exits via that nostril. With the nasal cycle, the nasal passages are no longer symmetrical. Most of previous studies did not consider the effect of different side directions on the saline distribution and flow field during the nasal cycle. A review of the impact of different delivery devices on nasal saline irrigation is summarised in Table 2.2.

**Table 2.2. Impact of different delivery devices on saline nasal irrigation.**

Authors	Year	Objective	Case study	Delivery device	Visualisation method	Remarks
Wormald et al. (63)	2004	Efficacy assessment of three different nasal irrigation methods on saline distribution	9 patients with CRS after FESS and 3 healthy subjects	1. Metered nasal spray 2. Nebulisation with RhinoFlow 3. Nasal douching	Nuclear medicine Imaging	All devices failed to reach sphenoid and frontal sinuses.
Harvey et al. (3)	2008	Studied the effect of the delivery device under each surgical condition on the distribution of solutions.	10 human cadaver heads	1. Neti Pot 2. Squeeze bottle 3. Pressurised spray	CT scan	The greatest and poorest distribution was observed with application of the Neti Pot and pressurised spray device after any surgery respectively. Poorly accessed areas are the frontal and sphenoid sinuses in the un-operated state. Cadaver heads are not representative of normal nasal anatomy.
Zhao et al. (1)	2015	Visualised dynamic flow of sinus irrigations by using CFD in pre- and postoperative sinonasal cavities	47-year-old male patient with CRS	1. Sinus rinse bottle 2. Sinugator	CFD simulation results	Fluid flow was unable to reach the maxillary ostium during irrigation after a Draf III procedure. Higher flow rate (sinus rinse bottle) caused slightly enhanced ethmoid sinus irrigation but resulted in less penetration of the contralateral maxillary sinus compared to the slow flow rate (Sinugator). Although irrigations were performed in both nostrils, there was no discussion of which side achieved higher distribution during nasal cycle.
Beule et al. (64)	2009	Postoperative irrigation was used to remove nasal crusts and to improve wound healing	19 cadaver heads	1. Spray 2. Squeeze bottle	Video-endoscopy	Squeeze bottle is a reliable method for irrigating the frontal neostium and sinuses after endoscopic Lothrop procedure and complete sphenoidectomy.  Cadaver heads are not representative of normal nasal anatomy.

Olson et al. (65)	2002	Compared different delivery devices for saline nasal irrigation	8 healthy adult volunteers	1. Positive-pressure 2. Negative-pressure 3. Nebuliser	CT scan Voxtool software	Positive-pressure irrigation retained a larger volume of contrast solution and irrigated the sinuses more than the other methods. Poorly irrigated areas were the sphenoid and frontal sinuses.
Snidvons et al. (66)	2008	Compared two delivery devices in delivering solution to the paranasal sinuses.	14 patients, with bilateral chronic rhinosinusitis	1. Nasal douche 2. Spray	CT scan	Both devices were unable to create enough pressure to deliver an irrigation solution into the paranasal sinus cavities.
Miller et al. (67)	2004	Compared the distribution patterns of topical medication delivery systems in the sinonasal region after FESS.	9 adult patients who had previously undergone bilateral endoscopic sinus surgery.	1. Spray bottle 2. Atomiser 3. Nebuliser 4. Bulb syringe	endoscopic	The bulb syringe was statistically better than atomiser and spray bottle in the ethmoidal region. Spray and atomiser were more effective than nebulisation in the posterior nasal cavity.
Valentine et al. (68)	2008	Compared sinonasal penetration of nasal douching to an optimised nasal nebuliser	14 cadavers	1. Squeeze bottle (200-ml) 2. Nebuliser	Video endoscopy	Squeeze bottle was better than nebuliser sinus device in all indices. Nebuliser reached ethmoid sinus (92% incidence). In contrast, the other sinuses were not reliably stained. Cadaver heads are not representative of normal nasal anatomy.
Campos et al. (69)	2013	Assessed different nasal douches regarding their physical rinsing parameters	Cadaver model	26 different nasal douches	-----	For nasal cavities and paranasal sinuses irrigation, compressible douching systems were suggested. Application of the sinus rinse (squeeze bottle) or the Rhino Douche looks to be beneficial for the postoperative follow-up. Cadaver heads are not representative of normal nasal anatomy.

All previous nasal irrigation models have not considered the effect of the nasal cycle on the applied geometry and most of them introduced saline into only one nare. It is currently unknown which is the best side for delivering irrigation to a targeted delivery site. While

all of these earlier studies have identified where the saline solution has travelled, none of these methods can provide the saline irrigation flow-field including pressure and shear stress exerted on the nasal mucosa and region of contact within the nose. The application of these methods in earlier studies has been limited to observation of the saline flow path and saline distribution in the nasal cavities. A systematic review on the efficacy of nasal saline irrigation in the treatment of sinus infective diseases (43), recommends a Neti Pot for nasal saline irrigation. This conclusion was based on clinical studies which evaluated the symptoms of patients using various delivery devices (70, 71). The irrigation device specifications (saline volume 120ml per nostril and aperture size of 6.65 mm) of a commercially available NeilMed NASAFLO Neti Pot were used in this study.

#### **2.4.2.2 Head position**

Nasal saline irrigation using a Neti Pot can be performed in different head position which can affect the irrigant distribution and penetration into the paranasal sinuses. Habib et al. (72) investigated the effect of two different head positions on the saline distribution in a cadaver model. Two head positions including the head-down-and-forward (angled to 40° below the horizontal plane), and lying-head-back (angled 60° below the horizontal plane), were considered. The results indicated that the lying-head-back position was superior for global distribution. Harvey et al. (3) also investigated the effect of saline distribution in a cadaver, using different delivery devices including the Neti Pot only at head positioned in the horizontal plane, and the irrigation was introduced to superior nostril. Changing the head position had previously been shown to affect the saline delivery to a specific region within the nasal cavities and paranasal sinuses (56). Head position is more important when using low pressure delivery devices because a low pressure irrigant may not be able to fully distribute throughout the nasal cavities, and the appropriate head orientation can direct the low pressure irrigant to a desired location. The Mygind head position is recommended for gravity-dependent devices (3) because it may allow the irrigant

drainage into the contralateral nasal cavity. Harvey et al. (3) mentioned that at a 90° head position, the fluid in the contralateral side of irrigation moves towards gravity direction to the lateral nasal wall. Different head positions are proposed for nasal saline irrigation, however, the effect of a wider range of head positions on the saline distribution using the Neti Pot has not previously been investigated.

## **2.5 Measurement methods**

Different measurement and visualisation methods are used to evaluate the distribution of nasal irrigation flow. PIV and CFD are two common tools used to investigate the flow field including velocity and wall shear stress distribution within the human respiratory system.

### **2.5.1 Particle image velocimetry (PIV)**

PIV is a powerful optical technique, which measures two or three-dimensional instantaneous velocities or other related spatial/temporal flow properties over a global domain. The PIV technique is an Eulerian measurement method that calculates fluid velocity as a function of position and time. Kelly et al. (73) measured the air velocity in a nasal cavity during natural breathing. In this study, their geometry was limited to one side of the nasal cavity. Nayebossadri (74) investigated the effect of human nasal blockage on nasal airflow dynamics, using a PIV method on a scaled-up silicon model of the nasal cavity constructed from the CT images of a healthy adult (74). Here the model was again limited to one side of the nasal cavity. One of the advantages of PIV is that it is a non-intrusive method which does not need hot-wires and pressure probes which can affect the flow pattern and which are limited to measure the flow velocity at a single point (75). While PIV has been previously used only in air-flow field measurement within the lower respiratory system, no studies have investigated nasal saline irrigation flow field in the nasal cavities and maxillary sinuses.

### 2.5.2 Numerical simulation

CFD models can provide results beyond those realisable by physical models, even when utilising complex geometries, because they are free from many of the constraints imposed on experimental methods, such as errors and the application of complex experiment boundary conditions. CFD models can also provide values for all the relevant variables (pressure, velocity, etc.) throughout the entire computational domain. However, validation assessment is required to determine whether the CFD predictions agree with physical reality, which can be done by using PIV measurements.

The validation of CFD models is performed usually by comparing the numerical CFD results to physical model test data. The complex nasal geometry used in the CFD model can be obtained from either MRI or CT scans. *In-vivo* image analysis is often clearer using MRI techniques compared to CT as it gives better soft tissue definition (76). MRI scans better show the effect of the nasal cycle on the geometry and complex morphology of the nasal airways (77). The previous CFD studies which observed nasal saline irrigation flow path within the nasal cavities used CT scans for geometry creation (1, 2, 78) and did not discuss the effect of the nasal cycle on the geometry.

CFD simulations have been used extensively in investigations of air-flow field and drug deposition within the nasal cavities and paranasal sinuses (74, 79-91).

Zhao et al. (1), applied CFD using CT imaging, however this technique poorly detects soft tissues to investigate nasal irrigation flow dynamics. Here, the saline path was studied and flow characteristics of velocity and pressure within the nasal geometry were overlooked. Investigation of the pressure and shear stress within the saline flow field should provide understanding of the relationship between saline flow characteristics and the mechano-stimulation of mucociliary function at a targeted region. The application of

CFD in saline irrigation has been previously limited to observational only and the saline flow field of pressure and shear stress within the nasal cavities is presently unreported.

## **2.6 Research questions**

A review of the current literature shows that none of the previous nasal irrigation studies have used morphologically accurate image scans, which includes nasal erectile soft tissue, to assess the effect of asymmetric nasal geometry on nasal irrigation pressure and wall shear stress distribution, and delivery sites over a range of realistic head positions and inflow directions. Additionally, no previous studies have utilised PIV techniques to validate CFD nasal irrigation flow fields' spatial/temporal characteristics within a morphologically realistic nasal geometry. This investigation will address these current knowledge gaps by addressing the following research questions:

- Can different head positions and inflow directions be used to target a nasal irrigation treatment site?
- How do different head positions and inflow directions affect the mucosal wall shear stress and pressure during nasal saline irrigation?
- How does nasal cycle status affect saline irrigation treatment?

## **2.7 Research hypotheses**

The working hypotheses of this study are:

- The asymmetric nasal geometry, caused by the nasal cycle, affects the nasal saline distribution by influencing the flow pressure field.
- Changing the head position affects the saline solution delivery to a specific region within the nasal cavities and paranasal sinuses.
- Different head positions and inflow directions affect the mucosal wall shear stress and pressure distributions.

## 2.8 Research plan and objective

In order to achieve the answers to the research questions and fulfil the working hypotheses stated, the following objectives have been identified:

- To determine the feasibility of using CFD in the assessment of nasal saline irrigation within a simplified nasal model.
- To apply a viable CFD method to investigate nasal saline flow patterns through both sides of an anatomically *in-vivo* representative nose model that includes the nasal cycle.
- To validate CFD method by comparing PIV and CFD results during nasal saline irrigation in *in-vivo* nasal cavities and the maxillary sinuses using an anatomically correct nasal model that considers the effect of the nasal cycle on the nasal cavities geometry.
- To investigate the effect of four different head positions and two inflow directions on nasal saline irrigation distribution, and target location delivery on an anatomically correct nasal model that considers the effect of the nasal cycle on the nasal cavities geometry.
- To measure the pressure field and wall shear stress mapping in the nasal cavities and maxillary sinuses during nasal saline irrigation using CFD on an anatomically correct nasal model that considers the effect of the nasal cycle on the nasal cavities geometry.
- To formulate recommendations on nasal saline irrigation based on CFD modelling that could lead to the more effective use of nasal saline irrigation in clinical practice.

This study investigates the flow paths and saline distribution within the nasal cavities and maxillary sinuses. It also maps the saline pressures and wall shear stress distribution in

the nasal cavities and maxillary sinuses to examine whether the irrigated saline could realise mechano-stimulation of mucociliary clearance in different regions of the nose.

In this study, the *in-vivo* nasal geometry representative of a point in the nasal cycle where the nasal air-flow rates were unequally shared between each side of the nose was derived from magnetic resonance imaging (MRI) scans of a normal subject. The investigations in this study are focused on the nasal cavities and maxillary sinuses because these are the targeted regions of interest for the management of CRS with saline irrigation. The purpose of this study is to identify the effect of different head positions and the differential airway resistance associated with the nasal cycle on the saline flow field through the nasal cavities and maxillary sinuses. The results of this investigation also contribute an understanding of how adjusting the user head position and in-flow direction can target a specific region of the nasal cavity and maxillary sinuses for irrigation treatment. The CFD methodology applied in this study was validated by comparing CFD and PIV results. PIV is a reliable measuring technique which is used in this study for the first time to measure the velocity field within an anatomically correct nasal model during nasal saline irrigation.

## **2.9 Summary**

This chapter has described the anatomy of the nasal cavities and paranasal sinuses. Nasal diseases and treatment methods have also been discussed. The physiological benefits of nasal saline irrigation on the ASL and mechano-stimulation of mucociliary clearance is explained. It was discussed how NaCl increases addition to the ASL mucus transport, and how shear stress and pressure provided by the irrigation can also increase ATP release and enhance mucociliary clearance. The function of the nasal cycle and its effect on the geometrical features of the nasal cavities were discussed, as well as the importance of the nasal cycle in regulating the functions of nasal cavities and paranasal sinuses. In order to investigate the inter-nasal fluid flow during the nasal cycle, it is essential to use *in-vivo*

asymmetrical geometry as a result of the nasal cycle to study both nasal passages. In order to reflect accurate *in-vivo* nasal geometry, MRI scans need to be taken from subjects experiencing different turbinate congestion states on each side of the nose.

This chapter concludes by reviewing the limitations of previous studies which attempted to investigate the efficacy of nasal saline irrigation using observational methods. The research questions and hypotheses have been developed in this study based on the findings of the literature review undertaken. The research plan and objectives of this study have been developed to answer these research questions.

# Chapter 3: CFD configuration testing in a simplified nasal model

## 3.1 Introduction

This chapter presents the construction of a simplified nasal cavity and maxillary sinuses model, which served as a pilot model. This simplified model was used to test and validate a CFD model configuration for later use in the investigation of nasal saline irrigation within realistic human nasal cavities and maxillary sinuses. The numerical methodology including the numerical setup, boundary conditions, and grid generation that formed the basis for nasal saline irrigation simulation is described in detail. The accuracy of the applied numerical method was confirmed by comparing the experimental measurement and observation results. This work was largely a feasibility study and building block for the later and more complex CFD investigations using realistic *in-vivo* nasal and paranasal sinus morphology. This includes the testing of the multiphase model and turbulence model to examine whether they are capable of predicting the air and saline interface and saline flow features.

## 3.2 Background

The simulation of nasal saline irrigation, due to the complexity of nasal morphology geometry, needs high computational cost and time (1). In order to test the CFD model methodology of realizing boundary conditions and turbulence method, a simplified representative nasal model was first used, prior to applying the CFD method in a more complex human nasal model. In this chapter, saline irrigation is computationally and physically simulated within a simplified nasal model containing the key features of differing inter-nasal geometry, representative of the nasal cycle, and both maxillary sinuses. Later, in Chapter 4, the approved numerical methodology was applied to complex realistic *in-vivo* nasal and paranasal sinus morphology. The initial investigation using a

simplified nasal model helps validate the construction of the numerical method detailed in Chapter 4. While nasal representative models have previously been applied in earlier nasal investigations, these were developed based on the average dimensions of the nasal cavity features rather than morphologically accurate *in-vivo* image data (92). Elad et al. (93) examined the physical stresses at the air-wall interface of the nasal cavity during breathing by using a simplified representative nasal model. In this chapter, a simplified nasal cavity and maxillary sinus model was used to test and validate a CFD model configuration for later use in the investigation of nasal saline irrigation within realistic human nasal cavities and maxillary sinuses. Previously, simplified representative nasal models have been used in airflow investigation to reduce the computational time and to find the most suitable numerical method for determining complex realistic nasal geometry (93-95).

### 3.3 Geometry

Hydraulic diameter is generally used for determining fluid flow characteristics in non-circular passages by simplifying the geometry to be represented as equivalent circular passageways. For this investigation into the human nose, the complex nasal geometry is replaced an equivalent hydraulic diameter to characterize the interaction between the moving fluid and stationary nasal walls (96, 97). This parameter is expressed by:

$$d_h = 4 \frac{\text{cross-sectional-area of passage}}{\text{wetted perimeter of passage}} \quad (3.1)$$

Hydraulic diameter ( $d_h$ ) as a characteristic dimension is applied in Reynolds number and hydrodynamic entrance length calculations. Hydraulic diameter analysis has previously been used to model fluid flow in the very narrow passages with Afiza et al. (98) representing the nasal valve model in their simplified model of a nasal cavity using hydraulic diameters.

Here, a simplified nasal model was developed to test and validate the CFD model configuration prior to applying it in a complex human nasal model. This simplified model represents three main geometrical features of nasal *in-vivo* morphology specifically around the nasal passages of different cross-sectional area, maxillary sinuses and ostia connecting the maxillary sinuses to the conducting nasal passageway.

Flow characteristics around these three regions of interest are important in providing a better understanding when later analysing flow characteristics within the complex *in-vivo* nasal geometry and also it is possible to ensure that such a CFD configuration can be applied later in investigation of nasal saline irrigation within realistic human nasal cavities and maxillary sinuses. The use of simplified geometry has been previously used by White et al. (99) who presented the distribution of hydraulic diameters of each nasal passage reflecting the nasal cycle using data obtained by MRI techniques. To reflect the effect of the nasal cycle on irrigation in the representative nasal model, it is essential to consider the differing level of erectile tissue engorgement within nasal passageways.

In this investigation nasal passages were modelled using two straight pipes and a 180° curved pipe. The pipe cross-section was chosen to be circular with different diameters on each side of the nose to represent the patent and congested passages in the nasal cycle. In this case shown by Figure 3.1, the geometry of the right passage is patent and the left passage is congested. The dimension of each passage was taken from previously published MRI nasal morphological data as the average hydraulic diameters for each passage (99). The maxillary sinuses were represented using cylinders of equivalent volume (Figure 3.1). Maxillary sinuses communicate with the nasal cavity through a short tube simulating realistic ostium dimensions. The two nasal passages were connected to each other via a 180° U-bend to represent the nasopharynx. The nares are represented by conical shapes. Specific dimensions used in this simplified model are listed in Table 3.1.

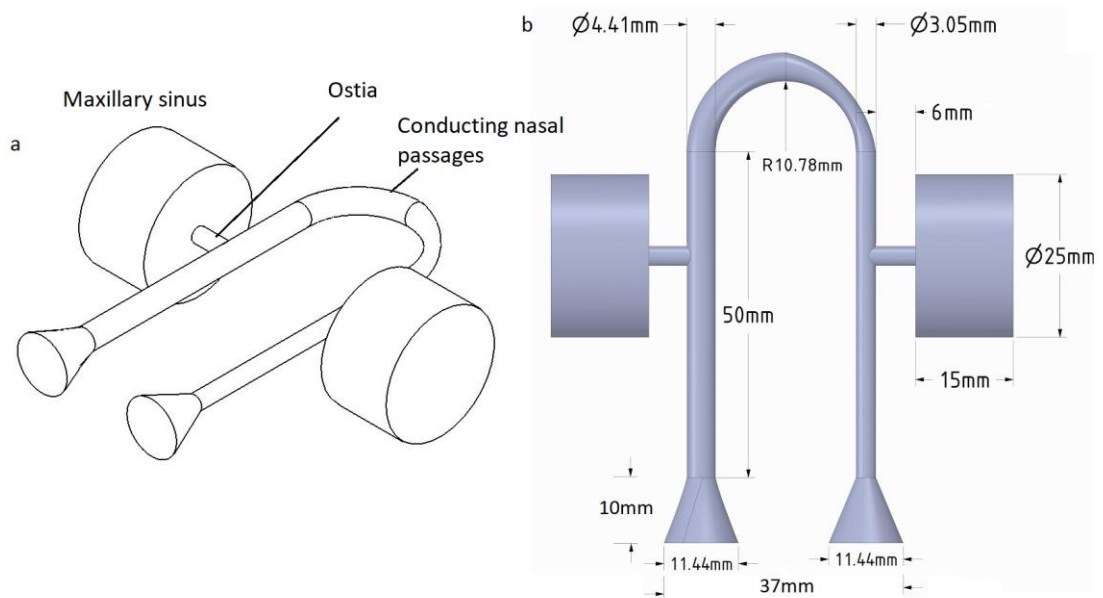


**Figure 3.1. Simplified model a) Isometric view b) Top view. The nasal passages were modelled using two straight pipes and a 180° curved pipe. The pipe cross-section was chosen to be circular with different diameters on the two sides to represent the patent and congested passages in the nasal cycle. The maxillary sinuses were represented using cylinders of equivalent volume.**

**Table 3.1. Simplified model dimensions.**

Section	Dimension	Ref.
Average hydraulic diameter-patent side (D1) (mm)	4.41	(99)
Average hydraulic diameter-congested side (D2) (mm)	3.05	(99)
Distance from nostril to ostium (mm)	44	(100)
Average length of the nasal passage (mm)	50	(101)
Average length of the ostia (mm)	6	(102)
Maxillary Volume (cm <sup>3</sup> )	7.3	(103)
Nostril diameter (mm)	11.44	(104)
Nares Width (mm)	37	(105)

### **3.4 Delivery device, head positions, and flow directions**

In this study, irrigation volume of 120 ml of saline solution per nostril were undertaken using a typical commercially available Neti Pot (NeilMed as discussed in chapter 2). This volume is recommended by the manufacturer of the delivery device as the common amount of irrigation delivery. To investigate the effect of head position on the saline flow field in the simplified model, three different head positions were considered in this initial study. Irrigation was performed at three different head positions (Figure 3.2): Mygind position (lying with head back); 90° (tilting the head sideways at 90° while standing upright); and, head back (while standing upright position, letting the head fall backwards).

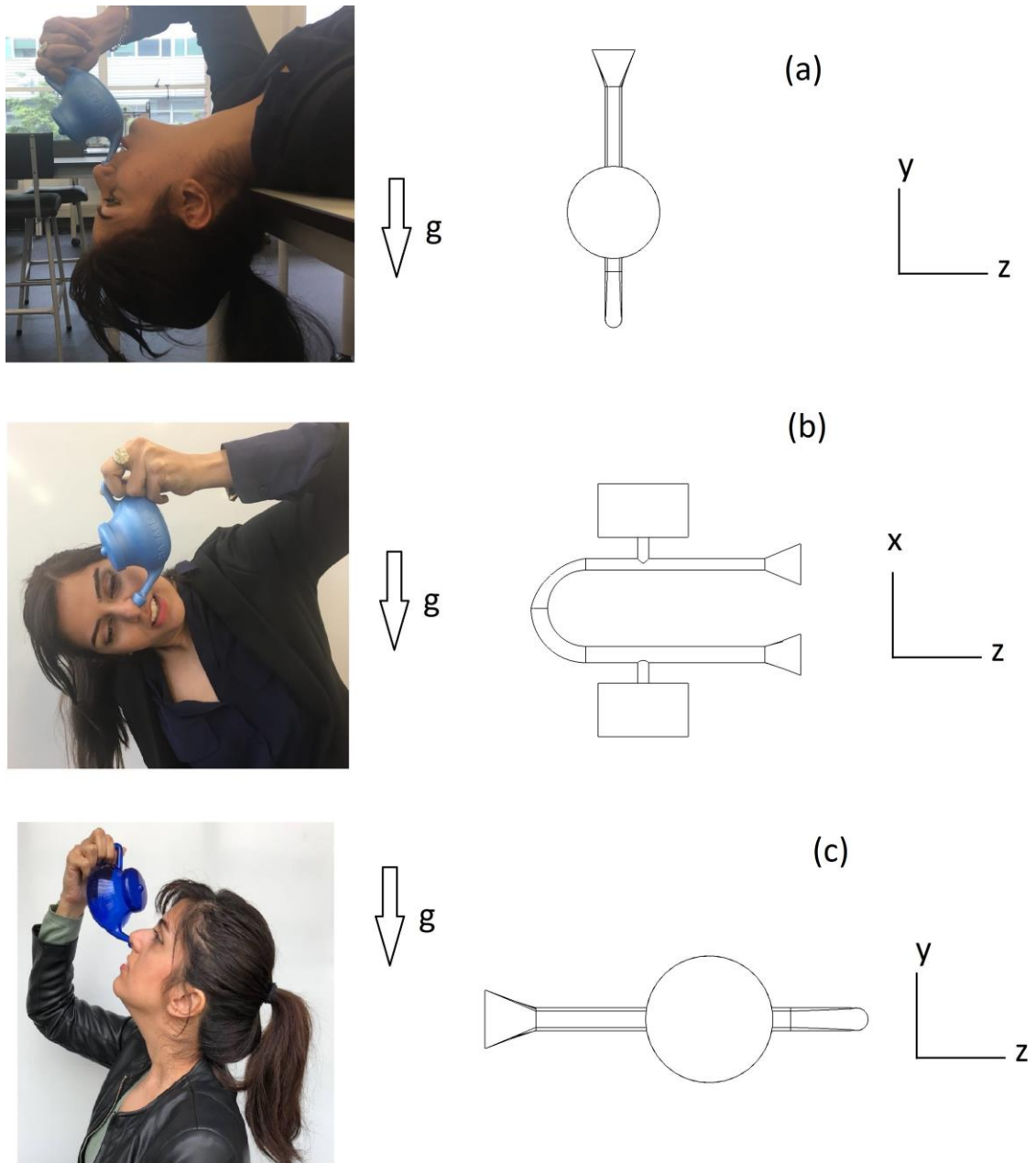


**Figure 3.2. a) Myring position b) 90° position c) head back position.**

In the current work, and for each head position, the irrigation was performed in each nostril to investigate the effect of nasal patency and congestion on saline distribution and flow characteristics within the nose and maxillary sinuses.

### **3.5 Numerical modelling**

Unsteady 3-D CFD simulations were used to investigate the saline irrigation. The transient simulation enables us to observe and investigate the saline flow within the

simplified model. A multi-VOF (volume of fluid) model was used to simulate the interaction between air and saline solution as it enabled the individual analysis of flow characteristics for each air and liquid phase. The turbulent field was simulated using a realisable K-epsilon ( $k-\epsilon$ ) model. “Realizable  $k-\epsilon$ ” is an appropriate model for this application as it gives the turbulence transfer among the two phases which plays a dominant role within the turbulent field (106). This model also provides satisfactory results for wall-bounded and internal flows and is suitable for complex shear flows such as those found within the nose during irrigation (107). The  $k-\epsilon$  turbulence model was also used and validated in an earlier saline CFD visualization study (1). “Realizable  $k-\epsilon$ ” has an improved performance for recirculation and streamline curvature compared to standard and RNG  $k-\epsilon$  (which is similar in form to the standard  $k-\epsilon$  but with further refinements). Comparing alternatives, the  $k-\omega$  turbulence model has the disadvantage of being extremely sensitive to inlet boundary conditions for internal flows, which is not the case for the  $k-\epsilon$  models. For this investigation, a tank and attached pipe, with the same dimensions as the Neti Pot, were used to model the delivery device in the computational simulations (Figure 3.3). Each irrigation was separately delivered to either the congested or patent side of the simplified nasal model for each of the three head positions. Here, the outlet of the attached pipe is connected to one nostril while the other nostril is open to the atmosphere. The pressure inlet boundary condition was assigned to the top of the tank and the pressure outlet was set at the other nostril to atmospheric pressure.

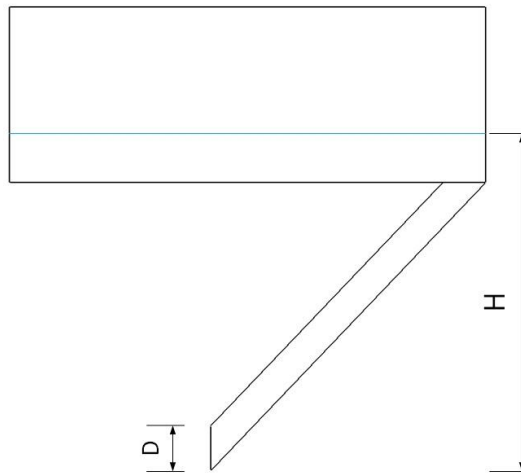


**Figure 3.3. A representative Neti Pot. H is the height of the 120 ml of saline in the Neti Pot and D is the diameter of the Neti Pot orifice.**

To ensure accurate resolution of transient flow behaviour in the computational model, the time step size was carefully selected such that the residuals reduce by around three orders of magnitude within one time-step.

To computationally analyse the fluid flow, it was essential to split the computational geometry into smaller subdomains and then discretize the governing equations and solve them inside each of these subdomains. The subdomains are called cells or elements, and a group of elements is called a mesh or grid. The governing equations are then discretised and solved inside each of these subdomains. Here, the whole geometry is comprised of multiple structured parts including the tank, pipe, and the simplified nasal model. However, these parts create a complex geometry which does not allow structured meshing. To overcome this problem, an unstructured mesh, comprised of tetrahedral cells was constructed to fill the complex geometries (108).

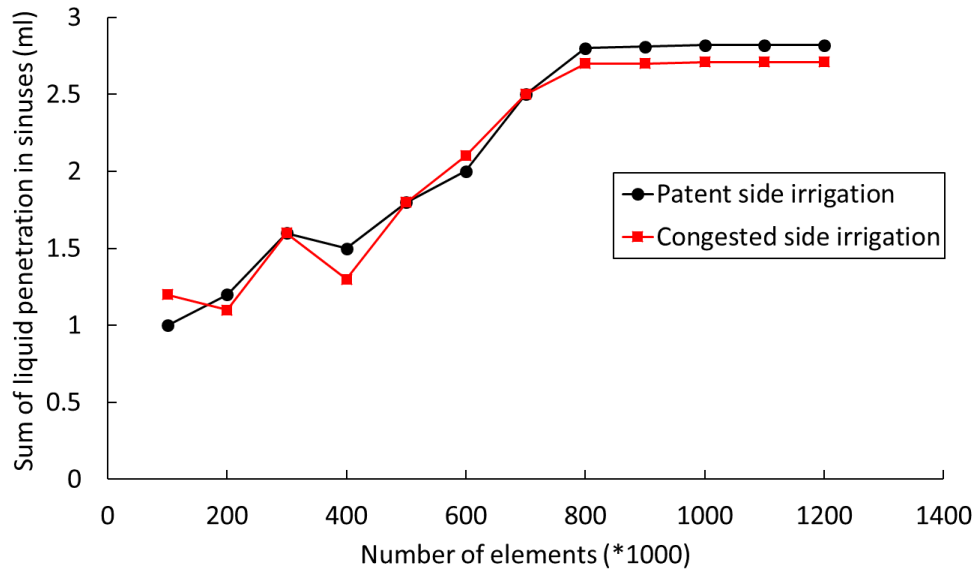


**Figure 3.4. Mesh sensitivity analysis at Mygind head position.**

A grid-independence test is a way of establishing the minimum number for the effective results of grids. This is done by increasing the number of mesh complexity and elements until the solution will not be affected by further increasing the number of grids. Here, grid-independence was tested in the Mygind head position by analysing the sum of saline penetration in both sinuses at the end of irrigation. For the simplified nasal model, the monitored variables were almost constant when the cell quantity was over 800,000 (Figure 3.4). The same number of cells was applied to other head positions and it was found that 800,000 elements is the optimum number for the simulation of saline in a simplified nasal model.

### **3.6 Experimental setup**

To validate the computational model and its computational methodology, it is necessary to compare the numerical results of saline irrigation within the simplified model to those of a physical model utilising the same geometry. To realise these two halves of the simplified clear acrylic nasal model were 3-D printed using a PolyJet 3-D printer to produce smooth and accurate parts. Selection of the clear acrylic as the material for the physical model enables observation of the saline movement within the simplified model

during irrigation. The physical simplified nasal model was fabricated by assembling the two 3D printed halves together (Figure 3.5).

The same tank and pipe sizes were applied in both the CFD simulation and physical experiment. Between the delivery device and physical model, a ball valve was used to control the time saline irrigation was introduced into the physical model. The height of the saline in the tank represents the 120 ml of saline in the Neti Pot, which measured 65mm. The valve was attached to the physical model with a small flexible rubber pipe to connect the outlet saline flow of the delivery device into the inlet of the physical model.

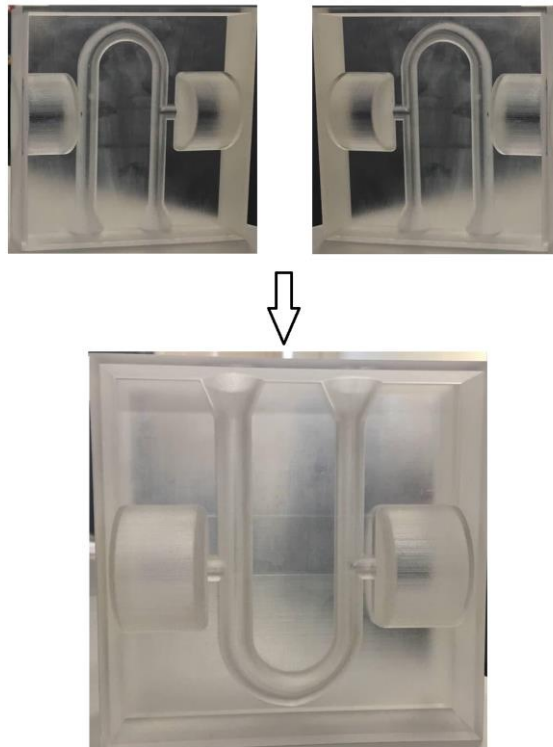


**Figure 3.5. 3-D Physical simplified nasal model.**

Qualitative flow visualization had been used previously to validate the numerical method in saline irrigation CFD simulation (2). For the visualization method in each case, a high-speed video camera recorded the flow displacement during irrigation within the physical model. The camera was placed in front of the physical model and all the videos were recorded using the same room-lighting condition. To compare the video images captured during physical testing with the numerical results, three images were extracted from the video recording at various time steps representing the beginning, middle and end of each irrigation. Here, noticeable and significant flow characteristics and behaviours could be observed and compared between the physical and computational models. Blue-coloured saline solution (liquid) (109) was used to irrigate the physical model to allow for better observation of the irrigated liquid within the physical model. Each irrigation was performed at three head positions and on each nostril separately. To ensure that the rate of saline discharge from the delivery device into the computational and physical models was the same, the mass flow rate of the delivery device was monitored in both cases. For the physical model, the discharge rate from the tank to the model was measured using a force sensor. This entailed a Force-sensing resistor (FSR) sensor being placed under the liquid stand feet to continuously measure the liquid mass within the tank (Figure 3.6). One of the stand's feet was cut and a block was designed to hold the force sensor and it was placed under the feet. By doing this, it is possible to minimize the displacement of the sensor which causes noise in the results. The displacement of the stand and the sensor causes some additional forces for instances which can be considered as sensor reading noise. The specifications of the force sensor are noted in Appendix A. The calibration of sensor was done by adding a specific amount of liquid to the tank, recording the corresponding voltage, and extracting the relation between the liquid mass and voltage. LabView-based software reported the discharged mass from the tank and pipe into the model in the form of a curve as a function of time.

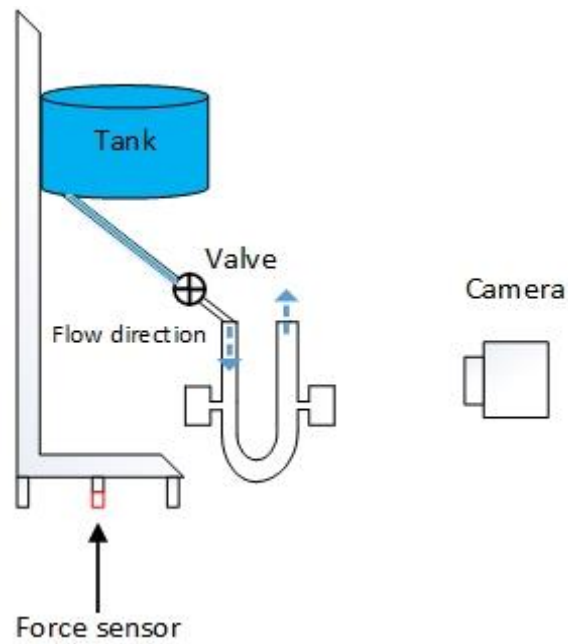


**Figure 3.6. Schematic view of experimental setup.**

The recording commenced for each irrigation from when the ball valve was opened, and the irrigation began, until all the liquid solution ended up in the tank.

The force sensor has previously been used to find the discharge rate of the tank into a physical model (110) that was used to develop a numerical model for predicting outflow by following the pipelines containing incompressible liquids. In this investigation the liquid penetration into the maxillary sinuses in both the computational model and physical models is compared at three time intervals  $t=8s$ ,  $t=16s$ , and  $t=24s$  for all head positions and inflow side irrigations. A hole was drilled in each side of the sinuses that was then sealed by plasticine to enable a sinus drain for when the experiment stopped at the targeted time intervals. An oil suction gun with a flexible tube was used to drain the liquid from each sinus, taking care that the ostium passage was also drained out. The total mass of liquid contained within the simplified model was measured using a digital micro scale before and after irrigation with the difference in the mass being the liquid contained within one sinus. This was repeated for next time interval, and the mass of liquid in the other sinus was measured at this point. The experiment was performed again from the

beginning and this time the irrigation was stopped at the next time interval. The liquid penetration into the sinuses was measured at three different time intervals.

### **3.7 Validation of results**

Validation of CFD model, boundary conditions, mesh and analysis technique was done by comparing the mass flow rate into the simplified nasal model obtained from the computational model and physical models. Then, the extracted video images from the flow observation were compared with the corresponding images from the computational result at time steps of  $t=8s$ ,  $t=16s$ , and  $t=24s$ . The liquid penetration in the sinuses was compared at these same three different time intervals.

#### **3.7.1 Mygind position irrigated from patent side**

Figure 3.7a compares the computational and physical model discharge rate of the tank into the model in the Mygind head position when irrigation is performed from the patent side. The aim of monitoring the flow rate in both experiment and numerical simulation is to ensure that the flow rate into the models has almost similar trends. Each test has been performed five times, and the mean value of all tests is shown in Figure 3.7. The standard deviation of the data is shown with as bars during 0-25s with a time interval of one second. The standard deviation can be expressed as:

$$\text{Standard deviation} = \sqrt{\frac{\sum(x-x_{mean})}{n}} \quad (3.2)$$

Where  $x$  is the value of each data point in each experiment,  $x_{mean}$  is the mean value, and  $n$  is the number of tests.

The first three seconds from the same results are shown in another graph (Figure 3.7b) to confirm the accuracy of this transient section. When the valve is quickly opened, the existing head pressure accelerates the fluid, and the rate of flow discharge increases from zero to a maximum value and then decreases as the liquid in the supply tank decreases.

At the beginning of the irrigation there are some dissimilarities between the computational and CFD models though to be associated with manual opening of the valve. The difference between the computational model and physical model results for this head position and side direction was found to be less than 10%, except where a variation was observed due to noises caused by movement of the sensor. Also, at the initial seconds of the irrigation, it can be observed that standard deviation is larger than the rest of the irrigation.

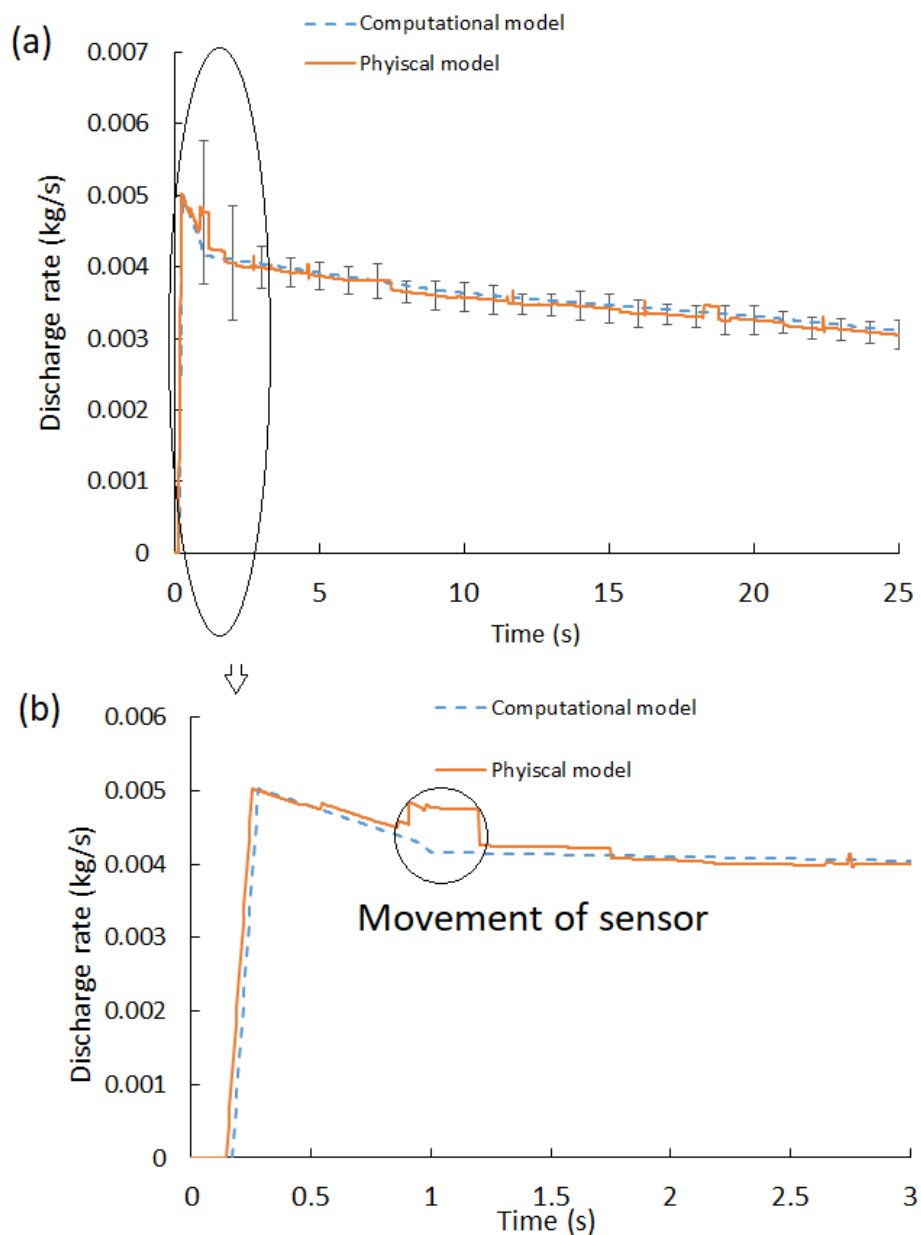
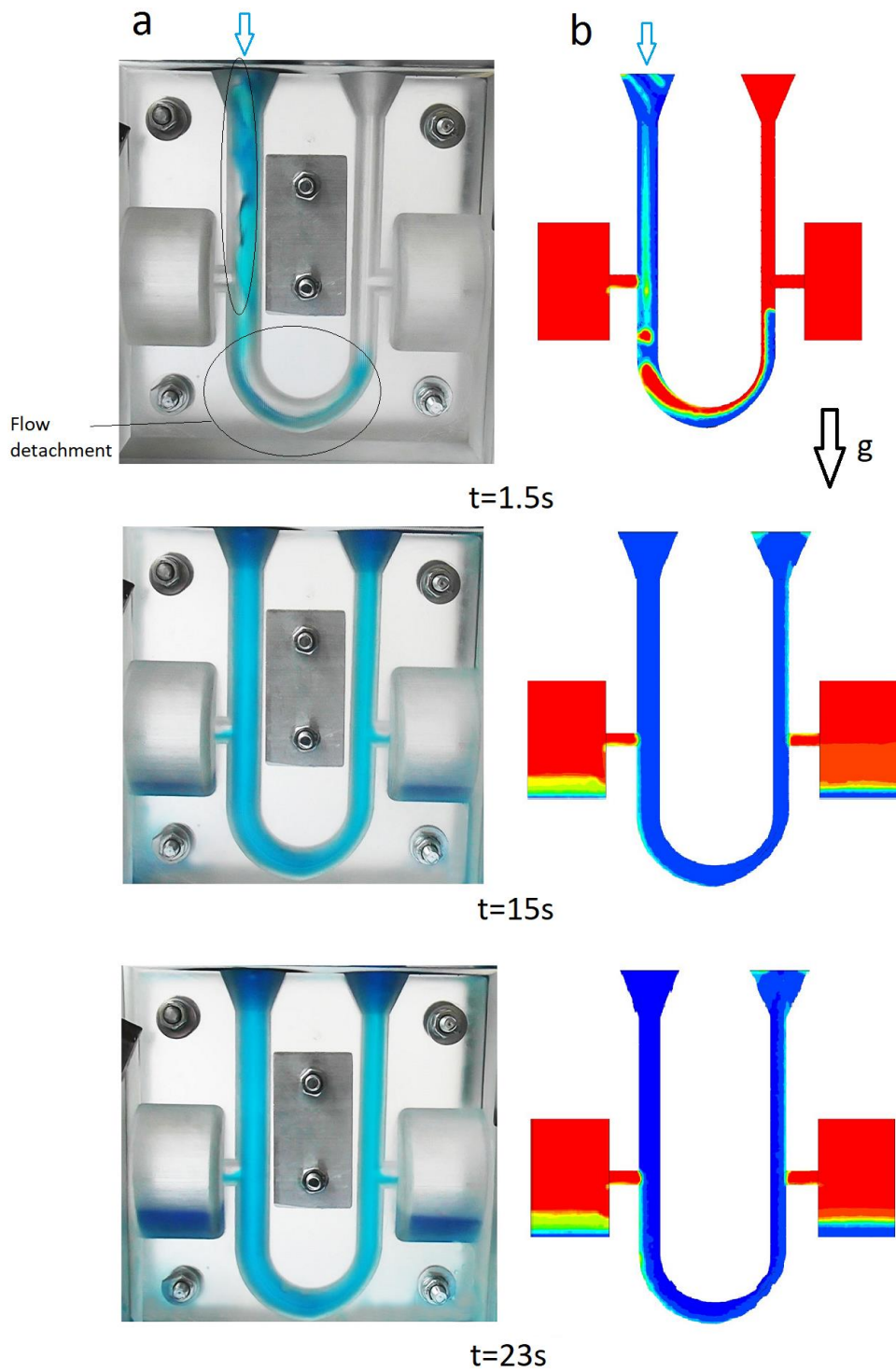


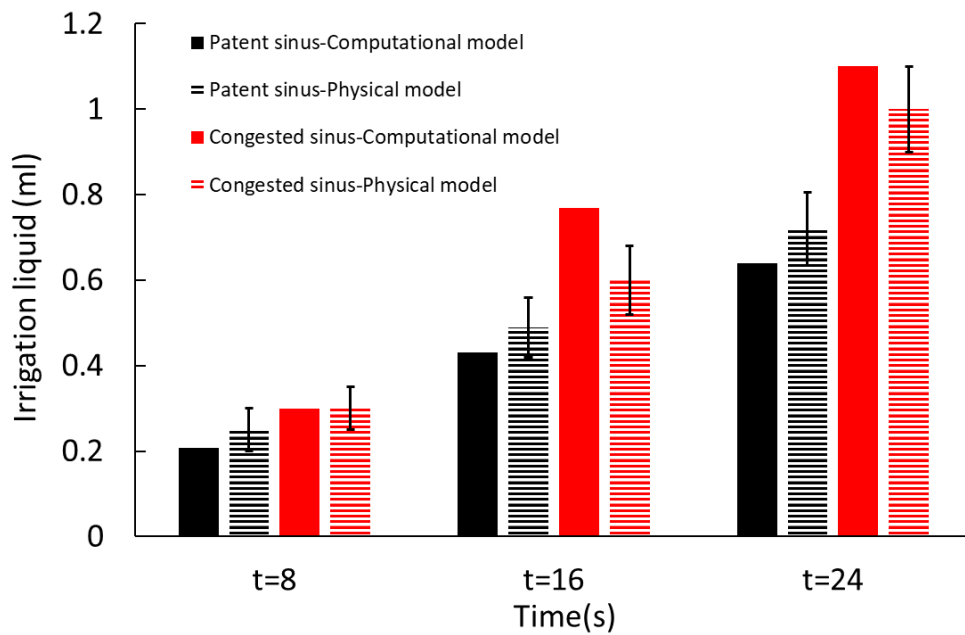
Figure 3.7. a) Discharge rate versus time in the Mygind head position with irrigation from the patent side over 25 seconds b) first three seconds of the same result.

Figure 3.8 shows images of the liquid flow field in the Mygind head position from the patent side at different time intervals of  $t=1.5s$ ,  $t=15s$ , and  $t=23s$ . At  $t=1.5s$ , both the CFD and the experimental results show that the flow does not completely fill the patent passage, and a flow detachment also occurs at the u-bend. At  $t=15s$  and  $t=23s$ , the flow in both passages and the sinus penetration are similar in both the CFD and physical experiment. The Mygind head position represents two vertical channels with the patent side irrigation inflow moving in the same direction as gravity. When passing to the congested side the irrigation fluid moves towards the outlet against the direction of gravity. During the first seconds of irrigation, the liquid film flows on the patent side wall. The flow detachment occurs at the u-bend from the inner wall and reattachment occurs at the outer wall. The level of penetrated liquid into the sinuses at  $t=15s$  and  $t=23s$  is similar for both the computational and physical models.



**Figure 3.8. a) Physical model and b) Computational model results of liquid irrigation in the Mygind head position from with irrigation from the patent side at different time intervals;  $t=1.5s$ ,  $t=15s$ , and  $t=23s$ . (blue= irrigation liquid and red=air).**

Figure 3.9 compares the amount of liquid in each sinus within the computational model and simplified physical models at different time intervals. Each experiment has been performed four times, and the average results are shown in Figure 3.9. The standard deviation of each data point is shown as bars on the physical model results. There is agreement between the amount of liquid which penetrated the sinuses in the computational and physical models with a maximum error of 24% occurring in the congested sinus when  $t=16s$ .



**Figure 3.9. Amount of irrigation liquid in each of the sinuses at different time intervals in computational and physical models in the Mygind head position when irrigated from patent side.**

### 3.7.2 Mygind position irrigated from congested side

This time irrigation is directed into the congested side of the nose model in the Mygind head position. The discharge rate of the model into the congested side is shown in Figure 3.10a. The first three seconds of the same results are shown in Figure 3.10b. The same flow behaviour found in the previous patent side inflow irrigation is apparent in the congested side irrigation, however, the smaller size of the congested side created a greater resistance to inflow. This constriction a greater draining time, hence, a lower mass flow discharge rate into the nose model.

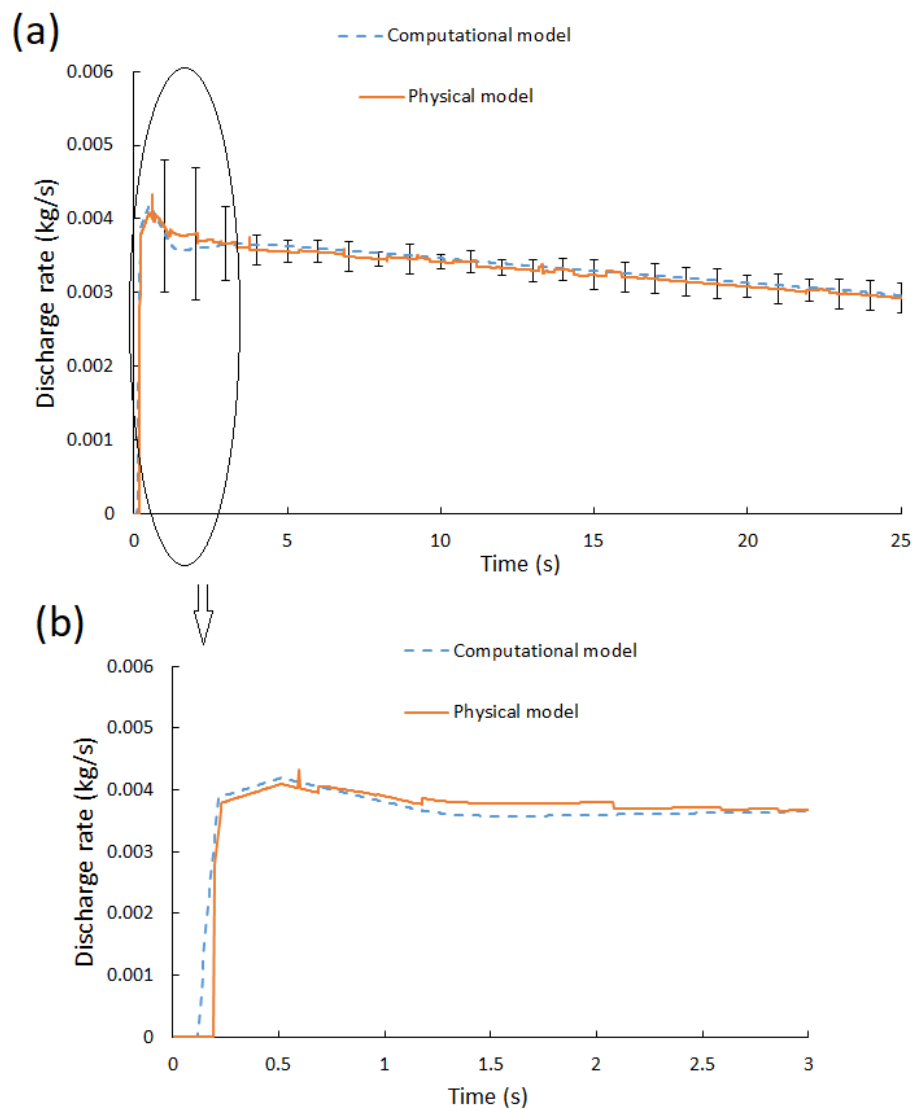
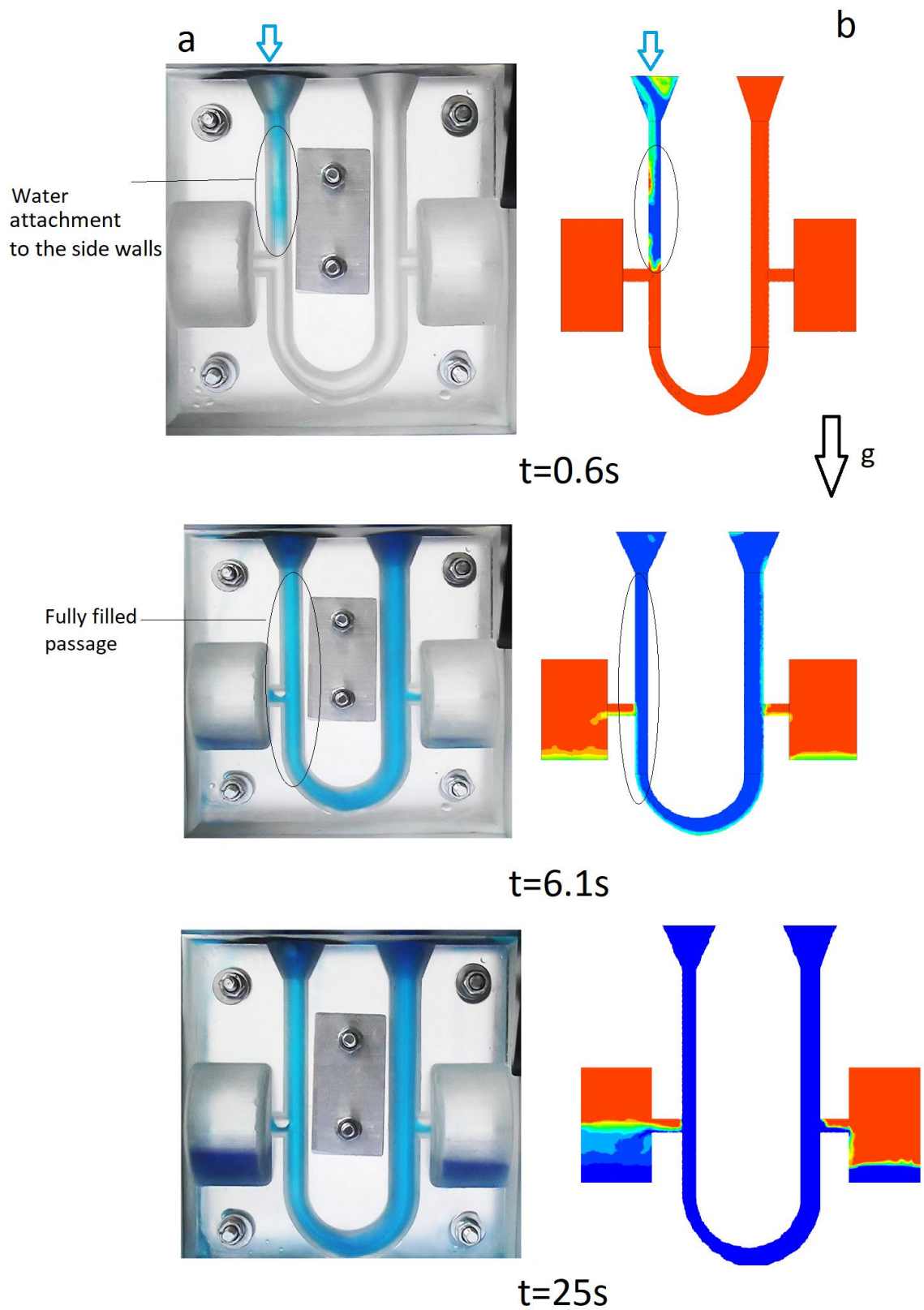


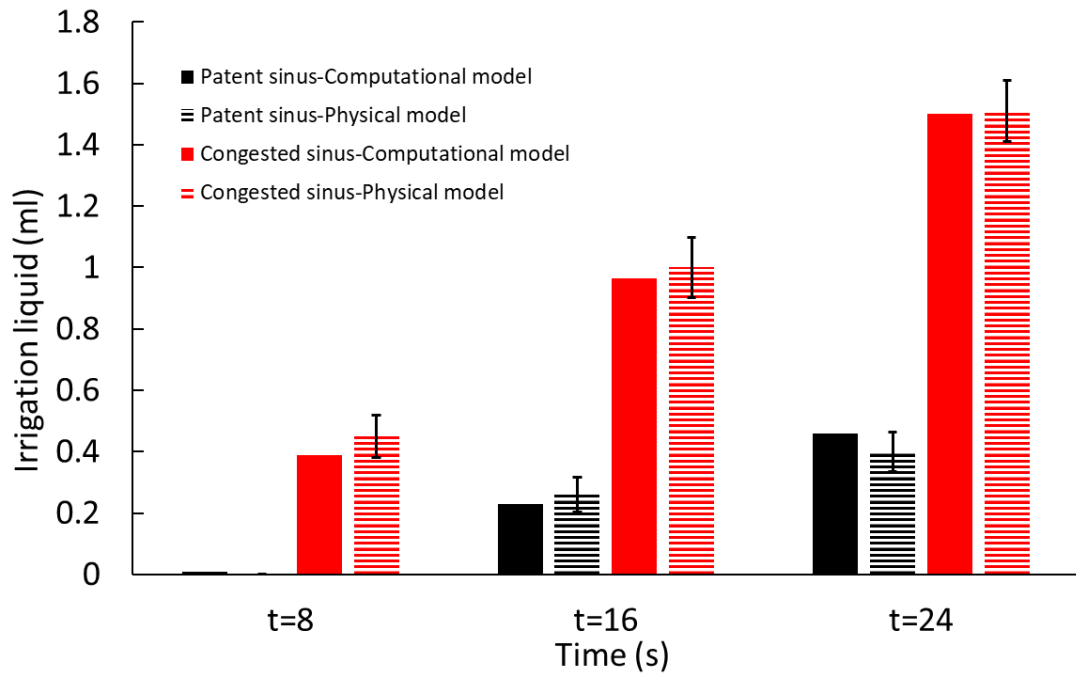
Figure 3.10. a) Discharge rate versus time in Mygind head position from the congested side over 25 seconds b) first three seconds of the same result.

Figure 3.11 depicts physical and computational results for the Mygind head position when the irrigation is performed from the congested side of the model. At the beginning of irrigation, the liquid moves in the same direction as gravity and tends to attach to the side walls, as shown in both the computational and physical models ( $t=0.6s$ ). However, due to the smaller cross-sectional area of the congested side compared to the patent side, the liquid attached to each sidewall reaches towards the other side, and liquid fills the passage as liquid starts to pass into the other side of the nose. The trapped air moves towards the outlet from the top side of the ostia. In the Mygind head position both sinuses were irrigated. At  $t=6.1s$  and  $t=25s$ , the features mentioned can be observed in both the computational and physical models.



**Figure 3.11. a) Physical model and b) Computational model results of irrigation at Mygind head position irrigated from the congested side at different time intervals  $t=0.6s$ ,  $t=6.1s$ , and  $t=25s$  (Blue= irrigation liquid and red=air).**

In this test, the amount of liquid which penetrated the sinuses at different time intervals was monitored for this head position and side irrigations. When liquid penetration is low, it is not possible to measure the liquid penetration in the sinuses as shown when  $t=8s$  (Figure 3.12). The maximum error of 13% was found for the sinus located at the congested side at  $t=8s$ .



**Figure 3.12.** Amount of irrigation liquid in each of the sinuses at different time intervals in computational and physical models at Mygind head position irrigated from congested side.

### 3.7.3 90° head position irrigated from patent side

Figure 3.13 (a) compares the discharge rate of the tank into the model. Here there is agreement between the results of mass flow rate into both models during the irrigation. The first three seconds of the same result is shown in Figure 3.11(b). There is a large variation at the beginning of the irrigation which is due to the displacement of the sensor during manual opening of the valve.

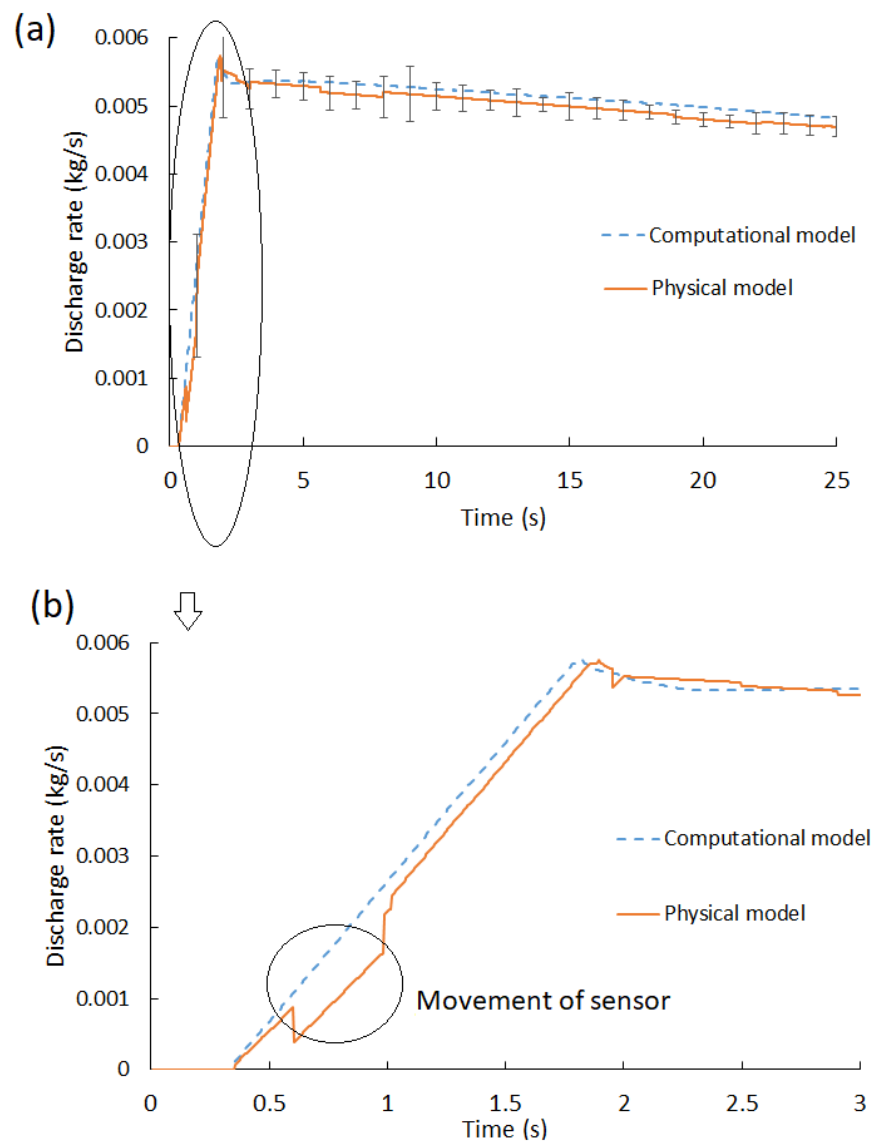
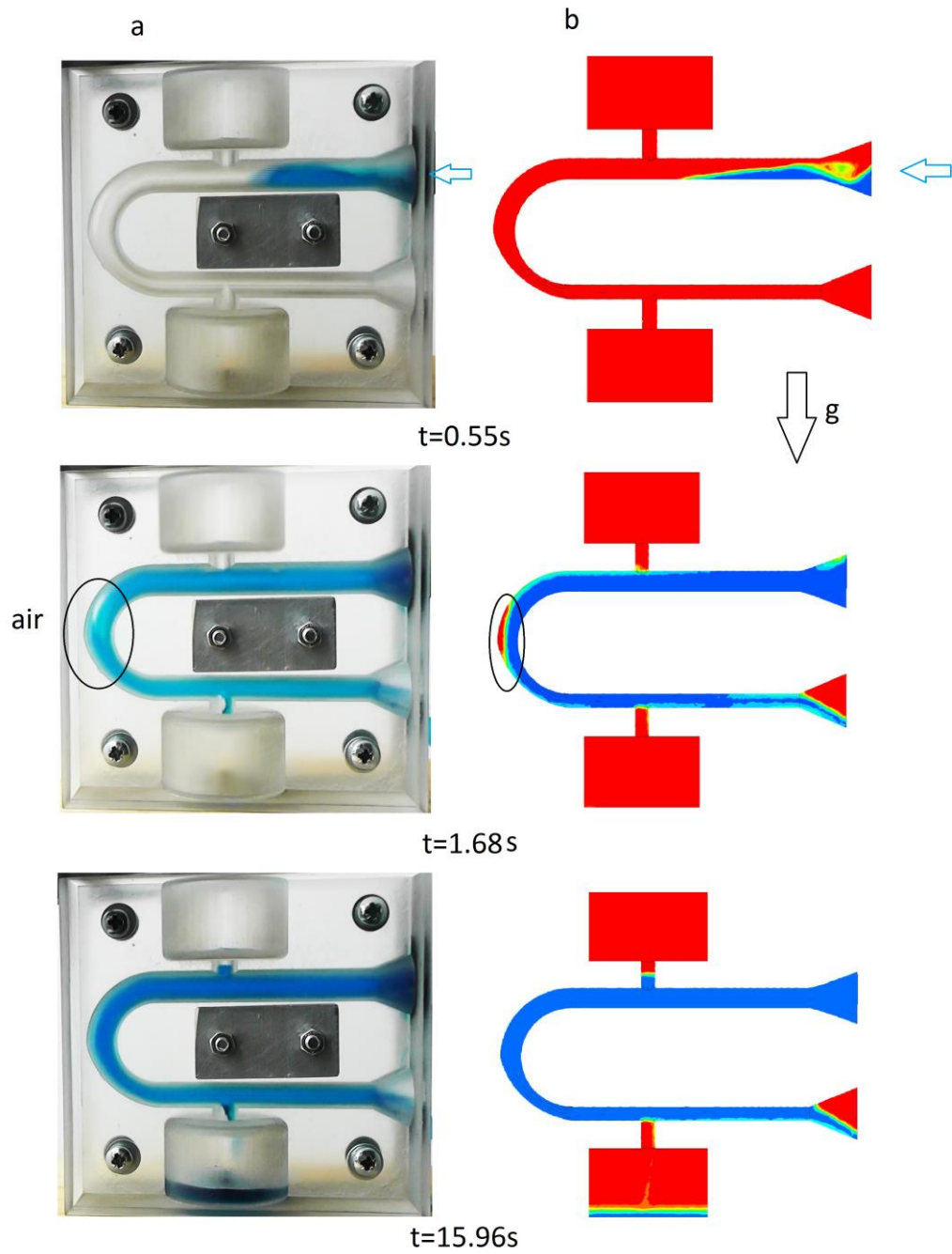


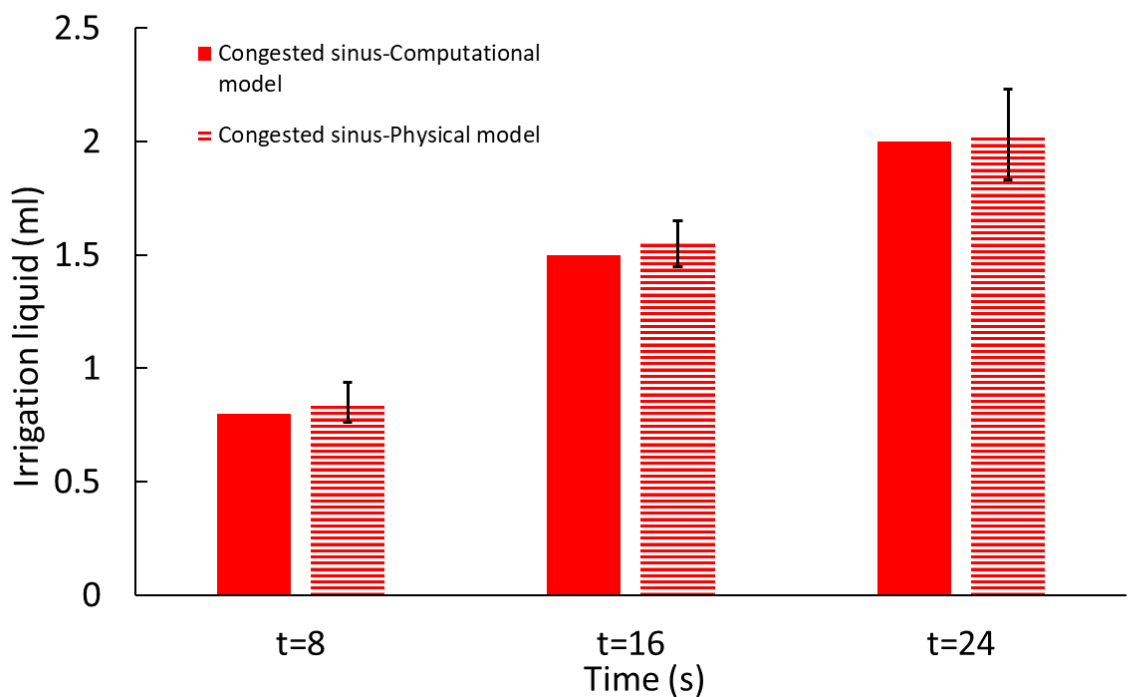
Figure 3.13. a) Discharge rate versus time in 90° head position irrigated from the patent side over 25 seconds. b) First three seconds of the same result.

Figure 3.14 presents the liquid irrigation in the 90° head position with irrigation inflow directed into the patent side of the physical and computational models. At the beginning (t=0.55s) of the irrigation, liquid did not completely fill the passage at the side of the direction of irrigation, and the similarity between the physical and computational models shows that the computational model could accurately predict the location of the liquid and air interface. At t=1.68s, the irrigated liquid could not penetrate into the sinus located on the side of the irrigation inflow in either the computational or the physical model. The trapped air at the u-bend can also be seen in both models. At t=15.9s, the level of sinus penetration into the sinus located on the congested side is similar between both models.



**Figure 3.14. a) Physical model and b) Computational model results of irrigation at 90° head position irrigated from patent side at different time intervals  $t=0.55s$ ,  $t=1.68s$ , and  $t=15.96s$  (Blue= irrigation liquid and Red=air).**

The amount of the liquid which penetrated both sinuses in the 90° head position when irrigated from the congested side is shown in Figure 3.15. No liquid penetration was observed for the upper patent maxillary sinus located at the side of the irrigation in either the computational or physical models. The entry of the sinus located at the side of the irrigation is against the direction of gravity and liquid cannot push out the trapped air within the sinus. A maximum error of 6.5% was found at t=8s for the sinus located on the congested side.



**Figure 3.15.** Amount of irrigation liquid in the sinus on the congested side at different time intervals in computational and physical models at 90° head position when irrigated from patent side. No liquid enters the maxillary sinus on the patent side.

### 3.7.4 90° head position irrigated from congested side

Changing the irrigation inflow side from the congested to the patent side in the 90° head position did not change the trend of discharge rate versus time (Figure 3.16). The congested side caused more flow restriction compared to the patent side due to its smaller diameter. Hence, the values of the discharge rate are lower compared to the patent side inflow condition. Noise in the results at the beginning of the experiment is attributed to the manual opening of the valve. The difference between the results was less than 10%.

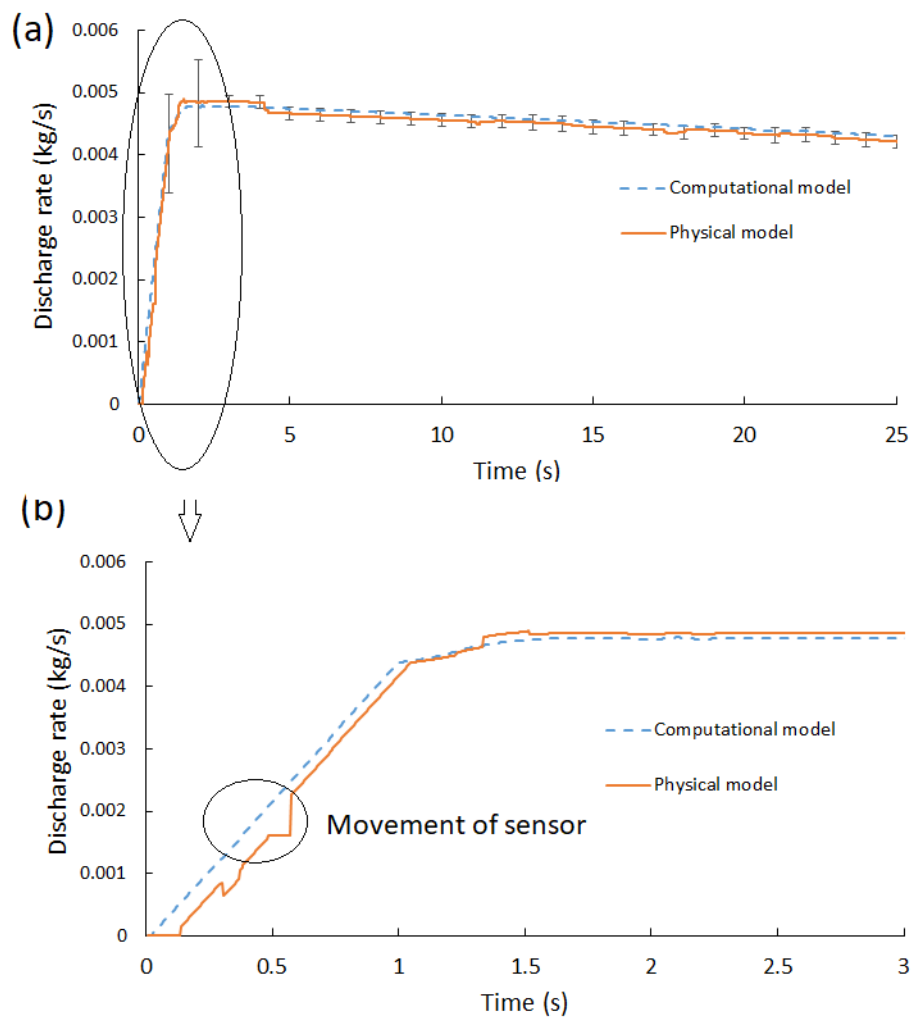


Figure 3.16. a) Discharge rate versus time in the 90° head position when irrigated from the congested side over 2 seconds. b) First three seconds of the same result.

Comparison of irrigation for both physical and computational models in the 90° head position within inflow from the congested side is shown in Figure 3.17. For this position and flow direction the irrigant in the CFD model could not penetrate the upper maxillary sinus on the congested side, as can be observed at all-time intervals in both the computational and physical models. This result was also observed in the physical model. The centrifugal force and the restrictions imposed by the geometry create a flow separation at the 180° u-bend. The irrigant becomes detached from the nasal wall (t=1.68s) in both the computational and physical models). The computational model simulated this flow detachment and similar phenomena were observed in the physical model.

At t=1.68s and t=26s, both the computational and physical models show similarities in the liquid pattern in the passage, the liquid penetration into the sinus located on the patent side, and the liquid outflow from the exit nostril.

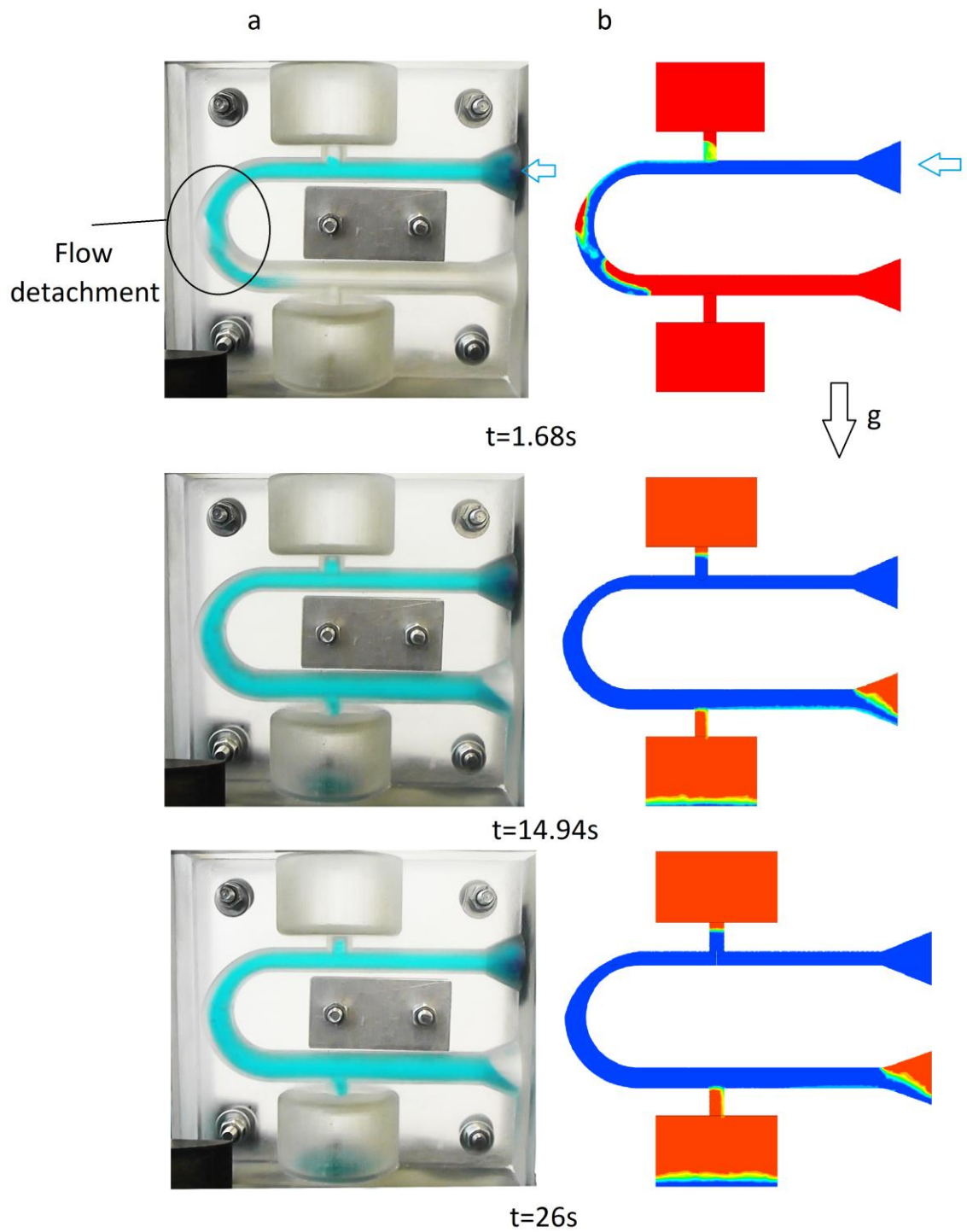
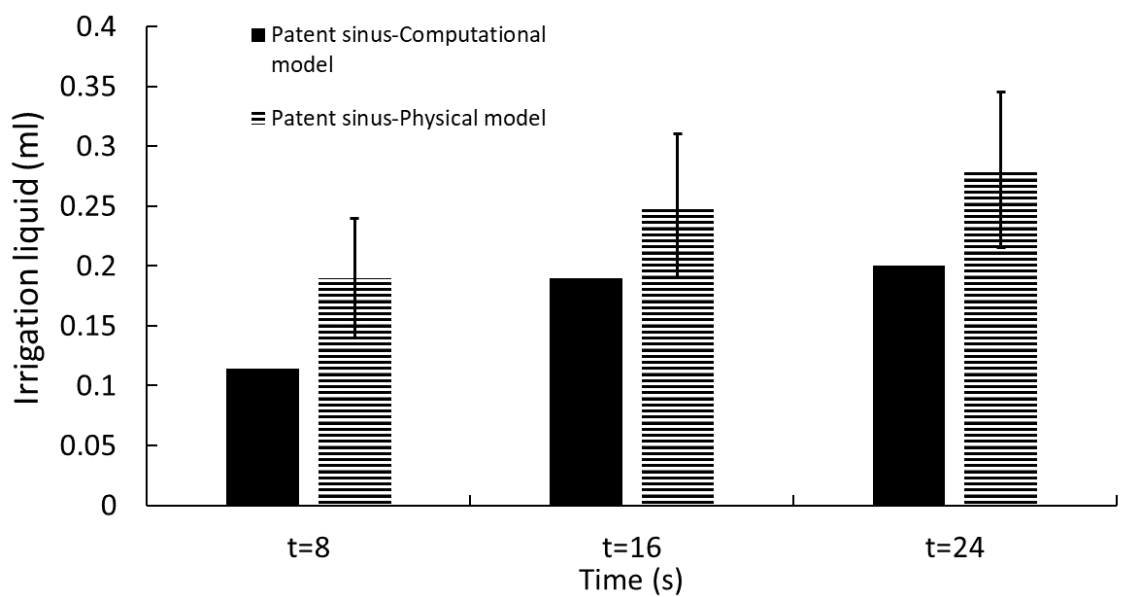


Figure 3.17. a) Physical model and b) Computational model results of irrigation in a  $90^\circ$  head position irrigated from the congested side at different time intervals  $t=1.68s$ ,  $t=14.94s$ , and  $t=26s$  (blue= irrigation liquid and red=air).

During the congested side irrigation, similar to that of the patent side, the liquid penetration into the sinus located on the upper side of irrigation is zero (Figure 3.18). In order to penetrate the sinus located at the upper side of the irrigation, liquid would have to move against the direction of gravity. Additionally, a lack of pressure also prevents the liquid from pushing against the trapped air. The maximum error difference between both models at  $t=8s$  is 40%, because the low penetration of the sinus makes it difficult to measure exactly.



**Figure 3.18.** Amount of irrigation liquid in the maxillary sinuses on the patent side at different time intervals in the computational and physical models in a  $90^\circ$  head position when irrigated from the congested side. No liquid enters the maxillary sinus on the congested side.

### 3.7.5 Head back position irrigated from patent side

The physical and computational models' discharge rate in the head back position irrigated from the congested side is shown in Figure 3.19a. The first three seconds of the same result are shown in Figure 3.19b. At the beginning of the irrigation there was an error of 45% are some errors caused by delay in opening the manual valve. After the first second of the irrigation, the force sensor could measure the discharge rate of the tank with a maximum error of 10%. There is noise with measured results for some time steps which occurred due to minor displacement of the sensor.

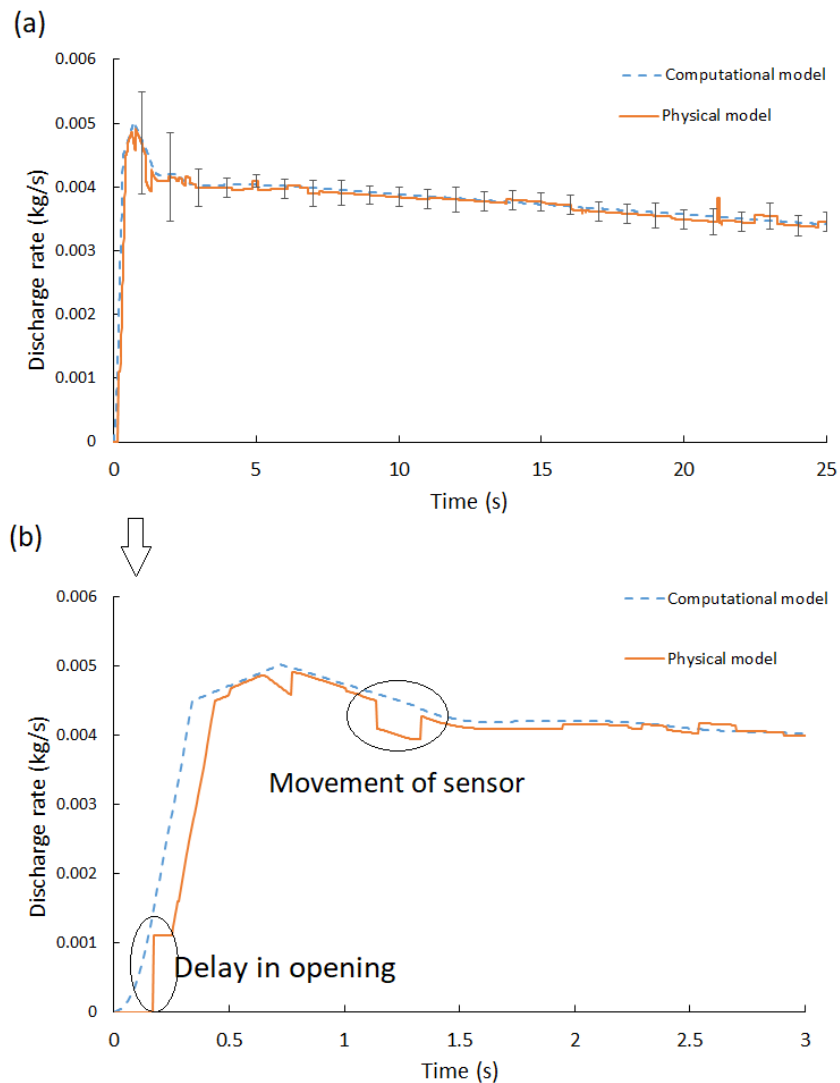


Figure 3.19. a) Discharge rate versus time at head back position with irrigation from the patent side over 25 seconds b) First three seconds of the same result.

The obtained results from both models indicate a similar trend. Images for the head back position were taken from the top side of the model. The numerical model can capture the air/liquid interface tracking the moving surface. At  $t=1.2s$  both computational and physical models demonstrate the sharp interface between the two phases before reaching the  $180^\circ$  u-bend shown by Figure 3.20. At  $t=7s$  and  $t=25s$ , when liquid reaches the outlet in both the computational and physical models, the flow moves out of the model from the bottom side of the nostril. The CFD shows the mid-plane and the liquid exit from the nostril is not visible, and in the physical model the colour of the liquid is light blue. This feature is annotated in both the computational and physical model results (Figure 3.20  $t=25s$ ).

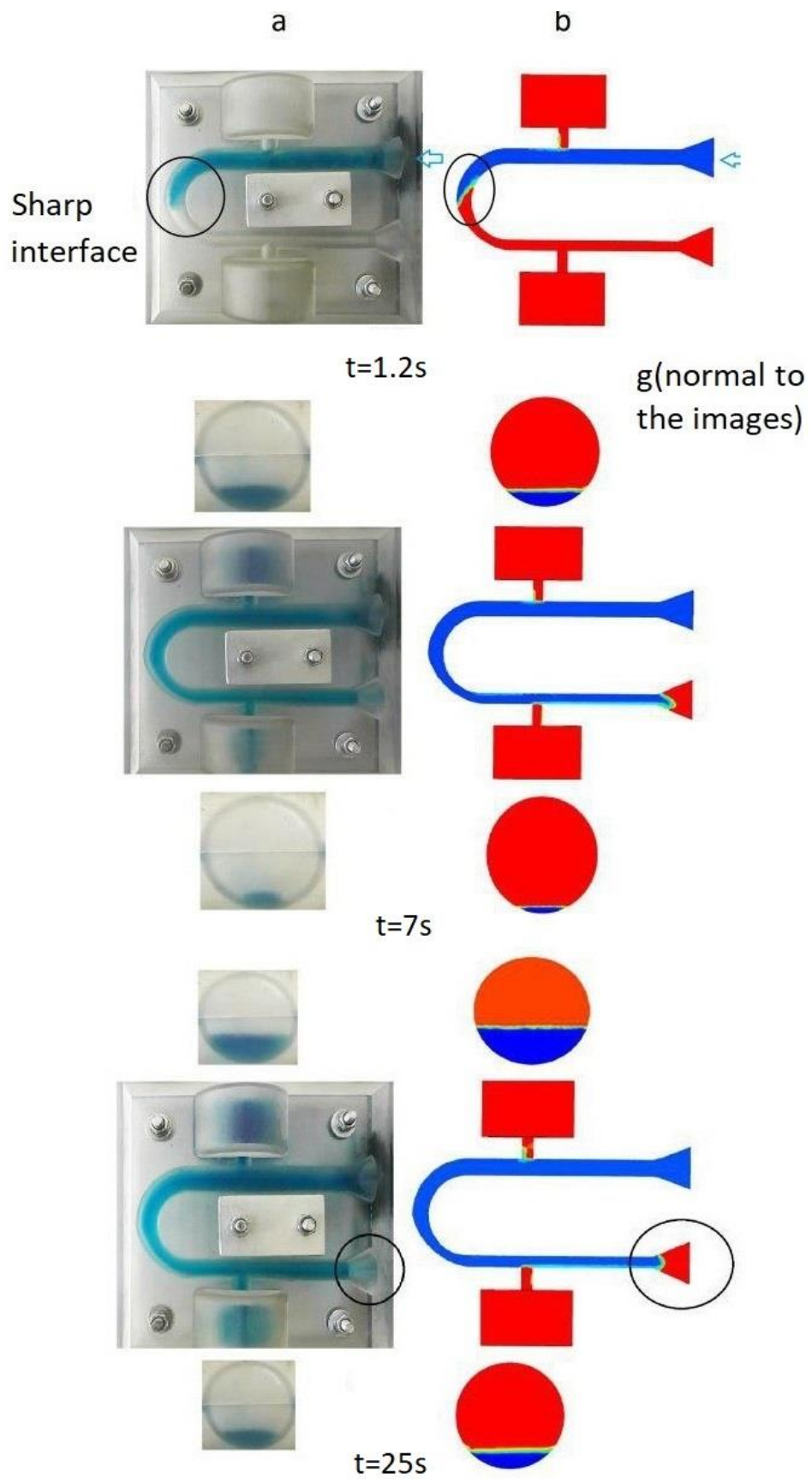
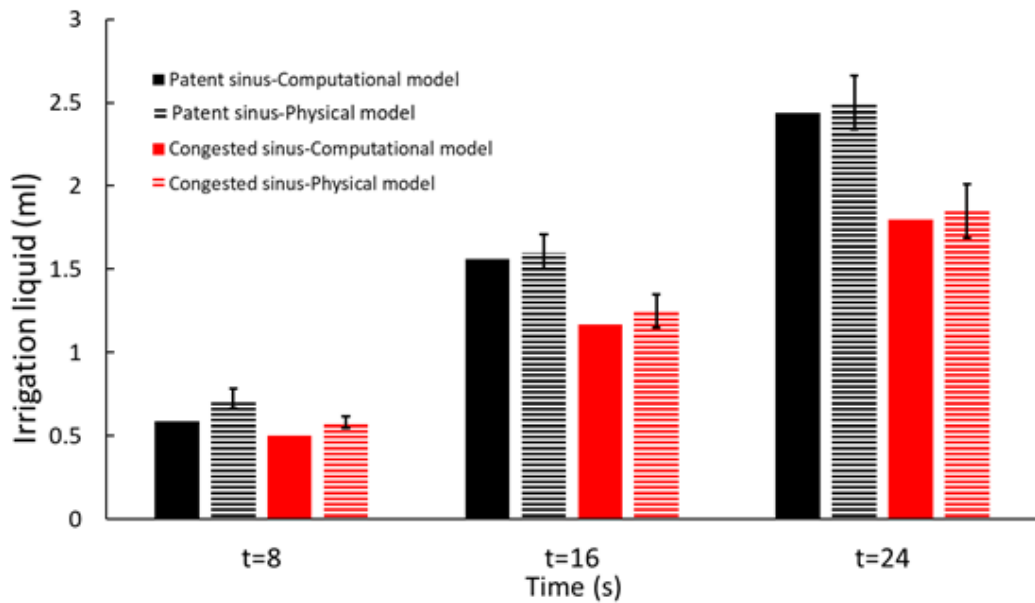


Figure 3.20. a) physical model and b) computational model results of irrigation at head back position irrigated from patent side at different time intervals  $t = 1.2s$ ,  $t = 7s$ , and  $t = 25s$  (blue= irrigation liquid and red=air).



**Figure 3.21. Amount of liquid in each of the sinuses at different time intervals in computational and physical models at head back position irrigated from patent side.**

Figure 3.21 shows the amount of liquid which penetrated the sinuses at different time intervals, with a maximum error of 25% occurring for t=24s, at the congested side.

### **3.7.6 Head back position irrigated from congested side**

The physical measured discharge rate versus time at head back position irrigated from congested side agrees with the computational model results shown by Figure 3.22a. The first three seconds of the same result are shown in Figure 3.22b. Again here, the maximum error of 35% occurred at the beginning of the irrigation. This was due to the delay in manual opening of the valve which caused some displacement in the system. All tests were performed several times to minimise the error at the beginning of the irrigation. However, the manual opening of the valve causes displacement and additional forces on the stand, which results in errors in this experiment. After the first second of the irrigation, the maximum error is 5%.

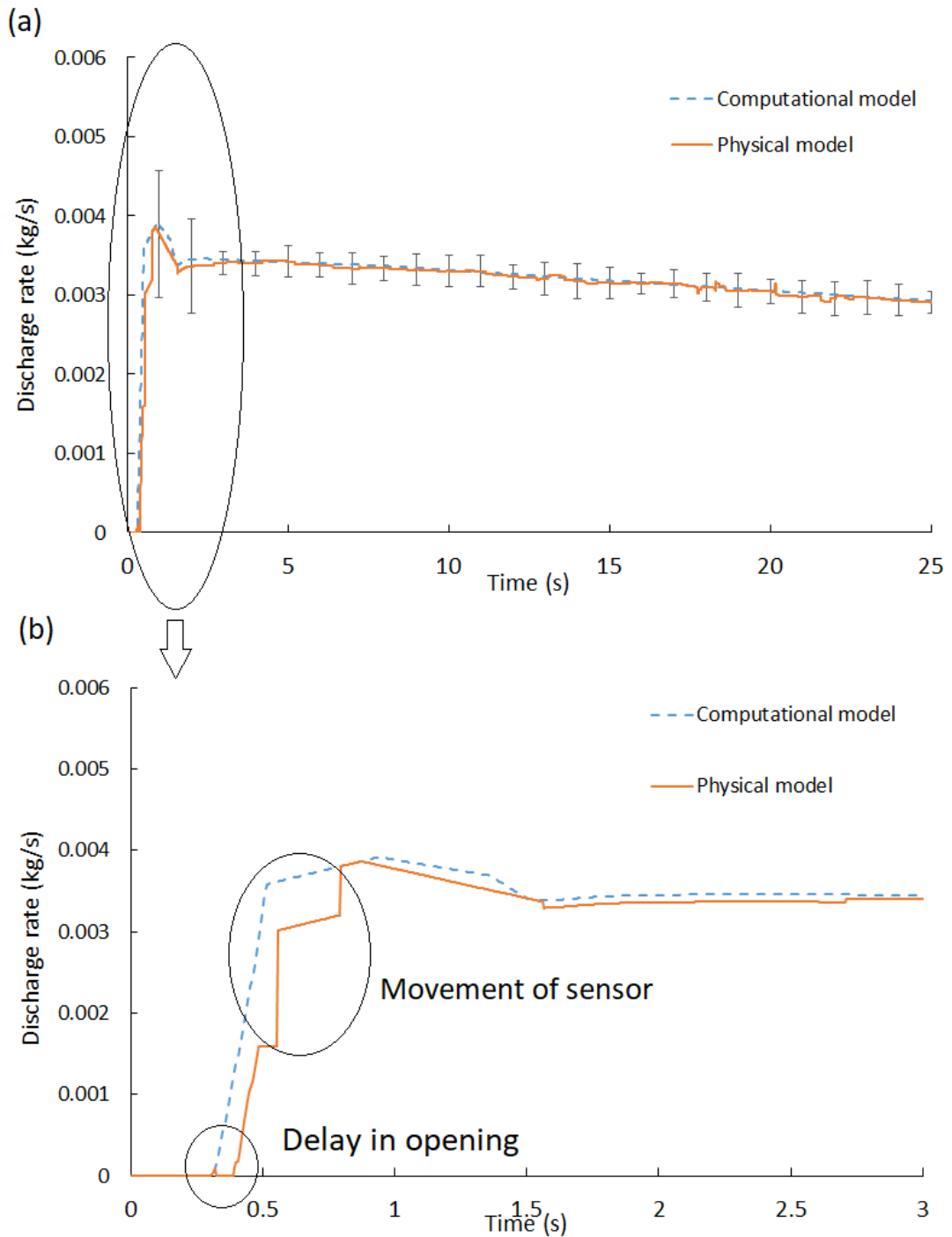


**Figure 3.22. a) Discharge rate versus time at head back position with irrigation from the congested side over 25 seconds. b) First three seconds from the same result.**

Liquid distribution within both the computational and physical models in a head back position irrigated from congested side is depicted in Figure 3.23. At  $t=0.5s$ , the liquid in both models reached the ostia entry located at the side of irrigation (congested) in both the computational and physical models.

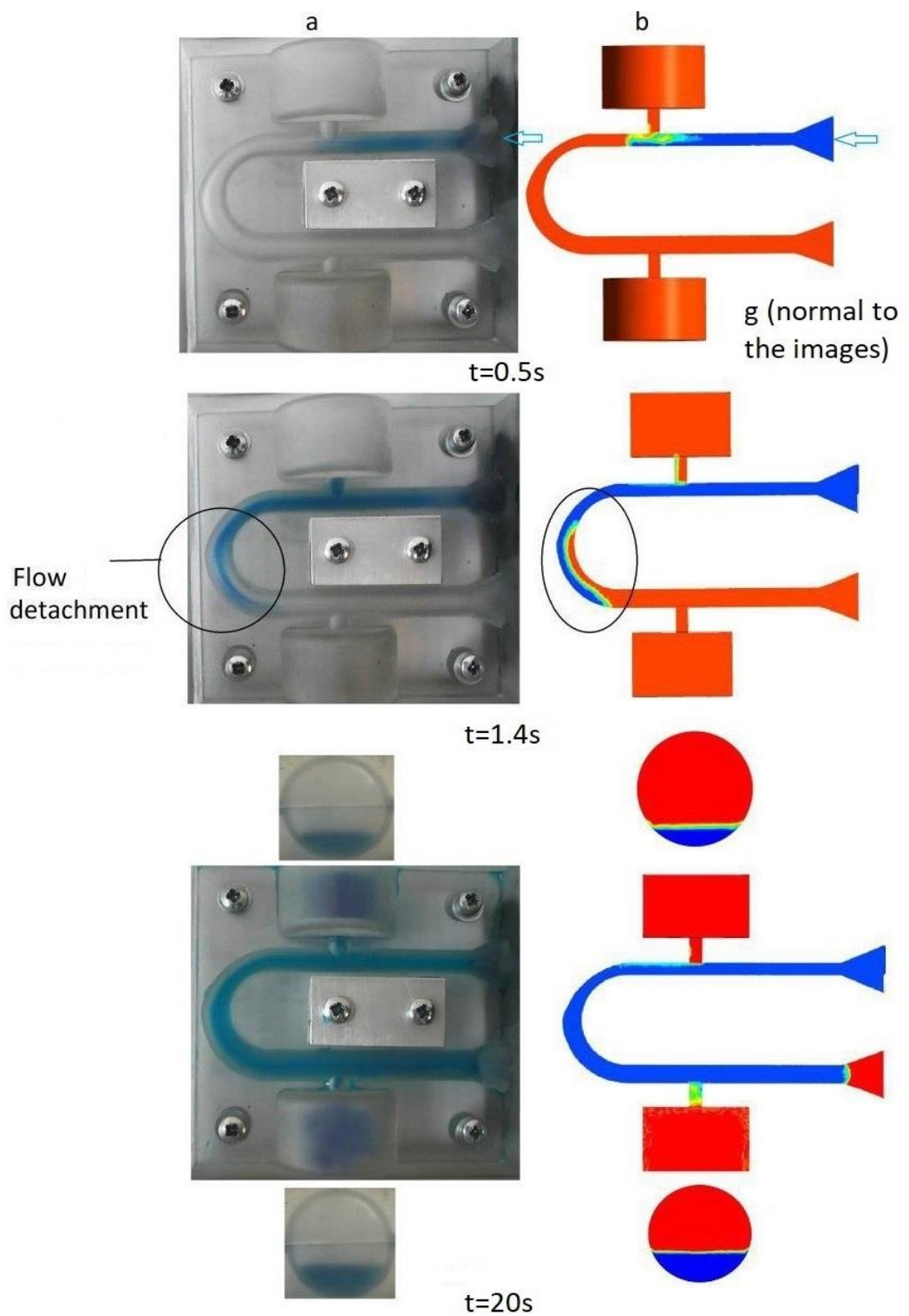
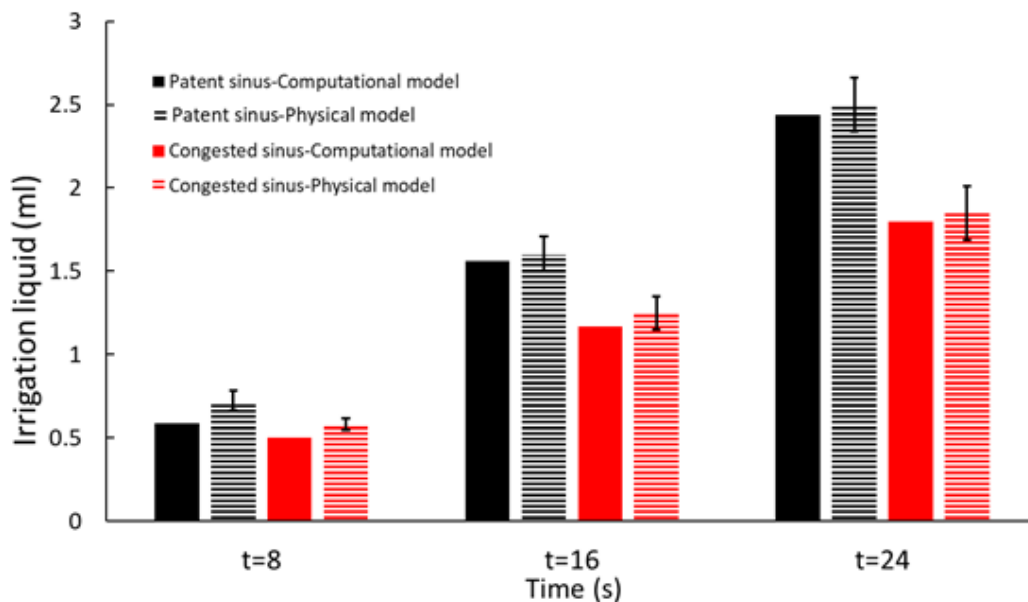


Figure 3.23. a) Physical model and b) Computational model results of irrigation at head back position irrigated from congested side at different time intervals  $t=0.5s$ ,  $t=1.4s$ , and  $t=20s$  (blue= irrigation liquid and red=air).

At  $t=1.4s$  the flow detachment in the nasopharynx u-bend was detected in both models. At  $t=20s$ , the liquid fully filled the passages and penetrated into both sinuses as observed in physical model and predicted by the computational model.

Figure 3.24 compares the liquid penetration into the sinuses in both the computational and physical models at the head back head position irrigated from the congested side. Irrigation during this head position resulted in balanced maxillary sinuses penetration on both sides. Both computational and physical models could produce similar results in the head back position. The maximum error of 15% was found in the sinus located at the patent side at  $t=8s$ .



**Figure 3.24.** Amount of irrigation liquid in each of the sinuses at different time intervals in computational and physical models in the head back position when irrigated from congested side.

### **3.8 Discussion**

The numerical methodologies and experimental apparatus of the validation system employed in the current work for the simplified model have been described. Observation and measurement methods were applied to validate the accuracy of the numerical method including the boundary conditions, turbulence model, and the mesh generation. The discharge rate of the delivery device into the model was monitored in both computational and physical models. The flow characteristics between the physical and computational models were compared using observation methods. At the Mygind head position, irrigated from the patent side, the irrigant at the side of irrigation mainly attached to the side of the walls at the beginning of the irrigation, and a flow detachment from the inner wall was formed and then filled as time progressed. A similar flow pattern was observed in the same head position irrigated from the congested side. At the 90° head position the liquid could not penetrate the sinus, irrespective of the side of irrigation. The flow at the side of irrigation was moving while there was a marked interface between the air and liquid. At the head back position, a flow detachment occurred at the u-bend for both side directions. The irrigant could penetrate both sinuses at both side directions. Similar flow patterns were observed in both models. The liquid penetration into the sinuses was measured at three time intervals in the physical model, in three different head positions and with irrigation from both patent and congested sides. Both the visualization and measurement results were consistent with the simulation, which validates the applied numerical method for this model. The validation shows that the applied numerical methodology including boundary conditions, turbulence model, and mesh, is capable of predicting the liquid motion within a model. This model also can predict specific flow features including detachment, separation, and penetration at different regions of the simplified model.

The simulation in this chapter shows that the irrigation using a Neti Pot can be divided into three stages: the initial stage of the irrigation in which the Neti Pot is full and the liquid mass flow rate reaches to a maximum value, the period between the beginning and end of the irrigation (main irrigation); and the final stage of the irrigation in which the Neti Pot is about to become empty and the mass flow rate suddenly drops. The mass flow rate results recorded during the main irrigation show that there is a small rate of change in the liquid flow rate into the model using unsteady state simulation. This means that the irrigation flow field remains mainly constant and achieves its maximum values. The main irrigation can be simulated using a steady state simulation. Based on this finding, the later physical and computational modelling undertaken in Chapters 5 and 6 will be undertaken using steady state flow conditions. This will assist in saving both computational time and cost when using a simulation of the real *in-vivo* nasal cavity models undertaken in Chapter 6.

### **3.9 Summary**

The aim of this chapter was to test and validated the proposed CFD methodology on a simplified nasal model so it can be later used in investigation of nasal saline irrigation within realistic human nasal cavities and maxillary sinuses. This chapter explains the numerical methodology including the application of a multi-VOF model and the turbulence field. Different flow features and characteristics were observed at different head positions and side directions, as discussed in the previous section.

By comparing the flow features (sharp interfaces, flow detachment, and sinus penetration) captured in the images taken from the physical and computational models and sinus penetration, it is found that the multiphase and turbulence models are able to predict the flow features. The experimental results generally agree with what the CFD calculations predicted, which verifies the methodology used in the CFD. The methodologies and

findings from this preliminary study formed the basis for progressively more complex models of the nasal cavities and CFD simulations.

By applying this CFD methodology within realistic human nasal cavities and maxillary sinuses in Chapter 4, it will be possible to investigate the saline distribution and pressure and mucosal wall shear stress distributions, to find the answers to this study's research questions.

# Chapter 4: *In-vivo* computational and realistic nasal model development

## 4.1 Introduction

To help understand nasal irrigation patterns, including the saline distribution, and flow properties, such as pressure and wall shear stress distribution, a realistic nasal model is required to validate the computational numerical analysis. This chapter describes the development of a realistic *in-vivo* nasal cavity and maxillary sinuses geometrical model generated by processing MRI nasal image data. The details of the numerical setup, boundary conditions, and grid generation for the CFD simulation of nasal saline irrigation within the realistic nasal geometry are discussed. The results of the CFD simulation will be presented later in Chapter 6.

## 4.2 Background

It was discussed in Chapter 2 that bathing the epithelial surface by hypertonic through saline irrigation helps to regulate cellular water flux and ASL hydration which also improves mucociliary clearance. The relationship between the irrigation-induced fluctuating wall shear stress and the pressure stresses stimulating extracellular nucleotides production, such as ATP, which produces an increase in nasal mucociliary clearance, was also discussed in Chapter 2. Barham and Harvey have previously mentioned that the mechanical shear provided by high volume irrigation benefits the mucociliary transport on the epithelium surface (111).

Therefore, the aim of CFD simulation here is to first investigate the flow paths and saline distribution within the nasal cavities and maxillary sinuses. This enables the identification of target delivery regions at different head positions and side directions, whereby the irrigant at these regions can improve the mucosa function by regulating the ASL hydration.

Secondly, the CFD simulation maps the saline pressures and wall shear stress distribution in the nasal cavities and maxillary sinuses in order to examine whether the irrigated saline can stimulate additional ASL hydration and mucociliary transport velocity (MTV) through mechano-stimulation of mucosal purinergic channels and thus mucociliary clearance in different regions of the nose.

### **4.3 Nasal cavities and maxillary sinuses geometry development**

#### **4.3.1 Processing MRI image data**

The geometry of the nasal cavity and maxillary sinuses can be obtained by segmentation of medical MRI head scan data. The segmentation of MRI images requires the selection of the regions defining the tissue to air boundaries within 3-D geometry of the nose and maxillary sinuses. By taking the MRI scan slice thickness into account, the 2-D pixel can be constructed to be a 3-D voxel. The combination of these image voxels creates the 3-D nasal volume of the desired geometry. In this study, Scan IP software was used to create the 3-D nasal geometry from 2-D *in-vivo* MRI data. This software package can be used for processing 3-D image data such as MRI, CT, and micro-CT. Two sets of MRI DICOM format data were applied for acquisition of the 3-D nasal geometry. Both sets of MRI image sets were captured from a 49 year-old European male without any nasal abnormality (examined by an ENT surgeon), with approval from the Auckland University of Technology Human Ethics Committee (ref. 10/121 date: 14/07/2010). MRI scans were representative of a time period of the nasal cycle where the inter-nasal airflow rates were unequally shared between each side of the nose to reflect the effect of the nasal cycle on nasal geometry. MRI scans were taken in a sagittal plane and the data files contained stacks of parasagittal slices. MRI images included data using two different filters on the MRI system. MRI Data Set 1230 had higher sharpness in the image boundaries vs the fuzzy resolution of the MRI Data Set 1232 (Figure 4.1). MRI Data set 1230 utilised a T1-weighted MRI, which provides images with the contrast obtained from the longitudinal

time of relaxation of electron spin. MRI Data set 1232 was a T2-weighted MRI, which provides images with the contrast based on traverse relaxation of electron spin being explored. The data set with the higher variation in grey scale that better differentiated between tissue types and air boundaries was chosen to create the 3-D geometric volume of the nasal cavity used in this investigation.

Image segmentation was performed using the Paint and Threshold method in Scan IP software. This involved turning the painted facets on the MRI slice into a voxel. The geometry obtained from the segmentation of the MRI scans of the complete nasal airway included two nasal passages (patent and congested), left and right maxillary sinuses, nasopharynx, and oropharynx, shown by Figure 4.2a. The flow investigation in this study is concerned with the nasal passages and the maxillary sinuses. Hence, the model was cut from the end region of the nasopharynx using ANSYS Design Modeller (Figure 4.2b).

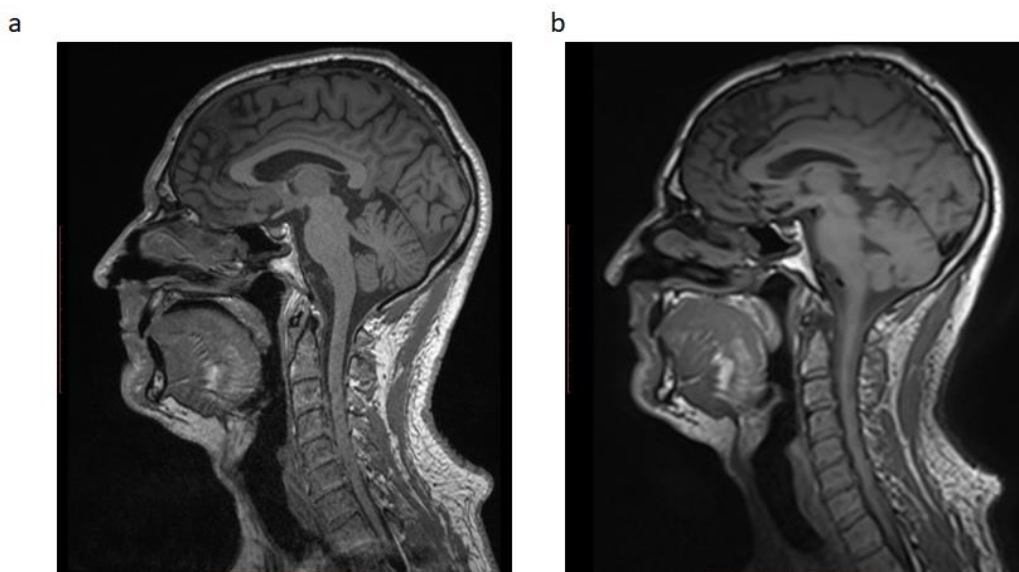


**Figure 4.1. Parasagittal slices of the head and neck used to create the nasal physical model a) MRI data set 1230 (T1-weighted) b) MRI data set 1232 (T2-weighted).**

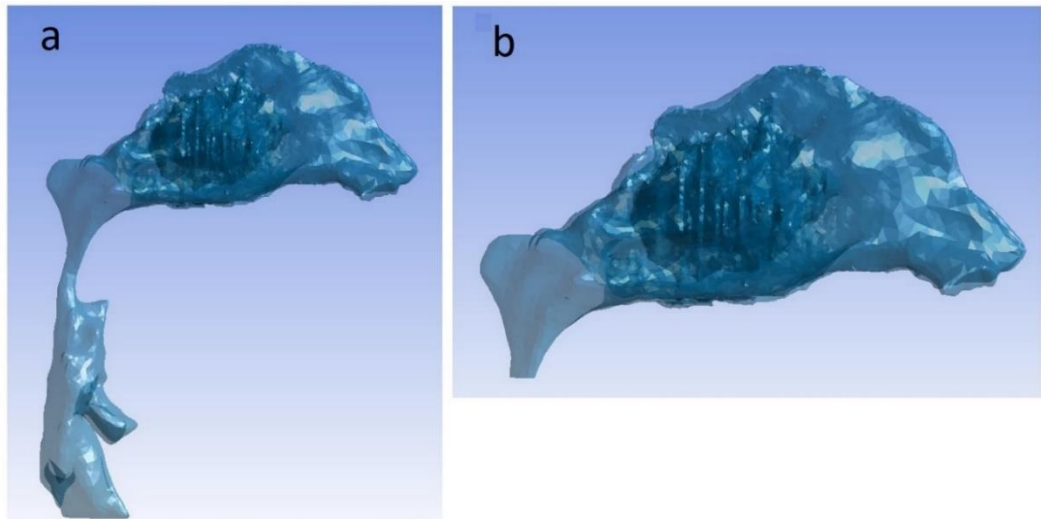


**Figure 4.2. Exported geometry from the Scan IP a) prior to and b) after removal of the oropharynx.**

The model was then exported to Meshlab software to smooth the rough surfaces. Here a Laplacian smoothing algorithm (112) was used to smooth the volume surface with the objective of easier model creation and a subsequent reduction in computational time when analysed using CFD techniques. Smoothing make the volume surface more realistic as terracing of the surface is an artificial artefact introduced by converting 2-D scans into 3-D volumes. From there, the model was exported to Meshmixer software and further manual smoothing was performed on the maxillary sinus surfaces using a flattening brush.

Figure 4.3 shows the final smoothed model which includes the two nasal passages from the nares to nasopharynx and two maxillary sinuses.

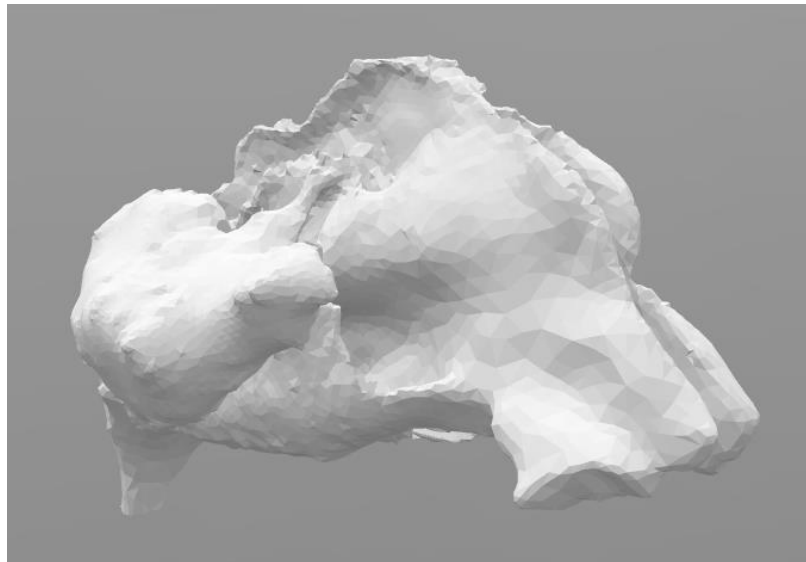


**Figure 4.3. Final smoothed nasal and maxillary sinuses solid model.**

It is difficult to create a standard geometry which can represent a wide range of geometries due to complexity of the Nasal cavity and maxillary sinuses. Liu et al. (113) analysed 30 different geometries from different ages and sex and created a standard geometry. The cross-sectional area of the nasal passage was extracted and plotted against the normalised distance. The standard geometry was then compared with original geometries of all subjects and it was shown that the standard model has the potential for use as a geometric standard.

The cross-sectional area of the nasal passage against the normalised distance of the geometry used in this study is compared with (113) and plotted in Figure 4.4.

The cross-sectional area of the standard geometry and the current geometry is close, and the current geometry can be a representative of a standard geometry. Therefore, the findings of this study can be applied to other geometries.

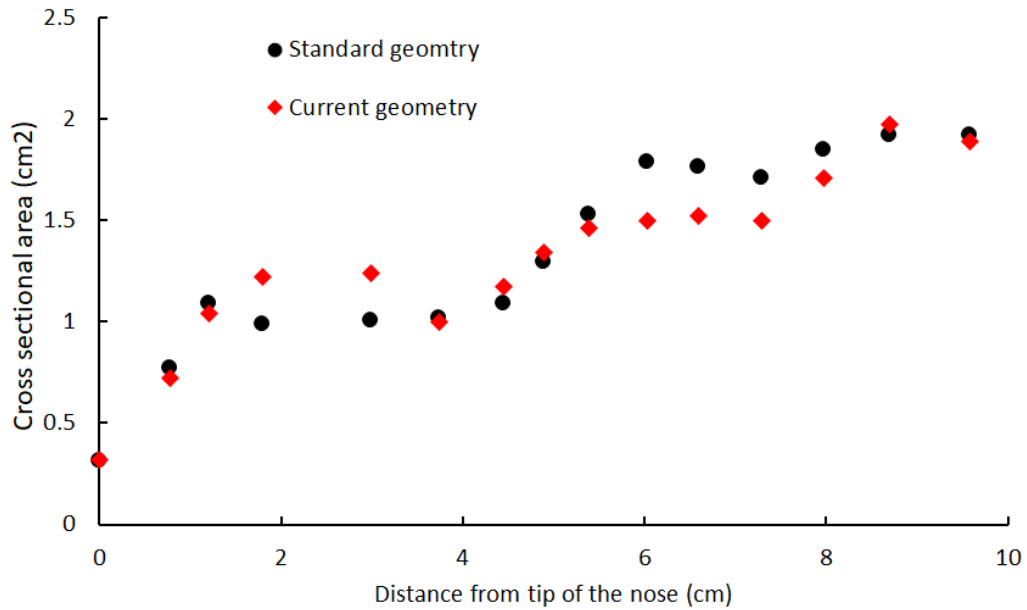


Figure 4.4. Cross sectional areas of the current nasal model and the standardized nasal model (113).

#### 4.4 Nasal saline irrigation CFD setup

##### 4.4.1 Model configuration

A series of 3D steady state CFD simulations were used to investigate nasal saline irrigation within a realistic nasal cavity and the maxillary sinuses. A commercial ANSYS Fluent software (17.2) and Reynolds-averaged Navier-Stokes equations (RANS) finite volume code was used to carry out these simulations. In RANS simulations, the turbulent field is predicted by the average of the Navier-Stokes equations, without predicting all eddies in the flow. The multi-VOF model was used to predict the saline motion within the nasal geometry as it overcomes some of the limitations of the simpler Volume of Fluid (VOF) model caused by the shared velocity and temperature formulation.

##### 4.4.2 Steady state modelling configuration

In Chapter 3 it was shown that using a Neti Pot to irrigate a simplified nasal cavity can be divided into three stages. The stage in which the saline mass flow rate through the simplified nasal model was changing slowly and was almost constant was called the main irrigation (occurring between the beginning and end of irrigation).

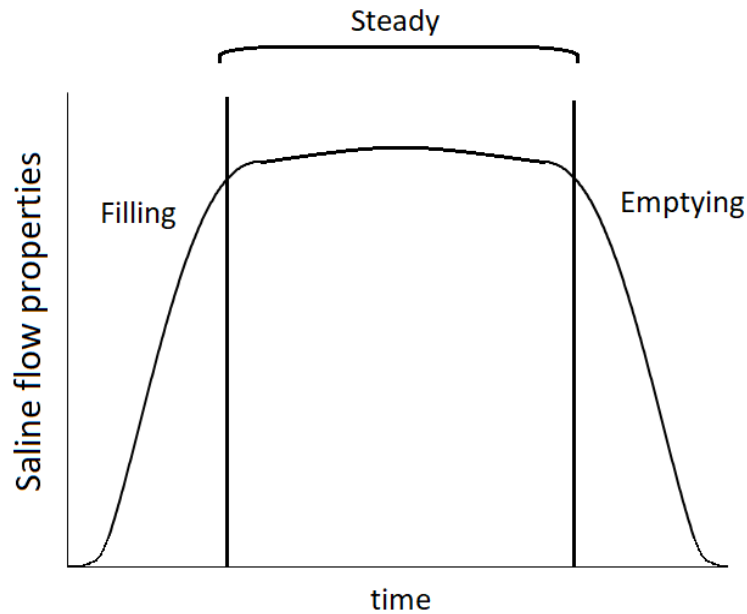


**Figure 4.5. Saline flow properties within the nasal cavities and maxillary sinuses during nasal saline irrigation.**

It was concluded that a steady state simulation is capable of simulating the main irrigation through realistic nasal cavities and maxillary sinuses, in preference to using an unsteady state simulation. Saline enters the nasal cavity and fills the nasal cavity in the first stage, then the rate of change in the saline flow field is almost constant and can be considered to be a steady state, and at the end of irrigation the saline starts to drain from the nasal cavities as shown in Figure 4.5. In this steady state simulation of nasal irrigation, saline enters the air-filled nasal cavity.

#### **4.4.3 Convergence criteria**

The most important convergence criteria for steady flow in a multi-VOF model is considered to be the difference between the mass rate at the inlet and outlet and the governing equations. In the simulations undertaken, the solution was considered to be converged when the difference in mass flow rate at the inlet and outlet between each computational iteration was less than 0.1%. These criteria have been used previously in (114). This means that, after this point the saline flow field in the nasal cavity remains effectively constant and the results show the peak values of the nasal irrigation flow field

including saline distribution, pressure distribution, and wall shear stress. Here, the converged simulation means that the simulation results shows the saline flow properties (maximum value) during the steady state in Figure 4.5.

#### **4.4.4 Turbulence model**

Earlier in Chapter 3, it was shown that the applied numerical model in this study (multiphase model, turbulence model, mesh generation, and boundary conditions) is able to predict the flow behaviour and features including flow detachment and penetration, and liquid and air interface, within the simplified model. The “realizable k- $\epsilon$ ” was used to simulate the turbulent field as it is an appropriate model when the turbulence transfer among the gas-liquid phases plays a dominant role (104) such as in this application. This model is reported to provides satisfactory results for wall-bounded and internal flows and is suitable for complex shear flows such as those found within the nose during irrigation (107). While, the k- $\epsilon$  turbulence model has also been used previously in CFD visualization for nasal saline irrigation within a realistic nasal cavity (1), as discussed in chapter 2, this earlier study did not consider *in-vivo* conditions of asymmetrical nasal geometry as a result of differing states of nasal cycle erectile tissue congestion.

#### **4.4.5 Boundary conditions**

In this investigation, the pressure inlet boundary condition on a circular opening at the nares representing the Neti Pot aperture was assigned to one nostril (Figure 4.4). The irrigation inlet pressure value was calculated as the head pressure of the Neti Pot containing 120ml of saline, as recommended by the manufacturer NeilMed. The other nostril was set to an atmospheric pressure outlet boundary condition.

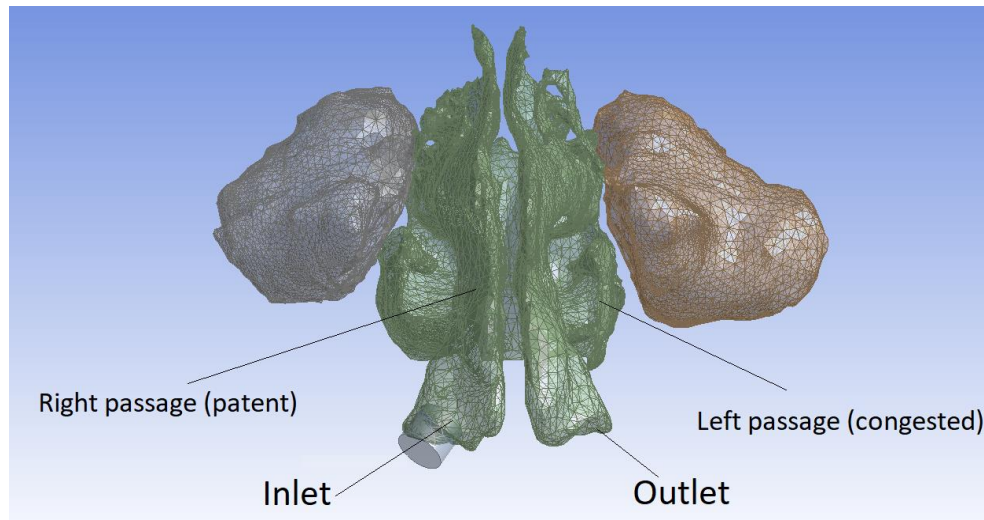


**Figure 4.6. Geometry and boundary conditions showing right side irrigation inlet.**

#### **4.4.6 Head positions**

To investigate the effect of different head positions on the saline-flow field within the nasal cavity and maxillary sinuses, four different head positions typically used for nasal irrigation treatment are investigated. These head positions are Mygind (Figure 4.6a), 90° (Figure 4.6b), head-back (Figure 4.6c), and head-forward (Figure 4.6d). The nostril boundary conditions were swapped and tested again in the four different head positions to account for the different states of erectile tissue congestion on either side of the nose. In the Mygind head position, the user lies in the position with their back on the bed and their head facing upward as pictured in Figure 4.5a. For the 90° head position, the head is tilted to the side at 90° and the irrigation is always introduced into the upper nare. For each head position, the inlet boundary conditions were assigned to right and left sides individually. For the head back position the user stands in an upright position, letting the head fall slowly backwards to 45°, and in the head forward position the head is inclined downwards at 45° to the horizontal axis. This assisted in observing the effect saline irrigation introduced to the congested or patent side had on the saline flow field within the realistic nasal model.

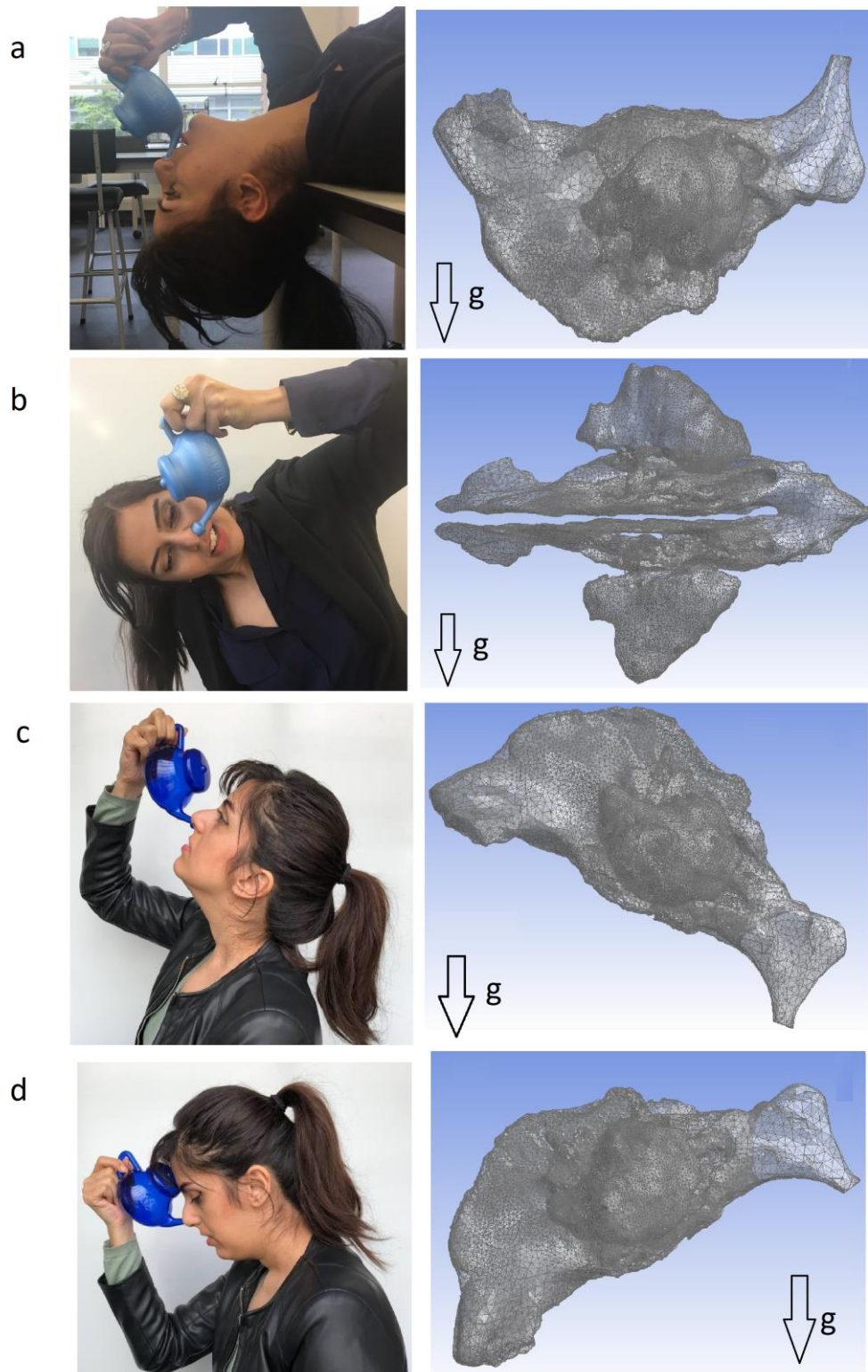


**Figure 4.7. Different head positions considered for simulation: a) Mygind, b) 90°, c) head back, and d) head forward.**

#### **4.4.7 Meshing and sensitivity analysis**

A structured mesh cannot be applied to the complex geometries in the nasal cavity system because the complexity of the geometries are not compatible with the application of Cartesian coordinates. To overcome this problem, an unstructured mesh, comprised of tetrahedral cells, was constructed to fill the complex curvilinear geometries of the nasal cavity (108). During convergence testing, the saline flow field as well as the pressure distribution in the nasal cavity and the amount of saline penetration into the sinuses in the Mygind head position, as shown in Appendix B, were monitored. The criteria for convergence was given as the deviation of results being less than 1% and the saline flow field being almost constant when the number of cells is over 3,200,000. Figure 4.8 shows the final mesh used in the CFD model.

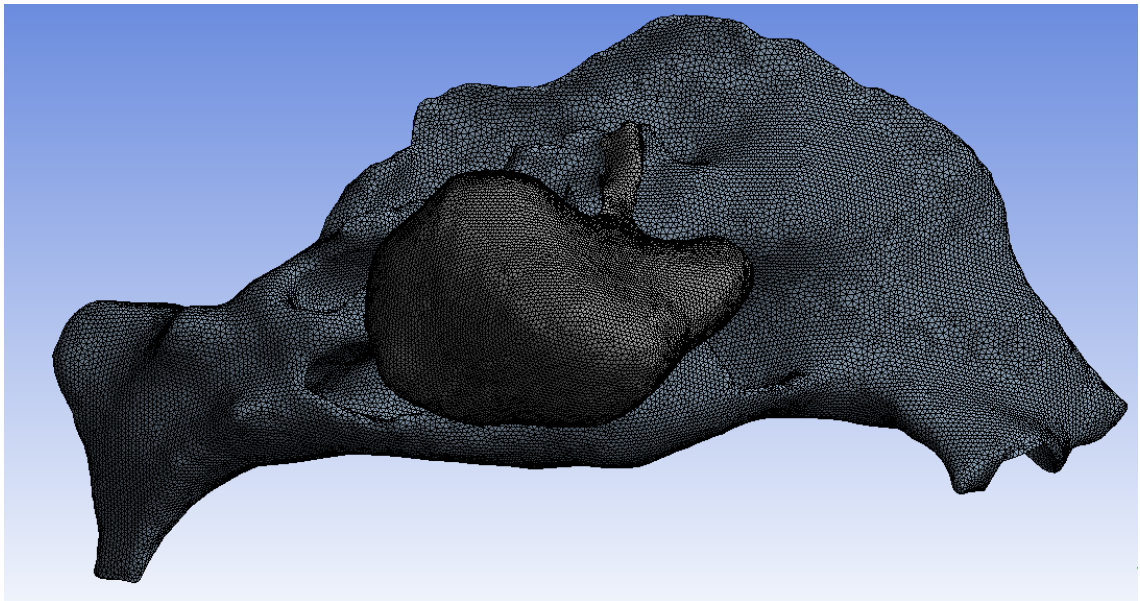


**Figure 4.8. Meshing of the nasal cavity and maxillary sinus.**

#### 4.5 Nasal model casting

The fabrication of the *in-vivo* realistic physical nasal model used in this study is based on the casting method explained by Hopkins et al. (115). This method includes the following steps:

- 3D print in Acrylonitrile Butadiene Styrene (ABS [a material used by 3D printers]) of an *in-vivo* nasal cavity (negative model)
- smooth the ABS surface
- create the casting box
- pour silicone;
- Dissolve the ABS material leaving the transparent nasal cavity.

The final silicone cast model is shown in Figure 4.9.



**Figure 4.9. Completed transparent silicone nasal cavity and maxillary sinuses physical model.**

Full details of the manufacturing process are presented in Appendix C of this work.

## 4.6 Summary

The acquisition and refinement of realistic *in-vivo* nasal cavities and maxillary sinuses geometry used in this study for both the numerical and experimental investigation has been described in this chapter. The numerical setup used in the CFD simulations has been discussed, including use of the multiphase model, turbulence model, steady state, meshing, and mesh sensitivity analysis.

Before analysing the numerical simulation results, it was necessary to undertake an experimental investigation to further validate the accuracy of the applied numerical method. Undertaken in Chapter 5, validation entailed comparison of computational model results to PIV measurements taken within an identified *in-vivo* physical model made from optically clear silicon material. The summary of design and manufacturing processes of the transparent nasal cavity model, including 3D printing and casting the model, are reported in this chapter. The next chapter will discuss the PIV setup and findings using the cast silicone nasal model. The PIV results will be used to validate the CFD *in-vivo* nasal model numerical simulation results during saline irrigation.

# **Chapter 5: Validation of CFD realistic nasal Model using Planar PIV**

## **5.1 Introduction**

Before analysing the numerical simulation results of the realistic nasal model, it was first necessary to undertake an experimental investigation to validate the accuracy of the CFD results. This chapter undertakes the validation of the complex nasal CFD model results using planar-PIV to compare fluid velocity fields in the transparent nasal cast model to those found during CFD simulation during saline irrigation.

## **5.2 Background**

PIV is an optical technique which measures two - or three-dimensional instantaneous velocities over a global domain. The PIV technique is an Eulerian measurement method which calculates fluid velocity as a function of position and time. The PIV apparatus consists of several components including tracer particles, laser, optics, camera, and post processing software.

PIV determines the fluid velocity by field measuring the displacement of small dispersed particles, called tracer particles, between two time instants. Here, the use of tracer particles suspended within the fluid should be large enough to scatter sufficient light for detection, while being small enough to follow the fluid flow without causing flow distortion. The pulse laser needs to provide a large amount of light in a brief time period (3-5 ns) to enable the optical arrangement to produce a light-sheet. This light-sheet creates an optical plane that illuminates the tracer particles suspended within the passing flow. The use of pulse lasers to deliver high light intensity eliminates motion blurring in particle images. The working principles of a basic-planar PIV system are presented in Figure 5.1. This system requires a digital camera set up perpendicular to the light-sheet to record the light scattered by the tracer particles.

The PIV system operates by each consecutive pair of laser light pulses enabling the camera to capture two consecutive images. These two images are called an image pair, and are temporally separated by a short time delay. Successful image pairs are divided into small subsections called interrogation windows. The spatial displacement of each of the individual particles within the interrogation windows for each of the paired images is calculated using a statistical computer-processing method known as cross-correlation. Based on the time delay and image magnification, the velocity vector for each particle is measured by calculating the spatial change per unit time for each interrogation window. Based on the time delay, the velocity vectors for each interrogation window can be calculated by  $U=d/t$  (where 'U' is the velocity, 'd' is the particle displacement, and 't' is the time delay), then plotted on a velocity map.

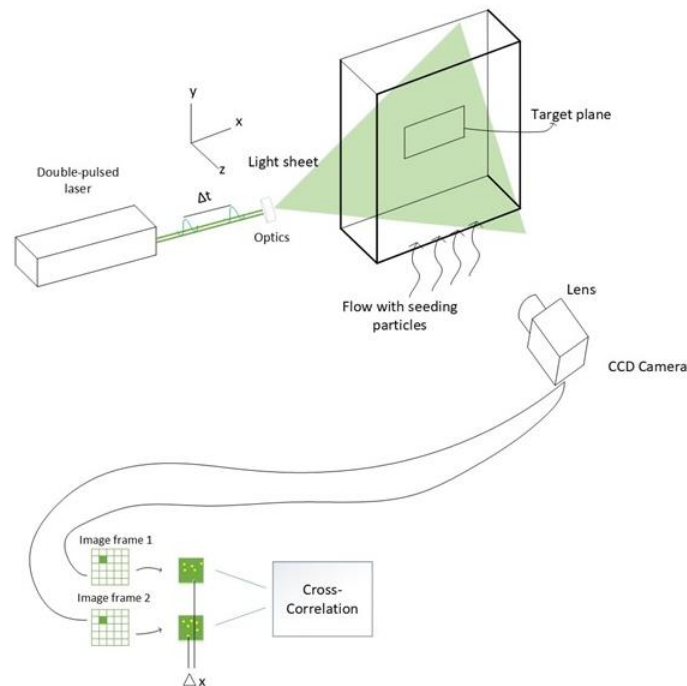


**Figure 5.1. Basic configuration of a Particle Image Velocimetry system (116).**

While PIV has been previously used only in air-flow field measurement within the lower respiratory system, no studies have investigated nasal saline irrigation flow field in the nasal cavities and maxillary sinuses. Most of the previous PIV studies in air-flow field measurement within the respiratory system have been used to validate the CFD methodology. Table 5.1 lists the summary of previous PIV studies used as a reference to validate the CFD results. These studies mainly compared the CFD and PIV results using velocity contours and velocity distribution on the monitoring lines. In this study, the same methodology used in the previous literature (Table 5.1) will be applied to compare the CFD and PIV results.

**Table 5.1. Summary of previous PIV studies used for CFD validation.**

Authors	Ref	Study	Validation/ Comparison	Max Error	Mean error
Heo et al	(117)	Airflow/post-surgery (Nasal cavity)	Comparison between velocity contours and flow features	Not mentioned	Not mentioned
Cozzi et al.	(118)	Airflow (Nasal cavity)	Comparison between velocity contours and flow features	Not mentioned	Not mentioned
Zubair et al.	(119)	Airflow (Nasal cavity)	Comparison between velocity contours and flow features	Not mentioned	Not mentioned
Ertbruggen et al.	(120)	Airflow (alveolated bend)	Comparison between velocity contours and flow features	27%	15%
Bailie et al.	(121)	Airflow (nasal obstruction)	Comparison between velocity contours and flow features	Not mentioned	Not mentioned
Doorly	(122)	Airflow (Nasal cavity)	CFD and visualization	Not mentioned	Not mentioned
Chung and Kim	(123)	Airflow (nasal cavity)	Comparison between velocity contours and flow features	Not mentioned	Not mentioned`

Li et al.	(124)	Airflow (Nasopharynx and pharynx)	Contour and flow feature comparison/ monitoring lines	40%	Not mentioned
Phuong et al.	(125)	Airflow (Upper respiratory system)	Comparison between velocity contours and flow features	30%	Not mentioned
Inthavong et al.	(126)	Particle (Nasal cavity)	Comparison between velocity contours	Not mentioned	Not mentioned
Butchman	(127)	Blood flow (Carotid artery)	Comparison between velocity contours and flow features	43%	Not mentioned
Xiong et al.	(128)	Blood flow (Carotid artery)	Comparison between velocity contours and flow features	14-85%	Not mentioned

### 5.3 Experimental setup

#### 5.3.1 Fluid circuit

The nasal cast model was placed in a flow circuit as shown in Figure 5.2. In order to later compare the CFD and PIV results, it is essential to replicate the same steady-state conditions that are input into the CFD model. To achieve this, a constant-pressure header tank was used to supply a steady pressure for the water seeded with tracer particles to pass through the transparent nasal cavity model. A pipe was also connected from the weir to the reservoir to return the overflow fluid back to the reservoir.

For this experiment, Nd:YAG was used for PIV measurement as it uses a double pulse laser as the light source. Care was taken as this light is dangerous to the human eye. This laser uses a crystal which is neodymium-doped yttrium aluminium garnet-NdY<sub>3</sub>Al<sub>5</sub>O<sub>12</sub>, as the lasing medium to generate a beam of a wavelength 1064 nm. Because the camera cannot capture this frequency, a frequency-doubling crystal (Potassium dihydrogen phosphate) converts the light it into a green-coloured beam with a wavelength of 532 nm.

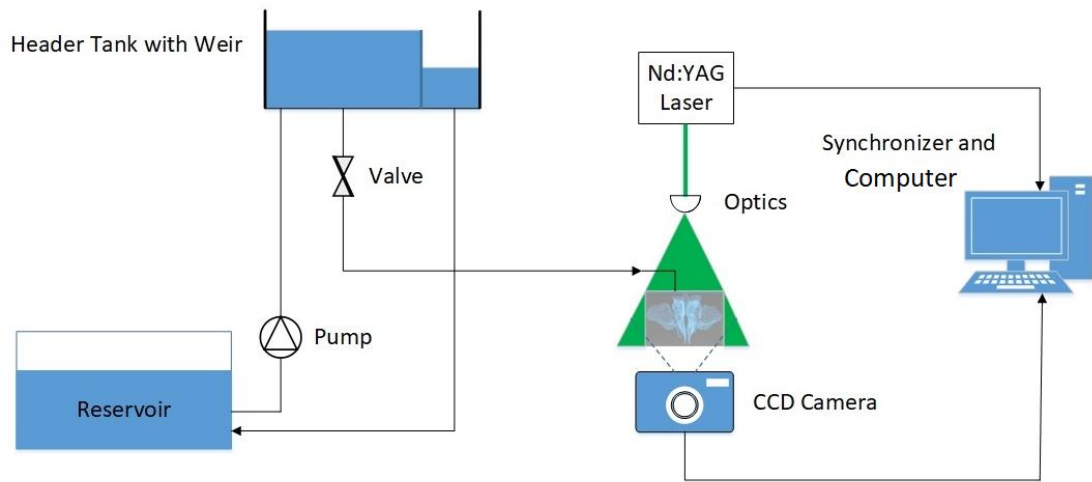


**Figure 5.2. Schematic view of the experimental fluid circuit.**

A series of optics is required to produce the light-sheet required for the 2-D PIV measurements undertaken in this study. The light-sheet was aligned on top of the model, which illuminated the particles as the flow passed through the nasal cast model. In this experiment, a digital charge-coupled device (CCD) TSI 4MP camera, which offered 2048x2048 pixel resolution, was used for detecting particle motion. The specifications of this camera are listed in Table 5.2. A 60mm Nikon lens that offered an aperture range from f-number 2.8 to 32 was mounted on the TSI CCD camera. Changing the f-number during the PIV procedure was necessary under different light conditions to capture the highest number of particles within the light-sheet. While CCD captured more light, which brightened the particles by using a larger apertures (smaller f-number), this larger aperture size also resulted in a decrease in the depth of field. To get the best results required a balance in these two parameters. The camera and laser were synchronised with a pulse/delay which generates transistor-transistor logic (TTL) signals. TTL is a digital logic design which act as on/off switch controlled by voltage level.

**Table 5.2. Digital camera specifications.**

Specs	TSI Power View Plus 4Mp
Sensor type	CCD
Pixel resolution	2048x2048
Pixel size	5.4 $\mu\text{m}$ x 5.4 $\mu\text{m}$
Frame rate	180 frames/sec
Output	12-bit
Features	Low noise High resolution High quantum efficiency
Lens mount	F-mount
Standard camera lens	Nikon 60mm F1.8 lens

To commence the experiment, the header tank valve was opened and flow was circulated through the model until it reached a steady state before PIV measurement commenced. This was achieved by turning on the laser and capturing images with the camera.

To minimise optical distortion during the PIV procedure, the refractive index of the fluid flowing within the model needed to match that of the transparent model featuring the non-uniform shape and curved walls.

Since the refractive index of the water does not match that of the silicone cast model used in this experiment it was replaced with a mixture of water and glycerol (129). This fluid mixture has been shown previously to be a reliable fluid that matches the refractive index of the silicone, quantified by the manufacturer as 1.43 (130). Water and glycerol have a refractive index of 1.47 and 1.33, respectively. In this study a mixture of 39% water and 61% glycerol by volume was used (the same as the fluid which was used by Spence et al.(75)), at a working temperature of 25°C to ensure a matching refractive index between

the fluid and the model. The density and dynamic viscosity of the working fluid are 1156.6 (kg m<sup>-3</sup>) and 10.6 (mPa s) respectively (131). To validate this refractive index matching, the water/glycerol mixture was passed through a transparent silicone pipe placed in front of a grid of black and white squares. Figure 5.3 clearly shows the grid is not distorted which validates the refractive index matching. The comparison between the PIV with water and glycerol, and the CFD with saline, is achieved by using dynamic similarity, which is explained in the next section.

Hollow glass spheres were used to seed the fluid in the reservoir. These seeding particles had a mean diameter of 16.2 μm and density of 1.1 g/cm<sup>3</sup> to closely match the fluid density, which was 1.15 g/cm<sup>3</sup>. Previous investigations have shown hollow glass sphere seeding particles have a low Stokes number (a particle with a low Stokes number follows fluid streamlines) and provides good light scattering efficiency to assist being detected by the camera (75).

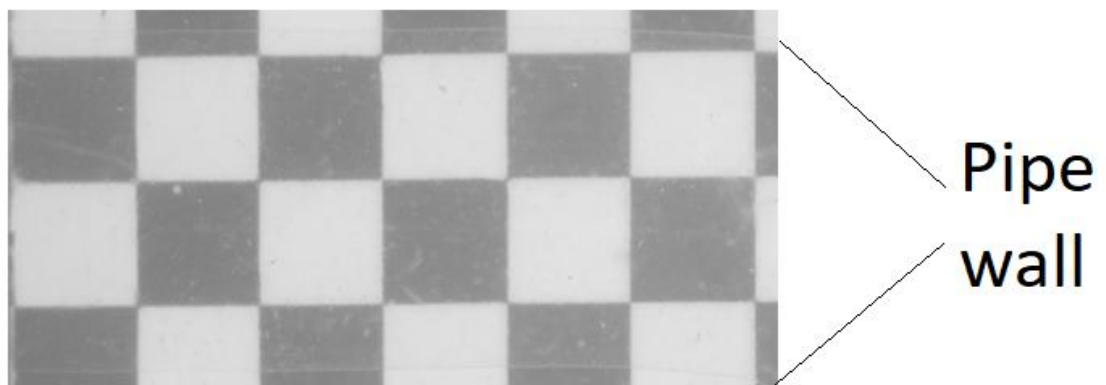


**Figure 5.3. Refractive index matching of the fluid with silicone model.**

### 5.3.2 Validation methodology

The PIV results of normalised velocity distribution were compared to comparable CFD simulation data using identical realistic *in-vivo* nasal morphology through one common coronal cross-section of the nasal cavity, the nasopharynx. As saline moves through one nasal passage, it reaches the posterior region of the nasal cavity and the saline turns around in the nasopharynx and enters the contralateral nasal passage. This region was chosen because the saline experiences high velocity components in the turning directions (x,z) and the depth velocity component (y) is negligible compared to the other two components, making it ideal for 2-D analysis. Here the y-component does not make up the majority of the absolute value throughout the nasopharynx (75). In another PIV study (132), the velocity field with a u-bend pipe was mapped and it was found that the velocity components in the turning directions make up the majority of the velocity magnitude. This prior work justifies the capture of the velocity field with a planar PIV in the nasopharynx plane. Dynamic similarity between the *in-vivo* physical and computational models was achieved by using equation (5.1) (130) to maintain a constant Reynolds number in the nostril of each model.

$$Q_{physical} = n \frac{\nu_{physical}}{\nu_{Computational}} Q_{computational} \quad (5.1)$$

Where  $Q_{computational}$  is the volumetric flow rate delivered by a constant head tank of 650 Pa (the pressure head of the Neti pot contains 120 ml of saline);  $n$  is the scale number which in this study is 1.5;  $\nu_{physical}$  is the kinematic viscosity of the water and glycerol mixture; and  $\nu_{Computational}$  is the kinematic viscosity of the saline. By doing this it is possible to ensure that the flow physics in the physical model are representative of the CFD model with different scales and working fluid. The model was scaled to increase the effective spatial accuracy in model construction and in setting-up and aligning the laser sheet with the narrow nasal passageways (75).

Another justification for analysing the nasopharynx coronal plane is that, during nasal irrigation, some other regions (depending on the different head positions and flow directions) remained unirrigated. This is caused by air being trapped in some specific regions of the nasal cavity. The existence of air in the target plane results in a “blooming” effect on the PIV camera CCD array, causing saturated pixels to contaminate the image and distort the cross-correlation calculations. Additionally, it was not possible to choose the sagittal plane for validating the CFD model since the maxillary sinuses blocks this view and cannot be fully filled with water-glycerol. The nasopharynx coronal plane was the only view which stayed filled with water-glycerol mixture for all different head positions and flow directions. Figure 5.4 shows the captured plane at each head position.

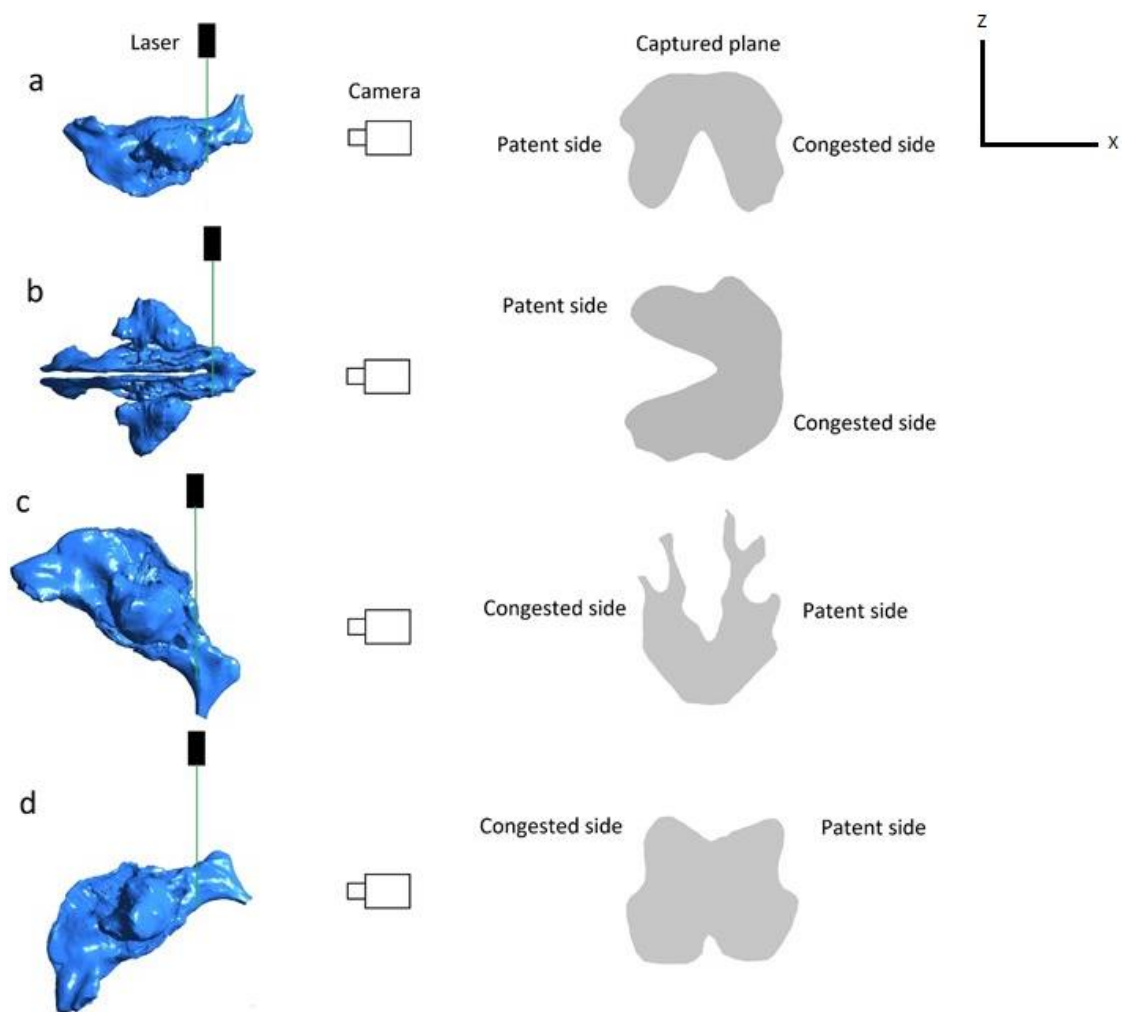
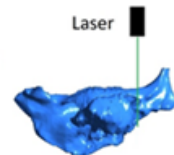


**Figure 5.4.** Images demonstrating the four different head positions a) Mygind b) 90° c) head back d) head forward.

## 5.4 Results

For each head position, comparison between PIV and CFD results were made using normalized velocity contours on the captured plane. To test quantitative agreement between the CFD simulation and the PIV experiment, three lines (vertical midline of the congested side, patent side, and a horizontal line connecting the two passages together) were selected to show the normalized velocity. The velocity values were calculated as scalar velocities using two velocity components  $U = \sqrt{u^2 + w^2}$  where  $u$  and  $w$  are velocity components in  $x$  and  $z$  direction. To avoid possible confusion in the velocity field comparison between the CFD and PIV results, all velocity magnitudes reported in this study were normalized by the mean velocity over the cross-section under consideration. Normalization of velocity magnitude ( $v_n$ ), by means of average velocity, adjusts the values measured in the CFD and PIV models to a common scale. This method has also been used in other earlier studies to compare and validate models with different geometrical scales (133). Also, three monitoring lines were chosen (L1, L2, and L3) to compare the normalised velocity. These lines are also made non-dimensional by dividing them by the length of each line.

### 5.4.1 Mygind head position irrigated from the right patent side



The CFD and PIV results during nasal irrigation from the right naris, compared in Figure 5.5, show close agreement in the velocity field, with the low-velocity zone appearing in the region which connects the patent side to the congested side. Both PIV and CFD results have the higher velocity region at the top region of the congested side. This occurs due to acceleration of the flow caused by an inclination where the saline moves down towards the superior nasal airway and olfactory slit.

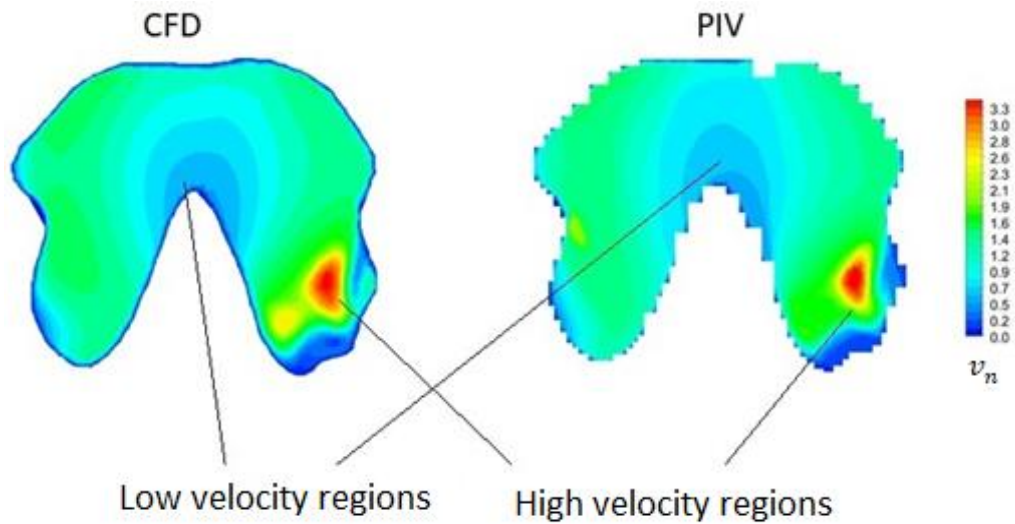


**Figure 5.5. Comparison between CFD predicted results and PIV measurements of the normalized velocity field through a coronal cross-section of the nasal cavity at the Mygind head position irrigated from the right patent side.**

Comparison of the normalised velocity values on the monitoring lines between the CFD and PIV results for the Mygind head position is shown in Figure 5.6. Here the velocity magnitude is almost constant in the CFD results at the patent side (L1), and it gradually increases at the bottom region in the PIV results. In the congested side, the velocity distribution predicted by CFD is similar to the PIV measurements, except the velocity peak at the end of the line is higher in the CFD simulation. The velocity-changing trend predicted by the CFD simulation is close to the PIV results. The average variation between CFD and PIV results for lines L1, L2, and L3 was 7%, 10% and 13% respectively.

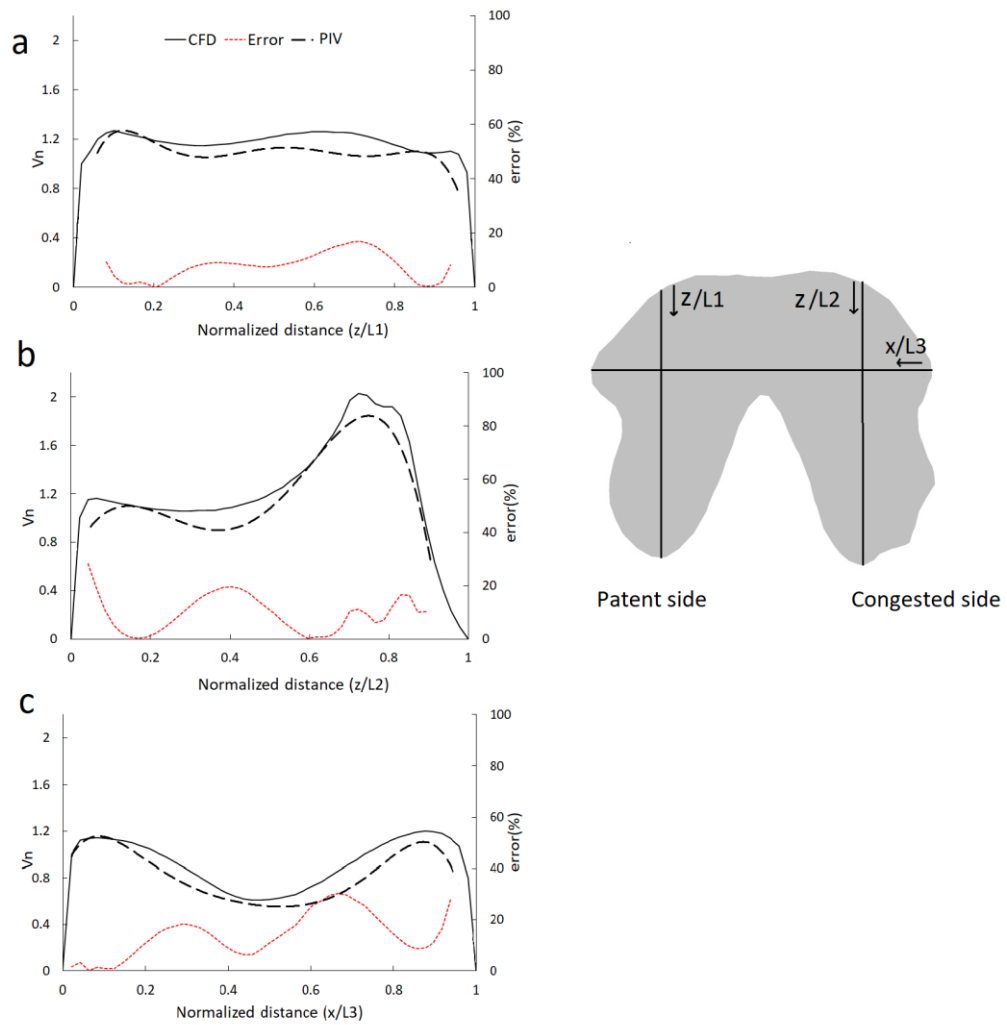
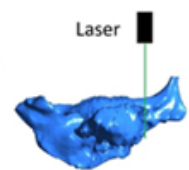


**Figure 5.6.** Comparison between CFD results and PIV measurements of the normalized velocity on a) L1, b) L2, and c) L3 on the coronal cross-section at Mygind head position irrigated from the right patent side (— CFD, ----PIV, and ---- error).

#### 5.4.2 Mygind head position irrigated from the left congested side



In the Mygind head position, when the nose was irrigated from the left congested naris, the saline splits into three passages (inferior, middle, and superior meati) prior to reaching the posterior region of the nasal cavity.

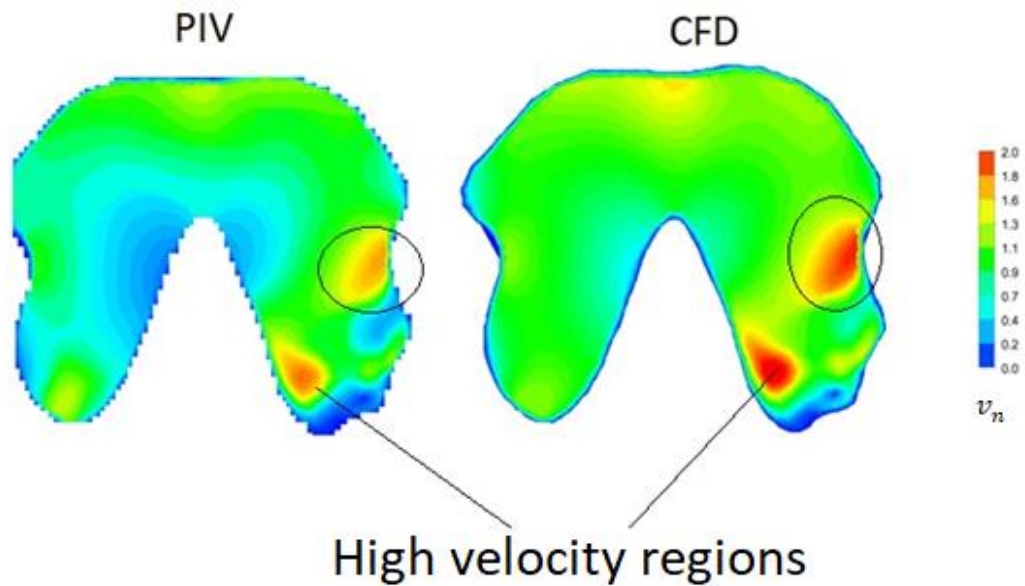


**Figure 5.7. Comparison between CFD results and PIV measurements of the normalized velocity field through a coronal cross-section of the nasal cavity at the Mygind head position irrigated from the left congested side.**

Before turning around in the nasopharynx where the PIV and CFD data is compared, a radial saline pressure gradient developed due to the bend shape of the nasopharynx. Because of this, saline was pushed from the inner side wall to the outer side wall accompanied by an axial velocity drop as shown in Figure 5.7.

Here saline streamed through the middle and superior meati which yielded a higher velocity magnitude as it reached the nasopharynx. At this point the axial velocity turned into the circumferential velocity (x and z direction). This high velocity region can be seen in Figure 5.7 which compares PIV experimental and CFD simulation results.

Figure 5.8 presents the normalized velocity on L1-L3 in the Mygind head position irrigated from the congested side. The velocity variation in the L1 position shows that the PIV could measure more flow details on the patent side, while the velocity changes in the predicted CFD results were not significant. At position L2, at the middle of the normalized distance there is a noticeable difference (23%) between the CFD and PIV

results. Here the velocity field in this region was over predicted by CFD possibly, due to the under-prediction of the eddy-viscosity which resulted in a 25% error between CFD and PIV results. The under-prediction of the eddy viscosity also allows the flow to experience less inertia and to accelerate more rapidly. The normalized velocities on L3 in both CFD and PIV results also show a similar pattern.

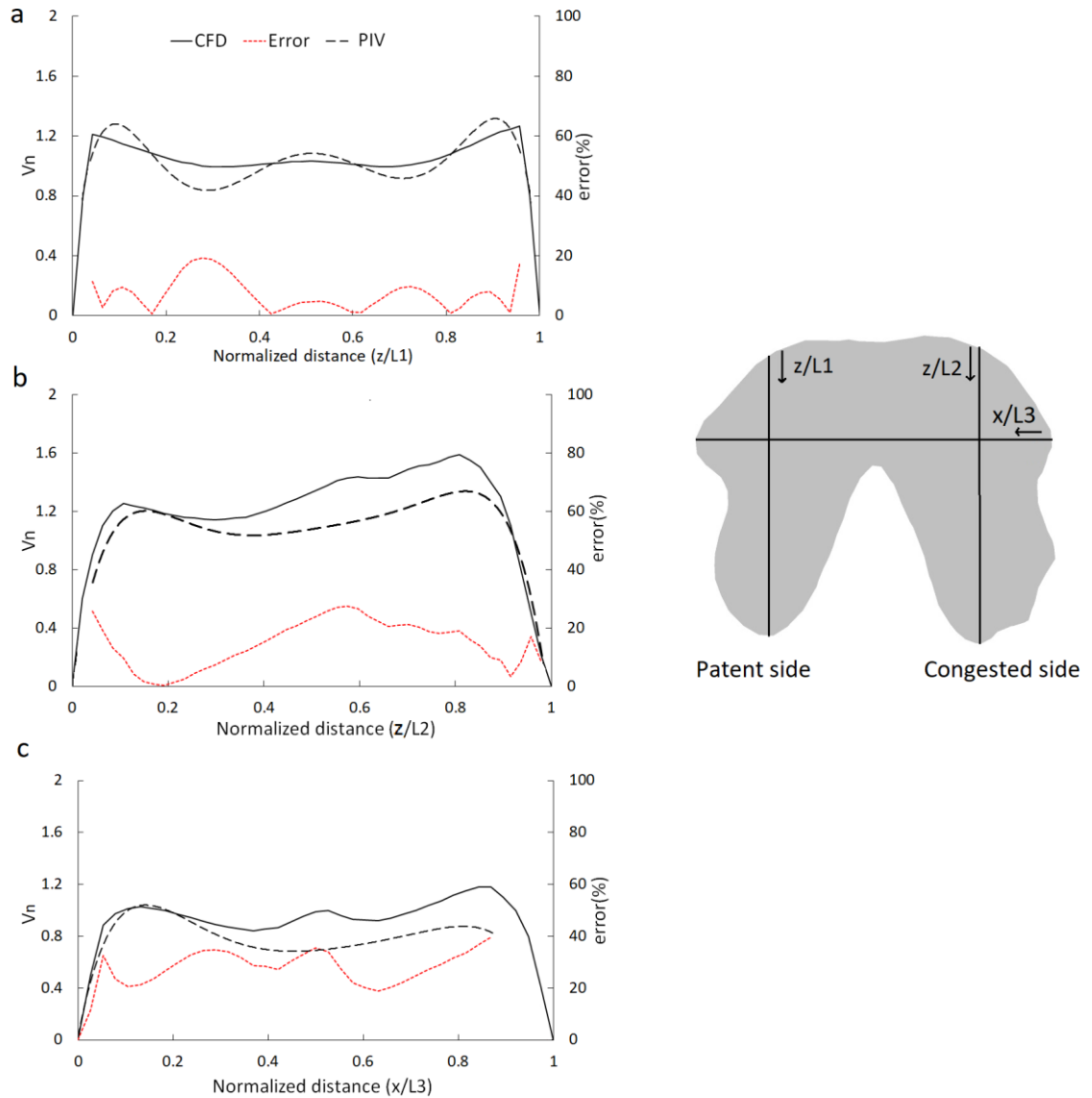
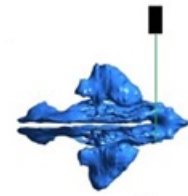


**Figure 5.8. Comparison between CFD results and PIV measurements of the normalized velocity on a) L1, b) L2, and c) L3 on the coronal cross-section at the Mygind head position irrigated from the left congested side (— CFD, ----PIV, and ---- error).**

### 5.4.3 90° head position irrigated from the right patent side



During irrigation in the 90° head position, saline turning around the nasopharynx was separated from the upper nasal wall. This flow separation was large, because the turning of flow direction within the nasopharynx coincided with the direction of gravity which led to flow separation being observed in both the CFD and PIV tests. This flow separation created an air trap in the upper side of the nasal cavity that resulted in a blooming and optical distortion effect in the PIV results. Because of this, both PIV and CFD results are shown only in the lower contralateral side of the plane in Figure 5.9 where the contour of the normalized velocity in a 90° head position irrigated from the patent side is presented. Both CFD and PIV tools predicted the same high-velocity regions, which occur at the outer wall of the curve as shown in Figure 5.9. The acceleration of flow velocity near the outer wall at 180° has previously been noted by other researchers (134) and can be observed in Figure 5.9 for both CFD and PIV tests (high velocity region). The over-prediction of the CFD in the velocity field near the inner wall is noticeable, and the highest difference between the CFD and PIV results can be seen in this region.

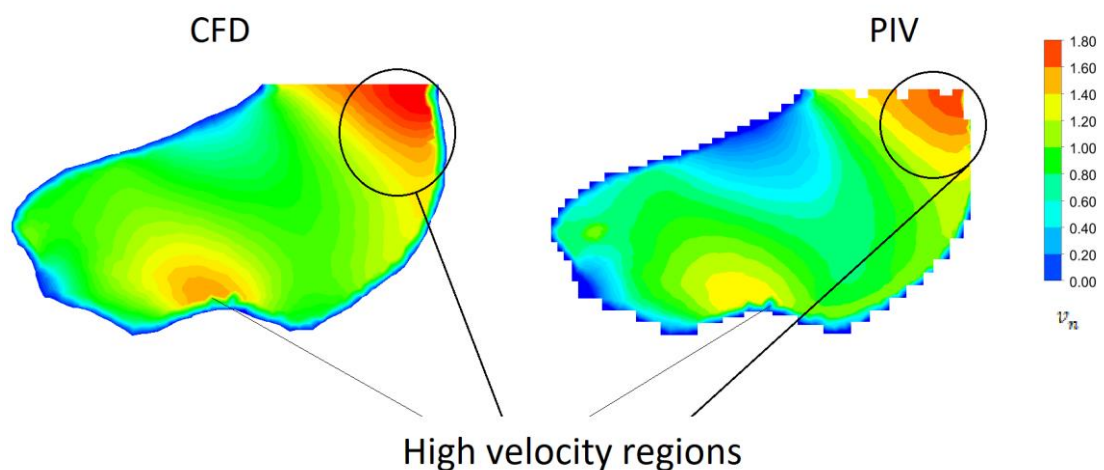


**Figure 5.9.** Comparison between CFD results and PIV measurements of the normalized velocity field through a coronal cross-section of the nasal cavity at 90° head position irrigated from the right patent side.

To further validate the CFD results in this user condition, the normalized velocity is shown on L2 and L3 in Figure 5.10. L1 is not included because it was located on the patent side where the trapped air distorted the PIV images. CFD results show a good quantitative agreement with the PIV experimental results. Here, the average relative error is 8.4% and 13% in L2 and L3 respectively.

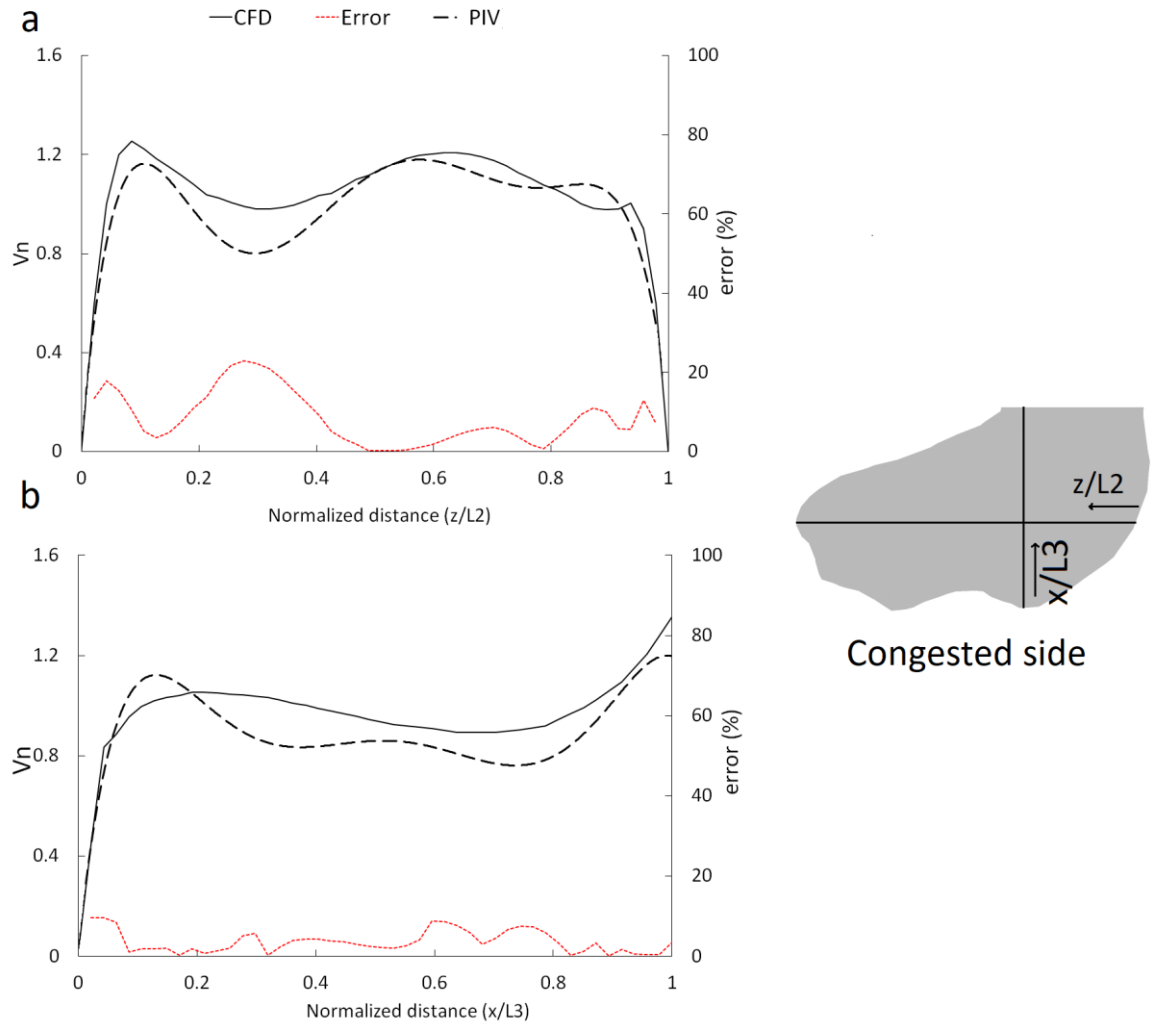
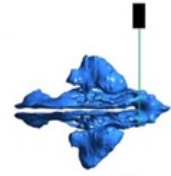


**Figure 5.10. Comparison between CFD results and PIV measurements of the normalized velocity on a) L2 and b) L3 on the coronal cross-section at 90° head position irrigated from the right patent side (— CFD, ----PIV, and ---- error).**

#### 5.4.4 90 ° head position irrigated from the left congested side



Despite changing the side of the direction of irrigation in flow to the left congested nare, a similar flow-pattern was observed at the nasopharynx to that found in the previous test. Saline flow detached from the outer wall, and caused an air trap to occur in the upper posterior region of the nasal cavity. Because of this, the PIV results are only compared to CFD data on the contralateral side (patent side). At the entry of the image plane, which is shown in Figure 5.11, the higher velocity region can be observed. In this region, the flow easily moves towards the other side (x direction).

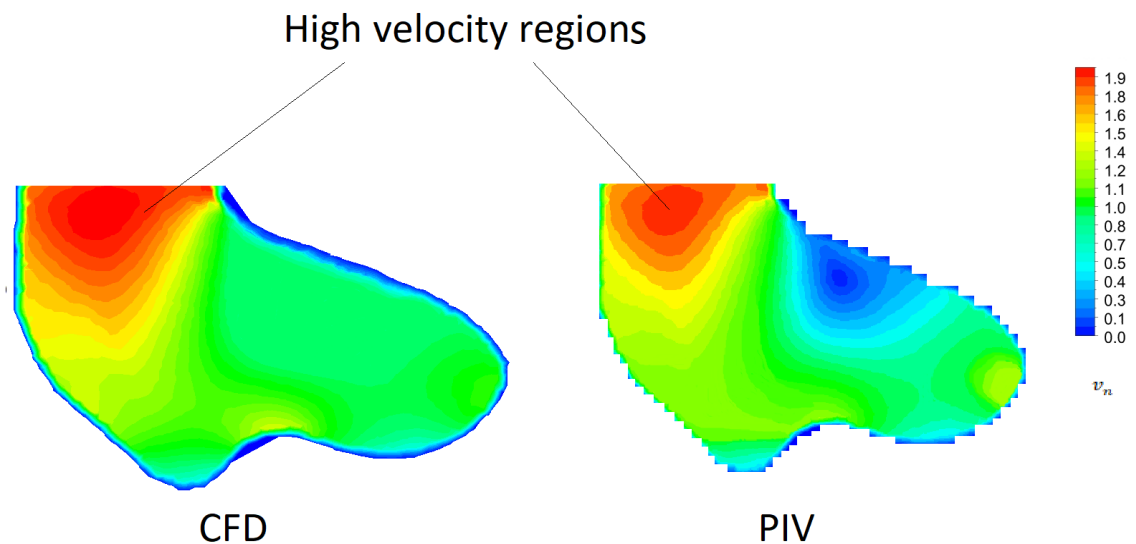
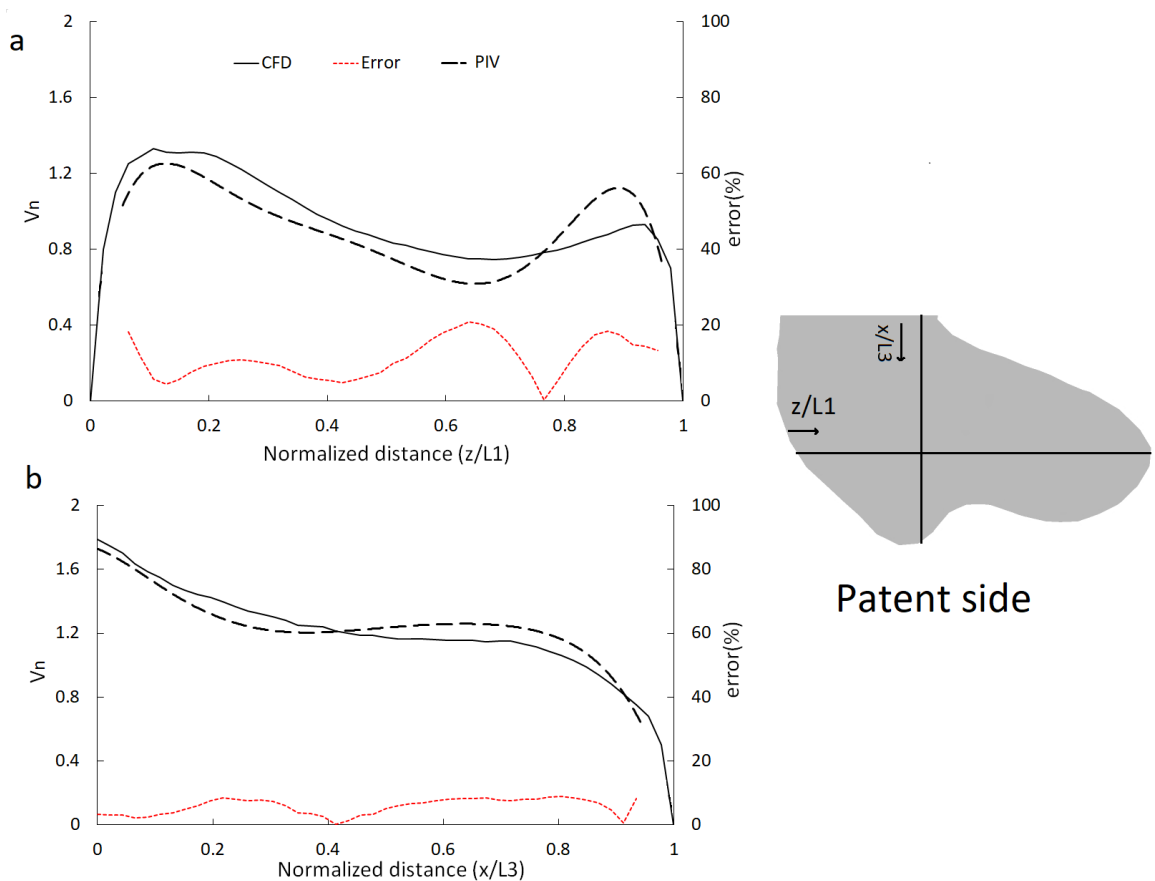


Figure 5.11. Comparison between CFD results and PIV measurements of the normalized velocity field through a coronal cross-section of the nasal cavity at 90° head position irrigated from the left congested side.

The normalized velocity on L1 and L3 at 90° head position are shown in Figure 5.12. Here the PIV results show a higher normalized velocity at the end of the normalized distance for both lines compared to the CFD simulations. The peak velocity for both CFD and PIV results were close at the beginning of the L3 plane. The velocity-variation trend is shown by Figure 5.12, in which saline velocity gradually becomes low at the middle, and relatively high at the beginning and end of the L1 plane.



**Figure 5.12. Comparison between CFD results and PIV measurements of the normalized velocity on a) L1 and b) L3 on the coronal cross-section at 90° head position irrigated from the left congested side (— CFD, ----PIV, and -.- error).**

### 5.4.5 Head back position irrigated from the right patent side

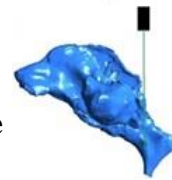
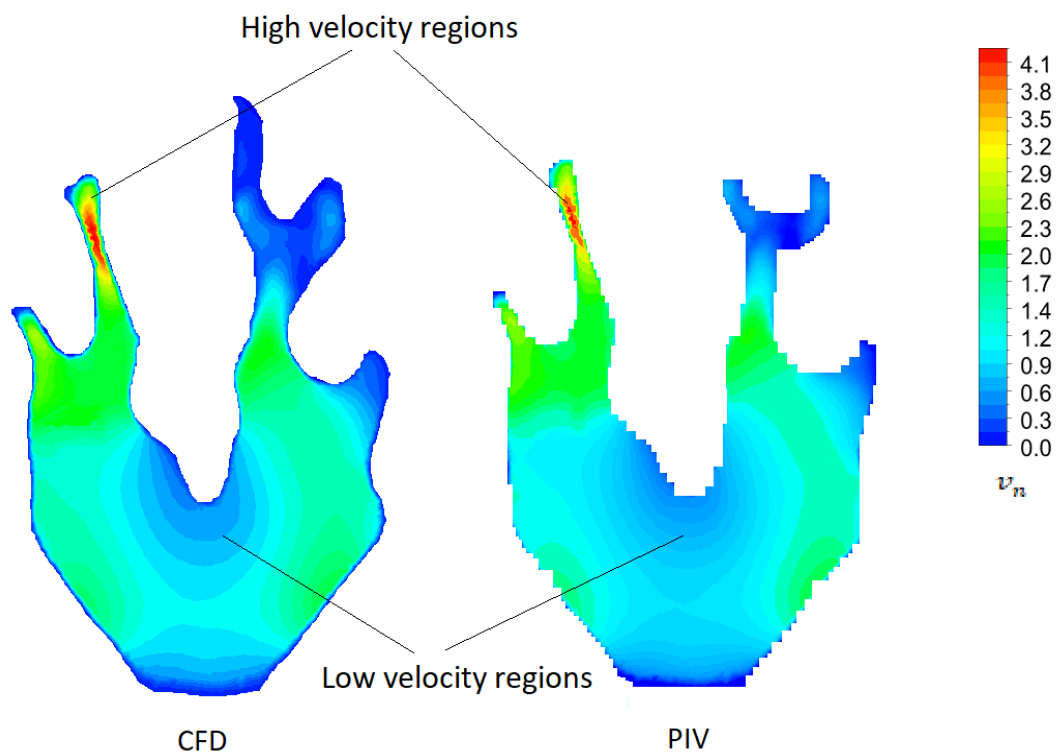
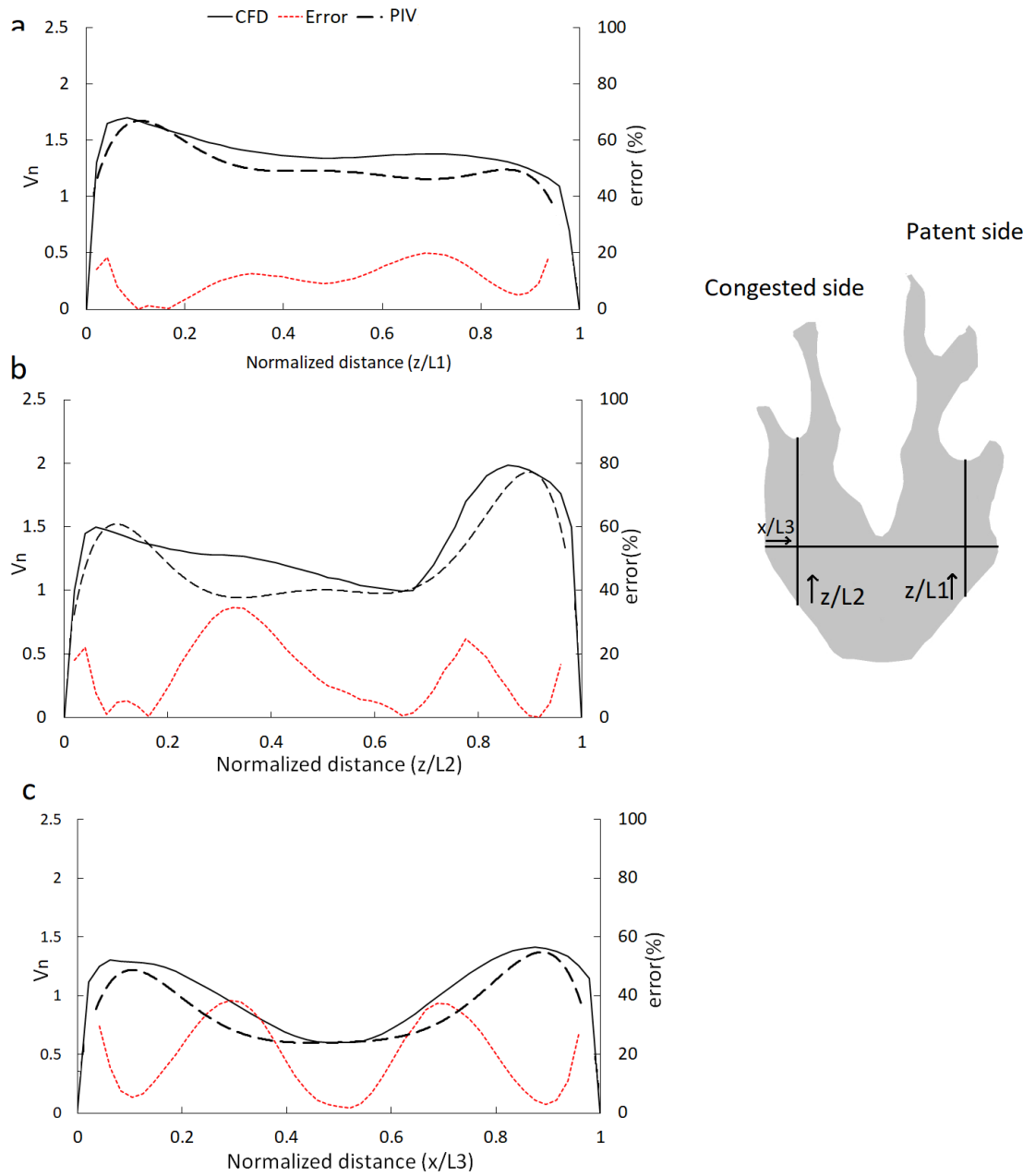


Figure 5.13 presents the velocity contour for the head back position irrigated from the patent side comparing both CFD and PIV results. The velocity contour demonstrates that the basic structure of the flow field is well-predicted by the CFD simulation. Here a high velocity region at the middle turbinate on the congested side can be observed in both CFD and PIV model results. The velocity variations at the region where the two passages are connected to each other are also similar, with the PIV experiment presenting more detail in this region.



**Figure 5.13. Comparison between CFD results and PIV measurements of the normalized velocity field through a coronal cross-section of the nasal cavity at head back position irrigated from the right patent side.**

Figure 5.14 presents the normalized velocity profiles for the head back position irrigated from the patent side plotted at three different locations (L1, L2, and L3) in the nasopharynx coronal cross-section. The CFD predictions for the head back position demonstrate a consistent result (average error for L1, L2, and L3 is 12%, 14%, and 18%) compared the PIV results. In L1, the velocity magnitude decreased in both PIV and CFD results as they progressed further upstream. At L2, it is notable that the CFD velocity magnitude changed in the midline, while the PIV result is almost constant. Here both CFD and PIV velocity results start to increase after  $z/L2=0.7$  which leads to a maximal error of approximately 35%. At L3, the largest relative error occurred (38%) between the CFD and PIV results. This finding is possible due to the PIV measurement being lower than the experimental velocity as a result of the PIV cross-correlation window's averaging effect and high velocity gradients experienced.



**Figure 5.14.** Comparison between CFD results and PIV measurements of the normalized velocity on a) L1, b) L2, and c) L3 on the coronal cross-section at head back position irrigated from the right patent side (— CFD, ----PIV, and - - - error).

#### 5.4.6 Head back position irrigated from left congested side

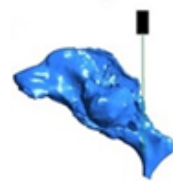


Figure 5.15 shows the in-plane coronal nasopharynx velocity magnitude contours and the CFD results compared to PIV measurements.

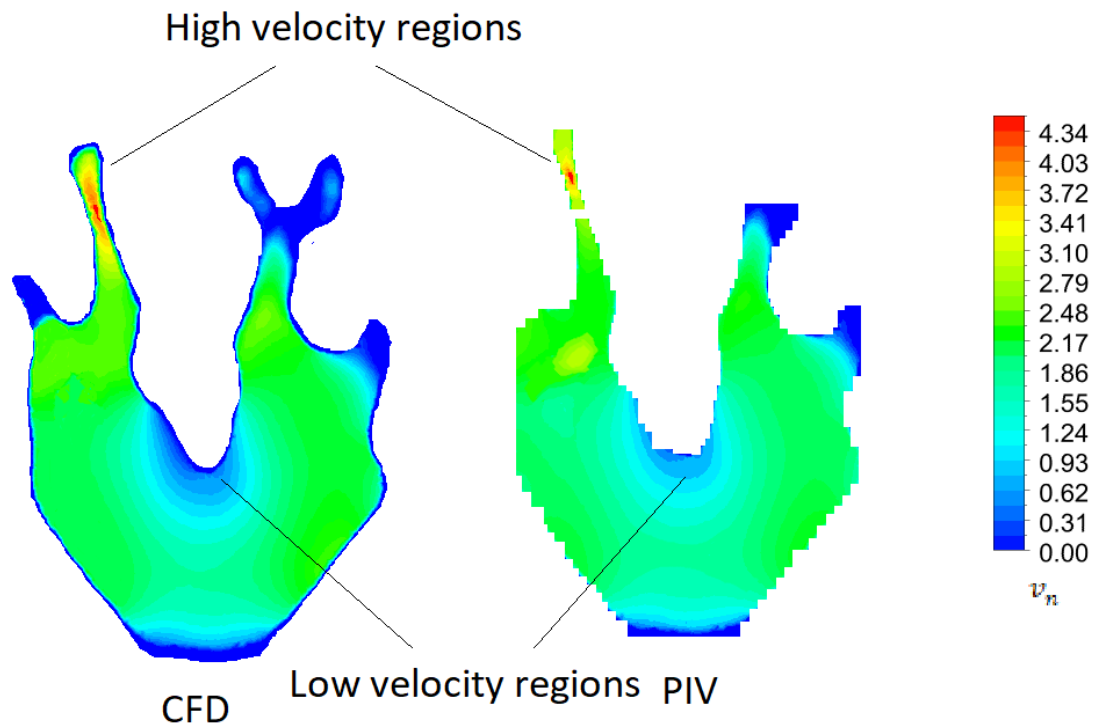
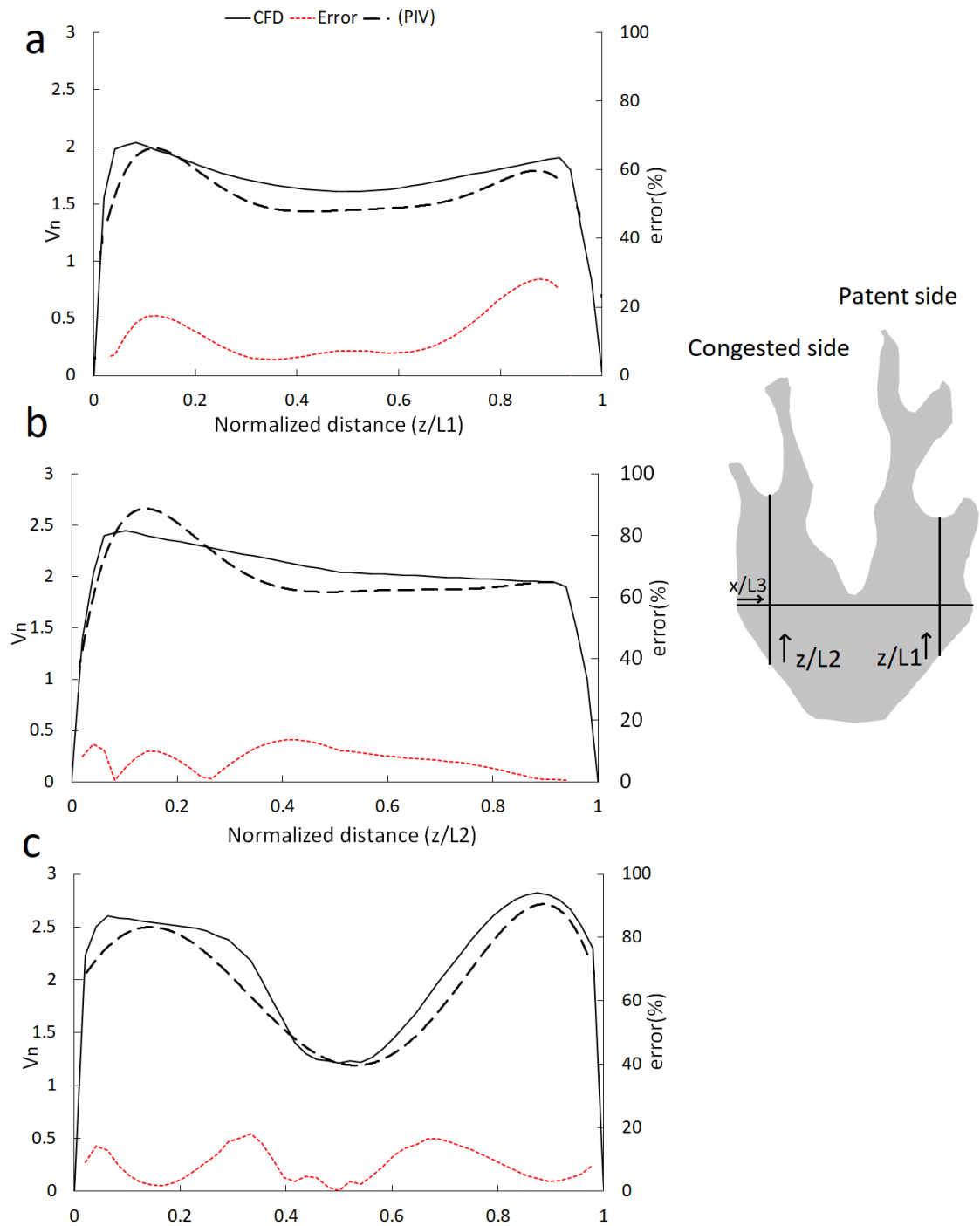


Figure 5.15. Comparison between CFD results and PIV measurements of the normalized velocity field through a coronal cross-section of the nasal cavity in head back position irrigated from the left congested side.

The results presented in Figure 5.16 show a good agreement between the PIV and CFD methods. In PIV, the flow field in meati branches could not be measured. This happened due to the existence of some air bubbles, which were trapped in the narrow regions. Figure 5.16 compares the saline velocities from both the PIV experiment and CFD simulation when the irrigation was performed in a head back position from the congested side. A low velocity region can be observed around the inner side of the nasopharynx in both PIV and CFD.

The velocity trends at planes L1, L2, and L3 are similar in both PIV and CFD. At the L2, the PIV could capture the same high velocity region that was also shown in Figure 5.16.



**Figure 5.16. Comparison between CFD results and PIV measurements of the normalized velocity on a) L1, b) L2, and c) L3 on the coronal cross-section at head back position irrigated from the left congested side (— CFD, ----PIV, and ..... error).**

### 5.4.7 Head forward position irrigated from patent side



The velocity contour in a head forward position irrigated from the patent side is presented in Figure 5.17. Here, in both PIV and CFD tests, the irrigant was detached from the top wall of the nasal cavity with air trapped on top of the coronal plane across the nasopharynx. For this head position, the CFD predictions are reasonably consistent with the PIV results and good agreement between these two can be observed especially in the high velocity regions. The highest velocities in the flow field were achieved in the right- and left-bottom corners of the plane, caused by an inclination where the saline moves down towards the inferior airway.

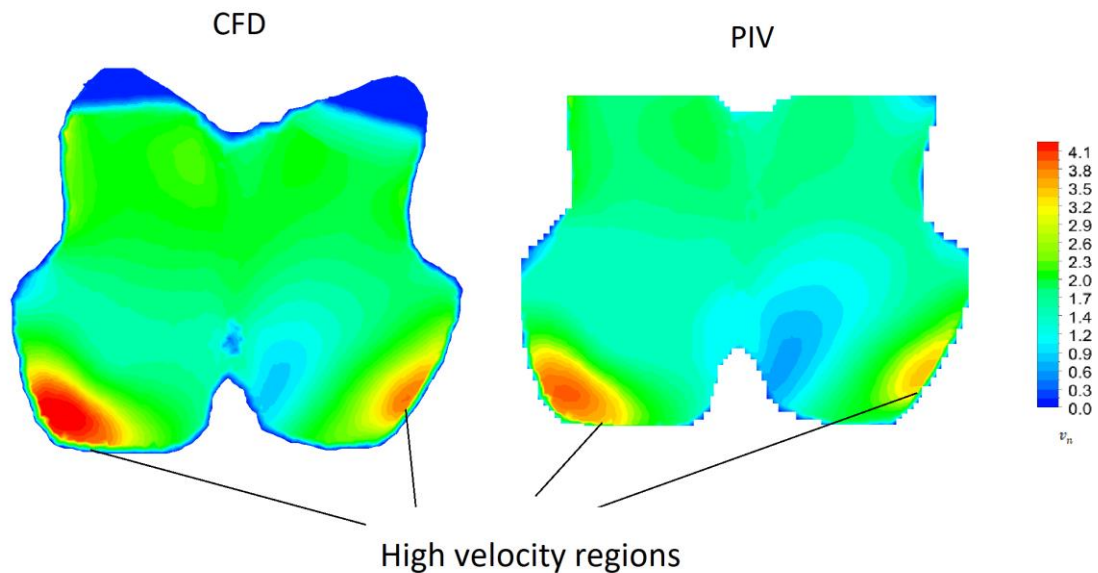


**Figure 5.17. Comparison between CFD results and PIV measurements of the normalized velocity field through a coronal cross-section of the nasal cavity at head forward position irrigated from the patent side.**

The normalized velocity profiles at L1, L2, and L3 are shown in Figure 5.18. CFD results for L1 and L2, which show the normalized velocity in the right and left passages, are similar, while the PIV could detect a difference in velocity magnitude between these two regions. In this test good agreement between PIV and CFD results is achieved with average relative errors of 21.3%, 12%, and 17% for L1, L2, and L3.

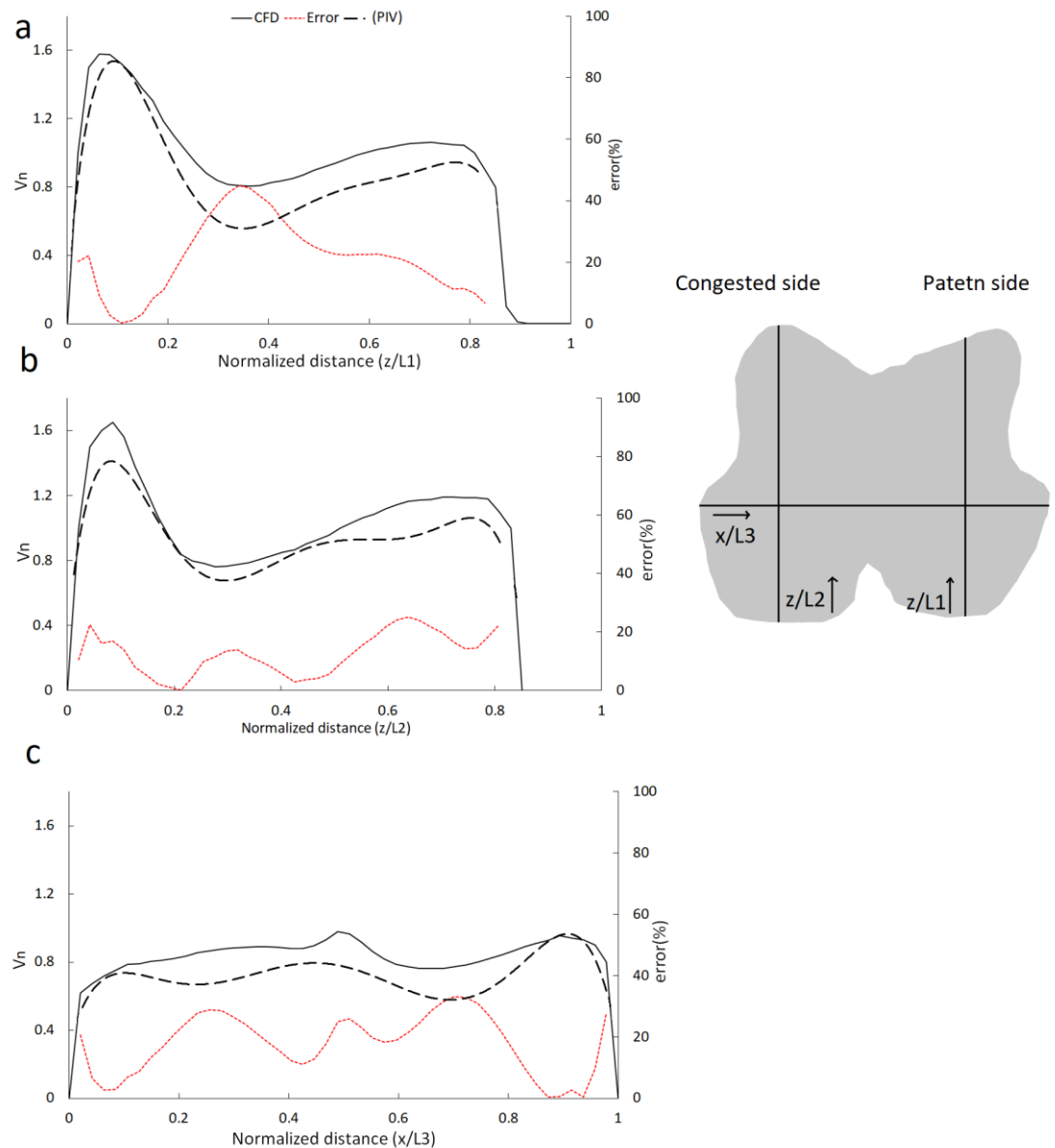
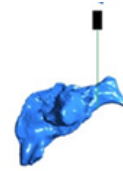


**Figure 5.18. Comparison between CFD results and PIV measurements of the normalized velocity on a) L1, b) L2, and c) L3 on the coronal cross-section at head forward position irrigated from the right patent side (— CFD, ----PIV, and ---- error).**

#### 5.4.8 Head forward position irrigated from left congested side



In a head forward position irrigated from the congested side, the irrigated saline could not fill the nasal passages. Here the nasopharynx was only partially filled and it was not possible to conduct the PIV experiment to measure the flow field in this region due to the optical distortion caused by trapped air. Because of this result no comparative validation possible between CFD and PIV analysis due to absence of data.

#### 5.5 Analysis of relative error between PIV and CFD results

Analysis of errors found between the PIV experiment and CFD simulation data were defined by comparing the difference between PIV experimental and CFD numerical results, as given by Buchmann et al. (127):

$$E_{rel} = \left| \frac{f_N - f_E}{f_N} \right| \quad (5.2)$$

Where  $f_N$  and  $f_E$  are the numerical and experimental data points.

A summary of the average error at different head positions and side directions are listed in Table 5.3.

**Table 5.3. Average error at different head positions and side directions.**

	L1	L2	L3
Mygind-irrigated from patent side.	7%	10%	13%
Mygind- irrigated from congested side.	10%	15%	21%
90°- irrigated from patent side.	*	8.4%	13%
90°- irrigated from congested side.	12.9%	*	7%
Head back- irrigated from patent side.	11.9%	14%	18%

Head back- irrigated from congested side.	6%	7.5%	8%
Head forward-irrigated from patent side.	21%	12%	17%

\*No data

Potential sources of errors in the PIV experiment include: variations and uncertainties in particle diameter, flow rate, laser reflections caused by air, and refractive index. However, the experimental systems and methods were carefully checked prior to testing to ensure that each of possible source of error were minimized. During testing, it was observed that the CFD model consistently over-predicted flow velocity. It is possible that the PIV measurements were lower than the actual physical flow velocities due to a cross-correlation window's averaging effect and high-velocity gradients present. Excluding the last head forward irrigation from the congested side, which did not produce a PIV result, all of the other experimental results were in consistent agreement with CFD data with an average error of between 7-21% for different locations at different head positions. It is not possible to measure the pressure distribution, and it is difficult to measure the mucosal wall shear stress distribution and saline distribution for the entire geometry using PIV. Overall, the CFD results are in good agreement with the PIV experiment data, which validates the CFD model results and suggests that further investigations into saline flow fields including saline distribution, pressure, and mucosal wall shear stress distributions within a realistic *in-vivo* nasal cavity, can be carried out using the CFD simulation.

## 5.6 Summary

A planar PIV setup was used to capture the velocity field in a transparent nasal cast model in different head positions and flow directions. This chapter provides validation for the use of CFD simulations to understand and predict the irrigation flow velocity fields in a realistic *in-vivo* human nasal cavities and maxillary sinuses. The inevitable existence of air in the PIV model caused optical distortion, limiting the region used for validation to

the nasopharynx as this was the only region to remain consistently filled with water and glycerol. For each head position (excluding head forward irrigation irrigated from left congested side), the velocity field was measured where the irrigated saline turned around from the side of the inflow direction to the contralateral nasal passage. The results found in this chapter support the use of CFD to predict the irrigation saline flow field, mucosal wall shear stress and pressure distribution, and saline distribution in the complex anatomy of the nasal cavities and maxillary sinuses, and this is undertaken in Chapter 6.

# Chapter 6: CFD irrigation flow field results within nasal cavities and maxillary sinuses

## 6.1 Introduction

Having validated the CFD saline velocity results in Chapter 5, this chapter then presents the numerical simulation results of saline flow field data results. These results include the saline distribution, pressure and mucosal wall shear stress distribution through a realistic *in-vivo* nasal cavity and maxillary sinus computational model. The simulation results focus on determining mucosal wall shear stress, pressure and saline distribution for four different head positions; Mygind, 90°, head-back, and head-forward (Figure 4.5). In each head position, irrigation was alternatively performed from either the right nostril (patent side) or the left nostril (congested side). The transient process (filling, steady, and emptying) of the saline irrigation within the nasal cavities and maxillary sinuses was discussed in Chapter 4. Here, the simulation results show the peak values of the nasal irrigation flow field, consisting of saline distribution, pressure distribution, and wall shear stress during steady state flow conditions.

## 6.2 Results

In each head position, a separate analysis was undertaken for saline irrigated into the right patent and left congested nasal passages. In the result, mucosal wall shear stress, pressure distribution, and saline distribution are shown for each head position and inflow side direction. These parameters were selected based on their ability to improve mucociliary transport through mucosal purinergic mechano-stimulation. Results are presented along the nasal airway using a non-dimensional airway position:  $X/L$ , where  $X$  is the nominal location and  $L$  is the total distance from the vestibule to the nasopharynx plane, (Figure 6.1).

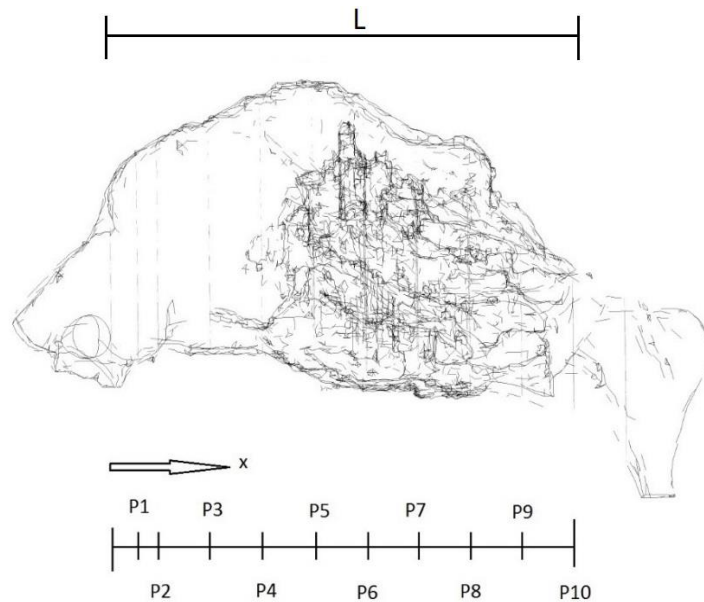


**Figure 6.1. Nasal geometry and selected planes.**

Ten coronal planes (P1-P10) were selected to show different flow properties during irrigation. The planes were selected to show the results in the important geometrical features of the nasal cavity and maxillary sinuses including the nasal vestibule, nasal valve, nasal airway, meati, olfactory cleft, maxillary sinuses' ostia entry, maxillary sinuses, and the nasopharynx.

### **6.2.1 Mygind head position irrigated from right patent side**



In this head position, the saline enters the nasal cavity in the same direction as gravity, and before reaching the nasopharynx it then moves against the gravity.

### 6.2.1.1 Saline distribution

To demonstrate the content of saline irrigation distributed to different regions of the nasal cavity and maxillary sinuses, the saline distribution contour is depicted in Figure 6.2. The level of asymmetry in both nasal passages is significant. In this head position, when the irrigation is directed from the right patent side, it is noticeable that the saline is distributed through both of the nasal cavities. While the irrigant is well distributed within the nasal cavity (nasal passage shows as completely blue), the sinus penetration in this head position and side direction is limited to the right maxillary sinus as seen P5-P8 in Figure 6.2. While there is no penetration in the left sinus located on the congested side (contralateral side of the irrigation), the irrigant partially fills the inferior region of the entry into the right sinus located at the side of irrigation inflow. Here, improvement in the mucociliary function at the sinus entry region may help improve drainage of the whole sinus cavity. The saline mucosal contact regions at this head position, which include almost all of the nasal cavities and right patent sinus entry region, benefit the hypertonic saline effects of cellular water flux and ASL hydration.

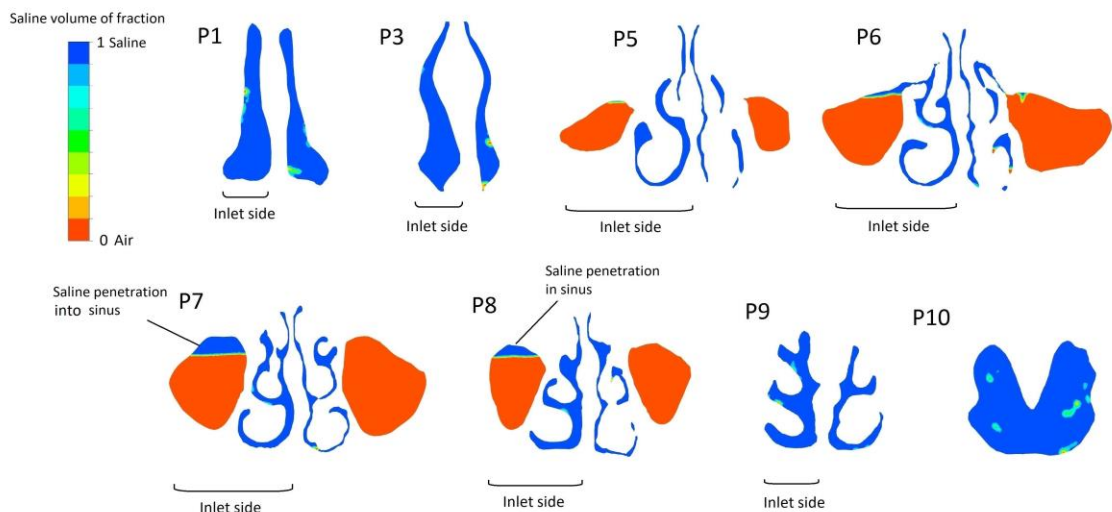


**Figure 6.2. Saline distribution contour at different coronal sections during Mygind head position irrigation from right patent side.**

### 6.2.1.2 Irrigation pressure distribution

As a result of fluid friction, irrigated saline loses its pressure when flowing through the nasal passages. Figure 6.3 presents the saline pressure distribution within the nose in the Mygind head position irrigated from the right patent side. Here saline gains pressure due to the passage orientation (same as gravity), and after that, before reaching the nasopharynx there is a pressure loss. When the saline reaches the left congested side, it can almost maintain the initial pressure. The right patent side also experienced a lower pressure drop compared to the left congested side due to the larger cross-sectional area of the right passage. The irrigated saline maintains a high pressure throughout the whole nasal cavity. It was demonstrated and discussed in Chapter 2 (Figure 2.6) (36) that at a pressure stress of between 0 and 490 Pa the ATP release increased rapidly, and after 490 Pa the ATP release increment relaxed. For pressure figures shown in this chapter, the 490 Pa is highlighted. Here, the pressure is a purinergic mechano-stimulation and the higher saline pressure within the nasal cavity may increase ATP release and improve the mucociliary function.

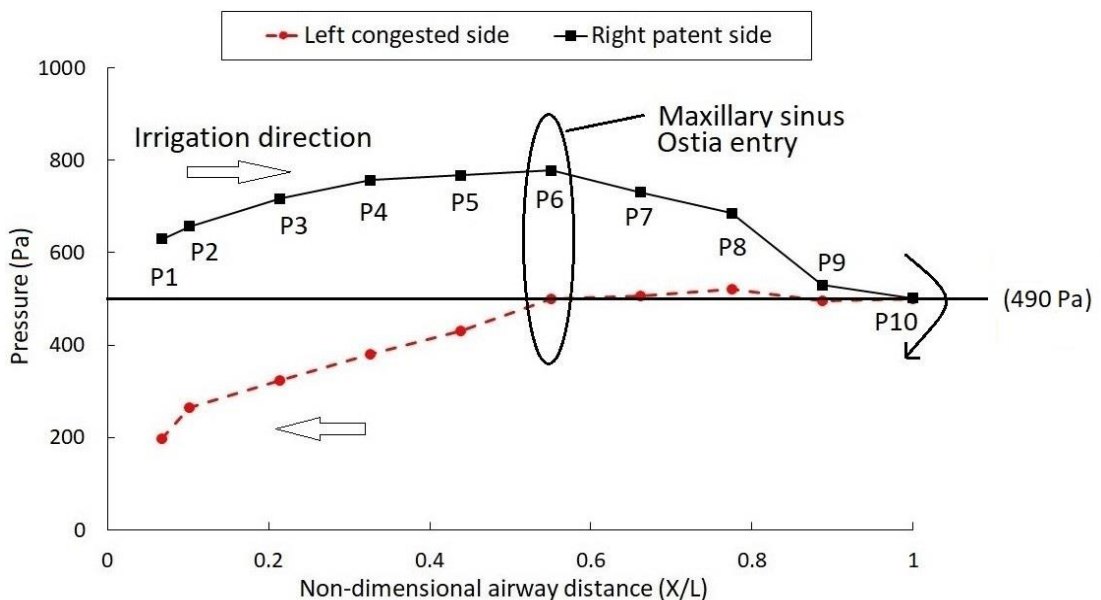


**Figure 6.3. Pressure distribution within the nasal cavity for the Mygind head position irrigated from right patent side.**

### 6.2.1.3 Wall shear stress

A higher wall shear stress level improves the mucociliary clearance within the nasal cavity. The level of shear stress in the nasal cavity is related to the local fluid irrigation velocities. The difference in geometry between the right patent and left congested nasal airways led to a different velocity magnitude distribution within each passageway. Here the saline velocity magnitude is higher in the left congested side due to its smaller cross sectional area. The wall shear stresses, which lead to mechano-physical responses in the epithelial surfaces, over the entire lateral wall surface of the left and right passages, is shown in Figure 6.4. The ATP release at the epithelial surface begins to increase from a wall shear stress of 0.01 Pa, and by increasing the wall shear stress the ATP release is enhanced, as discussed in (39, 135). In all shear stress results, 0.01 Pa is highlighted, which shows that ATP release starts from that level and the higher wall shear stress enhances the ATP release and therefore improves the mucociliary functions.

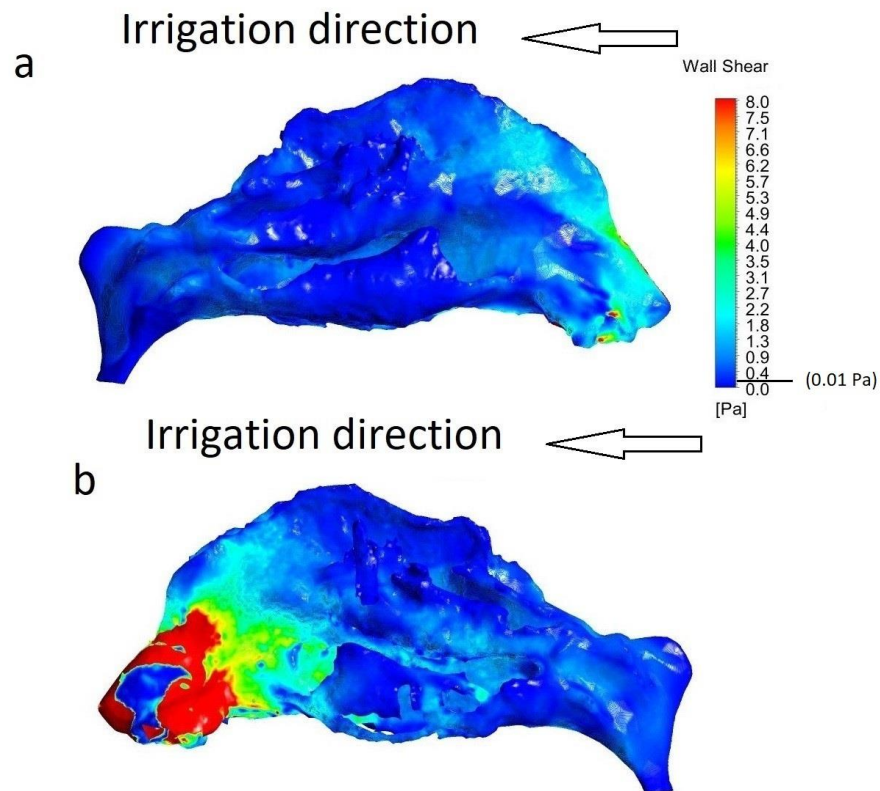


**Figure 6.4. Wall shear stress contour in Mygind head position irrigated from right patent side a) right patent passage b) left congested passage.**

The magnitude of wall shear stress in the left congested side is higher than that of the right patent side due to the higher velocity in the congested side. The highest wall shear stress occurs around the nasal vestibule and nasal valve regions in both passages. In the left congested side, the wall shear stress magnitude is high in the inferior and middle regions of the nasal passage. This means that the bulk of the flow passes via the inferior and middle airways and meati and the irrigation around the superior meatus and olfactory cleft is slower moving.

Figure 6.5 shows the average wall shear stress in the coronal planes in the Mygind head position for irrigation from the right patent nasal passage. The wall shear stress in the right patent passage is lower than in the left congested side. In both the congested and patent passages, a higher wall shear stress occurs in the nasal valve region and anterior region of the nasal cavity. Both are however above 0.01 Pa and therefore will realise increased MTV along both airways.

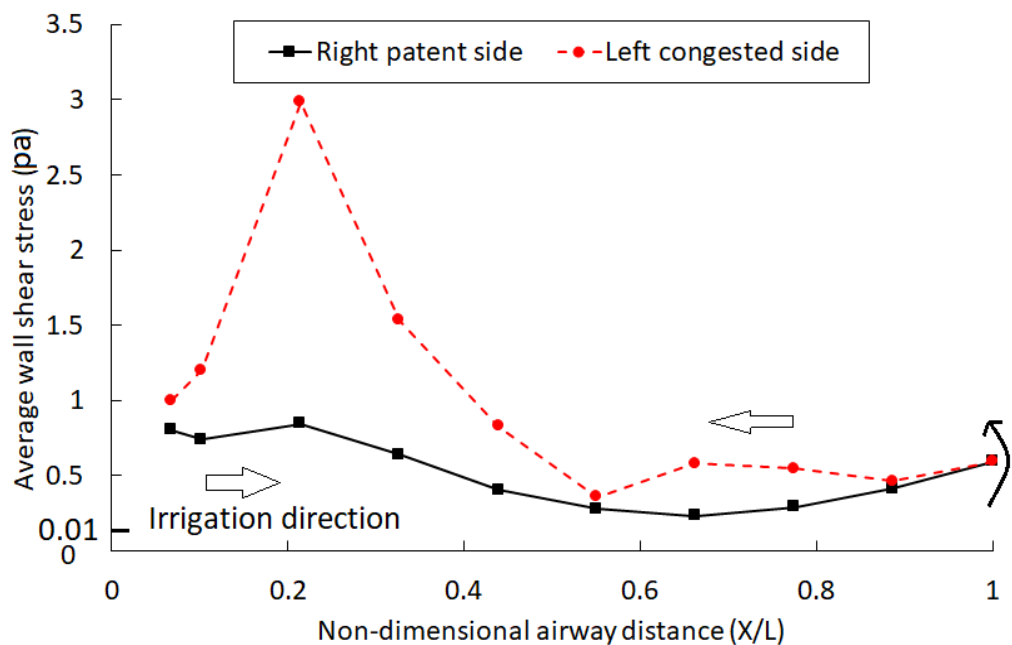
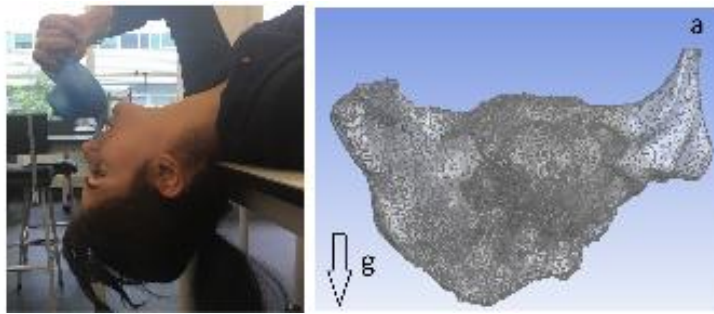


**Figure 6.5. Average wall shear stress distribution within the nasal cavity during Mygind head position irrigated from right patent side.**

The wall shear stress affects the physiological functions of the airways' surface in these regions and improves the nasal mucociliary clearance at this targeted region. The ATP release starts to increase from 0.01 Pa, and for wall shear stresses greater than 0.01 Pa the ATP release is still enhanced.

### 6.2.2 Mygind head position irrigated from left congested side



For the same Mygind head position, nasal irrigation was now directed into the left congested side of the nose. The irrigated saline moves towards gravity in the anterior region of the nasal cavity before moving against gravity in the posterior nasal cavity.

#### 6.2.2.1 Saline distribution

The saline distribution in the Mygind head position irrigated from the left congested passage at different coronal planes is shown in Figure 6.6. Here the irrigated saline is well-distributed in the left congested side where inflow occurs. On the other side, the saline detached from the inferior wall and could not reach the inferior airway as shown in P6-P8. Therefore, when the targeted site of consistent delivery is the inferior region of the passage, it is not recommended to irrigate from the contralateral congested side. The saline penetration into the maxillary sinuses was limited in this condition to the right patent side. Compared to the right patent side inflow irrigation, during left congested side directed irrigation there is an additional but limited irrigation penetration into the maxillary sinus located on the left congested side. The unirrigated region (inferior airway on the middle of the patent side) does not benefit from the hypertonic effect of the saline because there is no saline mucosal contact in these regions.

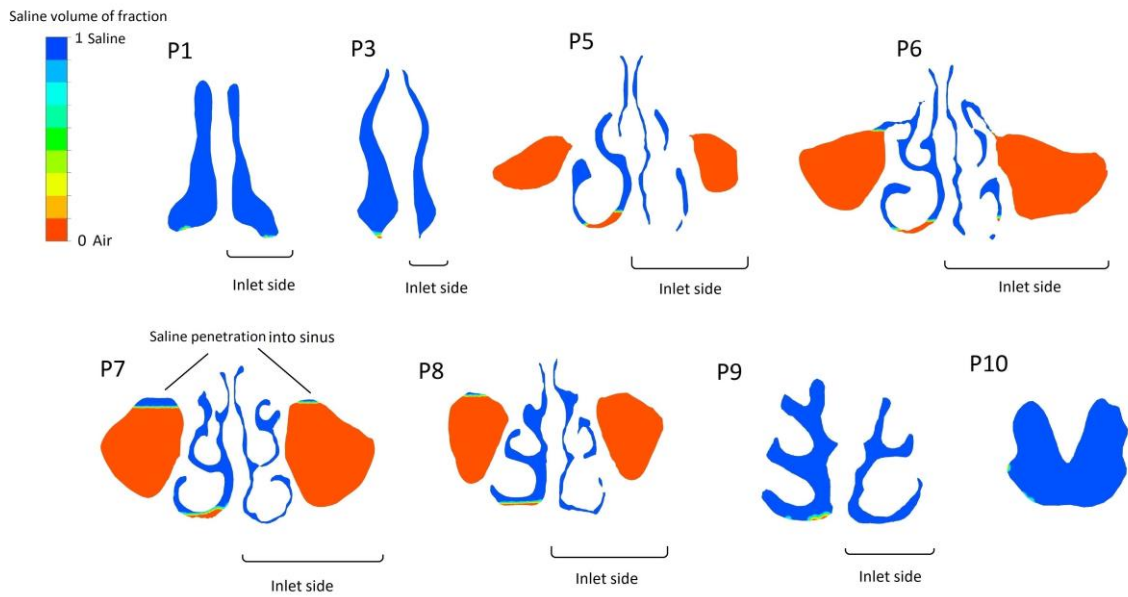


**Figure 6.6. Saline distribution contour at different coronal sections during Mygind head position irrigation from left congested side.**

### 6.2.2.2 Irrigation pressure distribution

In this irrigation, the small cross-sectional area of the left congested nasal passage caused a higher initial pressure drop to occur (Figure 6.7). A significant pressure drop can be seen in the flow in the left congested passage before the nasopharynx. In the nasopharynx, a significant pressure drop occurs due to the u-bend and flow expansion. By turning around the nasopharynx and entering the right patent passage, the flow gains pressure when moving past the turbinates. The average pressure on the left congested side is higher than the right patent side, which may increase the MTV along the left congested side more than on the right patent side.

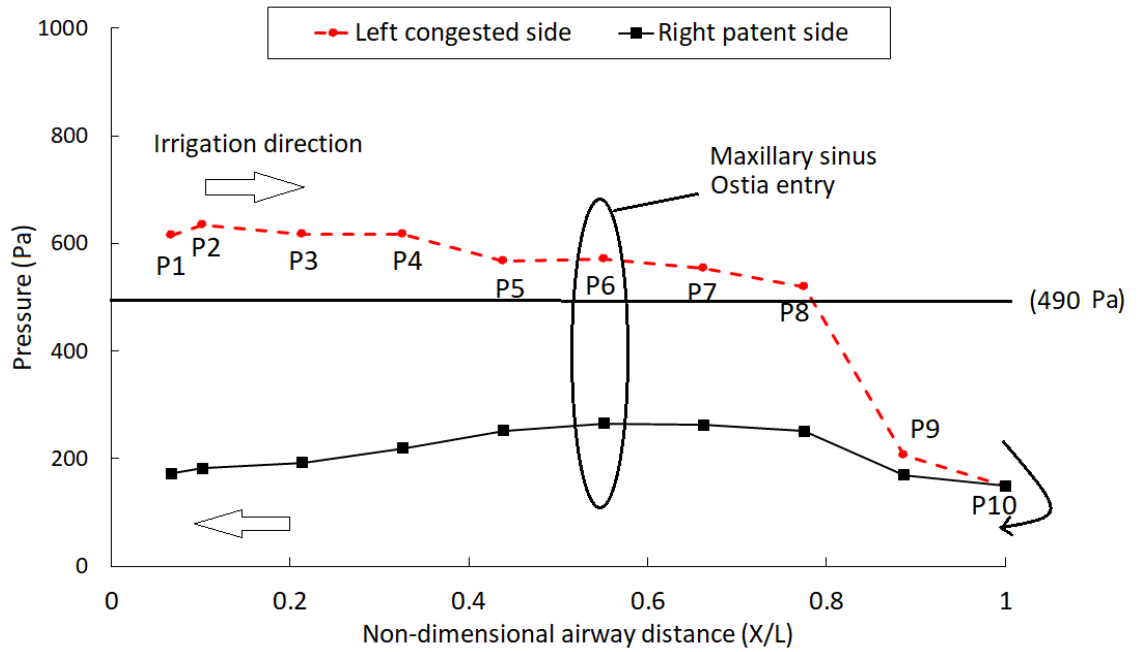


**Figure 6.7. Pressure distribution within nasal cavity for Mygind head position irrigated from left congested side.**

### 6.2.2.3 Wall shear stress

Wall shear stresses for the Mygind head position irrigated from the left congested side are mapped in Figure 6.8. The irrigated saline exerted higher shear stress in the left congested passage compared to the right patent side. The wall shear stress distribution around both nasal vestibules shows low wall shear stress regions, while at the entrance of the middle meatus passageway demonstrated a higher wall shear stress. Here the entrance of the middle nasal airway guides the saline to flow parallel to the airway passages, resulting in a high variation in saline velocity with respect to the surrounding walls. (Figure 6.8). By changing the side of irrigation to the left congested side, the wall shear stress distribution is more uniform at the side of the irrigation compared to irrigation inflow from the right patent side. The wall shear stress on both sides is more than 0.01 Pa, which means that wall shear stress acts as a mechano-stimulation on both sides.

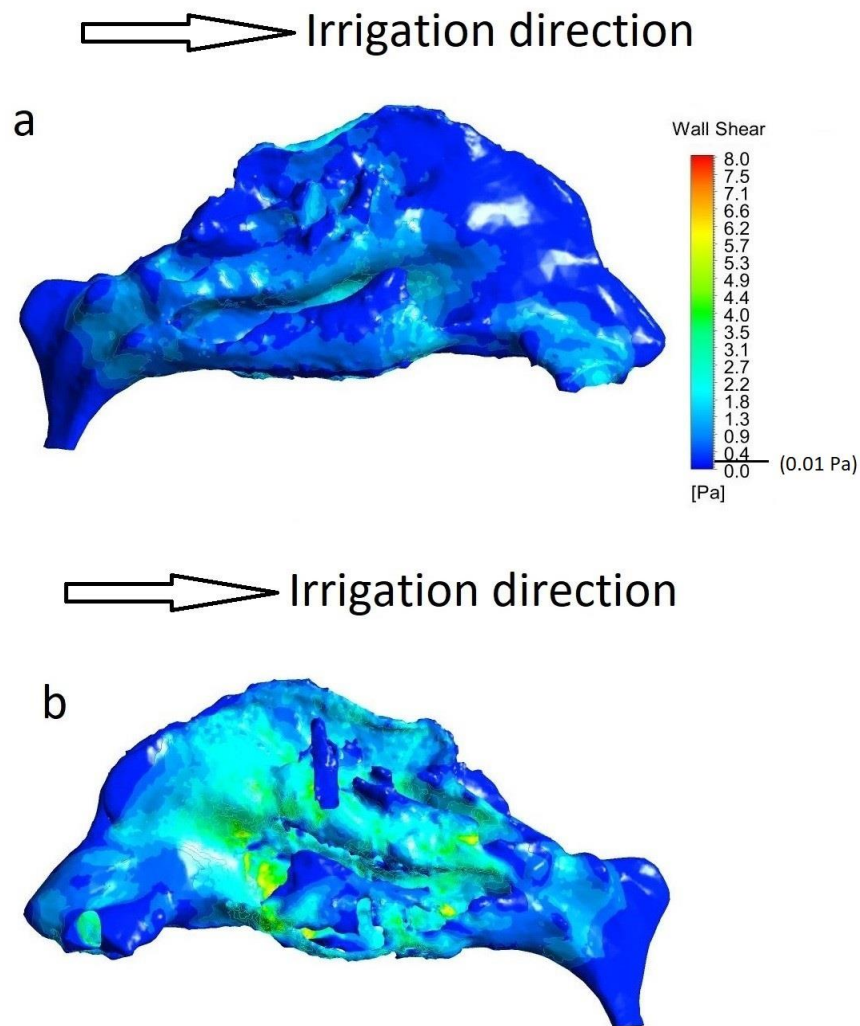


**Figure 6.8. Wall shear stress contour in Mygind head position irrigated from left congested side a) right patent passage b) left congested passage.**

Figure 6.9 shows the average wall shear stress distribution within the nasal cavity for the Mygind head position irrigated from the left congested passage. Here the wall shear stress on the patent passage does not change significantly with respect to the airway distance which suggests that the variation of the local saline velocity in the right patent side is not significant. The magnitude of the wall shear stress on the congested side is higher than the right patent side, especially around the nasal valve and the beginning of the turbinates. This may improve the functioning of the epithelial lining on the left congested side more than on the right patent side.

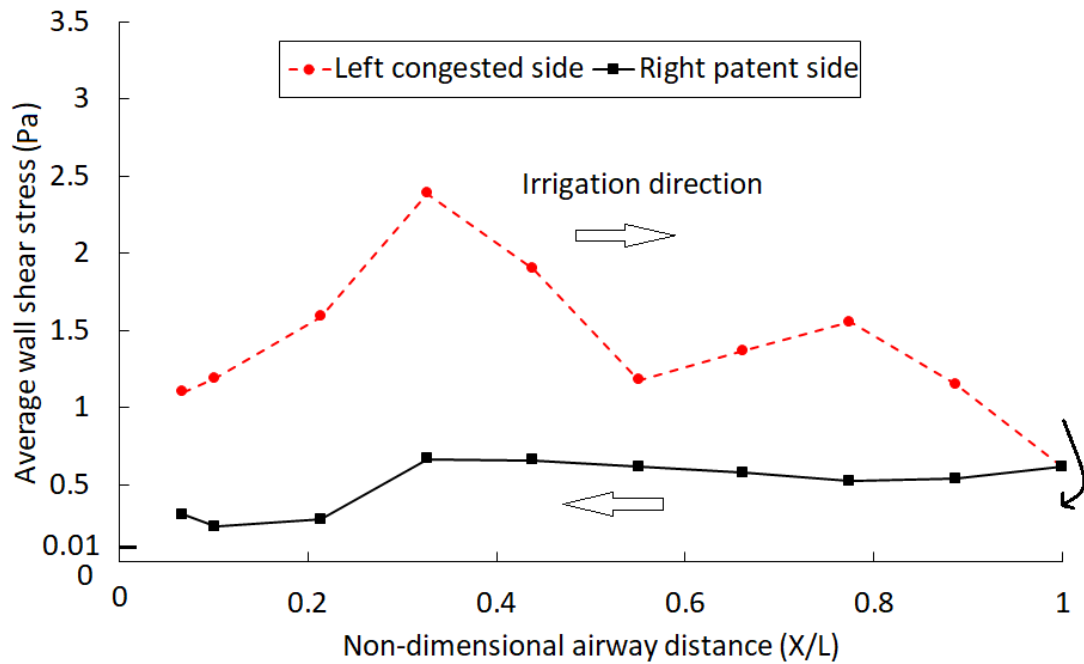
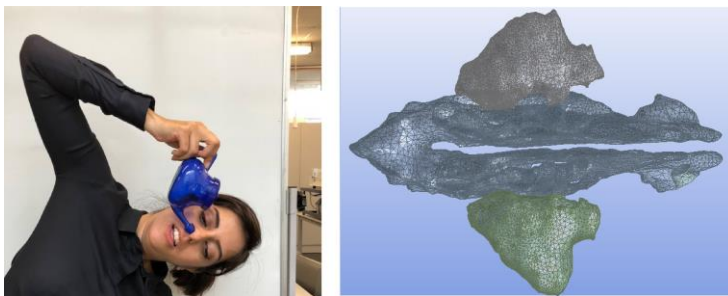


Figure 6.9. Average wall shear stress distribution within the nasal cavity during Mygind head position irrigated from left congested side.

### 6.2.3 90° head position irrigated from right patent side



In the 90° head position, the face is oriented parallel to the ground and the direction of the flow in the nasal passages is perpendicular to gravity. For the 90° head position, the irrigation is always introduced into the upper naris.

#### 6.2.3.1 Saline distribution

Figure 6.10 illustrates the saline distribution at different coronal sections of the nasal passages. The irrigated saline is fully distributed in the P1-P5 planes while after that the inferior meatus of planes P7 and P8 remained unirrigated. Before the nasopharynx (P9-P10), the presence of the radial pressure gradient caused flow separation to occur, and saline moved to the outer side before then returning along the inner septal wall. With right

patent side irrigation, the lack of flow restriction created flow detachment to occur before the nasopharynx. Here the trapped air in the right patent passage is highlighted in Figure 6.10. In the simplified CFD model, the saline could not penetrate into the maxillary sinus on the upper right side. Here the low pressure of the saline cannot push the trapped air out from the right maxillary sinus into the nasal passage. The irrigant barely penetrates into the sinus at the contralateral left side. For the 90° head position irrigated from the patent side, both sinuses as well as the anterior region of the side of irrigation remain unirrigated. This user condition is not recommended when the targeted delivery site is the nasopharynx or sinus regions. The cellular water flux and regulation of ASL hydration does not occur for detected unirrigated regions, as highlighted in Figure 6.10.

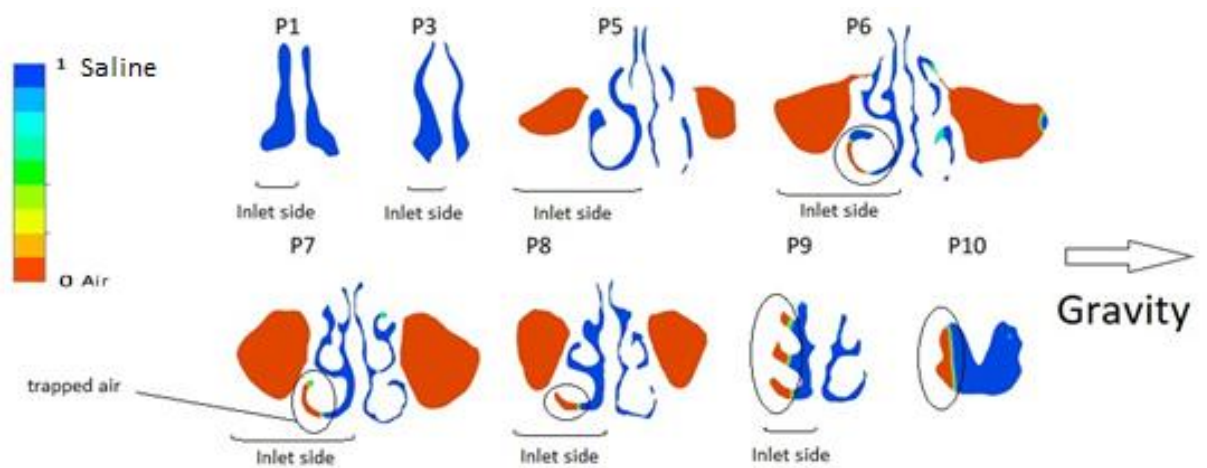


**Figure 6.10. Saline distribution contour at different coronal sections during 90° head position irrigation from right patent side.**

### 6.2.3.2 Irrigation pressure distribution

The pressure distribution within the nasal cavity during 90 degree head position irrigation from the right patent side is presented in Figure 6.11. The pressure loss along the right patent passage is not significant due to its greater cross sectional area. As flow passes from the maxillary sinus ostia entry located at the side of irrigation, it does not maintain enough pressure to change its direction and move against gravity. Therefore there is no sinus penetration on the side of the irrigation at a 90° head position. After flow turns around the nasopharynx and enters the left congested passage, a greater pressure loss occurs due to the nasopharynx bend and the nasal passage restriction when moving from the patent side to congested side. In the middle part of the left congested side, a noticeable pressure loss occurs due to the movement of the flow through the more narrowed geometry and the high curvatures of the middle and inferior meati and airway. The pressure on the epithelium surface results in an improvement in the mucociliary clearance. The saline pressure at the side of irrigation (right patent side) is high for both nasal passages and it might improve the MTV for the right patent side more than the left congested side.

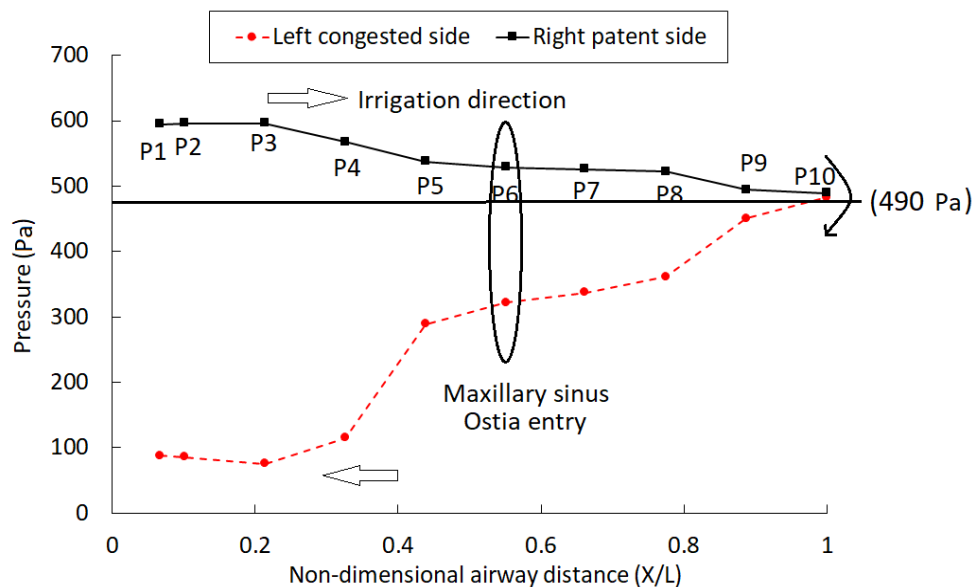


Figure 6.11. Pressure distribution within the nasal cavity for 90° head position irrigated from right patent side.

### 6.2.3.3 Wall shear stress

The wall shear stress distributions over the right patent nasal passage's wall demonstrate that the wall shear stress around the middle and inferior nasal airways and middle meatus is higher than 0.01 Pa. This indicates that the irrigant flow mainly moves close to the septal wall and moves mainly through the middle and inferior nasal airways and middle meatus (Figure 6.12). On the left congested side, due to gravitational force acting on the saline, the direction of the flow is mainly in the direction of the inferior meati resulting in a considerable level of wall shear stress being exerted on the left-side lateral walls. At this head position and inflow side direction, the wall shear stress is high at the septal wall and inferior and middle airways and meati on the right patent side, and at the lateral walls on the left congested side. The irrigated saline at the high wall shear stress regions may improve the MTV more than in the other regions.

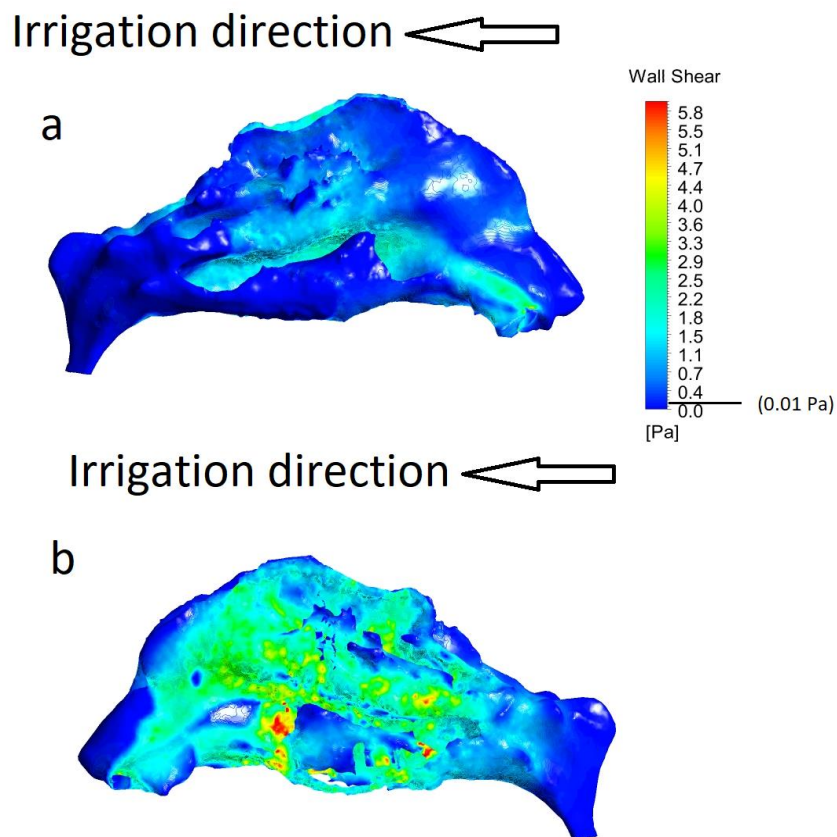
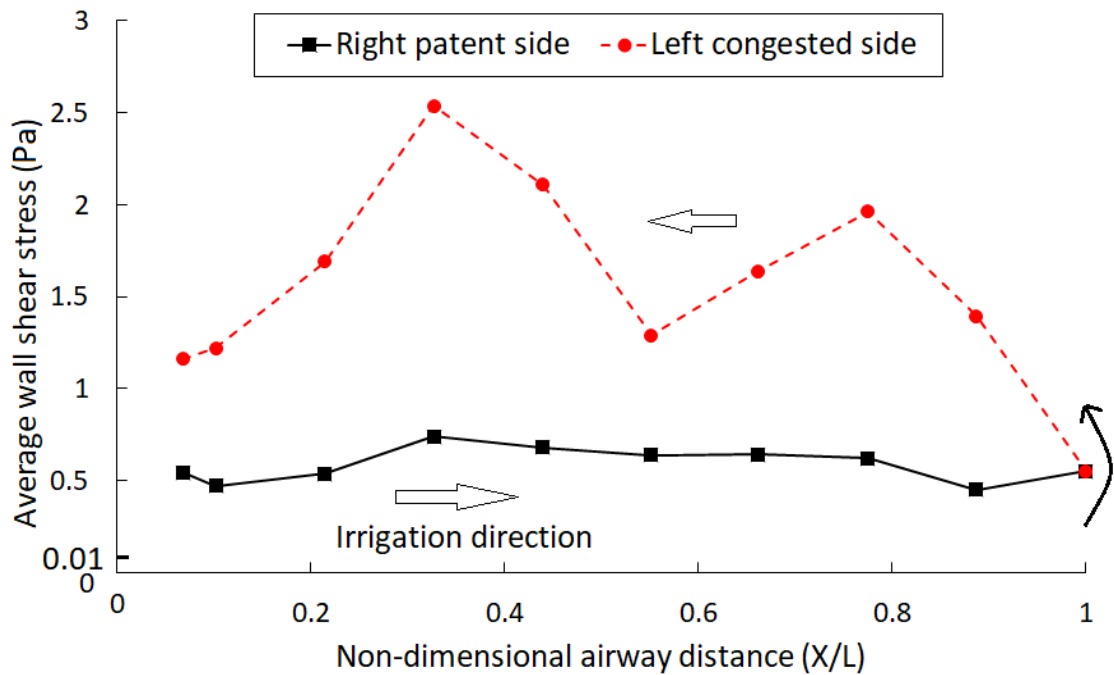


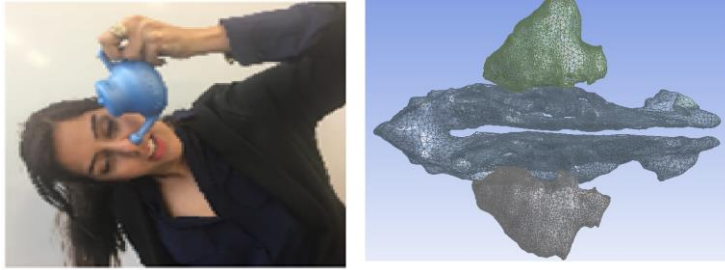
Figure 6.12. Wall shear stress contour at 90° head position irrigated from the right patent side a) right patent passage b) left congested passage.

Figure 6.13 shows the average wall shear stress within the nasal cavity in a 90° head position irrigated from the right patent passage. Of note is the wall shear stress on the inflow right patent side which slightly increases in the region around the turbinates. This regional increase in pressure is also seen in the left congested side. The irrigated saline in the left congested passage moves towards the narrow and high curvature meati and it is high when it enters and exits the meati. In this head position and inflow side direction, the movement of the flow towards the meati on the contralateral side of irrigation causes shear stress, which may provide mechanical purinergic stimuli for these regions more than for the other regions.



**Figure 6.13. Average wall shear stress distribution within the nasal cavity during 90° head position irrigated from right patent side.**

## 6.2.4 90° head position irrigated from left congested side



### 6.2.4.1 Saline distribution

For this head position inflow direction, the saline enters the left congested side and it fully fills it (Figure 6.14). The small cross-sectional area within this side permits the saline to be well-distributed to all the different regions. On the right patent side, the saline could not penetrate into the maxillary sinus on the side of the irrigation. Similar flow characteristics were observed in the simplified model. The same flow detachment as for the right patent side irrigation was observed in the left congested side irrigation, and the trapped air is annotated in P9 and P10 in Figure 6.14.

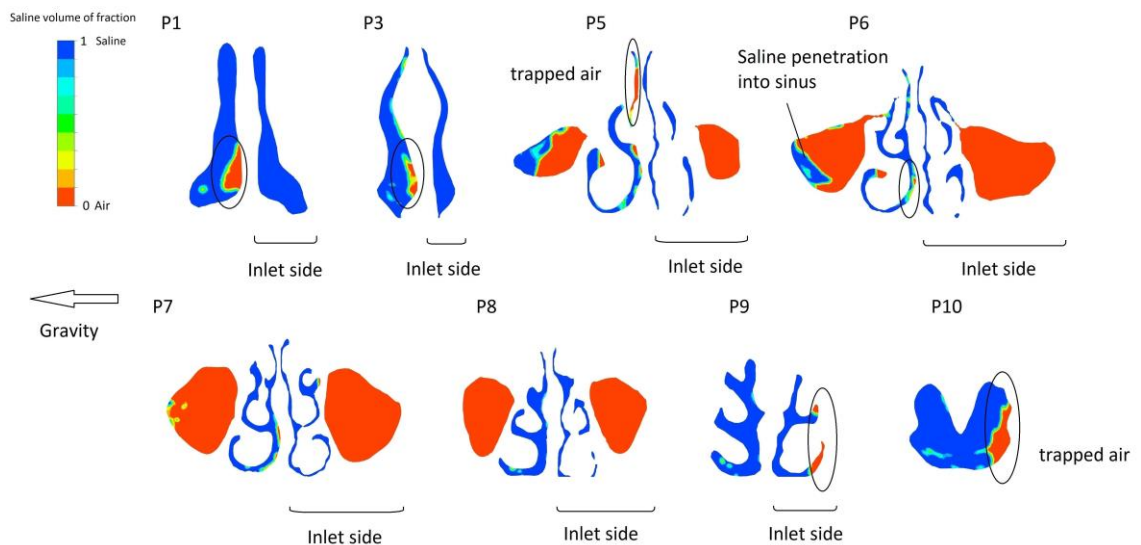


**Figure 6.14. Saline distribution contour at different coronal sections during 90° head position irrigation from the left congested side.**

Compared to the right patent side irrigation, this flow detachment is smaller in the left congested side irrigation. When saline reaches the right patent side, due to gravitational force, it tends to separate from the septal wall and flow in the inferior and middle meati. The flow separation started from P7 and it became bigger when it moved to the nasal vestibule. The trapped air in P6-P1 is highlighted (Figure 6.14). In the 90° head position, the congested side irrigation provides greater nasal cavity distribution and sinus penetration than the patent side irrigation. The irrigated saline provides no hypertonic benefits (cellular water flux and ASL hydration) for unirrigated regions, as highlighted in Figure 6.14, as there is no contact between the saline and mucosal surface in these regions.

#### **6.2.4.2 Irrigation pressure distribution**

When irrigation is performed from the left congested side, the smaller cross-sectional area restricts the flow and causes a greater fluid friction pressure loss compared to the other side. In the same way as for the right patent side irrigation, the irrigant pressure is not sufficient at the sinus ostia entry located at the side of the irrigation and it cannot move against gravity to enter the left maxillary sinus. Before it enters the right patent passage, an intense pressure drop occurs for the irrigated saline as it changes direction to move into the right side (Figure 6.15). Due to its low pressure, the saline cannot maintain its attachment to the septal wall and moves to the meati. This detachment was observed in the volume distribution contour in P6-P1 shown by Figure 6.14. At this head position and side direction, the pressure of the irrigated saline decreases as it moves along from the left congested side to the right patent passage. The purinergic mechano-stimulation of irrigated saline may decrease as it moves from the inlet nostril towards the outlet.

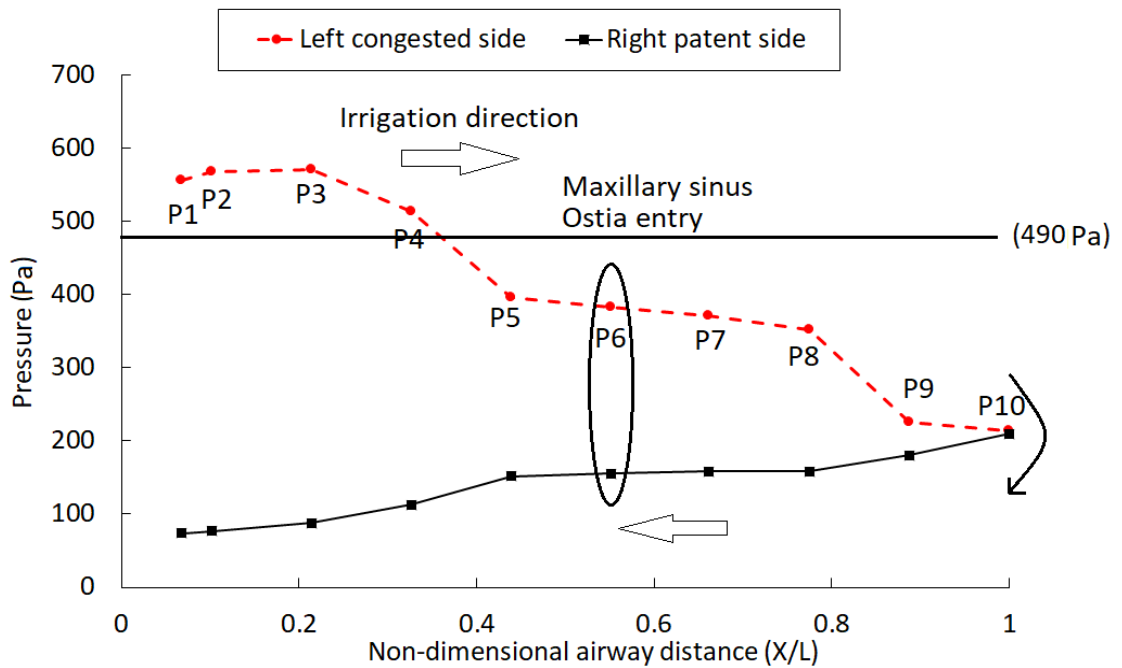


**Figure 6.15.** Pressure distribution within the nasal cavity for 90° head position irrigated from left congested side.

#### 6.2.4.3 Wall shear stress

The distribution of wall shear stress on both nasal passages is depicted in Figure 6.16. The flow movement into the left passage is mainly located close to the septal wall. By comparing the distribution of wall shear stress on both sides of the nose, it can be observed that the wall shear stress on the lateral walls on the left congested side is more than that found in the right patent side. This proves that on the contralateral side of irrigation, in the 90° head position, saline moves towards the meati, which is in the direction of gravity. Similar to the congested side irrigation, the irrigant follows a gravity-dependent pathway to the lateral nasal walls and exerts wall shear stress on the airway surface especially at the meati located at the contralateral side of the irrigation. The irrigated saline may increase the MTV at high wall shear stress regions more than at other regions.

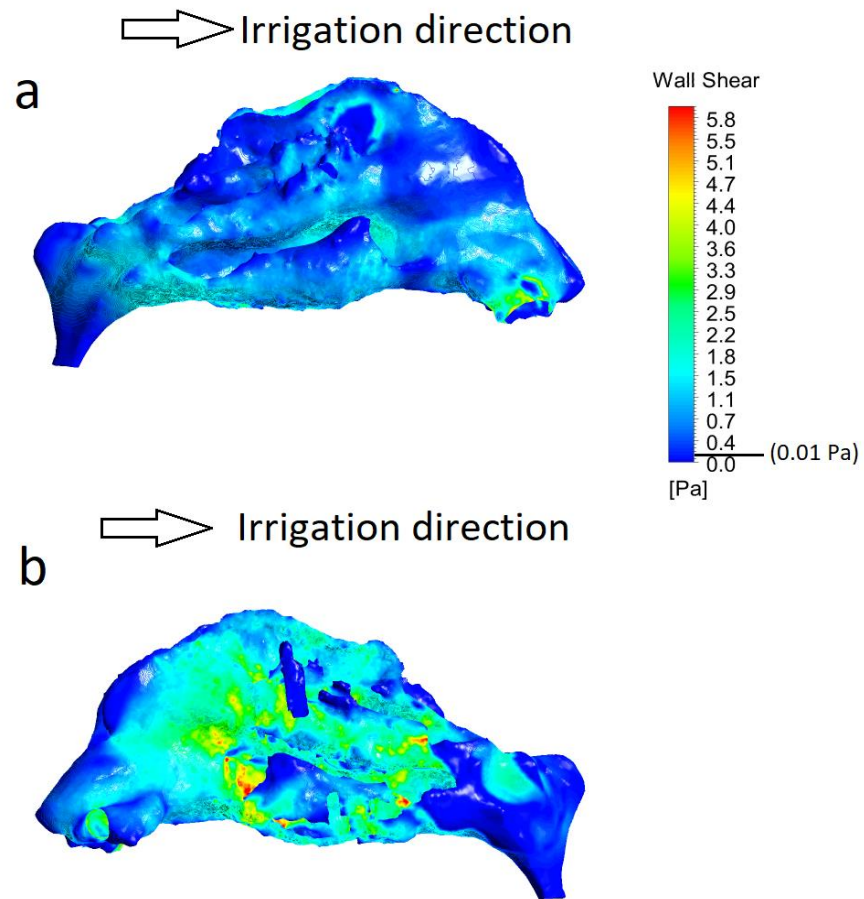


**Figure 6.16. Wall shear stress contour at 90° head position irrigated from the left congested side a) right patent passage b) left congested passage.**

The distribution of wall shear stress on the nasal cavity in both right patent and left congested conditions is shown in Figure 6.17. By changing the side of irrigation the wall shear stress did not change significantly and the same pattern found in the right patent side irrigation can be observed.

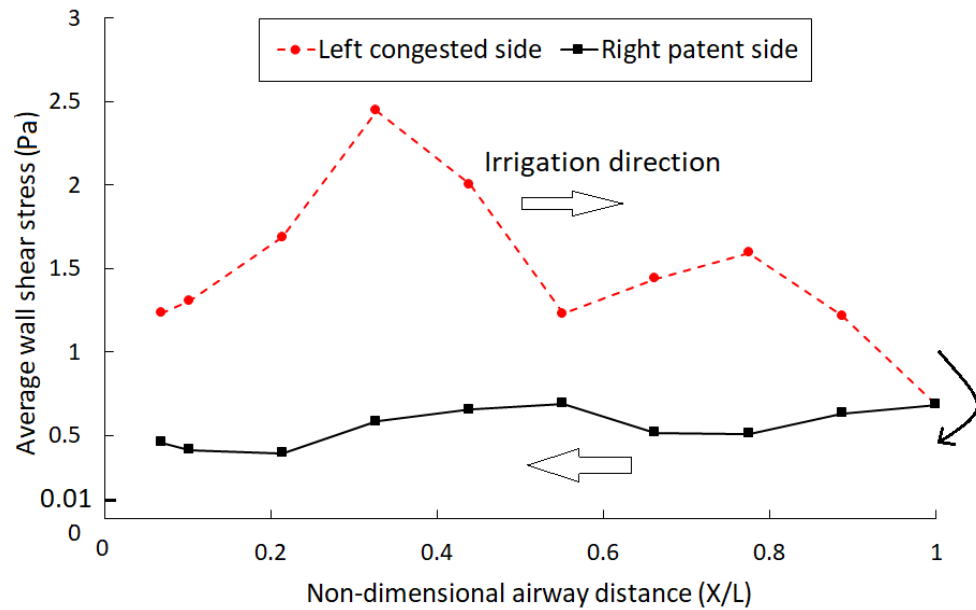
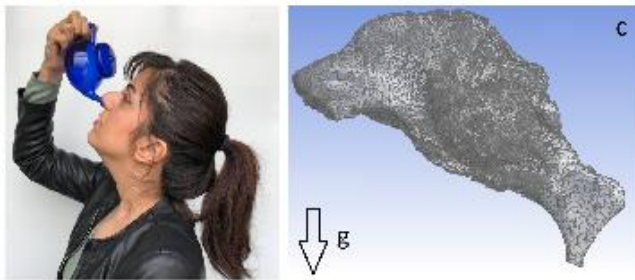


Figure 6.17. Average wall shear stress distribution within the nasal cavity during 90° head position irrigated from left congested side.

### 6.2.5 Head back position irrigated from right patent side



#### 6.2.5.1 Saline distribution

In the head back position, the face is oriented 45° upward from the ground. The saline distribution results from CFD simulation show that the irrigated saline fills the right passage fully and also penetrates both maxillary sinuses. Flow detachment from the anterior wall on the left congested side occurs at P1 while irrigant is moving towards the outlet which results in the nasal vestibule on the left congested side remaining unirrigated. This unirrigated region is annotated in Figure 6.18 (P1). The saline penetration into the posterior region of both maxillary sinuses due to the tilted position of the head, which is observed in P8 (Figure 6.18). The anterior region of the both sinuses remain unirrigated

in this head position and inflow side direction. This head position and side of inflow is suggested when the targeted delivery site is the posterior region of the sinuses. In this head position and side direction, nasal cavity and sinus penetration can be achieved and it can be used whenever maximum distribution is required in the nasal cavity and maxillary sinuses. At this head position and inflow side direction, the irrigated saline provides hypertonic benefits for the anterior region of the maxillary sinuses' mucosal surface.

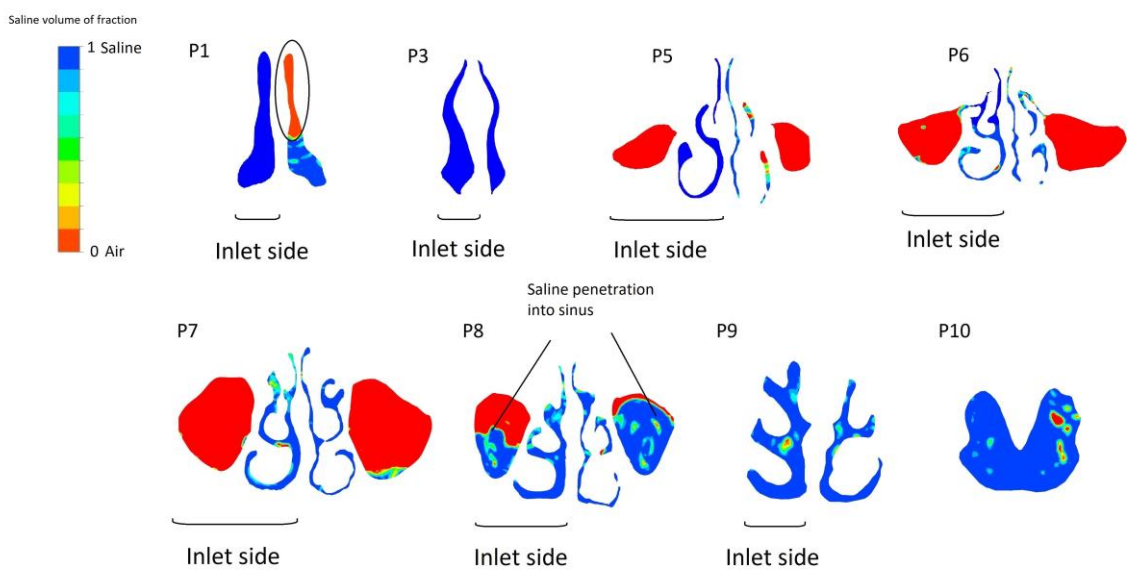


**Figure 6.18. Saline distribution contour at different coronal sections during head back position irrigation from the right patent side.**

### 6.2.5.2 Irrigation pressure distribution

Flow at the side of irrigation gains pressure while moving to the nasopharynx, which results in the full irrigation of the right patent nasal passage. At the end of the passage the saline turns around the nasopharynx and enters the left congested passage and the saline starts losing pressure due to the additional restriction to flow within the congested side and its orientation against gravity. While the saline passes the plane P6 (ostia entry), the saline has sufficient pressure (Figure 6.19) to push the trapped air into both maxillary sinuses and penetrate these spaces. The pressure at the posterior region of the nasal cavity is higher than at the anterior region, as the irrigated saline may increase the MTV at this region more than in other parts of the nasal cavity (36).

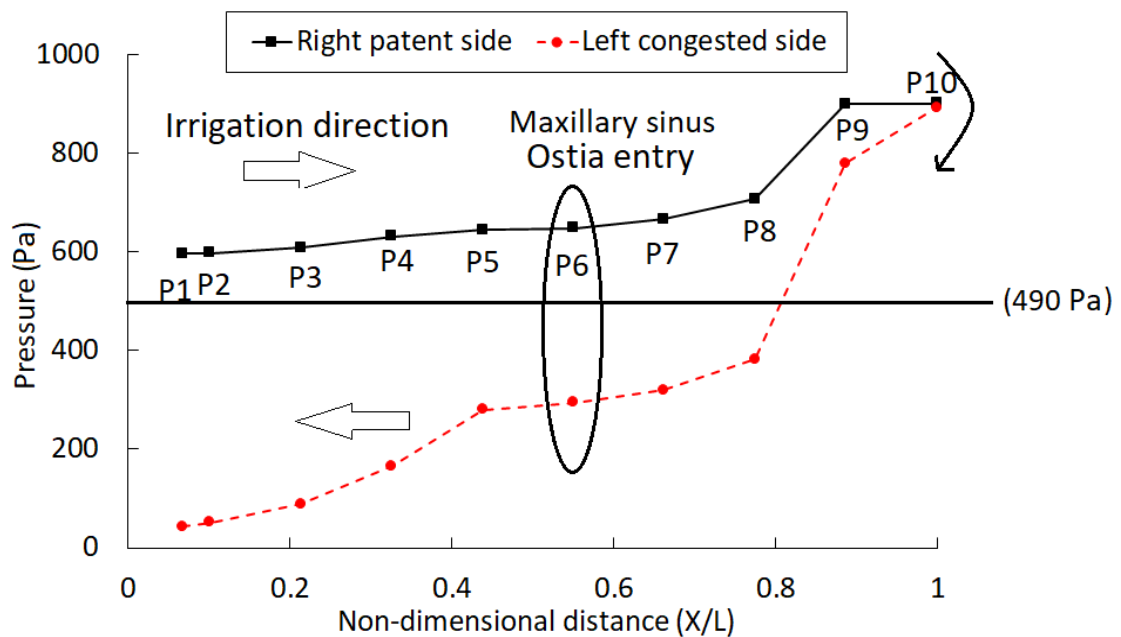


**Figure 6.19. Pressure distribution within the nasal cavity for head back position irrigated from right patent side.**

### 6.2.5.3 Wall shear stress

The wall shear stress distribution on the lateral walls in the head back position irrigated from the right passage is presented in Figure 6.20. Here the wall shear stress matches the saline path in both passages. In the right patent passage, the bulk of inflowing fluid moves through the inferior part of the nasal cavity. In the left congested passage, the saline is well distributed to different regions and the narrow geometry causes high local velocities which exert a significant level of wall shear stress on the lateral wall. In both nasal passages, especially at the side of irrigation, the wall shear stress at the nasal vestibule and nasal valve regions is negligible. Although saline fills the right patent passage, there is no observable wall shear stress at this region because saline mainly passes through the inferior region. The ATP release and MTV is higher in the high wall shear stress regions than in the rest of the nasal cavity.

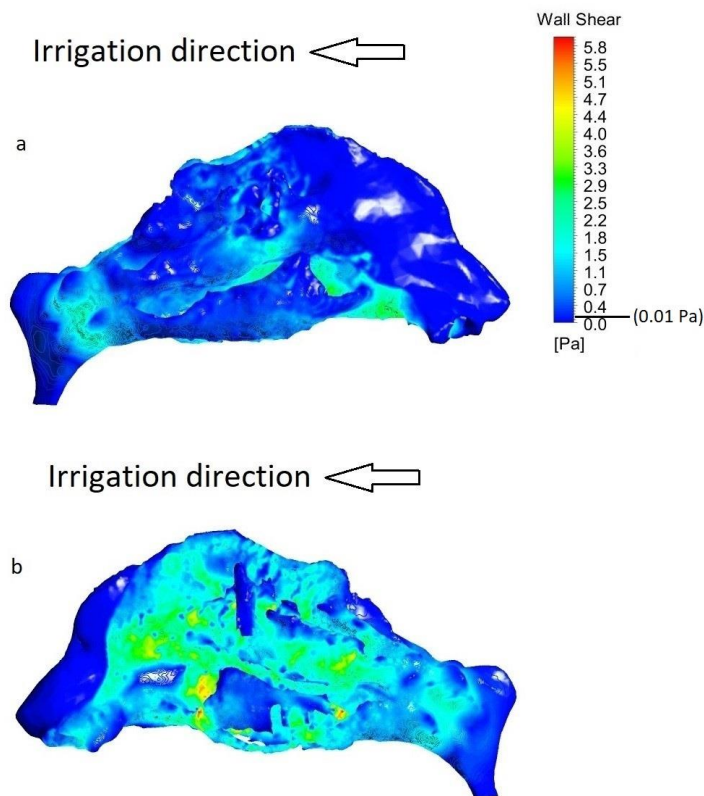


Figure 6.20. Wall shear stress contour at head back position irrigated from the right patent side a) right patent passage b) left congested passage.

Figure 6.21 shows the average wall shear stress within the nasal cavity in the head back position irrigated from the right patent passage. The flow detachment on the left congested side caused the wall shear stress in this region to decrease even around the nasal valve.

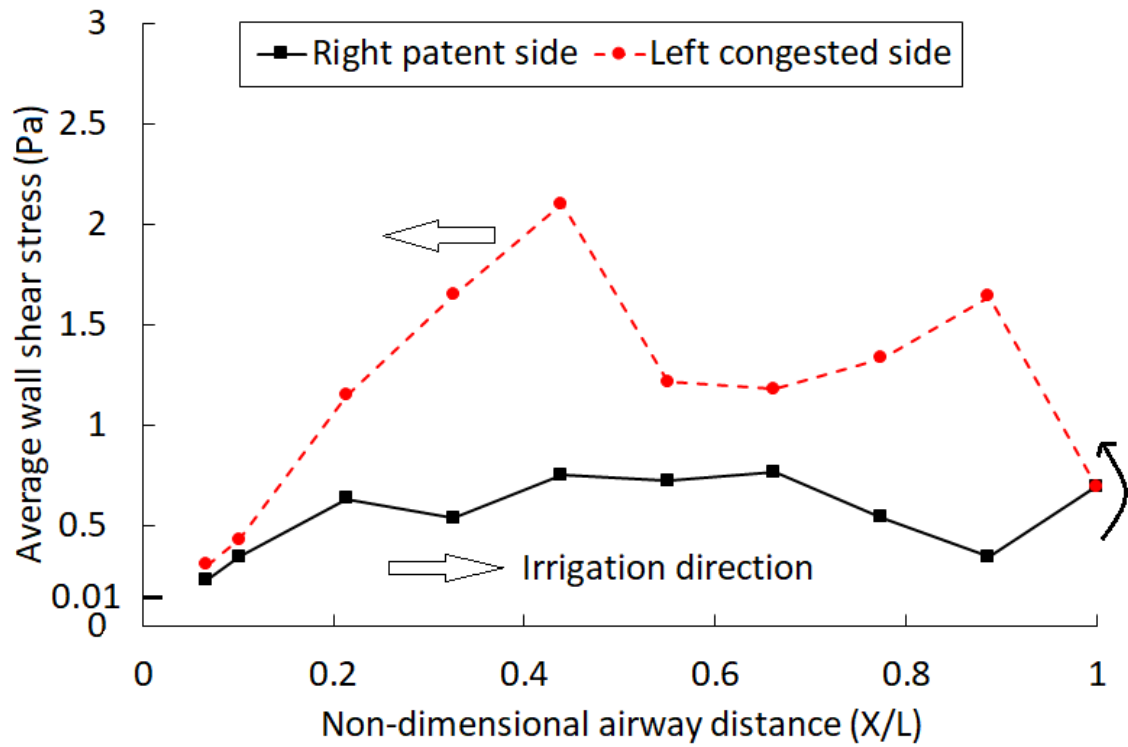
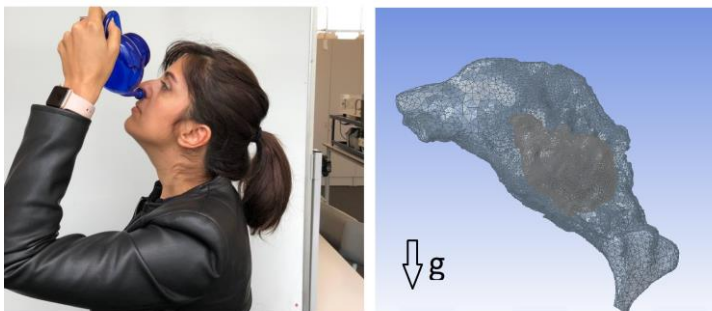


Figure 6.21. Average wall shear stress distribution within the nasal cavity during head back position irrigated from right patent side.

## 6.2.6 Head back position irrigated from left congested side



### 6.2.6.1 Saline distribution

During left congested side irrigation, the saline moves through the left congested passage and irrigates all of the regions in this passage, as shown in Figure 6.22. The left passage is tilted upwards at  $45^\circ$  to the direction of gravity and the flow moves easily to the contralateral side. After exiting the turbinate regions, the flow separates from the top wall due to its low pressure and the saline on the patent side at the P3 and P1 planes moves from the inferior region. The flow detachment results in an unirrigated region (Figure 6.22). In the head back position, the nasal cavity distribution can be achieved when irrigation is performed from the left congested side. The sinus penetration is limited compared to this head position with inflow from the other side and is limited to the end-region of the sinuses. There is no saline mucosal contact at the unirrigated regions (posterior regions of the maxillary sinuses and superior regions of the nasal vestibule and valve at the right patent side), therefore there will be no hypertonic effect on the mucosal surface.

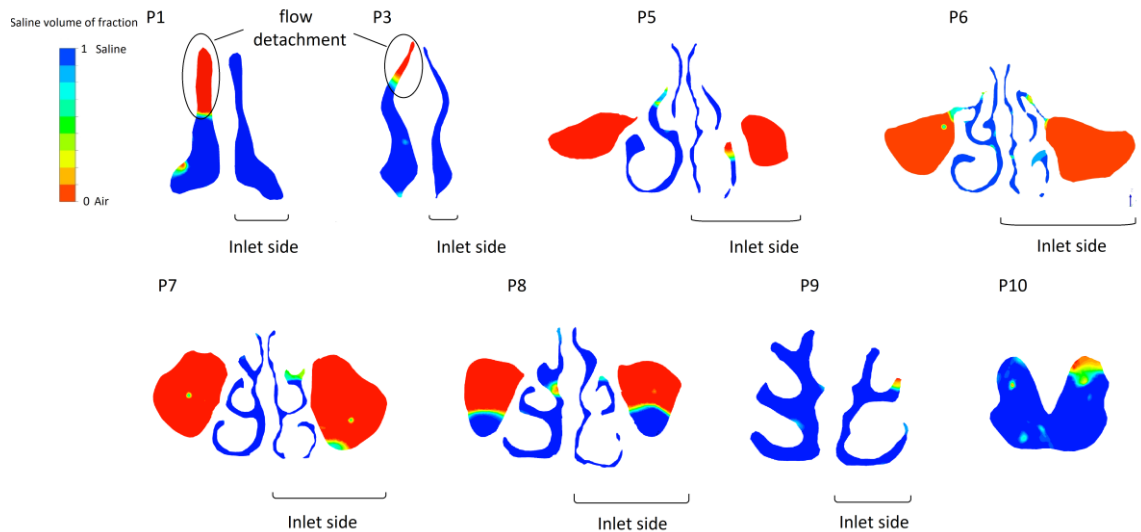


**Figure 6.22. Saline distribution contour at different coronal sections during head back position irrigation from left congested side.**

### 6.2.6.2 Irrigation pressure distribution

For this head orientation inflow direction the saline flow is conducted towards the left side due to gravity and the irrigated saline pressure gains match the pressure loss due to friction in the left congested side (Figure 6.23). After the saline turns around the nasopharynx and flows in an anterior direction towards right passage it moves against gravity resulting in a pressure loss occurring in the right patent passage. On the right side, after exiting the turbinate region and entering the nasal valve region, the pressure loss at the nasal valve separates the flowing saline from the anterior wall as it moves towards the nostril. Compared to the right patent side irrigation, the saline pressure is lower while passing from the maxillary sinuses ostia entry, and because of that the penetration is lower at this side irrigation. The pressure at the right patent side is almost constant and is higher than at the left congested side, and this may increase the MTV at the right patent side more than at the congested side.

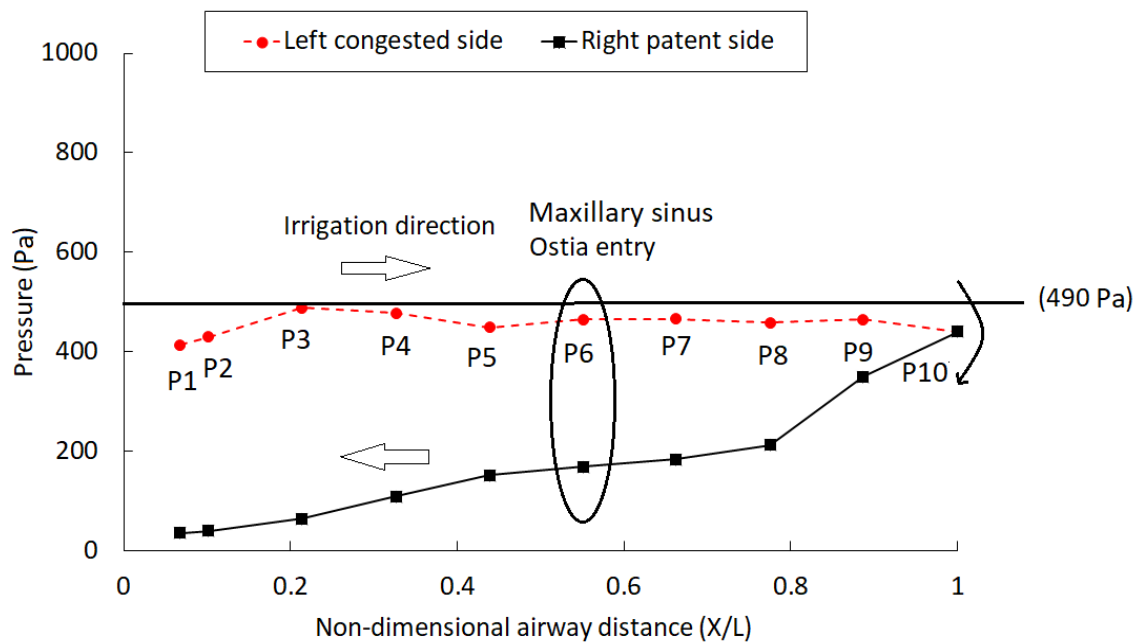


**Figure 6.23. Pressure distribution within the nasal cavity for head back position irrigated from left congested side.**

### 6.2.6.3 Wall shear stress

The distribution of wall shear stress on the lateral walls of both passageways is shown in Figure 6.24. In the left congested passage, the irrigated saline exerts a higher wall shear stress on the lateral walls compared to the other side as the saline fills the passage completely. In the right patent side, the distribution of wall shear stress is higher only in the posterior region. Zero wall shear stress is found in unirrigated regions including the superior nasal valve and vestibule in the right patent passage. In left congested side irrigation, the average wall shear stress on the side of the irrigation is high in the turbinate region of the left congested side. (Figure 6.25). Here the narrow passages guide the flow towards the whole passage, especially to the superior meatus and olfactory cleft regions. This results in uniform wall shear stress distribution in this passage. The high wall shear stress regions provide more purinergic mechano-stimulation than the low wall shear stress regions.

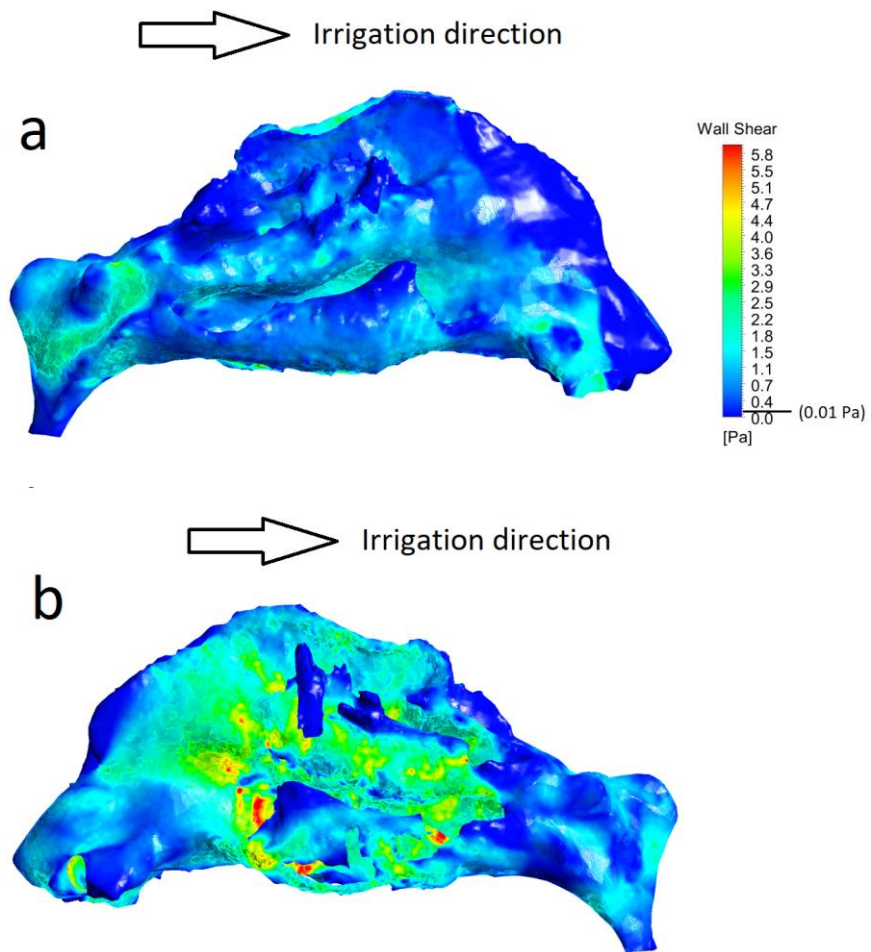


**Figure 6.24. Wall shear stress contour in head back position irrigated from the left congested passage a) right patent passage b) left congested passage.**

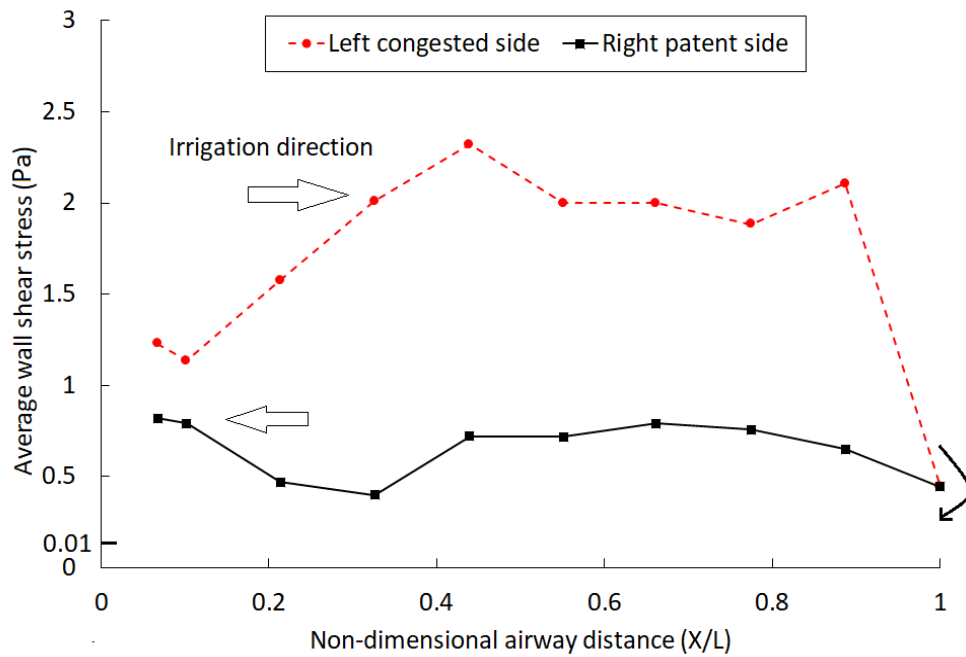


Figure 6.25. Average wall shear stress distribution within the nasal cavity during head back position irrigated from left congested side.

### 6.2.7 Head forward position irrigated from right patent side



#### 6.2.7.1 Saline distribution

The nasal passages in this head position are inclined downwards at  $45^\circ$  to the horizontal axis, which means that the irrigated saline on the inlet side of the nose moves against gravity. On the contralateral side where it flows out it moves with gravity. For this position and flow direction, the irrigated saline is fully distributed in the right patent passage and also penetrates into the right maxillary sinus. As it turns around the nasopharynx, the saline separates from the nasal floor wall and cannot fill the olfactory slit. It tends to exit the left congested side via the inferior airway. Here the flow does not pass through the left congested middle meatus which results in the maxillary sinus being

unirrigated (Figure 6.26). Right side maxillary sinus penetration occurs only at the side of the irrigation. In this head position, the head tilted forward and down, the saline penetration in the right sinus moves towards the anterior region, with the posterior region of this sinus remaining unirrigated. The irrigated saline provides hypertonic benefits (cellular water flux and ASL hydration) for the anterior region of the maxillary sinus at the patent side, and there will be no benefit for unirrigated regions, as highlighted in Figure 6.26.

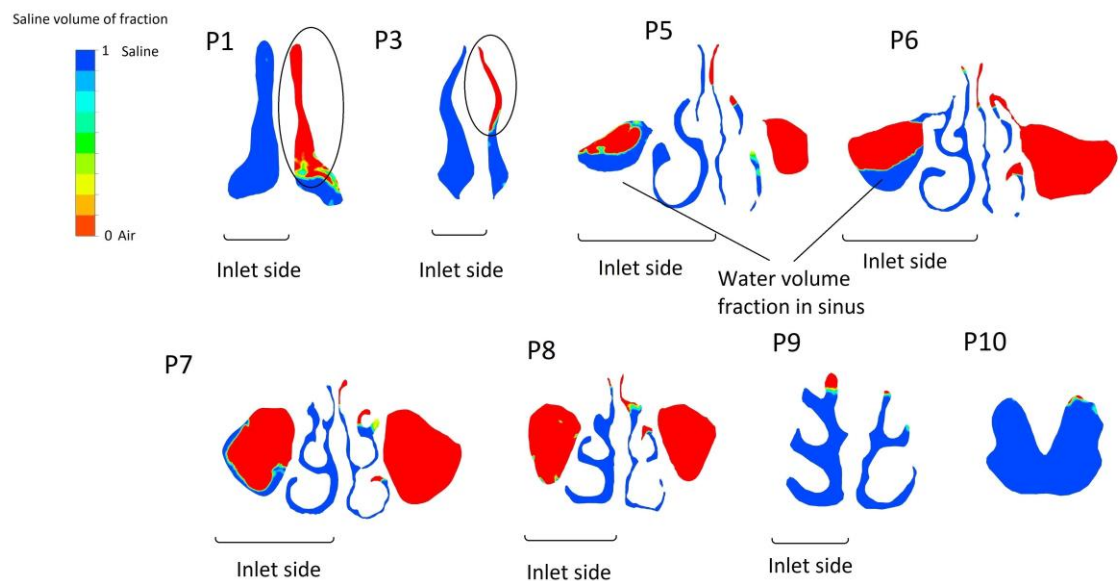


**Figure 6.26. Saline distribution contour at different coronal sections in head forward position irrigated from right patent side.**

### 6.2.7.2 Irrigation pressure distribution

In this head position inflow direction, a noticeable pressure loss occurs in the right patent inlet side of the nose. This pressure loss occurs due to both the orientation of the nasal passage with respect to gravity and flow frictional losses (Figure 6.27). On the left congested side, the irrigated saline could only maintain 1/6 of the inlet pressure and for this reason flow detachment from the anterior wall occurred. This resulted in an unirrigated region (Figure 6.26). The saline pressure on the contralateral side of the irrigation is lower than 100 Pa. The pressure at the anterior region of the right patent side is higher than the posterior region of the nasal cavities and whole left congested side. The irrigated saline may stimulate the ATP release at the anterior region of the right patent side is higher more than the rest of the nasal cavity.

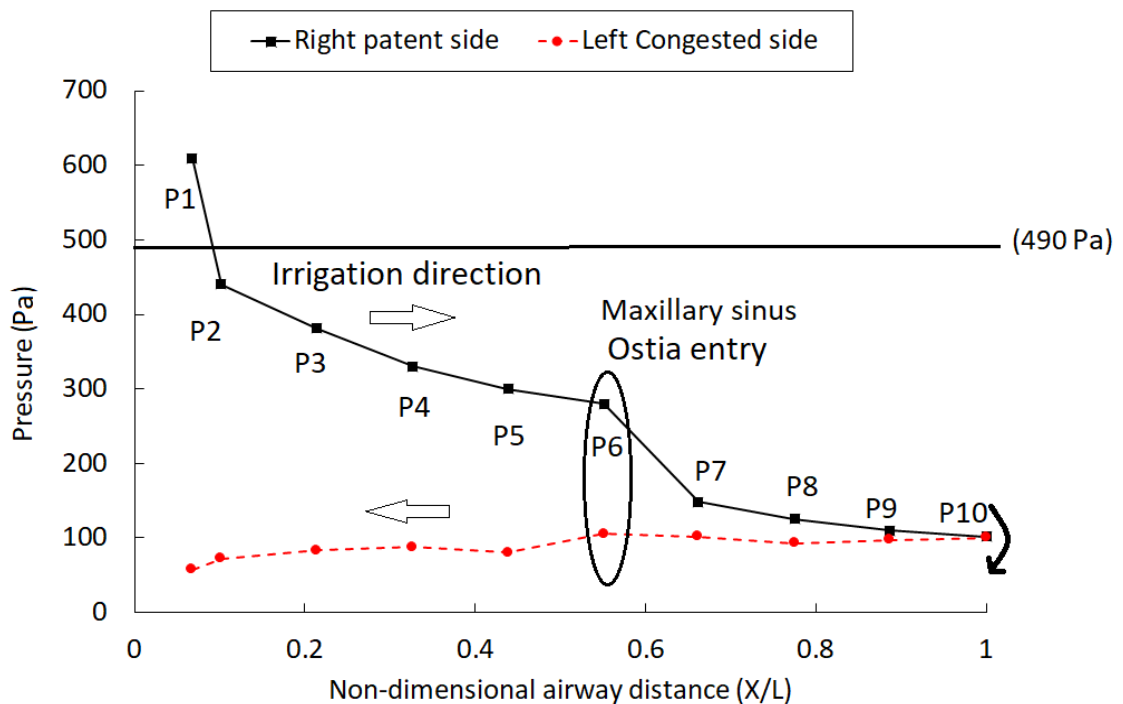


Figure 6.27. Pressure distribution within nasal cavity for head forward position irrigated from right patent side.

### 6.2.7.3 Wall shear stress

In Figure 6.28 the level of wall shear stress in the left congested passage is higher than in the right passage. In the left congested side, the wall shear stress at superior regions of the turbinate, nasal valve, and vestibule are near zero due to flow detachment occurring along the top wall. In this head position and side direction, the irrigant does not exert any wall shear stress at the superior region of the nasal valve, superior meatus, and olfactory cleft. For the zero shear stress regions, the irrigated saline may not affect the ATP release stimulation.

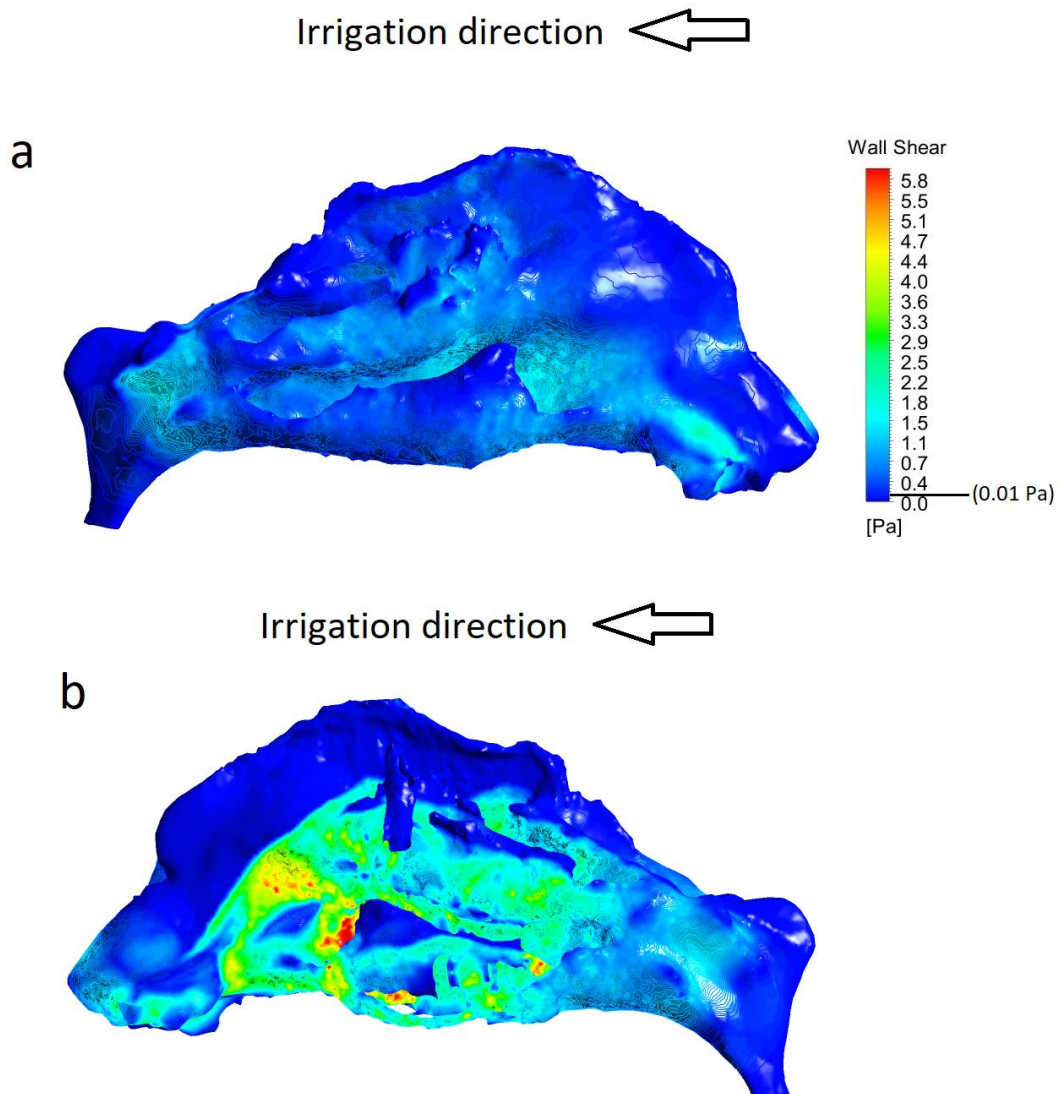


Figure 6.28. Wall shear stress contour at head forward position irrigated from the right patent side a) right patent passage b) left congested passage.

The average wall shear stress shows that the wall shear stress on the left congested side is less than 2 Pascal (Figure 6.29). The maximum average wall shear stress is at P9 when the saline turns around the nasopharynx and enters the left congested side. The saline accelerates while turning around the nasopharynx and this increases the local velocity which results in higher wall shear stress. The wall shear stress at this posterior region of the nasal cavity at the left congested side and the irrigated saline may increase the MTV in this region more than the rest of the nasal cavity.

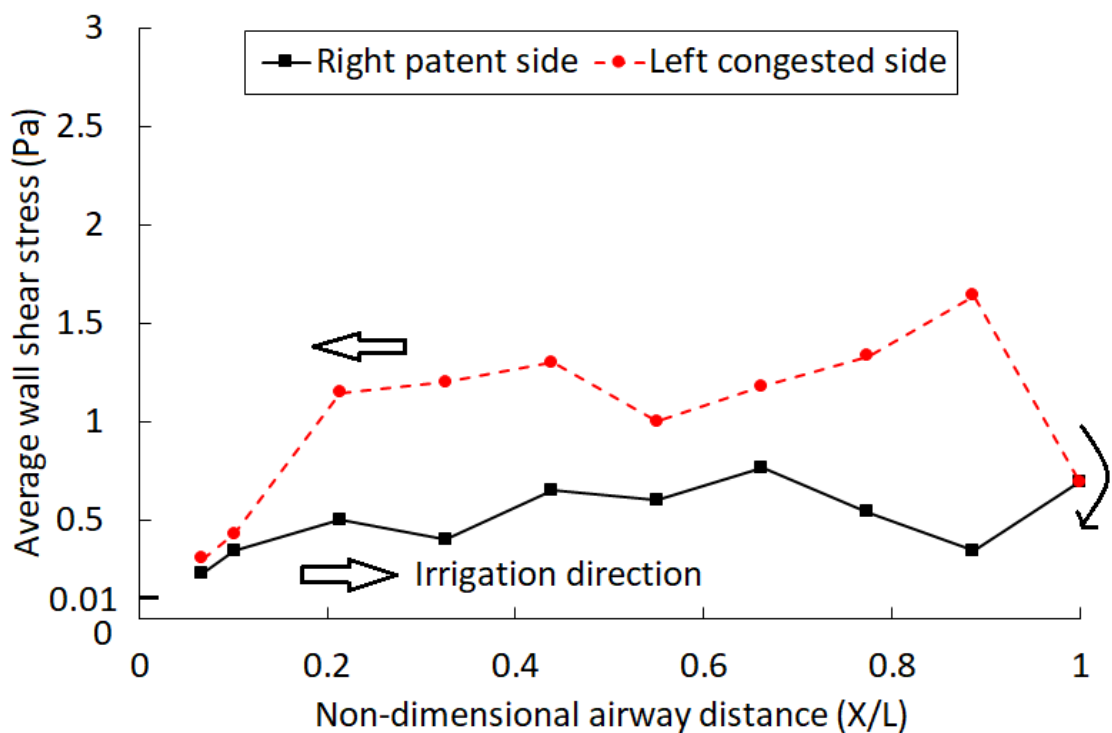


Figure 6.29. Average wall shear stress distribution within the nasal cavity for head forward position irrigated from right patent nasal passage.

## 6.2.8 Head forward position irrigated from left congested side



### 6.2.8.1 Saline distribution

On the side of irrigation inflow, the irrigated saline moves opposed at  $45^\circ$  to the direction of gravity into the left congested passage. The saline distribution within the left congested side shows that irrigated saline is well distributed in this passageway (Figure 6.30). On the contralateral side, the flow moves with gravity to the nostril, via the inferior airway and inferior meatus. With left congested side irrigation, the saline distribution within the right patent passage is limited and most of the regions remain unirrigated. Here the irrigant can neither distribute along the contralateral side nor penetrate either sinus when irrigation is performed from the left congested side. In the head forward position, congested side irrigation is not recommended as both sinuses and the patent side remain unirrigated. The irrigated saline does not provide a hypertonic effect for the right patent side at this head position and side direction.

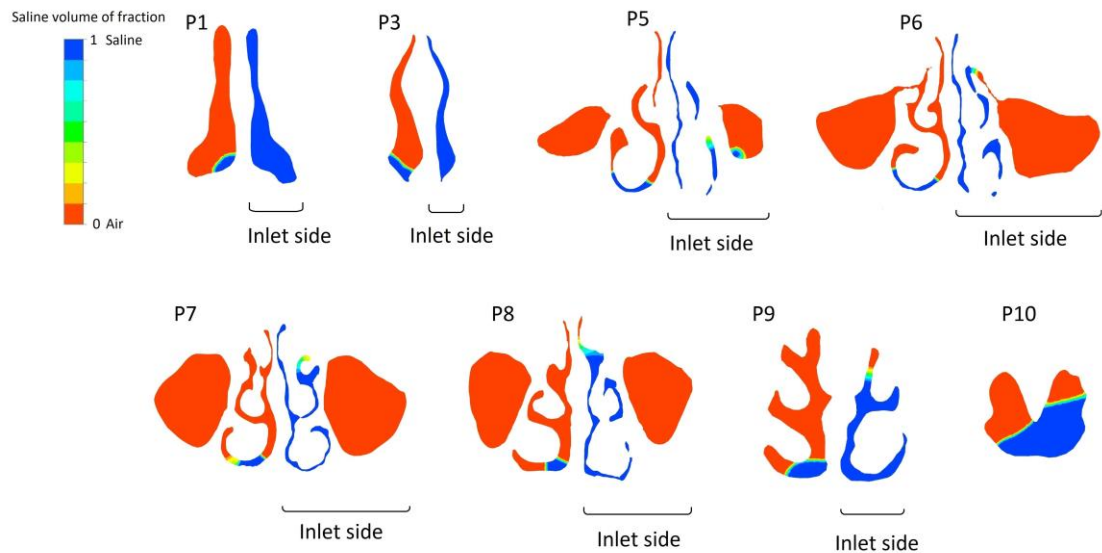


**Figure 6.30. Saline distribution contour at different coronal sections in head forward position irrigated from left congested passage.**

### 6.2.8.2 Irrigation pressure distribution

The pressure loss due to the inlet flow movement against gravity combined with the friction loss within the left congested side passage, limit the saline distribution in the right patent side (Figure 6.31). Here, when saline turns around the nasopharynx and enters the right patent side, the saline cannot maintain pressure and it is not capable of being well distributed on this side. The saline pressure at the entrance of the right patent side is less than 50 Pascal which results in most of the right patent passage being filled with air, (Figure 6.30). The saline pressure is insufficient, to push the trapped air into the passage when passing by the maxillary sinus ostium. Therefore, there is no sinus saline penetration in the head forward position irrigated from the left congested side. The same as for the patent side irrigation, at this inflow side irrigation, the pressure at the anterior region of the nasal cavity is higher than for the rest of the nasal regions. The pressure of the irrigated saline as a mechano-stimulation factor may increase the MTV of this region more than for the posterior region of the right patent side and the whole left congested side.

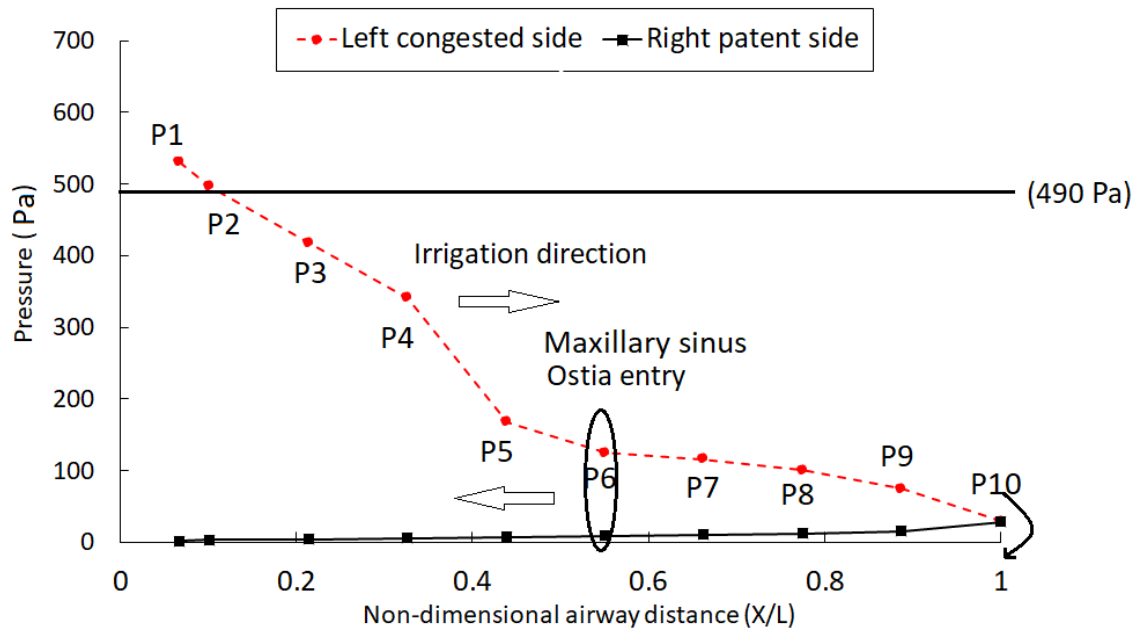


**Figure 6.31.** Pressure distribution within nasal cavity for head forward position irrigated from left congested side.

### 6.2.8.3 Wall shear stress

The wall shear stress along both passageway lateral walls is presented in Figure 6.32. In the right patent passage, the wall shear stress on the lateral walls is zero, and wall shear stress is noticeable only on the nasal floor. On the side of the irrigation, the orientation of the flow is against gravity and the restricted passage on the left congested side both serve to constrain the saline flow and causes less variation in local flow velocities. Because there is no saline distribution along the right patent passage and there is an absence of exerted wall shear stress on the surface lining, no additional stimulation of mucociliary transport will occur. In the congested nasal passage the irrigant can stimulate additional mucociliary transport only in the inferior and middle airways and meati regions. Figure 6.33 shows that the average wall shear stress is not significant. On the right patent side, the average wall shear stress is less than 0.5 Pa, because of the low irrigation flow occurring along this side.

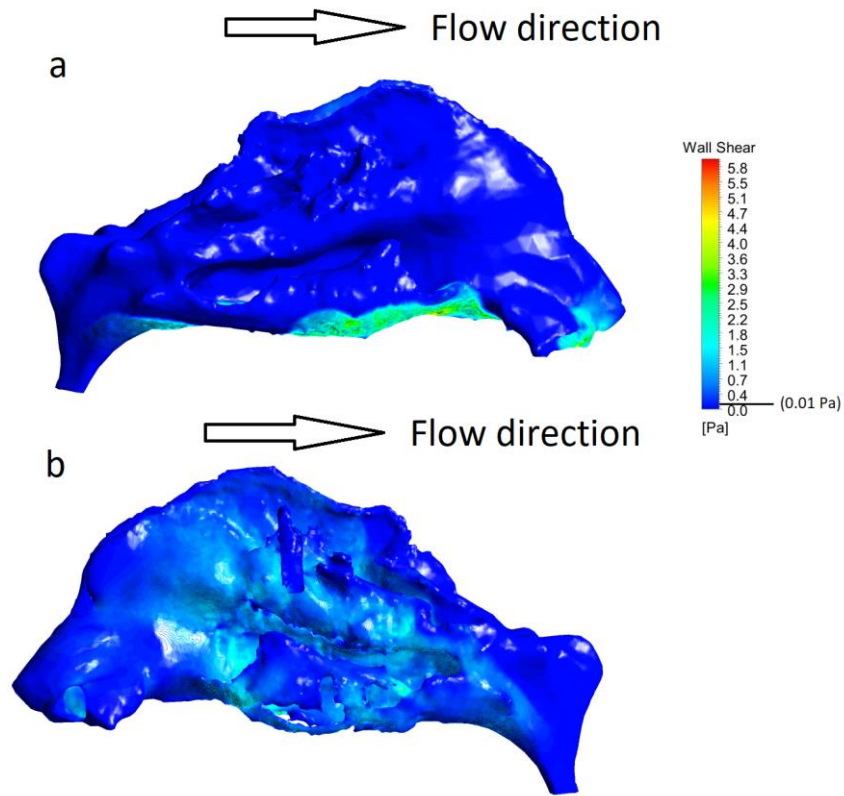


Figure 6.32. Wall shear stress contour at head forward position irrigated from the left congested passage a) right patent passage b) left congested passage.

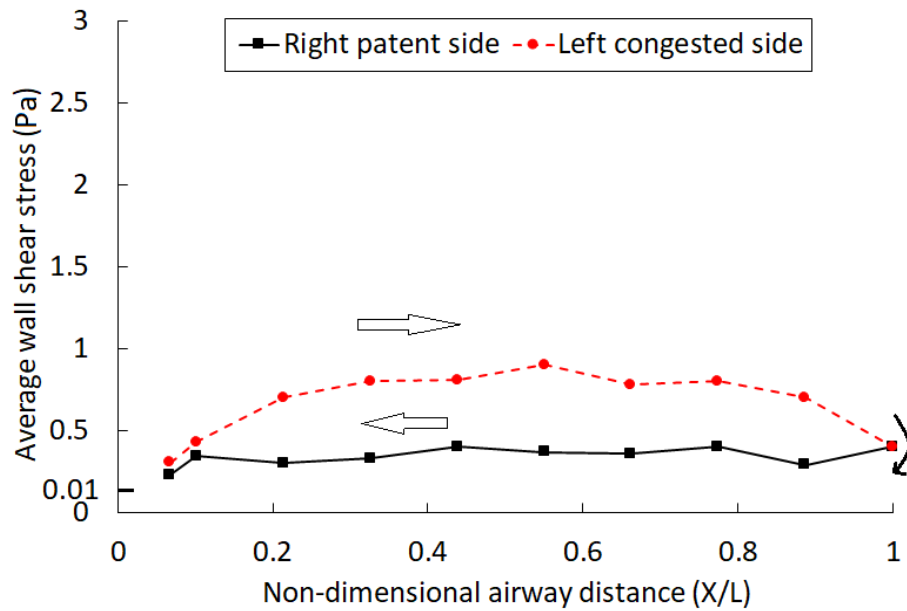


Figure 6.33. Average wall shear stress distribution within the nasal cavity for head forward position irrigated from left congested side.

## **6.3 Discussion**

### **6.3.1 Mygind head position (patent and congested side irrigation)**

With patent side irrigation, the large cross sectional area did not cause more friction loss for the saline when compared to the congested side. Due to the flow direction in the Mygind position, saline could maintain its pressure before entering the congested adjoining passage. This resulted in distribution of the irrigated saline to most regions of the patent nasal airway when irrigated from the patent side. The wall shear stress mapping in the patent side irrigation showed that the wall shear stress is only significant in the anterior regions of the nasal cavity of both passages. The saline pressure decreases at the anterior region of the left congested side. Saline pressure as a mechano-stimulation may increase the MTV of the whole patent passage and the posterior region of the left congested side. However, the wall shear stress as another mechano-stimulation factor increases the MTV at the anterior region of the left congested side more than in the rest of the regions.

This head position and side direction is recommended for nasal cavity irrigation, as irrigated saline may stimulate the mucociliary clearance of all the nasal cavity's mucosal surface.

On the congested side irrigation, a significant pressure loss occurred and low-pressure saline entered all of the congested passage. This resulted in the inferior airway of the patent passage remaining unirrigated. At this head position, congested side irrigation is not recommended when the targeted delivery site is the inferior airway of the patent passage.

With the congested side irrigation, the level of wall shear stress in both the congested and the patent passageways was higher than that with the patent sided irrigation. As shear stress is linearly related to local speed, wall shear stress on the congested side was higher

than that found in the patent side especially near the entrance of the middle nasal cavity. In the congested side irrigation, the irrigated saline could exert more uniform wall shear stress distribution on the whole nasal cavity compared to the patent side irrigation. At this head position and side direction, both saline pressure and wall shear stress at the left congested side is higher than at the right patent side. This may result in a better stimulation of mucociliary clearance along the whole epithelium surface at the left congested side than at the right patent side. Saline distribution results for the Mygind head position are supported by findings in the literature (136, 137).

### **6.3.2 90° head position (patent and congested side irrigation)**

In the 90° head position, for both patent and congested side irrigations the saline could reach most parts of the nasal cavity. On both sides, a flow separation occurred in the nasopharynx and this flow separation was larger when irrigation was from the patent side. This is because when the flow moved from the congested side to the patent side, the small cross sectional area of the congested side restricted the flow and caused an early separation from the lateral walls. When irrigation was performed from the patent side, the irrigation saline could maintain the pressure through both passages with the main pressure loss occurring at the entrance of the nasal valve region. The inferior, middle, and superior meati at the superior region of the nasal cavity and nasopharynx at the side of irrigation are not irrigated when irrigation is performed from the patent side. This head position and side direction is not recommended when one of the mentioned regions is targeted.

The inferior meatus at the superior region of the nasal cavity and a small region of the nasopharynx on the side of irrigation remain unirrigated when irrigation is performed from the congested side.

In this head position, the bulk of the fluid flow remains close to the septal wall on the side of the irrigation and tends to separate from the airway and move to the meati on the other

side. This results in high septal wall shear stress at the side of irrigation and high lateral wall shear stress at the contralateral side. For patent side irrigation, the higher saline pressure at the side of irrigation, and higher wall shear stress at the contralateral side of irrigation, may result in uniform stimulation of mucociliary clearance along the whole epithelium surface. At the left congested side irrigation, both saline pressure and wall shear stress at the side of irrigation is higher than at the contralateral side. This may result in a better stimulation of mucociliary clearance along the whole epithelium surface at the left congested side than at the right patent side.

The wall shear stress distribution in the 90° head position was similar when irrigation was performed from either the patent and congested sides. This head position is applicable when improvement of the nasal mucociliary function of the meati surface is required.

### **6.3.3 Head back position (patent and congested side irrigation)**

During the head back position, the flow of the nasal passages were aligned upward at a 45° incline against gravity. On the inlet side of the irrigation, the flow moved in a gravity direction to fill the passage. However, when it was irrigated from the congested side, a high pressure loss occurred due to the friction along the nasal passage walls. Because of this, low-pressure saline entered the patent passage and could not fill this passage completely, leading to flow separation occurring from the anterior wall. This resulted in the superior region of the patent passage not being irrigated. In this head position the bulk of flow passes through the inferior airway and the irrigant saline does not exert sufficient wall shear stress at the superior nasal vestibule, nasal valve, meatus, and airways. The superior nasal vestibule at the contralateral side of irrigation is unirrigated at this head position. It is recommended that for this head position irrigation inflow should be directed to the patent side. At right patent side irrigation, both saline pressure and wall shear stress at the anterior region of the left congested side is less than at the other regions of the nasal cavities. The irrigated saline may improve the mucociliary clearance of the anterior region

of the left congested side less than at other regions. Here again, at left congested side irrigation, both saline pressure and wall shear stress at the side of irrigation is higher than at the contralateral side. This may result in a better stimulation of mucociliary clearance along the whole epithelium surface at the left congested side than at the right patent side.

#### **6.3.4 Head forward position (patent and congest side irrigation)**

In the head forward position, the irrigated saline moved against gravity on the inlet side, which resulted in a high pressure loss occurring. This pressure loss prevented the saline from being distributed to the contralateral passage. This was more significant when saline was irrigated from the congested passage, which caused a high pressure drop for the moving saline, and in the patent passage, it could only fill the inferior airway. In this head position, the wall shear stress distribution was not beneficial to stimulate mucociliary transport in both nasal passages when irrigation was performed from the congested side. This means that the irrigant does not provide any improvement in the mucus transport function. In head forward positions, congested side irrigation is not recommended as most of the contralateral side of the irrigation remains unirrigated. For both sides of irrigation, the saline pressure is high at the anterior region of the side of irrigation, which may result in a better stimulation of mucociliary clearance along the epithelium surface at this region.

#### **6.3.5 Nasal cavity distribution (all head positions)**

It was discussed that the contact of hypertonic saline with the mucosal surface regulates the cellular water flux and ASL hydration. At each head position and inflow side direction, the contact and unirrigated regions were identified. The higher distribution of saline within the nasal cavity results in more effective nasal saline irrigation. Saline distribution within the nasal cavity and maxillary sinuses using CFD have been done by (1, 78). Although irrigations were performed in both nostrils, there was no discussion of which side achieved higher distribution during the nasal cycle.

Figure 6.34 shows the percentage of saline -volume distribution within the nasal cavity at different head positions. At each head position, the percentage of the saline within the nasal cavity is higher when irrigation is performed from the patent side except for the 90° head position. At a patent side irrigation, 97%, 89%, 93%, and 88% of the nasal cavity mucosal surface is irrigated at Mygind, 90°, head back, and head forward positions respectively.

As previously discussed, the irrigant can maintain its initial pressure while it is moving from the inlet towards the outlet when irrigation is performed from the patent side. For the 90° head position, the restrictions imposed by the geometry create a flow detachment before the nasopharynx. This flow detachment is greater when saline moves from the passage with a larger cross-sectional area, which results in more trapped air when irrigation is performed from the patent side. Therefore, at this head position, the congested side is recommended for achieving a higher nasal cavity mucosal surface irrigation compared to a patent side irrigation.

At a congested side irrigation, 95%, 95%, 92%, and 44% of the nasal cavity mucosal surface is irrigated at Mygind, 90°, head back, and head forward positions respectively.

The highest nasal cavity distribution is found when the irrigation is performed in the Mygind head position irrigated from the patent side. Following that, the Mygind position from the congested side, and the 90° position (again from the congested side), achieve the next highest nasal cavity mucosal surface irrigation.

When irrigation is performed from the congested side in the head forward position, the saline distribution within the nasal cavity is less than that found in other user conditions. The results of head forward position are consistent with the findings of Zhao et al.'s study (138). Their findings show that the saline distribution within the contralateral side of irrigation is poor.

Using different head position has previously been done by (139). They investigated four different head positions in their study: Lying head back, Head back, Ragan (on side, head down), and Praying to Mecca Position. They concluded that medication reaches the middle meatus in Mygind and Ragan positions, which are consistent with the current study.

### **6.3.6 Maxillary sinus penetration**

The saline penetration into the maxillary sinuses depends on different factors including the irrigant pressure when passing the ostial openings, the orientation of the ostial openings with respect to gravity and flow direction, and ostial size which varies depends upon state of nasal congestion. Many studies have investigated maxillary sinus penetration (1, 3, 65, 66, 69, 78). All of these studies have not considered the effect of the nasal cycle and in-flow side direction. The current study is the first one which has investigated saline irrigation on most anatomically correct nasal cavity to-date. Additionally, considered all the common head positions for the Neti Pot as a delivery device.

Figure 6.35 presents the  $V_{\text{saline}}/V_{\text{sinus}}$  at different head positions and inflow directions.  $V_{\text{saline}}/V_{\text{sinus}}$  shows the percentage of each sinus volume which was filled with irrigant.

With the Mygind head position, the saline pressure is high while passing the ostial openings (Figure 6.35). However, in this head position, the direction of the ostial opening is against gravity and saline tends to pass the ostium and distribute within the nasal cavity. The saline residue (penetrated saline in the sinus) is only in the maxillary sinus on the side of irrigation (8% of the sinus was filled) when it is performed from the patent side. The sinus penetration at the Mygind head position stays around the ostia entry region which provides hypertonic benefits for the mucosal surface of this region only at the maxillary sinuses.

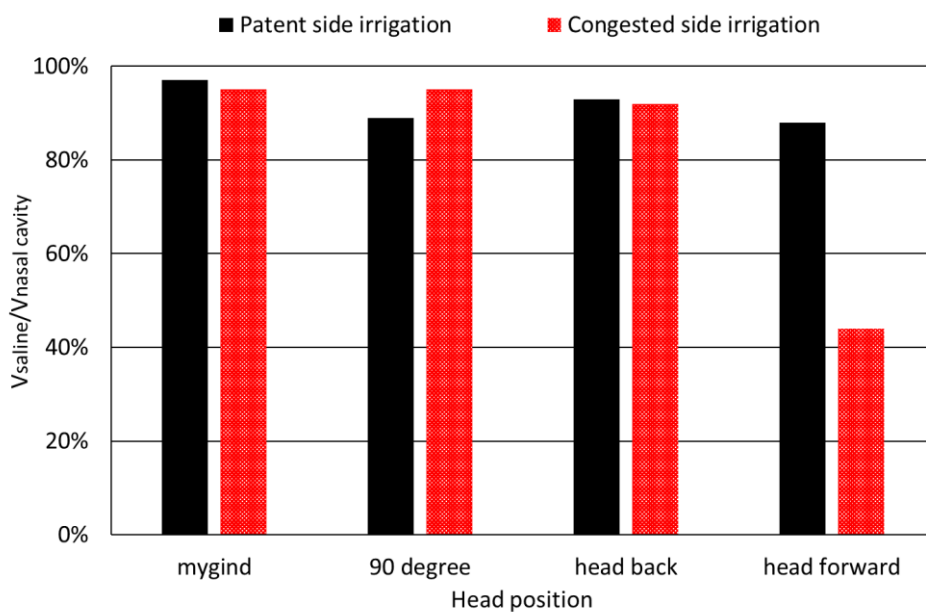


**Figure 6.34. Percentage of saline volume within the nasal cavity at different head positions and inflow directions.**

In the 90° head position, the irrigant could not penetrate the side of the irrigation when irrigated from the congested side, and there was a limited penetration in the maxillary sinus on the contralateral side and only 2% of the sinus was filled. At same head position, by changing the side of the direction to the congested side, 13% of the sinus located at the patent side was filled. At this head position, the saline cannot penetrate the sinus at the side of irrigation, as demonstrated in the simplified model in Chapter 3. The sinus penetration moves towards the lateral side of the sinus at the contralateral side of irrigation and provides hypertonic benefits for this region at the maxillary sinuses.

In the head back position, the residual saline in both sinuses was noticeable when irrigation was performed from the patent side, with 23% and 21% of the right and left sinuses being filled with saline, respectively. This balanced sinuses' penetration was also observed in the simplified model in Chapter 3. The penetrated saline in the sinuses stays

around the anterior region of the sinuses and this helps the cellular water flux and ASL hydration of this region.

The movement of the flow on the side of the irrigation is towards gravity and the ostial direction is the same as gravity. Therefore, the saline can penetrate the sinuses especially when irrigation is performed from the patent side.

During the head forward position, the saline could penetrate the maxillary sinus on the side of the irrigation when irrigation was performed from the patent side (26% of the sinus was filled with saline). Opposite to the head back position, the penetrated saline in the sinuses stays around the posterior region of the sinus and this helps the cellular water flux and ASL hydration of this region.

For all head positions, the saline penetration into the sinuses was higher when irrigation was performed from the patent side compared to the congested side. The saline penetration into the maxillary sinus on the congested side was always less than that of the maxillary sinus at the patent side. This could also be due to middle meatal congestion.

The highest penetration in both sinuses was found at the head back position irrigated from the patent side, while the least penetration was found at the 90° position irrigated from the patent side, and the head forward position irrigated from the congested side.

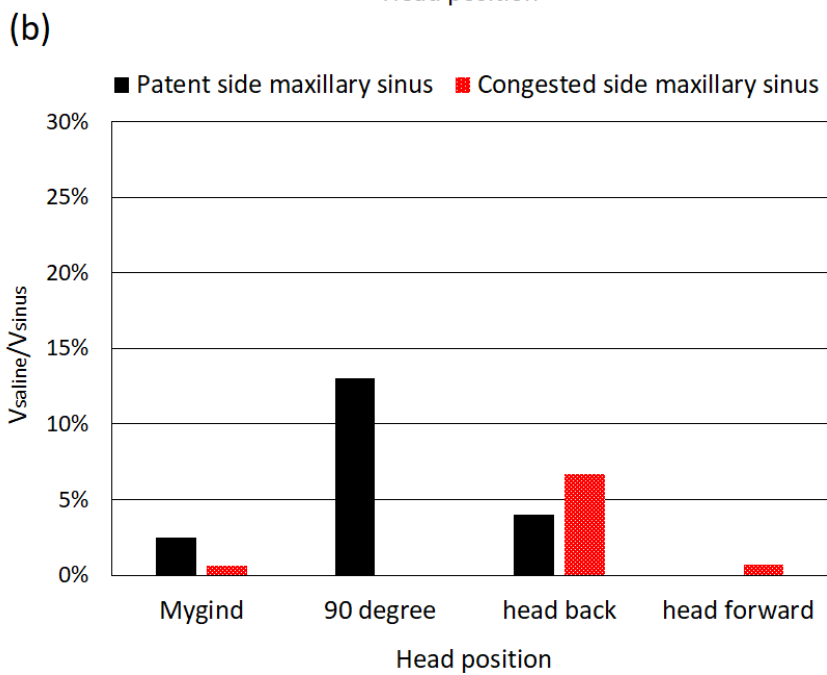
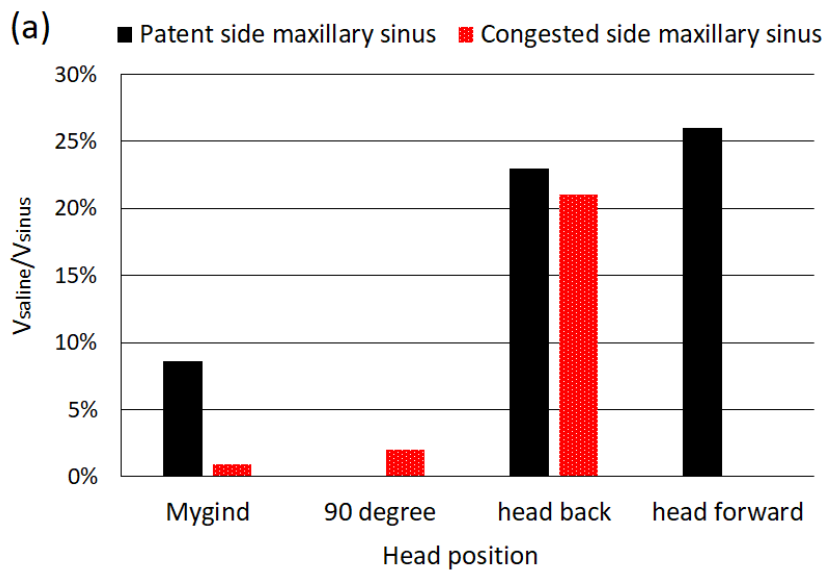


**Figure 6.35. Saline residual in maxillary sinuses at different head positions for a) patent side irrigation b) congested side irrigation.**

The findings are summarized in Table 6.1. In addition, the findings of this study are presented as a clinical guide sheet in Appendix D.

**Table 6.1. Remarks on the different user conditions.**

Head position	Side direction	(Distribution and penetration)	(Pressure and wall shear)
Mygind	Patent	<ul style="list-style-type: none"> <li>• Good nasal cavity distribution.</li> <li>• Limited sinus penetration on the patent side.</li> <li>• The sinus penetration stays around the sinus entry region.</li> </ul>	<ul style="list-style-type: none"> <li>• High saline pressure throughout whole nasal cavity.</li> </ul>
Mygind	Congested	<ul style="list-style-type: none"> <li>• Good nasal cavity distribution.</li> <li>• Inferior airway of the patent side remained unirrigated.</li> <li>• Limited sinus penetration.</li> <li>• The sinus penetration remained around the sinus entry region.</li> </ul>	<ul style="list-style-type: none"> <li>• High saline pressure at the side of the irrigation</li> <li>• High saline pressure loss at nasopharynx due to flow turn-around and passage expansion.</li> <li>• Uniform wall shear stress at the congested side.</li> </ul>
90°	Patent	<ul style="list-style-type: none"> <li>• Inferior meatus remained unirrigated in anterior region</li> <li>• Inferior, middle, and superior meati were unirrigated at the superior region of the nasal cavity</li> <li>• Nasopharynx on the patent side was unirrigated</li> <li>• No sinus penetration</li> </ul>	<ul style="list-style-type: none"> <li>• High saline distribution on side of the irrigation.</li> <li>• Sudden pressure drop at the contralateral side when flow exited the meati.</li> <li>• High wall shear stress on contralateral side around the meati regions.</li> </ul>
90°	Congested	<ul style="list-style-type: none"> <li>• Inferior meatus at superior region of the nasal cavity remained unirrigated.</li> <li>• Small region of the nasopharynx on the congested side was unirrigated</li> <li>• Flow detachment at unirrigated region was observed at septal wall in the inferior and middle meati on the patent side.</li> </ul>	<ul style="list-style-type: none"> <li>• Saline loses pressure when it reaches the patent side due to congested side cross sectional area.</li> <li>• High wall shear stress at contralateral side around the meati regions.</li> </ul>
Head back	Patent	<ul style="list-style-type: none"> <li>• Good nasal cavity distribution</li> <li>• Superior nasal vestibule at the congested side was unirrigated.</li> <li>• Saline penetration into both sinuses.</li> <li>• Saline stays in the end region of the sinuses due to the head orientation.</li> </ul>	<ul style="list-style-type: none"> <li>• High saline pressure at both passages.</li> <li>• Sudden pressure drop when saline enters the meati on the congested side.</li> <li>• No wall shear stress at superior nasal vestibule at congested side.</li> <li>• No wall shear stress at superior nasal valve, vestibule, meati, and olfactory cleft.</li> </ul>
Head back	Congested	<ul style="list-style-type: none"> <li>• Good nasal cavity distribution</li> </ul>	<ul style="list-style-type: none"> <li>• High saline pressure at the side of irrigation.</li> </ul>

		<ul style="list-style-type: none"> <li>• Superior nasal vestibule was unirrigated.</li> <li>• Limited sinus penetration.</li> <li>• Saline stays in the end region of the sinuses due to the head orientation.</li> </ul>	<ul style="list-style-type: none"> <li>• Uniform wall shear stress at the congested side except at the superior region of the nasal cavity.</li> <li>• No wall shear stress at the superior nasal valve and vestibule</li> </ul>
Head forward	Patent	<ul style="list-style-type: none"> <li>• Superior nasal vestibule and valve were unirrigated.</li> <li>• Saline penetration into the sinus located at the side of the irrigation.</li> <li>• The saline stays in the anterior region of the sinus due to the head orientation.</li> </ul>	<ul style="list-style-type: none"> <li>• Very low saline pressure at contralateral side of the irrigation.</li> <li>• High pressure drop at side of irrigation due to passage orientation.</li> <li>• No wall shear stress at the superior nasal vestibule, valve, meatus, and olfactory cleft</li> </ul>
Head forward	Congested	<ul style="list-style-type: none"> <li>• No saline distribution on patent side</li> <li>• Saline moves at the patent side only via inferior airway.</li> <li>• Nasopharynx region was unirrigated at the side of irrigation.</li> <li>• No sinus penetration</li> </ul>	<ul style="list-style-type: none"> <li>• Very low saline pressure on contralateral side of the irrigation.</li> <li>• High pressure drop at side of irrigation due to passage orientation and geometry</li> <li>• Very low wall shear stress throughout the whole nasal cavity.</li> </ul>

#### 6.4 Summary

CFD simulation was used to measure the flow field of saline distribution, pressure, and wall shear stress in the nasal cavities and maxillary sinuses during saline irrigation at four different head positions during patent and congested inlet nasal irrigation. In this chapter, the distribution of the irrigated saline was investigated and the saline mucosal contact and unirrigated regions were identified to determine which regions of the nasal cavities and maxillary sinuses that benefit from the hypertonic effect of saline. Saline pressure and mucosal wall shear stress distribution, which are known as mechano-stimulation factors, were mapped to investigate the regions where saline irrigation may result in a better stimulation of mucociliary clearance for different head positions and side directions. It was found that at all head positions and side irrigations, the mucosal wall shear stress at the congested side is higher than at the right patent side. Also the saline pressure at the

side of irrigation is higher than at the contralateral side of irrigation. In general, during patent side irrigation, both saline pressure and mucosal wall shear stress result in a stress capable of providing a uniform stimulation of mucociliary clearance along the whole epithelium surface of both nasal cavities. At a congested side irrigation, the irrigated saline result in a better stimulation of mucociliary clearance along the whole epithelium surface of the left congested side than at the right patent side.

## Chapter 7: Conclusions and future work

### 7.1 Conclusions

The flow fields associated with hypertonic saline elicited ASL hydration and purinergic mechano-stimulation of mucociliary transport and the human nasal cavities and maxillary sinuses has been investigated during nasal saline irrigation using CFD simulations. The potential of increased MTV and ASL hydration benefit the treatment of inflammatory and paranasal diseases, such as CRS, and post-nasal and sinus surgery recovery. The saline irrigation delivery can be divided into three stages: first, saline enters the nasal cavity and fills the nasal cavities and maxillary sinuses; second, the rate of change in the saline flow field is almost constant and can be considered to be a steady state; finally, at the end of irrigation, the saline starts to drain from the nasal cavities. The simulation results in this study (steady state) show the peak values of the nasal irrigation flow field including saline distribution, pressure distribution, and wall shear stress. These results are then compared to previously published MTV mechano-stimulation data. The applied CFD numerical methodology in this study firstly was used in a simplified nasal geometry to validate the computational configuration using physical measurement and observation methods. The results of this initial investigation were used to guide the selection of the most suitable method for the later investigation of nasal saline irrigation within realistic human nasal cavities and maxillary sinuses.

In the later study using both experimental and numerical analysis, an anatomically accurate *in-vivo* nasal airway geometry was used that included the nasal passages and maxillary sinuses. This model was constructed using segmentation of medical MRI head *in-vivo* scan data. This *in-vivo* nasal airway geometry reflected the nasal cycle status with one side of the nose being ‘congested’ and the other ‘patent’. A scale-up transparent silicone cast model was manufactured using rapid prototyping techniques. The first scale-

up MRI nasal model has been constructed by (140). The 20 scale models conducted by (141, 142) to reach a more detailed flow patterns and reduce the relative size and intrusiveness of measurement devices.

Irrigation simulations were done for steady state condition with boundary conditions representing the application of the Neti pot as the delivery device for nasal irrigation. The effect of head position on the distribution of its contents in the nasal cavity and maxillary sinuses was investigated by considering four common head positions: Mygind, 90°, head-back, and head-forward. In each head position, the inlet boundary condition was assigned to the right and left sides separately. Harvey et al. (3) used a cadaver model to investigate the impact of a Neti pot on nasal irrigation. The Cadaveric model failed to consider the effect of the nasal cycle on nasal geometry. The current study tried to reflect the nasal cycle on in-vivo nasal geometry. The Neti pot was recommended by (70) due to proper nasal cavity distribution.

The validity of the complex nasal CFD model was tested using planar-PIV to compare irrigation fluid velocity flow fields found in the transparent nasal cast model with those found during CFD simulation. This method has previously been done by (143, 144). Doorly et al. (122) investigated airflow characteristics using replica model of nasal cavity by the PIV and flow visualization. They measured velocity in different regions of nasal cavity.

The later investigation into saline flow fields, including saline distribution, pressure, and mucosal wall shear stress distributions within a realistic *in-vivo* nasal cavity, were carried out using the validated CFD model.

It was found that different head positions and side irrigations significantly modify the saline flow field and distribution in the nasal cavities and maxillary sinuses. A relationship between the level of saline distribution and the saline pressure in the nasal

cavity was discovered. The higher the saline pressure is, the greater is the amount of saline distributed through the nasal cavity. The maximum saline distribution in the nasal cavity was observed in the Mygind head position. Karagama et al. (145) investigated saline distribution within a nasal cavity using the Neti Pot. They concluded Mygind position was more effective for delivery into the middle meatus. The results of the current study for Mygind position are in agreement with (145). In all head positions, except the 90° head position, the saline distribution in the nasal cavity was greater when saline was irrigated from the patent side compared to the congested side. Congested side irrigation had decreased saline pressure due to the restricted geometry, however the moving saline could not maintain this pressure when it reached the patent side, resulting in unirrigated regions. In the Mygind head position, the average saline pressure in the coronal sections was increased to 800 Pa in the mid-region of the nasal cavity. The least saline distribution in the nasal cavity occurred in the head forward position irrigated from the congested side. Here the orientation of the nasal cavity with respect to gravity, and the restricted geometry of the congested side, decreased the saline pressure significantly and the saline pressure measured 50 Pa when it reached the patent side. This resulted in saline only moving from the inferior region of the nasal airway, and almost all of the nasal cavity on the patent side remained unirrigated.

At a patent side irrigation, the Mygind, head back, 90°, and head forward positions achieve from the highest to the lowest nasal cavity mucosal surface irrigation, with 97%, 93, 89%, and 88% respectively. At a congested side irrigation, the Mygind, 90°, head back, and head forward positions achieve from the highest to the lowest nasal cavity mucosal surface irrigation, with 95%, 95%, 92%, and 44% respectively. At each of these head positions and side directions, the unirrigated regions are identified and summarized in both the clinical guide sheet and summary of findings. It is recommended not to use a particular head position and side direction if the targeted delivery region is in the

unirrigated regions of that head position and side direction. The results in this study are consistent by the findings in the literature (3, 63, 66, 146).

All the results have shown that the saline penetration into the maxillary sinuses cannot be solely determined by saline pressure. With the ostial orientation with respect to gravity also influencing sinus saline penetration. The saline penetration into the sinus on the patent side is greater in all user conditions except for the head back position irrigated from the congested side. In the Mygind head position, where the ostial orientation is against gravity, the saline penetration is limited. This limited penetration into the sinuses was due to high saline pressure. In the Mygind head position the sinus penetration stays around the ostia entry region which improves the mucociliary function at the sinus entry region, which may help improve drainage of the whole sinus cavity.

In the head back position irrigated from the patent side, there was an equal saline penetration into both sinuses. The maximum sinus penetration in both sinuses was found at the head back position irrigated from the patent side, where 23% and 21% of the patent and congested sinuses respectively became filled with the irrigant.

These results reveal clinically useful information so that the saline irrigation user can achieve maximum distribution and mucociliary clearance in the nasal cavity or to a specific location.

Wall shear stress mapping showed that with the Mygind head position irrigated from the patent side, the wall shear stress is high only around the nasal vestibule and valve regions. When irrigation is performed from the congested side, the wall shear stress is better distributed among the nasal passageways especially on the congested side.

In the 90° head position, for either the congested side or patent side irrigation, the wall shear stress around the meati located at the contralateral side of the irrigation is

significant. This head position is recommended as it may improve the mucociliary clearance function in this targeted region.

In both head back and head forward positions, the wall shear stress distribution around the superior nasal vestibule, nasal valve and meatus, is negligible and unlikely to stimulate additional mucociliary transport in these regions.

Wall shear stresses, which lead to beneficial mechano-physical responses in the epithelial surface, were mapped for the nasal cavity in different head positions and inlet side irrigations. The wall shear stresses were higher on the congested side compared to the patent side due to the more narrowed geometry and higher curvatures of the turbinates. The wall shear stress was highest in regions including the turbinates and nasal valve for most of the head positions and inlet side directions. The irrigated saline at high mucosal wall shear stress regions may provide more purinergic mechano-stimulation than at the low wall shear stress regions.

The saline pressure which can act as a mechanoc-stimulation at the side of irrigation is higher than at the contralateral side of irrigation. In general, at patent side irrigation, both saline pressure and mucosal wall shear stress may result in a uniform stimulation of mucociliary clearance along the whole epithelium surface of both nasal cavities. At the congested side irrigation, the irrigated saline result in a better stimulation of mucociliary clearance along the whole epithelium surface of the left congested side than at the right patent side.

A summary of the most significant original contributions of this research is given below:

- First PIV measurement in an *in-vivo* nasal cavity and maxillary sinuses during nasal saline irrigation
- The most anatomically correct nasal cavity to-date that considers the effect of the nasal cycle on nasal cavity geometry

- First measurements of the pressure field and wall shear stress mapping in the nasal cavity and maxillary sinuses during nasal saline irrigation
- First study to consider all the common head positions for the Neti Pot as a delivery device
- Confirmation of the significant effect of different side irrigations on saline distribution and flow fields in the nasal cavities and maxillary sinuses.
- First to identify irrigation treatment orientation based on desired nasal treatment site.
- First to develop clinical treatment guide sheet.

The answer to the research questions of this study are:

- Can different head positions and inflow directions be used to target a nasal irrigation treatment site?
  - ✓ Different head positions and side irrigations significantly modify the distribution in the nasal cavities and maxillary sinuses. The unirrigated regions are identified and it is recommended not to use a particular head position and side direction if the targeted delivery region is in the unirrigated regions of that head position and side direction.
- How do different head positions and inflow directions affect the mucosal wall shear stress and pressure during nasal saline irrigation?
  - ✓ The wall shear stress mapping showed that changing the head positions and inflow side directions affects the mucosal shear stress and pressure distributions. The wall shear stresses were higher on the congested side than on the patent side due to the narrower geometry and higher curvatures of the turbinates. The pressure distribution mapping showed that when irrigation is performed from the congested side, the smaller cross-sectional

area restricts the flow and causes a greater friction pressure loss compared to the other side. The orientation of the nasal cavities with respect to gravity at different head positions, affected the saline pressure significantly.

- How does nasal cycle status affect saline irrigation treatment?
  - ✓ The small cross sectional area of the congested side restricts the flow and affects the saline mucosal contact regions (Hypertonic effect) and pressure and wall shear stress distributions (MTV mechano-stimulation). It was found that at both side irrigations, the mucosal wall shear stress at the congested side is higher than at the right patent side. Also the saline pressure at the side of irrigation is higher than at the contralateral side of irrigation. During patent side irrigation, both saline pressure and mucosal wall shear stress result in a stress capable of providing a uniform stimulation of mucociliary clearance along the whole epithelium surface of both nasal cavities. At a congested side irrigation, the irrigated saline result in a better stimulation of mucociliary clearance along the whole epithelium surface of the left congested side than at the right patent side.

The significant original contributions of this study have been aligned to answer the research questions of this study as follows:

- The applied geometry in this study examines how the nasal cycle affects nasal saline distribution by influencing the flow pressure field because of changing the side of the irrigation.
- The experimental investigation (PIV measurement) of this study validates the accuracy of the numerical results.

- The results obtained from the numerical investigation of this study show how changing the head position and side direction affects the saline distribution to different regions of the nasal cavities and maxillary sinuses.
- This study also examines the mucosal wall shear stress and pressure distribution at different head positions and side directions to determine whether the irrigant has the potential to stimulate additional mucociliary transport.

The answers to the research questions have proven the research hypothesis of this study.

However, some limitations of this study should be noted.

In this study, a steady state simulation was considered and the simulations showed the results of the steady state phase of the irrigation. This model is not capable of showing the filling and emptying stages of the irrigation. Future work needs to be extended for emptying and filling stages of irrigation. This can be achieved by performing unsteady state simulation. Also, the delivery device needs to be attached to the nostril in the simulations.

Another limitation of this study is in the limited range of subjects and the limited range of conditions tested. Simulations should be repeated for geometries from different ethnicity, age, and sex. Also, it is essential to investigate the saline flow characteristics within unhealthy nasal cavities and maxillary sinuses. The influence of FESS on nasal anatomy and flow fields should also be investigated.

Other delivery devices with different mechanisms may lead to various flow characteristics within the nasal cavities and maxillary sinuses. In this study, only the Neti pot was considered as the delivery device which is a limitation for this study. The effect of different boundary conditions such as different inlet pressure and mass flow rate representing a specific delivery device (Squeeze bottle) should be considered.

## 7.2 Future work

There are a number of gaps and limitations in this study and would benefit from further research including:

- The work presented in this thesis reveals the significant effect the nasal cycle has on the flow fields within the nasal cavities and maxillary sinuses. Future investigation should include the study of a larger number of nasal geometries to ensure the flow features presented are representative of a wider population. The influence of FESS on nasal anatomy and flow fields should also be investigated.
- The effect of different delivery devices such as squeeze bottle on the effectiveness of nasal saline irrigation in terms of mechano-stimulation and hypertonic stimulation and the effect of inlet pressure variation on the flow field characteristics as an influencing factor should also be investigated.
- Unsteady simulations can be performed to investigate the saline characteristics during the filling and emptying stages.

## REFERENCES

1. Zhao K, Craig JR, Cohen NA, Adappa ND, Khalili S, Palmer JN. Sinus irrigations before and after surgery-Visualization through computational fluid dynamics simulations. *Laryngoscope*. 2015.
2. Craig JR, Zhao K, Doan N, Khalili S, Lee JYK, Adappa ND, et al. Cadaveric validation study of computational fluid dynamics model of sinus irrigations before and after sinus surgery. *Int Forum Allergy Rhinol*. 2016;6(4):423-8.
3. Harvey RJ, Goddard JC, Wise SK, Schlosser RJ. Effects of endoscopic sinus surgery and delivery device on cadaver sinus irrigation. *Otolaryngol Head Neck Surg*. 2008;139(1):137-42.
4. Harvey RJ, Debnath N, Srubiski A, Bleier B, Schlosser RJ. Fluid residuals and drug exposure in nasal irrigation. *Otolaryngol Head Neck Surg*. 2009;141(6):757-61.
5. Harvey R, Hannan SA, Badia L, Scadding G. Nasal saline irrigations for the symptoms of chronic rhinosinusitis. *Cochrane Database Syst Rev*. 2007;3.
6. Proctor DF, Andersen IHP. *The nose, upper airway physiology and the atmospheric environment*: Elsevier Biomedical Press; 1982.
7. Dykewicz MS, Hamilos DL. Rhinitis and sinusitis. *Journal of Allergy and Clinical Immunology*. 2010;125(2 SUPPL. 2):S103-S15.
8. Cauna N. The rat as a suitable animal in experimental rhinology. *Laryngologie Rhinologie Otologie*. 1975;54(12):942-50.
9. Wexler DB, Davidson TM. The Nasal Valve: A Review of the Anatomy, Imaging, and Physiology. *Am J Rhinol*. 2004;18(3):143-50.
10. Dykewicz MS, Hamilos DL. Rhinitis and sinusitis. *Journal of Allergy and Clinical Immunology*. 2010;125(2):S103-S15.
11. Baraniuk JN. Neural regulation of mucosal function. *Pulmonary Pharmacology and Therapeutics*. 2008;21(3):442-8.
12. Cole P. Nasal Respiratory Function. *The Nose*. 1993:3-60.
13. Pendolino AL, Lund V, Nardello E, Ottaviano G. The nasal cycle: a comprehensive review. *Rhinology Online*. 2018;1:67-76.
14. White DE, Bartley J, Nates RJ. Model demonstrates functional purpose of the nasal cycle. *Biomed Eng Online*. 2015;14(1).
15. Nasal Cycle, Turbinates & Sleep 2016 [Available from: <https://noserevisionsurgeryandsurgeons.blogspot.com/2016/12/nasal-cycle-turbinates-sleep.html>].
16. Djupesland PG. Nasal drug delivery devices: Characteristics and performance in a clinical perspective-a review. *Drug Delivery and Translational Research*. 2013;3(1):42-62.
17. Lundberg JO. Nitric oxide and the paranasal sinuses. *Anatomical Record*. 2008;291(11):1479-84.
18. Qian W, Djupesland PG, Chatkin JM, McClean P, Furlott H, Chapnik JS, et al. Aspiration flow optimized for nasal nitric oxide measurement. *Rhinology*. 1999;37(2):61-5.
19. Negus S. The function of the paranasal sinuses. *AMA Archives of Otolaryngology*. 1957;66(4):430-42.
20. Pendolino AL, Lund VJ, Nardello E, Ottaviano G. The nasal cycle: a comprehensive review. *Rhinology Online*. 2018;1:67-76.
21. Beule AG. Physiology and pathophysiology of respiratory mucosa of the nose and the paranasal sinuses. *GMS Current Topics in Otorhinolaryngology, Head and Neck Surgery*. 2010;9:Doc07.
22. Knops J, McCaffrey T, Kern E. Inflammatory diseases of the sinuses: physiology. *Clinical applications. Otolaryngologic clinics of North America*. 1993;26(4):517-34.
23. Gysin C, Alothman G, Papsin B. Sinonasal disease in cystic fibrosis: clinical characteristics, diagnosis, and management. *Pediatric pulmonology*. 2000;30(6):481-9.
24. Principi N, Esposito S. Nasal irrigation: An imprecisely defined medical procedure. *Int J Environ Res Public Health*. 2017;14(5):516.
25. Boek WM, Graamans K, Natzijs H, van Rijk PP, Huizing EH. Nasal mucociliary transport: New evidence for a key role of ciliary beat frequency. *Laryngoscope*. 2002;112(3):570-3.

26. Steven Cataldo M, Pedro M, Erickson T. Physiology of Oscillating Positive Expiratory Pressure (OPEP) devices: Expiratory flow bias and justification for vPEP® Device.
27. Widdicombe J. Regulation of the depth and composition of airway surface liquid. *Journal of Anatomy*. 2002;201(4):313-8.
28. Osguthorpe JD, Hadley JA. Rhinosinusitis: current concepts in evaluation and management. *Medical Clinics of North America*. 1999;83(1):27-41.
29. Schwiebert EM, Zsembery A. Extracellular ATP as a signaling molecule for epithelial cells. *Biochimica et Biophysica Acta (BBA) - Biomembranes*. 2003;1615(1):7-32.
30. Davis CW, Lazarowski E. Coupling of airway ciliary activity and mucin secretion to mechanical stresses by purinergic signaling. *Respir Physiol Neurobiol*. 2008;163(1):208-13.
31. Knowles MR, Robinson JM, Wood RE, Pue CA, Mentz WM, Wager GC, et al. Ion composition of airway surface liquid of patients with cystic fibrosis as compared with normal and disease-control subjects. *Journal of Clinical Investigation*. 1997;100(10):2588-95.
32. Boucher RC. Molecular insights into the physiology of the 'thin film' of airway surface liquid. *Journal of Physiology*. 1999;516(3):631-8.
33. Tarran R, Grubb BR, Gatzky JT, Davis CW, Boucher RC. The relative roles of passive surface forces and active ion transport in the modulation of airway surface liquid volume and composition. *The Journal of general physiology*. 2001;118(2):223-36.
34. P Reeves E, Molloy K, Pohl K, G McElvaney N. Hypertonic Saline in Treatment of Pulmonary Disease in Cystic Fibrosis 2012. 465230 p.
35. Button B, Boucher RC, Group UoNCVL. Role of mechanical stress in regulating airway surface hydration and mucus clearance rates. *Respir Physiol Neurobiol*. 2008;163(1):189-201.
36. Button B, Picher M, Boucher RC. Differential effects of cyclic and constant stress on ATP release and mucociliary transport by human airway epithelia. *Journal of Physiology*. 2007;580(2):577-92.
37. Tarran R. Regulation of airway surface liquid volume and mucus transport by active ion transport. *Proceedings of the American Thoracic Society*. 2004;1(1):42-6.
38. Avraham-Chakim L, Elad D, Zaretsky U, Kloog Y, Jaffa A, Grisaru D. Fluid-Flow Induced Wall Shear Stress and Epithelial Ovarian Cancer Peritoneal Spreading. *PLOS ONE*. 2013;8(4):e60965.
39. Tarran R, Button B, Boucher RC. Regulation of normal and cystic fibrosis airway surface liquid volume by phasic shear stress. *Annu Rev Physiol* 2006. p. 543-61.
40. Basser PJ, McMahon TA, Griffith P. The mechanism of mucus clearance in cough. *Journal of Biomechanical Engineering*. 1989;111(4):288-97.
41. Pynnonen MA, Mukerji SS, Kim HM, Adams ME, Terrell JE. Nasal saline for chronic sinonasal symptoms: a randomized controlled trial. *Archives of Otolaryngology–Head & Neck Surgery*. 2007;133(11):1115-20.
42. Nguyen SA, Psaltis AJ, Schlosser RJ. Isotonic saline nasal irrigation is an effective adjunctive therapy to intranasal corticosteroid spray in allergic rhinitis. *American journal of rhinology & allergy*. 2014;28(4):308-11.
43. Achilles N, Mösges R. Nasal saline irrigations for the symptoms of acute and chronic rhinosinusitis. *Curr Allergy Asthma Rep*. 2013;13(2):229-35.
44. Sin B, Togias A. Pathophysiology of allergic and nonallergic rhinitis. *Proceedings of the American Thoracic Society*. 2011;8(1):106-14.
45. Greiner AN, Meltzer EO. Overview of the treatment of allergic rhinitis and nonallergic rhinopathy. *Proceedings of the American Thoracic Society*. 2011;8(1):121-31.
46. Hermelingmeier KE, Weber RK, Hellmich M, Heubach CP, Mösges R. Nasal irrigation as an adjunctive treatment in allergic rhinitis: a systematic review and meta-analysis. *American journal of rhinology & allergy*. 2012;26(5):e119-e25.
47. DeCastro A, Mims L, Hueston WJ. Rhinosinusitis. *Primary Care - Clinics in Office Practice*. 2014;41(1):47-61.
48. Min YG. The pathophysiology, diagnosis and treatment of allergic rhinitis. *Allergy, Asthma and Immunology Research*. 2010;2(2):65-76.

49. Al Badaai Y, Samaha M. Outcome of endoscopic sinus surgery for chronic rhinosinusitis patients: A Canadian experience. *Journal of Laryngology and Otology*. 2010;124(10):1095-9.
50. Rudmik L, Hoy M, Schlosser RJ, Harvey RJ, Welch KC, Lund V, et al. Topical therapies in the management of chronic rhinosinusitis: An evidence-based review with recommendations. *Int Forum Allergy Rhinol*. 2013;3(4):281-98.
51. Papsin B, McTavish A. Saline nasal irrigation. Its role as an adjunct treatment. *Canadian Family Physician*. 2003;49(FEB.):168-73.
52. Lee JM, Nayak JV, Doghramji LL, Welch KC, Chiu AG. Assessing the risk of irrigation bottle and fluid contamination after endoscopic sinus surgery. *Am J Rhinol Allergy*. 2010;24(3):197-9.
53. Wei CC, Adappa ND, Cohen NA. Use of topical nasal therapies in the management of chronic rhinosinusitis. *The Laryngoscope*. 2013;123(10):2347-59.
54. Suh JD, Kennedy DW. Treatment options for chronic rhinosinusitis. *Proceedings of the American Thoracic Society*. 2011;8(1):132-40.
55. Liang J, Lane AP. Topical Drug Delivery for Chronic Rhinosinusitis. *Curr Otorhinolaryngol Rep*. 2013;1(1):51-60.
56. Thomas WW, Harvey RJ, Rudmik L, Hwang PH, Schlosser RJ. Distribution of topical agents to the paranasal sinuses: An evidence-based review with recommendations. *Int Forum Allergy Rhinol*. 2013;3(9):691-703.
57. Rabago D, Zgierska A. Saline nasal irrigation for upper respiratory conditions. *Am Fam Physician*. 2009;80(10):1117-9.
58. Ho EY, Cady KA, Robles JS. A case study of the Neti pot's rise, americanization, and rupture as integrative medicine in US media discourse. *Health communication*. 2016;31(10):1181-92.
59. Rabago DP, Guerard E, Bukstein D. Nasal irrigation for chronic sinus symptoms in patients with allergic rhinitis, asthma and nasal polyposis: a hypothesis generating study. *WMJ: official publication of the State Medical Society of Wisconsin*. 2008;107(2):69.
60. Heatley DG, McConnell KE, Kille TL, Levenson GE. Nasal irrigation for the alleviation of sinonasal symptoms. *Otolaryngol Head Neck Surg*. 2001;125(1):44-8.
61. Hajizadeh Aghdam A, Ohl SW, Khoo BC, Shervani-Tabar MT, Nobari MRH. Effect of the viscosity on the behavior of a single bubble near a membrane. *International Journal of Multiphase Flow*. 2012;47:17-24.
62. Abadie WM, McMains KC, Weitzel EK, editors. Irrigation penetration of nasal delivery systems: a cadaver study. *International forum of allergy & rhinology*; 2011: Wiley Online Library.
63. Wormald PJ, Cain T, Oates L, Hawke L, Wong I. A comparative study of three methods of nasal irrigation. *Laryngoscope*. 2004;114(12):2224-7.
64. Beule A, Athanasiadis T, Athanasiadis E, Field J, Wormald PJ. Efficacy of different techniques of sinonasal irrigation after modified Lothrop procedure. *Am J Rhinol Allergy*. 2009;23(1):85-90.
65. Olson DEL, Rasgon BM, Hilsinger Jr RL. Radiographic comparison of three methods for nasal saline irrigation. *Laryngoscope*. 2002;112(8 Pt 1):1394-8.
66. Snidvongs K, Chaowanapanja P, Aeumjaturapat S, Chusakul S, Praweswararat P. Does nasal irrigation enter paranasal sinuses in chronic rhinosinusitis? *Am J Rhinol*. 2008;22(5):483-6.
67. Miller TR, Muntz HR, Gilbert ME, Orlandi RR. Comparison of topical medication delivery systems after sinus surgery. *Laryngoscope*. 2004;114(2):201-4.
68. Valentine RJ, Athanasiadis T, Thwin M, Singhal D, Weitzel EK, Wormald PJ. A prospective controlled trial of pulsed nasal nebulizer in maximally dissected cadavers. *Am J Rhinol*. 2008;22(4):390-4.
69. Campos J, Heppert W, Weber R. Nasal douches for diseases of the nose and the paranasal sinuses - A comparative in vitro investigation. *Eur Arch Otorhinolaryngol*. 2013;270(11):2891-9.
70. Passàli D, Damiani V, Passàli FM, Passàli GC, Bellussi L. Atomized nasal douche vs nasal lavage in acute viral rhinitis. *Archives of Otolaryngology - Head and Neck Surgery*. 2005;131(9):788-90.
71. Gelardi M, Mezzoli A, Fiorella ML, Carbonara M, Di Gioacchino M, Ciprandi G. Nasal irrigation with lavonase® as ancillary treatment of acute rhinosinusitis: A pilot study. *Journal of Biological Regulators and Homeostatic Agents*. 2009;23(2):79-84.

72. Habib ARR, Thamboo A, Manji J, Dar Santos RC, Gan EC, Anstead A, et al. The effect of head position on the distribution of topical nasal medication using the Mucosal Atomization Device: A cadaver study. *Int Forum Allergy Rhinol.* 2013;3(12):958-62.
73. Kelly JT, Prasad AK, Wexler AS. Detailed flow patterns in the nasal cavity. *Journal of Applied Physiology.* 2000;89(1):323-37.
74. Nayebossadri S. *Computational and Experimental Study of Nasal cavity Airflow Dynamics*: Queen Mary University of London; 2012.
75. Spence CJT. *Experimental Investigations of Airflow in the Human Upper Airways During Natural and Assisted Breathing.* 2011.
76. Chang AE, Matory YL, Dwyer AJ, Hill SC, Girton ME, Steinberg SM, et al. Magnetic resonance imaging versus computed tomography in the evaluation of soft tissue tumors of the extremities. *Ann Surg.* 1987;205(4):340-8.
77. Kahana-Zweig R, Geva-Sagiv M, Weissbrod A, Secundo L, Soroker N, Sobel N. Measuring and characterizing the human nasal cycle. *PloS one.* 2016;11(10):e0162918.
78. Craig JR, Palmer JN, Zhao K. Computational fluid dynamic modeling of nose-to-ceiling head positioning for sphenoid sinus irrigation. *International Forum of Allergy and Rhinology.* 2017;7(5):474-9.
79. Jo G, Chung SK, Na Y. Numerical study of the effect of the nasal cycle on unilateral nasal resistance. *Respiratory Physiology and Neurobiology.* 2015;219:58-68.
80. Patel RG, Garcia GJM, Frank-Ito DO, Kimbell JS, Rhee JS. Simulating the nasal cycle with computational fluid dynamics. *Otolaryngology - Head and Neck Surgery (United States).* 2015;152(2):353-60.
81. Yu S, Liu Y, Sun X, Li S. Influence of nasal structure on the distribution of airflow in nasal cavity. *Rhinology.* 2008;46(2):137-43.
82. Weinhold I, Mlynski G. Numerical simulation of airflow in the human nose. *Eur Arch Otorhinolaryngol.* 2004;261(8):452-5.
83. Schroeter JD, Garcia GJM, Kimbell JS. Effects of surface smoothness on inertial particle deposition in human nasal models. *Journal of Aerosol Science.* 2011;42(1):52-63.
84. Shanley KT, Zamankhan P, Ahmadi G, Hopke PK, Cheng YS. Numerical simulations investigating the regional and overall deposition efficiency of the human nasal cavity. *Inhal Toxicol.* 2008;20(12):1093-100.
85. Frank DO, Zanation AM, Dhandha VH, McKinney KA, Fleischman GM, Ebert CS, et al., editors. *Quantification of airflow into the maxillary sinuses before and after functional endoscopic sinus surgery.* *Int Forum Allergy Rhinol*; 2013: Wiley Online Library.
86. Schroeter JD, Kimbell JS, Asgharian B. Analysis of particle deposition in the turbinate and olfactory regions using a human nasal computational fluid dynamics model. *J Aerosol Med.* 2006;19(3):301-13.
87. Abouali O, Keshavarzian E, Farhadi Ghalati P, Faramarzi A, Ahmadi G, Bagheri MH. Micro and nanoparticle deposition in human nasal passage pre and post virtual maxillary sinus endoscopic surgery. *Respir Physiol Neurobiol.* 2012;181(3):335-45.
88. Xi J, Longest PW. Numerical predictions of submicrometer aerosol deposition in the nasal cavity using a novel drift flux approach. *Int J Heat Mass Transf.* 2008;51(23-24):5562-77.
89. Inthavong K, Zhang K, Tu J. Numerical modelling of nanoparticle deposition in the nasal cavity and the tracheobronchial airway. *Computer Methods in Biomechanics and Biomedical Engineering.* 2011;14(7):633-43.
90. Lee JH, Na Y, Kim SK, Chung SK. Unsteady flow characteristics through a human nasal airway. *Respir Physiol Neurobiol.* 2010;172(3):136-46.
91. Liu Y, Matida EA, Gu J, Johnson MR. Numerical simulation of aerosol deposition in a 3-D human nasal cavity using RANS, RANS/EIM, and LES. *Journal of Aerosol Science.* 2007;38(7):683-700.
92. Naftali S, Rosenfeld M, Wolf M, Elad D. The Air-Conditioning Capacity of the Human Nose. *Annals of Biomedical Engineering.* 2005;33(4):545-53.
93. Elad D, Naftali S, Rosenfeld M, Wolf M. Physical stresses at the air-wall interface of the human nasal cavity during breathing. *Journal of Applied Physiology.* 2006;100(3):1003-10.

94. Zhang J. Characteristic size research of human nasal cavity and the respiratory airflow CFD analysis. *Journal of Biosciences and Medicines*. 2013;1(02):23.
95. Afiza E, Takakura Y, Atsumi T, Iida M. Airflow Patterns within Real and 3D Simplified Models of Nasal Cavities ( II . Numerical Study) *Proc Schl Eng Tokai Univ*. 2015:109-19.
96. Sabersky RH, Acosta AJ, Hauptmann EG. *Fluid Flow: A First Course in Fluid Mechanics*. 1989.
97. Fox RW, McDonald AT. *Introduction to Fluid Mechanics*. 1992.
98. Afiza E, Takakura Y, Atsumi T, IIDA M, editors. Airflow Patterns within Real and 3D Simplified Models of Nasal Cavities (I. Experimental Study) *Proceedings of the School of Engineering, Tokai University, Series E*; 2015.
99. White DE, Al-Jumaily AM, Bartley J, Lu J. Correlation of nasal morphology to air-conditioning and clearance function. *Respir Physiol Neurobiol*. 2011;179(2):137-41.
100. Cankurtaran M, Çelik H, Coşkun M, Hizal E, Cakmak O. Acoustic rhinometry in healthy humans: Accuracy of area estimates and ability to quantify certain anatomic structures in the nasal cavity. *Annals of Otolaryngology, Rhinology and Laryngology*. 2007;116(12):906-16.
101. Azifa E, Takakura Y, Iida M. Function of Ostia in Airflow Patterns within Nasal Cavity Model with Maxillary Sinus. *American Scientific Research Journal for Engineering, Technology, & Sciences*. 2016;21(1).
102. Afiza E, Takakura Y, Iida M. Function of Ostia in Airflow Patterns within Nasal Cavity Model with Maxillary Sinus. *American Scientific Research Journal for Engineering, Technology, and Sciences (ASRJETS)*. 2016;21(1):41-60.
103. Pirner S, Tingelhoff K, Wagner I, Westphal R, Rilk M, Wahl FM, et al. CT-based manual segmentation and evaluation of paranasal sinuses. *European Archives of Oto-Rhino-Laryngology*. 2009;266(4):507-18.
104. Afiza E, Takakura Y, Atsumi T, Iida M. Airflow Patterns within Real and 3D Simplified Models of Nasal Cavities. *Proceedings of the School of Engineering, the School of Information Science and Technology, Tokai University*. 2015;40:10.
105. Zaidi AA, Mattern BC, Claes P, McEcoy B, Hughes C, Shriver MD. Investigating the case of human nose shape and climate adaptation. *PLoS Genetics*. 2017;13(3).
106. Durand M, Pourchez J, Louis B, Pouget J-F, Isabey D, Coste A, et al. Plastinated nasal model: a new concept of anatomically realistic cast. *Rhinology*. 2011;49(1):30-6.
107. *FLUENT User's Guide*. 2006.
108. Tu J, Inthavong K, Ahmad G. *Computational Fluid and Particle Dynamics in the Human Respiratory System*: Springer; 2013.
109. Grobler A, Weitzel EK, Buele A, Jardeleza C, Cheong YC, Field J, et al. Pre-And postoperative sinus penetration of nasal irrigation. *Laryngoscope*. 2008;118(11):2078-81.
110. Rafigh S. *Transient hydraulic flow modelling for failure of pipelines transporting incompressible liquids* University College London; 2013.
111. Barham HP, Harvey RJ. Nasal saline irrigation: Therapeutic or homeopathic. *Brazilian Journal of Otorhinolaryngology*. 2015;81(5):457-8.
112. Önerci TM. *Nasal Physiology and Pathophysiology of Nasal Disorders* Springer; 2013.
113. Liu Y, Johnson MR, Matida EA, Kherani S, Marsan J. Creation of a standardized geometry of the human nasal cavity. *Journal of applied physiology*. 2009;106(3):784-95.
114. Mohsin M, Kaushal D. A 2D-CFD (VOF model) analysis of invert trap for bed load removal in an open rectangular sewer drain. *Particulate Science and Technology*. 2017;35(1):54-66.
115. Hopkins LM, Kelly JT, Wexler AS, Prasad AK. Particle image velocimetry measurements in complex geometries. *Exp Fluids*. 2000;29(1):91-5.
116. Buchmann NA. *Development of Particle Image Velocimetry for In Vitro Studies of Arterial Haemodynamics*: University of Canterbury, Christchurch.; 2010.
117. Heo GE. Experimental and numerical investigations on the flow field inside pre- and post-surgery models of posterosuperior septectomy. *10TH INTERNATIONAL SYMPOSIUM ON PARTICLE IMAGE VELOCIMETRY*. 2013
118. Cozzi F, Felisati G, Quadrio M. VELOCITY MEASUREMENTS IN NASAL CAVITIES BY MEANS OF STAB -*Journal of Physics: Conference Series*. 2017;882:012010.

119. Zubair M, Ahmad KA, Abdullah MZ, Sufian SF. Characteristic airflow patterns during inspiration and expiration: Experimental and numerical investigation. *Journal of Medical and Biological Engineering*. 2015;35(3):387-94.
120. Van Ertbruggen C, Corieri P, Theunissen R, Riethmuller M, Darquenne C. Validation of CFD predictions of flow in a 3D alveolated bend with experimental data. *Journal of biomechanics*. 2008;41(2):399-405.
121. Bailie N, Gallagher G, Cole J, Watterson J. Computational fluid dynamics in the investigation and treatment of nasal obstruction. *WIT Transactions on State-of-the-art in Science and Engineering*. 2008;35.
122. Doorly D, Taylor D, Schroter R. Mechanics of airflow in the human nasal airways. *Respir Physiol Neurobiol*. 2008;163(1-3):100-10.
123. Chung S-K, Kim SK. Digital particle image velocimetry studies of nasal airflow. *Respir Physiol Neurobiol*. 2008;163(1-3):111-20.
124. Li H, Tian Z, Tu J, YANG W, Yeoh G, Xue C, et al. Studies of airflow through a human nasopharynx and pharynx airway. *STUDIES*. 2006;13:15.
125. Phuong NL, Ito K. Investigation of flow pattern in upper human airway including oral and nasal inhalation by PIV and CFD. *Building and Environment*. 2015;94:504-15.
126. Inthavong K, Yang W, Fung M, Tu J. External and near-nozzle spray characteristics of a continuous spray atomized from a nasal spray device. *Aerosol Science and Technology*. 2012;46(2):165-77.
127. Buchmann NA, Yamamoto M, Jermy M, David T. Particle image velocimetry (PIV) and computational fluid dynamics (CFD) modelling of carotid artery haemodynamics under steady flow: a validation study. *Journal of Biomechanical Science and Engineering*. 2010;5(4):421-36.
128. Xiong F, Chong C. PIV-validated numerical modeling of pulsatile flows in distal coronary end-to-side anastomoses. *Journal of biomechanics*. 2007;40(13):2872-81.
129. Budwig R. Refractive index matching methods for liquid flow investigations. *Exp Fluids*. 1994;17(5):350-5.
130. Spence CJT, Buchmann NA, Jermy MC, Moore SM. Stereoscopic PIV measurements of flow in the nasal cavity with high flow therapy. *Exp Fluids*. 2011;50(4):1005-17.
131. Yazdi SG, Geoghegan PH, Docherty PD, Jermy M, Khanafer A. A Review of Arterial Phantom Fabrication Methods for Flow Measurement Using PIV Techniques. *Annals of Biomedical Engineering*. 2018;46(11):1697-721.
132. Lee GH, Choi YD, Han SH. Measurement of developing turbulent flow in a U-bend of circular cross-section. *Journal of mechanical science and technology*. 2007;21(2):348-59.
133. Chang H, El Masry OA. A model study of flow dynamics in human central airways. Part I: Axial velocity profiles. *Respiration physiology*. 1982;49(1):75-95.
134. Azzola J, Humphrey J, Iacovides H, Launder B. Developing turbulent flow in a U-bend of circular cross-section: measurement and computation. *Journal of fluids engineering*. 1986;108(2):214-21.
135. Even-Tzur N, Kloog Y, Wolf M, Elad D. Mucus secretion and cytoskeletal modifications in cultured nasal epithelial cells exposed to wall shear stresses. *Biophysical journal*. 2008;95(6):2998-3008.
136. Thanaviratananich S, Ruengpolviwat S, Phuttharak W, Kasemsiri P, Chaisiwamongkol K. Paranasal Sinus Accessibility of Large Volume Saline by Intranasal Instillation in Various Head Positions. *J Med Assoc Thai*. 2017;100(6):S240-S8.
137. Roh HJ, Kim TW, Lee JH, Lee HS, Goh EK, Wang SG. Sinonasal Distribution of Nasal Drops and Spray according to Head Positions. *Korean Journal of Otorhinolaryngology-Head and Neck Surgery*. 2004;47(8):736-40.
138. Zhao K, Craig JR, Cohen NA, Adappa ND, Khalili S, Palmer JN. Sinus irrigations before and after surgery - Visualization through computational fluid dynamics simulations. *Laryngoscope*. 2016;126(3):E90-E6.
139. Raghavan U, Logan B. New method for the effective instillation of nasal drops. *The Journal of Laryngology & Otology*. 2000;114(6):456-9.

140. Schreck S, Sullivan K, Ho C, Chang H. Correlations between flow resistance and geometry in a model of the human nose. *Journal of Applied Physiology*. 1993;75(4):1767-75.
141. Scherer PW, Hahn I, Mozell M. The biophysics of nasal airflow. *Otolaryngologic Clinics of North America*. 1989;22(2):265-78.
142. Hahn I, Scherer PW, Mozell MM. Velocity profiles measured for airflow through a large-scale model of the human nasal cavity. *Journal of Applied Physiology*. 1993;75(5):2273-87.
143. Liu X, Yan W, Liu Y, Choy YS, Wei Y. Numerical investigation of flow characteristics in the obstructed realistic human upper airway. *Computational and mathematical methods in medicine*. 2016;2016.
144. Cozzi F, Felisati G, Quadrio M, editors. *Velocity Measurements in Nasal Cavities by Means of Stereoscopic Piv-Preliminary Tests*. *Journal of Physics: Conference Series*; 2017: IOP Publishing.
145. Karagama Y, Lancaster J, Karkanevatos A, O'Sullivan G. Delivery of nasal drops to the middle meatus: which is the best head position? *Rhinology*. 2001;39(4):226-9.
146. Singhal D, Weitzel EK, Lin E, Feldt B, Kriete B, McMains KC, et al. Effect of head position and surgical dissection on sinus irrigant penetration in cadavers. *Laryngoscope*. 2010;120(12):2528-31.
147. Geoghegan P, Buchmann N, Spence C, Moore S, Jermy M. Fabrication of rigid and flexible refractive-index-matched flow phantoms for flow visualisation and optical flow measurements. *Experiments in fluids*. 2012;52(5):1331-47.
148. Xiong G-x, Zhan J-M, Jiang H-Y, Li J-F, Rong L-W, Xu G. Computational fluid dynamics simulation of airflow in the normal nasal cavity and paranasal sinuses. *American journal of rhinology*. 2008;22(5):477-82.
149. Hauman C, Chandler N, Tong D. Endodontic implications of the maxillary sinus: a review. *International endodontic journal*. 2002;35(2):127-41.
150. Harvey RJ, Psaltis A, Schlosser RJ, Witterick IJ. Current concepts in topical therapy for chronic sinonasal disease. *Journal of Otolaryngology--Head & Neck Surgery*. 2010;39(3).

## Appendix A: Sensor data sheet

The specifications of the FSR force sensor used in this study are listed in Table A.1.

**Table A.1. Force sensor data sheet.**

Device thickness	0.2 to 1.25 mm
Force sensitivity range	Up to >10 kg
Pressure sensitivity range	< 1.5 psi to >150 psi
Force resolution	Better than 0.5% full scale
Stand-off resistance	>1M $\Omega$
Device rise time	1-2 msec
Temperature range	-30°C to +70°C
Maximum current	1 mA/cm <sup>2</sup> of applied force
Positional accuracy	0.075 to 0.5mm

## **Appendix B: Mesh sensitivity analysis**

The mesh sensitivity analysis was performed for all four head positions. Three planes were selected (P1, P5, and P10) to monitor the effect of increasing the mesh elements on the average pressure in the respective planes. The mesh sensitivity analysis for the Mygind head position is shown in Figure B.1. With pressure distribution and sinus penetration as the monitored value. The criteria for convergence were given as: the deviation of results being less than 1%, and the pressure distribution and sinus penetration being almost constant when the number of cells is over 3,200,000. It should be noted that due to the computational time and cost, the simulations for other head positions and side directions were repeated with 3,200,000 and 4,000,000 elements. The results of the simulations using these two different numbers of elements were similar, which shows that 3,200,000 is the optimum number of elements for all different head positions and side directions.

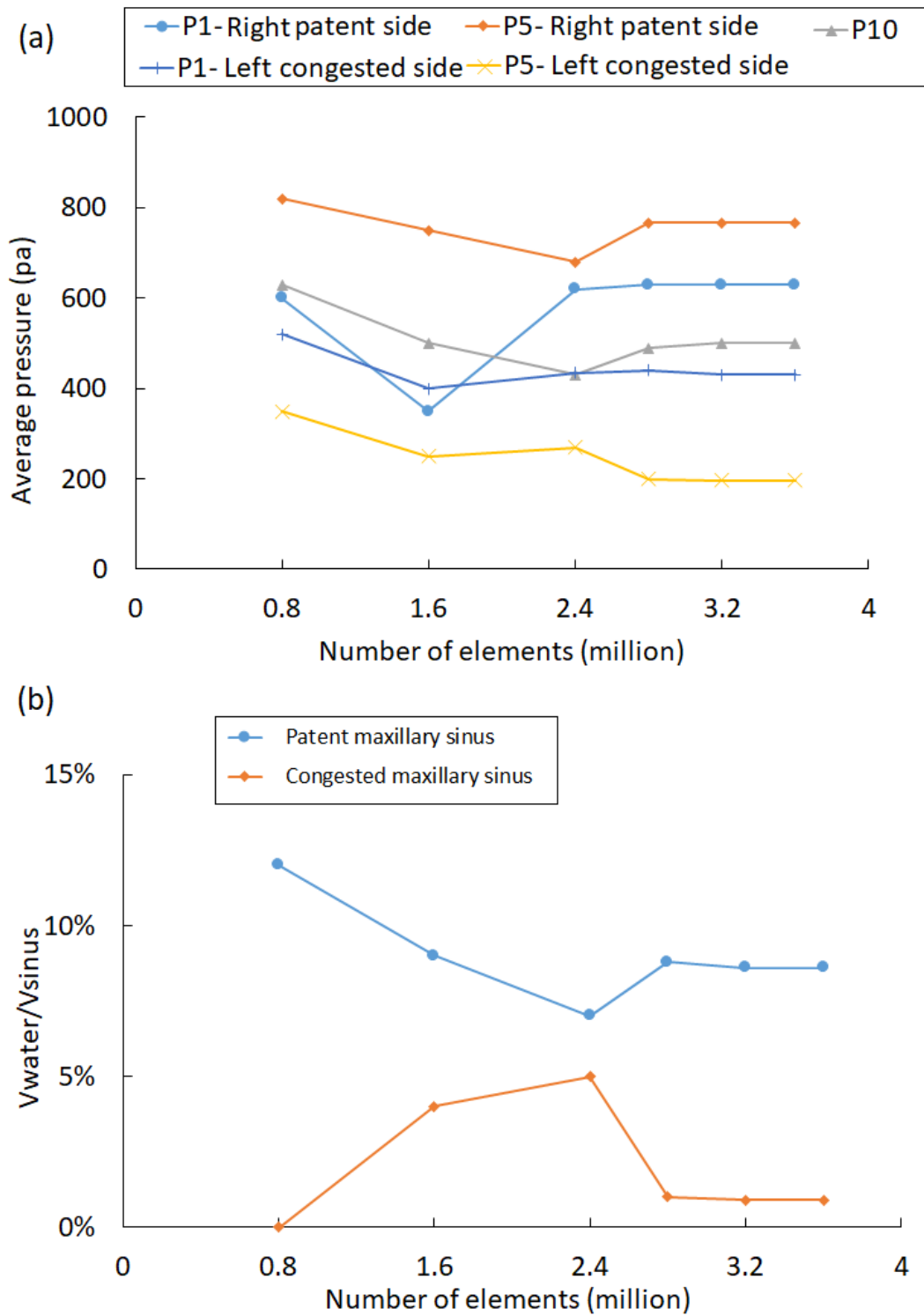


**Figure B.1. Mesh sensitivity analysis at Mygind head position irrigated from right patent side a) pressure distribution and b) sinus penetration.**

## Appendix C: Model creation

A summary of model creation was mentioned in Chapter 4. Here, the details of the manufacturing process are described.

### C.1. Rapid prototyping of the nasal cavity and maxillary sinuses.

For the model fabrication, the nasal geometry was scaled 1.5:1, to enable a higher accuracy in model construction. To reduce the amount of silicone used and to provide a realistic entry and exit condition, a volume box was attached to the nostrils. Here, the nostrils were extended by 2mm and attached to the volume box. Figure C.1 shows the final model used in the experiment.

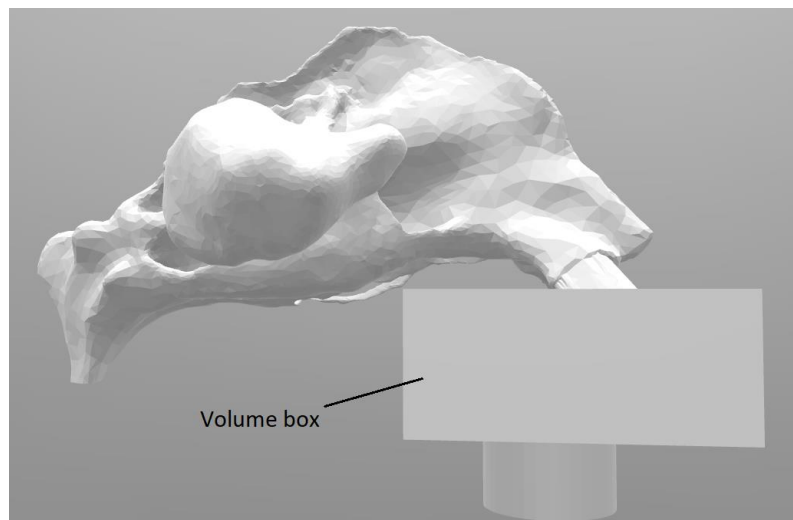


Figure C.1. Designed solid model for model casting.

To create a 3-D printed ABS nasal cavities and maxillary sinuses model, the whole of the nasal geometry and maxillary sinuses were exported as a stereo-lithography (STL) file, which is a format compatible with rapid prototyping machines. The STL file uses negative geometry for the construction of the transparent model and was rapid prototyped at the University of Canterbury using a Tier Time UP BOX FDM printer (Figure C.2). The model was constructed using Acrylonitrile Butadiene Styrene (ABS). This material is a relatively cheap petroleum-based product with the advantage that it is readily dissolved by acetone. Prior to being cast in silicone any surplus scaffolding support material was carefully removed.



**Figure C.2. Rapid prototyped model.**

### C.2. Preparing the ABS surface

This rapid prototyping process builds the nasal cavities and maxillary sinuses geometry layer by layer so hand finishing was required to remove any terracing. This smoothing involved abrading the model carefully with 240-grit and 400-grit sand paper. The 3D-printed parts also initially have a porous nature so to block the permeability of the model's surface, acetone was brushed lightly on the model to partially dissolve and smooth the outer surface. This procedure prevented silicone penetrating into the ABS surface.

### C.3. Casting box creation

A casting box of dimensions 200x155x110 mm was designed to enclose the 3D printed nasal cavities and maxillary sinuses and enable the silicone nasal model to be cast (Figure C.3). Each side of the box was cut out from an 8mm acrylic sheet using a MARS 1/3 non-metal sheet laser cut machine. The box was assembled using pan-head machine screws, sealed with silicone sealant and filled with water to check for leaks.

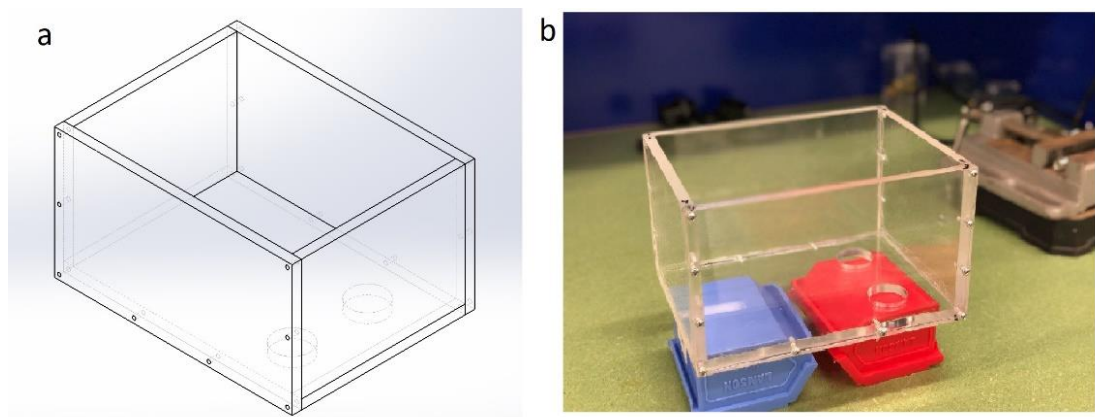


**Figure C.3. a) Picture view of casting box and b) constructed casting box.**

#### **C.4. Silicone preparation and pouring**

After carefully positioning the ABS nasal model within the casting box, it was filled with transparent silicone - Dow Corning Sylgard 184. This optically transparent silicone is a reliable material for fabricating refractive-index-matched flow phantoms for optical flow measurements (147). Sylgard 184 has a low refractive index ( $n=1.43$ ) which can be matched to glycerol in aqueous solution. Matching the refractive index between the fixed model and flowing liquid is important as it ensures that curvatures in the geometry do not distort the PIV measurements. Sylgard 184 is supplied with a curing agent which is mixed in a ratio of 10 parts base to 1-part curing agent, by weight.

The monomer and catalyst were thoroughly mixed in a plastic beaker using a plastic stirrer to ensure a homogeneous refractive index throughout the model. During this process, the curing agent creates a substantial number of bubbles throughout the mixture (Figure C.4) due to the high viscosity of the silicone (6.2 Pa at 20°C). It was necessary to remove all of the air bubbles from the mixture, as they would have destroyed the clarity of the model. This was done by placing the final mixture in a vacuum chamber (Figure C.5) to degas the silicone at a gauge pressure of -75kPa. Some bubbles which remained on top of the mixture were subsequently removed by a plastic stick.

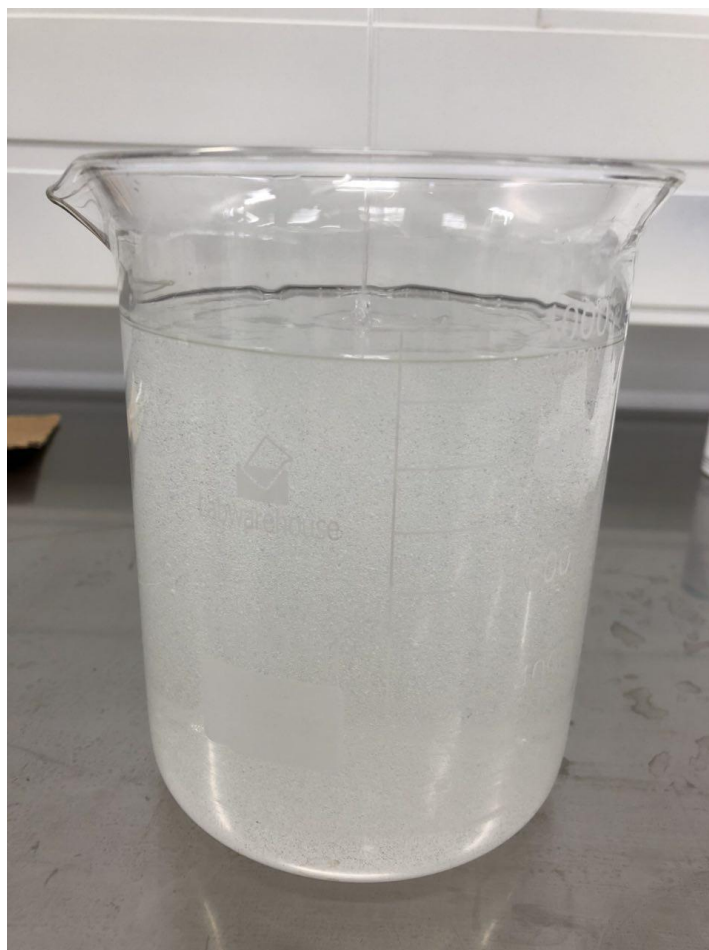


**Figure C.4. Mixing of the monomer and catalyst.**

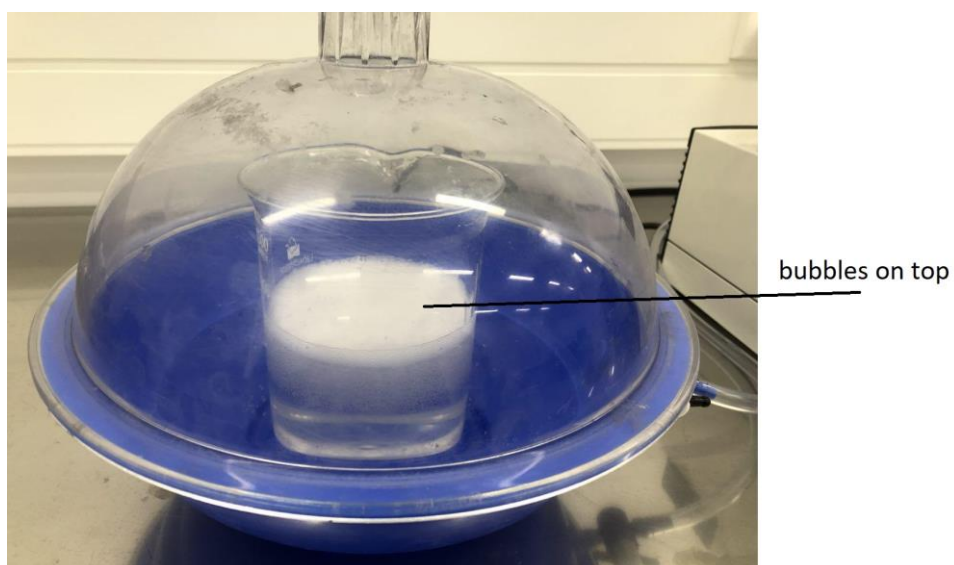


**Figure C.5. Degassing procedure using vacuum chamber.**

Once degassed, the silicone was then poured into the casting box using an open funnel to conduct the silicone around the model taking care not to entrain additional air bubbles (Figure C.6). After pouring the silicone into the mould, any additional bubbles created were removed using a tube attached to a syringe. The silicone took two days to cure at room temperature, when once cured, had the casting box was removed. Figure C.7 shows the cured silicone and the ABS model before and after removal of the casting box.



**Figure C.6. Silicone pouring using a funnel around the ABS model.**

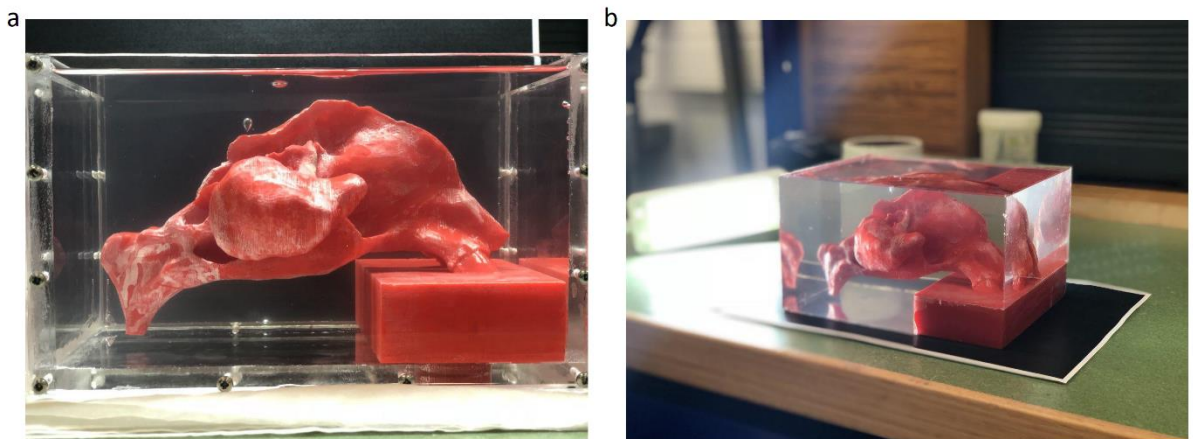


**Figure C.7. Cured silicone and the ABS model a) before and b) after removing the casting box.**

### C.5. Removing the ABS nasal cavity and maxillary sinuses

After removing the casting box, it was necessary for the negative model to be removed from the cured silicone physical nasal model. This required considerable care to prevent damage to the complex fragile silicone-surfaces. To initiate this process, the combined ABS nasal cavities, maxillary sinuses and cured silicone assembly was immersed in a bucket of acetone to dissolve the 3-D printed negative nasal model. After dissolving the ABS material in the nostrils and nasal valves, a flexible plastic tube was attached to an air pump and inserted into the nasal passages to circulate the acetone to remove further ABS material while the model remained immersed in the acetone. The congested side of the nasal model was a narrower passage, which meant that removing the ABS material from this region was particularly complicated. To allow for more acetone distribution into the model, the silicone block was put into an ultrasonic tank (Figure C.8). The model was put into a bucket of acetone and suspended in a water bath so as not to have direct contact between the model and ultrasonic actuator. The resonator heated up the water; which was subsequently replaced every 30 minutes with cold water.

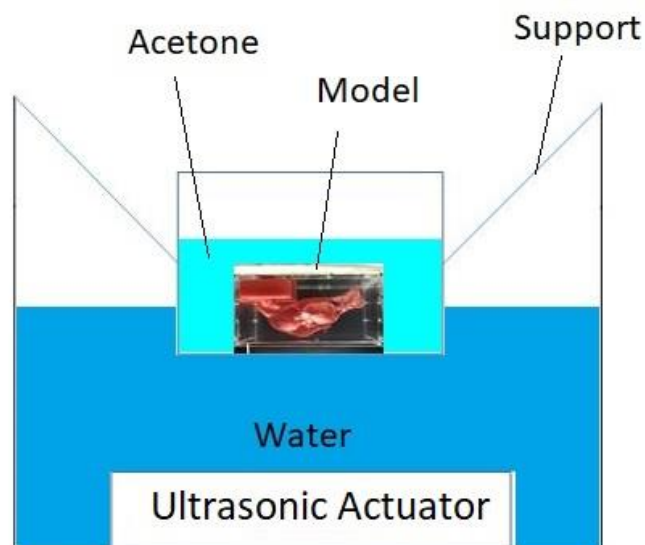


Figure C.8. Schematic view of the model in the ultrasonic resonator.

The ABS material could not be completely removed in some of the more narrow and complex nasal regions such as the olfactory cleft, the ostia, and the maxillary sinuses. The orientation of the model was changed from time-to- in order for the acetone to reach these restricted regions.

In this model, the last regions to have the ABS material removed were the maxillary sinuses and the ostia. Based on previous studies nasal irrigation penetration into these regions is thought to be very limited (148-150). To assist in dissolving the ABS material, two 0.2mm needles were inserted through the sides of the silicone model into the maxillary sinuses. Acetone was then injected through the needle into the sinus space. Once all of the ABS material had been removed, the final silicone model was washed with ethanol to clear the nasal passages (Figure C.9) and flush out any remaining acetone solution.



**Figure C.9. Completed transparent silicone nasal cavity and maxillary sinuses physical model.**

## **Appendix D: Clinical guide sheet**

Figure D.1 shows the clinical outcome of this study as a guide sheet.

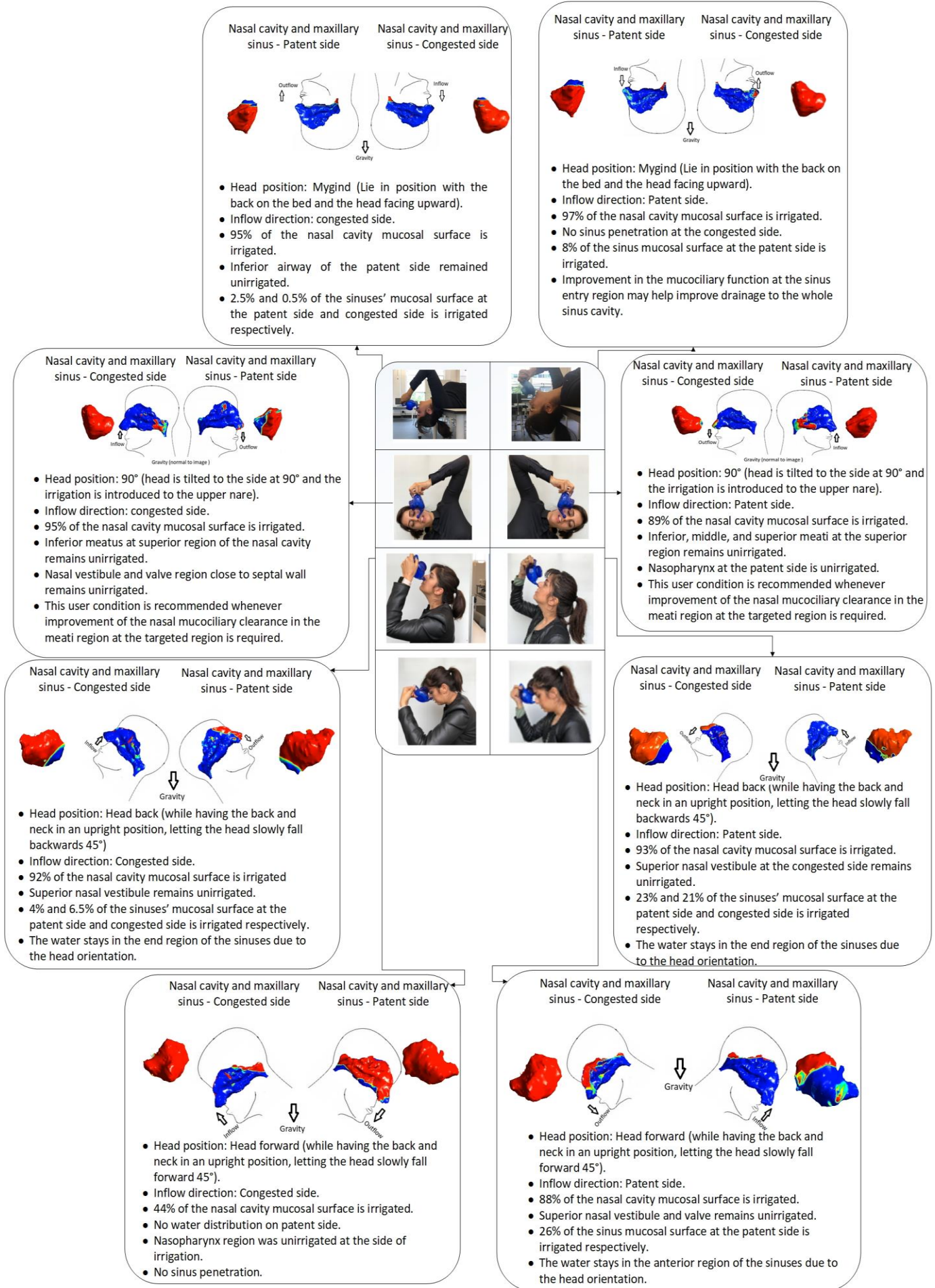


**Figure D.1. Clinical treatment guide sheet.**